Universiteit
Leiden
The Netherlands

Atomic insights into hydrodesulfurization

Prabhu, M.K.

Citation
Prabhu, M. K. (2021, June 3). *Atomic insights into hydrodesulfurization*. Retrieved from https://hdl.handle.net/1887/3182531

Version:	Publisher's Version
License:	Licence agreement concerning inclusion of doctoral thesis in the Institutional Repository of the University of Leiden
Downloaded from:	https://hdl.handle.net/1887/3182531

Note: To cite this publication please use the final published version (if applicable).

Cover Page

Universiteit Leiden

The handle https://hdl.handle.net/1887/3182531 holds various files of this Leiden University dissertation.

Author: Prabhu, M.K.
Title: Atomic insights into hydrodesulfurization
Issue Date: 2021-06-03

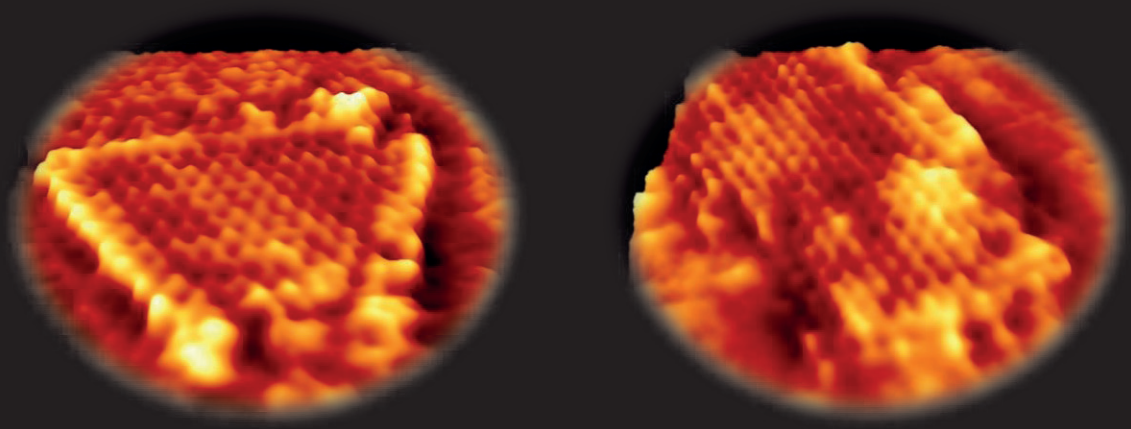

Atomic Insights into Hydrodesulfurization

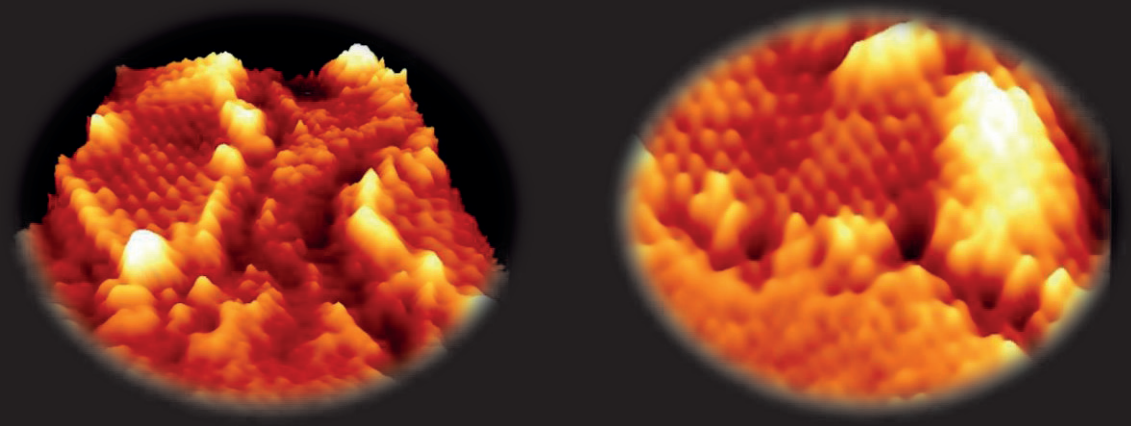

Mahesh Krishna Prabhu

ATOMIC INSIGHTS INTO HYDRODESULFURIZATION

Atomic Insights into Hydrodesulfurization

Proefschrift

ter verkrijging van
de graad van doctor aan de Universiteit Leiden,
op gezag van rector magnificus prof.dr.ir. H. Bijl,
volgens besluit van het college voor promoties
te verdedigen op donderdag 03 Juni 2021
klokke 10:00 uur

door

Mahesh Krishna Prabhu

geboren te Kochi, India

in 1991

Samenstelling promotiecommissie

Promotor:

Prof. Dr. M.T.M. Koper	Leiden University

Co-promotor:

Dr. I.M.N. Groot	Leiden University

Overige commissieleden:

Prof. Dr. E. Bouwman	Leiden University
Prof. Dr. H. S. Overkleeft	Leiden University
Dr. J. Meyer	Leiden University
Dr. M. Heyde	Fritz-Haber-Institut der Max-Planck-Gesellschaft
Prof. Dr. E. T. C. Vogt	Utrecht University

ISBN :

An electronic version of this thesis is available at :

https://scholarlypublications.universiteitleiden.nl

The work described in this thesis was carried out in the Huygens-Kamerlingh Onnes Laboratory and the ultra-microscopy lab of the Gorlaeus Laboratory, Leiden University. The project was financially supported by the Leiden Institute of Chemistry.

The cover shows STM images of a Co-promoted MoS_2 model catalyst acquired during the hydrodesulfurization of methylthiol under industrially relevant reaction conditions.

Table of contents

1. **Introduction** **1**
2. **Experimental Methods** **11**
   - 2.0 The ReactorSTM setup 11
     - 2.0.1 Scanning tunneling microscope 12
     - 2.0.2 High-pressure STM 13
   - 2.1 X-ray photoelectron spectroscopy 15
   - 2.2 Low-energy electron diffraction 16
   - 2.3 References 17
3. **Structural Characterization of a Novel 2D Material: Cobalt Sulfide Sheets on Au(111)** **19**
   - 3.1 Introduction 20
   - 3.2 Experimental details 20
   - 3.3 Computational details 21
   - 3.4 Results and discussions 22
   - 3.5 References 30
   - Supporting information 35
4. **Simultaneous sulfidation of Mo and Co oxides supported on Au(111)** **53**
   - 4.1 Introduction 54
   - 4.2 Experimental Methods 55
     - 4.2.1 Substrate cleaning 55
     - 4.2.2 Deposition of Co and Mo oxides 55
     - 4.2.3 Sulfidation 56
     - 4.2.4 Scanning tunneling microscopy 56
     - 4.2.5 X-ray photoelectron spectroscopy 56
   - 4.3 Results 57
   - 4.4 Discussion 67
   - 4.5 Conclusions 69
   - 4.6 References 69
   - Supporting information 76
5. **Low-temperature synthesis strategy for MoS_2 slabs supported on TiO_2(110)** **83**
   - 5.1 Introduction 84
   - 5.2 Materials and Methods 85
   - 5.3 Results and Discussions 86
   - 5.4 Conclusions 98
   - 5.5 References 98
   - Supporting information 105
6. **In Situ Observation of a CoMoS Model Hydrodesulfurization Catalyst at Industrially-Relevant Conditions Using the ReactorSTM** **111**
   - 6.1 Introduction 112
   - 6.2 Experimental Methods 113
   - 6.3 Results and Discussions 116

6.4 Conclusions 134
6.5 References 135
6.6 Supporting information 141
7. **Outlook** **149**
7.1 References 151

i **Summary** **153**
ii **Sammenvatting** **155**
iii **Acknowledgments** **157**
iv **Curriculum Vitae** **158**
v **List of publications** **159**

Chapter 1

Introduction

A catalyst is a substance that provides an alternative pathway with a lower activation energy for a chemical reaction to occur. This allows for the reaction to proceed faster at a given reaction condition, thereby saving energy and resources. In some cases, the reaction also proceeds with higher selectivity, so that unwanted byproducts are minimized or eliminated. A catalyst merely participates in a chemical reaction but is not consumed by it.[1] When a catalyst acts in the same phase as the reactants, it is called a homogeneous catalyst while when the catalyst is in a different phase as compared to the reactants, it is called a heterogeneous catalyst.[1] Chemical substances that enhance the activity, selectivity, or stability of a catalyst are called promoters. Catalysis has been traditionally used by humans for manufacturing products such as beer, yoghurt, cheese, soaps, ether and oil of vitriol since the ancient times, likely without knowing its true impact. In today's society, well-established and indispensable chemical engineering industries such as clean fuel production[2], bulk chemicals[3,4], pharmaceuticals[4,5], plastics and polymers[6,7], food processing[8], and biotechnology[9] have catalysis at their backbone. In fact, catalysis is fundamental to the very origins of life as we know it because without it, many fundamental biochemical reactions necessary to sustain life would not be possible.[10]

While the term 'catalysis' was first used in the work of Jöns Jakob Berzelius in 1835[11], the discovery of catalysis predates to 1794 in the published work of Scottish chemist Elizabeth Fulhame.[12,13] Perhaps, the first large-scale commercial product that involved catalysis was the Döbereiner lamp in the 19th century where a platinum sponge catalyst was used.[14] In the late 19th century, Wilhelm Ostwald investigated acid and base catalyzed reactions and the associated reaction rates for which he was awarded the 1909 Nobel Prize in chemistry. The ground work behind a large number of modern catalytic processes involving oxidation and hydro/dehydrogenation was performed by the Russian chemist Vladimir Ipatieff in the early 20th century.[15] Ipatieff's work particularly focused on metals and metal oxide catalysts under high-pressure such as iron, copper and γ-alumina, which are extensively used in the petrochemical and refining industry today. Discovery and industrial applications of a large number of catalytic processes in the early 1900s such as the Haber-Bosch process for ammonia production and the Ostwald process for nitric acid were largely driven by the politics before and during the two world wars and led to a rapid industrialization of society.[16]

The industrialization of human society has, however, led to a world-wide dependence on fossil fuels, which continues to increase even to this day as the developing countries start to grow economically and industrialize rapidly. The fossil fuel dependence is further supplemented by the growing population. As of today, 2.5 billion tons of crude oil are processed on a daily basis to meet the existing demand.[17] The trade of crude oil has become so important that the world economy is significantly influenced by it.[18]

As a result, clean gasoline and ultra-low sulfur diesel (ULSD) consumption is expected to grow by 1% and 2% annually, respectively.[19] Over the last century, it has become very clear that the sulfurous impurities present in crude oil are released into the atmosphere as SO_x gases when the fractionated products are consumed, particularly through combustion. Given the risks posed by these gases on the environment and human health[20], a catalytic process called hydrodesulfurization (HDS) has been widely used to selectively remove these S-containing components from the crude oil fractions at the oil refineries with the help of hydrogen and a heterogeneous catalyst.

Typical crude oil contains a wide range of S-containing molecules such as aliphatic thiols, disulfides, thioethers, cyclic sulfur compounds and aromatic sulfur compounds.[21] Over the last 100 years, HDS has been carried out using heterogeneous catalysts containing Co- and Ni-promoted MoS_2 slabs supported on alumina. These catalysts have a broad-spectrum HDS activity and have efficiently met the residual sulfur standards of up to ~100 ppm as they are very efficient in removing the non-aromatic sulfur compounds from refined crude oil fractions.[22] However, the regulations on SO_x emissions worldwide have become significantly more stringent in the last decade. In the developed countries, the emission standards for sulfur have dropped to less than 10 ppm while in many developing countries especially in Asia, between 2015 to 2018, the on-road emission regulations have decreased from 350 ppm of residual sulfur to 10-50 ppm.[23] By 2025, it is expected that nearly all of the developing countries will adopt a sulfur emission standard of less than 10 ppm at least.[23] This rapid drive towards cleaner fuels has led to an increasing demand for hydrotreating of fuels worldwide. In a very recent kinetic study, it was shown that the left-over sulfur compounds after desulfurizing diesel using industrial catalysts to 100 ppm of residual sulfur are primarily the refractory substituted dibenzothiophenes.[22] The existing Co(Ni)-promoted MoS_2 catalysts have a very poor activity towards desulfurizing these refractory sulfur compounds mainly due to steric hindrance effects. However, to meet the future sulfur thresholds of <10 ppm, the residual aromatic sulfides like thiophene derivatives and substituted dibenzothiophenes also must be removed. Despite these issues, until today, the existing catalysts have not been replaced significantly on the industrial scale in spite of several improvements in their synthesis strategies.[19,24–27] In order to meet the catalytic demands of an ever decreasing emission threshold, it has become necessary to engineer a more efficient catalyst for HDS.

In order to develop a more-efficient HDS catalyst, fundamental understanding at the atomic level of the existing Co(Ni)-promoted MoS_2 catalysts is necessary. The precise working mechanism as well as the atomic structure of the active phase of the conventional HDS catalyst has been under considerable scientific discussion despite the process being well-established. This is an issue that is not isolated to HDS, but can also be encountered in many other heterogeneous catalytic processes.[28,29] This is mainly because atomic-scale insights into the structure of the catalyst while the reactions occur were not available to scientists until about two decades ago as the characterization techniques that provide information on the structure and chemistry of the active phase were still under development.[28–30] Early catalysis research in general considered a reactor with catalyst in it as a black-box and all the scientific

interpretations of the data were based on the analysis of the catalyst before and after the reaction, usually at conditions which were very different from the ones in which the reactions were carried out. This led to a large number of hypotheses and speculations, and as a result, contradictory models were suggested.[28,29]

Early surface-science approaches to catalysis did not help with solving some of these issues. While many of these studies gave detailed insights into the atomic structure of the catalyst, these studies were carried out under clean ultra-high vacuum (UHV) conditions, usually on single-crystal surfaces while industrial catalysis is carried out at high-pressure and high temperature, and on a more complex material. A 5 to 9 orders of magnitude difference in the pressure between surface-science experiments and industrial catalysis is typical.[28,29,31–34] The term 'pressure gap' has been used to refer to this large discrepancy in the pressure. Furthermore, an industrial catalyst is structurally very complex. A typical catalyst contains the active phase, the promoters, the co-promoters, and several other additives to optimize the activity and selectivity. The reductionist approach of a single-crystal model catalyst that is used in fundamental studies does not capture all the complex structural aspects of an industrial catalyst. The term 'materials gap' has been used to refer to this structural discrepancy between model catalysts used in fundamental studies and the industrial catalysts.[31–34] As the surface-science techniques evolved, in situ studies on catalysis were carried out under controlled environments.[35] These studies focused on the adsorption/desorption processes of the reactants and products and quasi in situ approaches where the reaction was quenched before characterization. Recently, spectroscopy and microscopy techniques such as infrared spectroscopy[36], Raman spectroscopy[37], X-ray diffraction[38], X-ray absorption spectroscopy[39], X-ray photoelectron spectroscopy (XPS)[40], Mössbauer spectroscopy[41,42], nuclear magnetic resonance[43], high-resolution electron microscopy[44], and scanning probe microscopy techniques such as a scanning tunneling microscope (STM)[45] have been developed and upgraded to perform such in situ characterization of catalysts. Many of these techniques have been combined with prior information from surface-science studies of single crystals and model catalysts to develop a comprehensive understanding of the catalytic process.

While these studies can give very important insights into the behavior of the active phase of an HDS catalyst, in order to link the observations to industrial catalysts, operando studies carried out at high-pressure are necessary.[28,29,31–35] As mentioned above, many of these fundamental studies are carried out under controlled conditions wherein a large pressure gap still exists with the industrial HDS conditions. The structure of the catalyst has a very strong dependence on the gas environment it is exposed to and dynamically changes according to the reaction conditions. These changes are typically related to adsorbate-induced reconstruction of the active phase and could completely change the morphology of the working catalyst.[46] Therefore, the operando atomic structural characterization of the catalyst during the reaction is very important. Simultaneous recording of any activity data, if possible, provides additional information to link the atomic structure to the observed activity.[28,29,31–35] Such structure-

activity relationships allow for the smart design of a HDS catalyst that is necessary to meet the near-future demands of clean fuels.

Scanning probe microscopy techniques in particular are very useful in this regard as their principle of operation allows them to work under a wide range of pressures and temperatures, and in media which are relevant for industrial catalysis. Several high-pressure scanning tunneling microscopes in particular have been developed in the last decades in order to try and bridge the pressure gap in catalysis.[34,47–49] The ReactorSTM especially has been very successful in this regard as it can operate under the conventional UHV conditions as well as industrially relevant high-pressure conditions allowing for a model catalyst to be studied at a very broad range of reaction conditions without the loss of atomic resolution.[48] The ReactorSTM has been used in the recent past to provide operando structural insights into very important catalytic processes such as CO oxidation[50], automobile three-way catalysis[50], Fischer-Tropsch synthesis[51], and importantly, hydrodesulfurization.[52]

In this thesis, four chapters are presented with an objective of providing atomic-level insights into model catalysts that are relevant for HDS and to bridge the gap between prior surface-science studies of HDS model catalysts and the industrial catalysts.

In the Chapter 3, atomic-level structural characterization of 2D CoS_2, a novel MoS_2-like 2D transition metal dichalcogenide (TMDC) is presented. CoS_2 is formed as a byproduct of typical recipes for synthesizing HDS model catalysts and is one of the phases that have been observed in operando studies on industrial HDS catalysts where Co is used as a promoter.[53] Prior surface-science experiments show that Co can form MoS_2-like S-Co-S layered sheets on supports like Au(111) while density functional theory (DFT) calculations show that free-standing S-Co-S sheets are highly unstable.[54–56] In our study, this disagreement is resolved by using a combination of experiments and DFT calculations. The results show that S-Co-S layered 2D CoS_2 sheets are stabilized by the interactions with the Au(111) support. The methods presented in this chapter can be applied to resolve the atomic structure of any supported 2D material.

In the Chapter 4, an alternative approach to synthesizing an HDS model catalyst via the simultaneous sulfidation of Co and Mo oxide nanoparticles on Au(111) is presented. The sulfidation of a mixed oxide precursor is the industrial method-of-choice for HDS catalyst preparation. A combination of STM and XPS is used to track the changes in chemistry and morphology at various stages of the model catalyst synthesis. The results presented in this chapter show that Co-promoted MoS_2 model catalyst for HDS can be prepared by this strategy. However, the yield of the Co-promoted MoS_2 is low because of the kinetically hindered sulfidation of the Mo oxide phasez.

In the Chapter 5, we take a detour from model catalysts involving a weakly-interacting metal supports like Au(111) to one involving a strongly-interacting oxide support, namely, MoS_2 slabs supported on TiO_2(110). TiO_2 is also one of the supports that are used in the industry and by choosing this support,

an important step is made towards bridging the materials gap with the industrial catalyst. Previously reported research work to synthesize MoS_2 slabs on TiO_2(110) has predominantly made use of many high-temperature synthesis methods. The synthesis temperatures used in these studies are much higher than those used in the synthesis of an industrial HDS catalyst. In this chapter, a low-temperature synthesis strategy and the structural characterization of MoS_2 nanoclusters supported on TiO_2(110) are presented. A combination of STM and XPS is used to investigate the morphology and the chemistry of the Mo sulfide phases formed. The results presented in this chapter show that both flat-lying MoS_2 slabs and MoS_x stripe phases are formed. The formation of these phases is driven by the strong interaction of the support with both Mo and S. Such phases have never been observed to form in the high-temperature synthesis methods.

In the chapter 6, we present the first direct observation of a Co-promoted MoS_2 model catalyst supported on Au(111) studied in situ using the ReactorSTM under industrially relevant conditions of high-pressure and high temperature. A mixture of H_2 and CH_3SH are used to simulate the industrial HDS environment, with CH_3SH as the test gaseous aliphatic thiol contaminant. The results presented in this chapter show that the edges of the Co-promoted MoS_2 nanoclusters are very sensitive to the gasses they are exposed to. Under HDS conditions, a highly dynamic behavior of the Co-substituted edges of the Co-promoted MoS_2 slabs is observed. The behavior of the Mo-terminated edges is however, observed to match well with that of Mo-terminated edges of an unpromoted MoS_2 catalyst. Furthermore, a large number of irregularly-shaped CoMoS slabs with high index terminations are also observed to form during the desulfurization of methylthiol. Evidence from ex situ XPS analysis suggests that a migration of Co atoms from the CoMoS phase to the CoS_2 phase occurs when the CoMoS slabs are exposed to HDS reaction gasses. The findings of this study give us very important insights into the complex behavior of an HDS catalyst in action and further exemplifies the need to study catalysis at industrial reaction conditions.

References

(1) Laidler, K. J. A Glossary of Terms Used in Chemical Kinetics, Including Reaction Dynamics (IUPAC Recommendations 1996). *Pure Appl. Chem.* 1996, *68* (1), 149–192. https://doi.org/10.1351/pac199668010149.

(2) Bensebaa, F. Clean Energy. In *Interface Science and Technology*; 2013; Vol. 19, pp 279–383. https://doi.org/10.1016/B978-0-12-369550-5.00005-7.

(3) Armor, J. N. A History of Industrial Catalysis. *Catal. Today* 2011, *163* (1), 3–9. https://doi.org/10.1016/j.cattod.2009.11.019.

(4) Hagen, J. *Industrial Catalysis: A Practical Approach*; 2015. https://doi.org/10.1002/9783527684625.

(5) Furuya, T.; Kamlet, A. S.; Ritter, T. Catalysis for Fluorination and Trifluoromethylation. *Nature*. 2011, pp 470–477. https://doi.org/10.1038/nature10108.

(6) Dove, A. P. Organic Catalysis for Ring-Opening Polymerization. *ACS Macro Letters*. 2012, pp 1409–1412. https://doi.org/10.1021/mz3005956.

(7) Kaminsky, W. Polymerization Catalysis. *Catal. Today* 2000, *62* (1), 23–34. https://doi.org/10.1016/S0920-5861(00)00406-5.

(8) Tavano, O. L. Protein Hydrolysis Using Proteases: An Important Tool for Food Biotechnology. *Journal of Molecular Catalysis B: Enzymatic*. 2013, pp 1–11. https://doi.org/10.1016/j.molcatb.2013.01.011.

(9) Chen, Z.; Zeng, A. P. Protein Engineering Approaches to Chemical Biotechnology. *Current Opinion in Biotechnology*. 2016, pp 198–205. https://doi.org/10.1016/j.copbio.2016.07.007.

(10) Lilley, D. M. J. The Origins of RNA Catalysis in Ribozymes. *Trends in Biochemical Sciences*. 2003, pp 495–501. https://doi.org/10.1016/S0968-0004(03)00191-9.

(11) Berzelius, J. J. *Årsberättelser Om Vetenskapernas Framsteg*; Bavarian State Library, 1835.

(12) Fulhame, E. *An Essay on Combustion, with a View to a New Art of Dying and Painting*, First Amer.; James Humphreys, 1794.

(13) Elizabeth Fulhame, a Forgotten Chemistry Pioneer. *Phys. Today* 2020, *2020* (4), 0617a. https://doi.org/10.1063/pt.6.4.20200617a.

(14) Döbereiner. Neu Entdeckte Merkwürdige Eigenschaften Des Suboxyds Des Platins, Des Oxydirten Schwefel-Platins Und Des Metallischen Platin - Staubes. *Ann. Phys.* 1823, *74* (7), 269–273. https://doi.org/10.1002/andp.18230740705.

(15) Nicholas, C. P. Dehydration, Dienes, High Octane, and High-pressures: Contributions from Vladimir Nikolaevich Ipatieff, a Father of Catalysis. *ACS Catal.* 2018, *8* (9), 8531–8539. https://doi.org/10.1021/acscatal.8b02310.

(16) Tyndall, J. Development of the Industrial Relevance of Catalysis and Its Physiochemical Basis. *Catal. Letters* 2000, *67* (1), 5–13. https://doi.org/10.1023/a:1016674822904.

(17) Silvy, R. P. Refining Catalyst Market Begins to Recover in 2010. *Oil Gas J.* 2010, *108* (15), 40–43.

(18) Hamilton, J. D. Oil and the Macroeconomy since World War II. *J. Polit. Econ.* 1983, *91* (2), 228–248. https://doi.org/10.1086/261140.

(19) de León, J. N. D.; Kumar, C. R.; Antúnez-García, J.; Fuentes-Moyado, S. Recent Insights in Transition Metal Sulfide Hydrodesulfurization Catalysts for the Production of Ultra Low Sulfur Diesel: A Short Review. *Catalysts*. 2019. https://doi.org/10.3390/catal9010087.

(20) Munawer, M. E. Human Health and Environmental Impacts of Coal Combustion and Post-Combustion Wastes. *Journal of Sustainable Mining*. 2018, pp 87–96. https://doi.org/10.1016/j.jsm.2017.12.007.

(21) Simanzhenkov, V.; Idem, R. *Crude Oil Chemistry*; 2003. https://doi.org/10.1201/9780203014042.

(22) Wu, G.; Yin, Y.; Chen, W.; Xin, F.; Lu, Y.; Qin, K.; Zhang, L.; Song, Y.; Li, M. Catalytic

Kinetics for Ultra-Deep Hydrodesulfurization of Diesel. *Chem. Eng. Sci.* 2020, *214*. https://doi.org/10.1016/j.ces.2019.115446.

(23) Miller, J.; Jin, L. *Global Progress toward Soot-Free Diesel Vehicles in 2019*; 2019.

(24) Shafiq, I.; Shafique, S.; Akhter, P.; Yang, W.; Hussain, M. Recent Developments in Alumina Supported Hydrodesulfurization Catalysts for the Production of Sulfur-Free Refinery Products: A Technical Review. *Catal. Rev. - Sci. Eng.* 2020. https://doi.org/10.1080/01614940.2020.1780824.

(25) Babich, I. V.; Moulijn, J. A. Science and Technology of Novel Processes for Deep Desulfurization of Oil Refinery Streams: A Review. *Fuel*. 2003, pp 607–631. https://doi.org/10.1016/S0016-2361(02)00324-1.

(26) Brunet, S.; Mey, D.; Pérot, G.; Bouchy, C.; Diehl, F. On the Hydrodesulfurization of FCC Gasoline: A Review. *Applied Catalysis A: General*. 2005, pp 143–172. https://doi.org/10.1016/j.apcata.2004.10.012.

(27) Song, C.; Ma, X. New Design Approaches to Ultra-Clean Diesel Fuels by Deep Desulfurization and Deep Dearomatization. In *Applied Catalysis B: Environmental*; 2003; Vol. 41, pp 207–238. https://doi.org/10.1016/S0926-3373(02)00212-6.

(28) Topsøe, H. Developments in Operando Studies and in Situ Characterization of Heterogeneous Catalysts. In *Journal of Catalysis*; 2003; Vol. 216, pp 155–164. https://doi.org/10.1016/S0021-9517(02)00133-1.

(29) Chakrabarti, A.; Ford, M. E.; Gregory, D.; Hu, R.; Keturakis, C. J.; Lwin, S.; Tang, Y.; Yang, Z.; Zhu, M.; Bañares, M. A.; Wachs, I. E. A Decade+ of Operando Spectroscopy Studies. *Catalysis Today*. 2017, pp 27–53. https://doi.org/10.1016/j.cattod.2016.12.012.

(30) Rodriguez, J. A.; Hanson, J. C.; Chupas, P. J. *In-Situ Characterization of Heterogeneous Catalysts*; John Wiley & Sons, 2013; Vol. 2013. https://doi.org/10.1016/s1351-4180(13)70477-x.

(31) Ertl, G. Heterogeneous Catalysis on Atomic Scale. In *Journal of Molecular Catalysis A: Chemical*; 2002; Vol. 182–183, pp 5–16. https://doi.org/10.1016/S1381-1169(01)00460-5.

(32) Imbihl, R.; Behm, R. J.; Schlögl, R. Bridging the Pressure and Material Gap in Heterogeneous Catalysis. *Physical Chemistry Chemical Physics*. 2007, p 3459. https://doi.org/10.1039/b706675a.

(33) Stoltze, P.; Nørskov, J. K. Bridging the "Pressure Gap" between Ultrahigh-Vacuum Surface Physics and High-Pressure Catalysis. *Phys. Rev. Lett.* 1985, *55* (22), 2502–2505. https://doi.org/10.1103/PhysRevLett.55.2502.

(34) Somorjai, G. A.; York, R. L.; Butcher, D.; Park, J. Y. The Evolution of Model Catalytic Systems; Studies of Structure, Bonding and Dynamics from Single Crystal Metal Surfaces to Nanoparticles, and from Low Pressure ($<10^{-3}$ Torr) to High-pressure ($>10^{-3}$ Torr) to Liquid Interfaces. *Physical Chemistry Chemical Physics*. 2007, pp 3500–3513. https://doi.org/10.1039/b618805b.

(35) Weckhuysen, B. M. Snapshots of a Working Catalyst: Possibilities and Limitations of in Situ

Spectroscopy in the Field of Heterogeneous Catalysis. *Chem. Commun.* 2002, *2* (2), 97–110. https://doi.org/10.1039/b107686h.

(36) Zaera, F. New Advances in the Use of Infrared Absorption Spectroscopy for the Characterization of Heterogeneous Catalytic Reactions. *Chemical Society Reviews*. 2014, pp 7624–7663. https://doi.org/10.1039/c3cs60374a.

(37) Wachs, I. E. In Situ Raman Spectroscopy Studies of Catalysts. *Top. Catal.* 1999, *8* (1–2), 57–63. https://doi.org/10.1023/a:1019100925300.

(38) Gustafson, J.; Shipilin, M.; Zhang, C.; Stierle, A.; Hejral, U.; Ruett, U.; Gutowski, O.; Carlsson, P. A.; Skoglundh, M.; Lundgren, E. High-Energy Surface X-Ray Diffraction for Fast Surface Structure Determination. *Science (80-.).* 2014, *343* (6172), 758–761. https://doi.org/10.1126/science.1246834.

(39) Frenkel, A. I.; Wang, Q.; Marinkovic, N.; Chen, J. G.; Barrio, L.; Si, R.; Cámara, A. L.; Estrella, A. M.; Rodriguez, J. A.; Hanson, J. C. Combining X-Ray Absorption and X-Ray Diffraction Techniques for in Situ Studies of Chemical Transformations in Heterogeneous Catalysis: Advantages and Limitations. *J. Phys. Chem. C* 2011, *115* (36), 17884–17890. https://doi.org/10.1021/jp205204e.

(40) Vogelaar, B. M.; Steiner, P.; van der Zijden, T. F.; van Langeveld, A. D.; Eijsbouts, S.; Moulijn, J. A. Catalyst Deactivation during Thiophene HDS: The Role of Structural Sulfur. *Appl. Catal. A Gen.* 2007, *318*, 28–36. https://doi.org/10.1016/j.apcata.2006.10.032.

(41) Millet, J. M. M. Mössbauer Spectroscopy in Heterogeneous Catalysis. *Advances in Catalysis*. 2007, pp 309–350. https://doi.org/10.1016/S0360-0564(06)51006-5.

(42) Niemantsverdriet, J. W.; Delgass, W. N. In Situ Mössbauer Spectroscopy in Catalysis. *Top. Catal.* 1999, *8* (1–2), 133–140. https://doi.org/10.1023/a:1019144607553.

(43) Hunger, M. In Situ Flow MAS NMR Spectroscopy: State of the Art and Applications in Heterogeneous Catalysis. *Progress in Nuclear Magnetic Resonance Spectroscopy*. 2008, pp 105–127. https://doi.org/10.1016/j.pnmrs.2007.08.001.

(44) Simonsen, S. B.; Chorkendorff, I.; Dahl, S.; Skoglundh, M.; Sehested, J.; Helveg, S. Ostwald Ripening in a Pt/SiO_2 Model Catalyst Studied by in Situ TEM. *J. Catal.* 2011, *281* (1), 147–155. https://doi.org/10.1016/j.jcat.2011.04.011.

(45) Bowker, M.; Davies, P. R. *Scanning Tunneling Microscopy in Surface Science, Nanoscience and Catalysis*; 2010. https://doi.org/10.1002/9783527628827.

(46) Salmeron, M. The Structure of Surfaces in Equilibrium with Gases and Liquids. In *Encyclopedia of Interfacial Chemistry: Surface Science and Electrochemistry*; 2018; pp 292–298. https://doi.org/10.1016/B978-0-12-409547-2.13634-0.

(47) Jensen, J. A.; Rider, K. B.; Chen, Y.; Salmeron, M.; Somorjai, G. A. High-pressure, High Temperature Scanning Tunneling Microscopy. *J. Vac. Sci. Technol. B Microelectron. Nanom. Struct.* 1999, *17* (3), 1080. https://doi.org/10.1116/1.590697.

(48) Herbschleb, C. T.; Van Der Tuijn, P. C.; Roobol, S. B.; Navarro, V.; Bakker, J. W.; Liu, Q.; Stoltz, D.; Cañas-Ventura, M. E.; Verdoes, G.; Van Spronsen, M. A.; Bergman, M.; Crama, L.;

Taminiau, I.; Ofitserov, A.; Van Baarle, G. J. C.; Frenken, J. W. M. The ReactorSTM: Atomically Resolved Scanning Tunneling Microscopy under High-Pressure, High-Temperature Catalytic Reaction Conditions. *Rev. Sci. Instrum.* 2014, *85* (8). https://doi.org/10.1063/1.4891811.

(49) Laegsgaard, E.; Österlund, L.; Thostrup, P.; Rasmussen, P. B.; Stensgaard, I.; Besenbacher, F. A High-Pressure Scanning Tunneling Microscope. *Rev. Sci. Instrum.* 2001, *72* (9), 3537–3542. https://doi.org/10.1063/1.1389497.

(50) Van Spronsen, M. A.; Van Baarle, G. J. C.; Herbschleb, C. T.; Frenken, J. W. M.; Groot, I. M. N. High-Pressure Operando STM Studies Giving Insight in CO Oxidation and NO Reduction over Pt(110). *Catal. Today* 2015, *244*, 85–95. https://doi.org/10.1016/j.cattod.2014.07.008.

(51) Navarro, V.; Van Spronsen, M. A.; Frenken, J. W. M. In Situ Observation of Self-Assembled Hydrocarbon Fischer-Tropsch Products on a Cobalt Catalyst. *Nat. Chem.* 2016, *8* (10), 929–934. https://doi.org/10.1038/nchem.2613.

(52) Mom, R. V.; Louwen, J. N.; Frenken, J. W. M.; Groot, I. M. N. In Situ Observations of an Active MoS_2 Model Hydrodesulfurization Catalyst. *Nat. Commun.* 2019, *10* (1). https://doi.org/10.1038/s41467-019-10526-0.

(53) Plais, L.; Lancelot, C.; Lamonier, C.; Payen, E.; Briois, V. First in Situ Temperature Quantification of CoMoS Species upon Gas Sulfidation Enabled by New Insight on Cobalt Sulfide Formation. *Catal. Today* 2020. https://doi.org/10.1016/j.cattod.2020.06.065.

(54) Kibsgaard, J.; Morgenstern, K.; Lægsgaard, E.; Lauritsen, J. V.; Besenbacher, F. Restructuring of Cobalt Nanoparticles Induced by Formation and Diffusion of Monodisperse Metal-Sulfur Complexes. *Phys. Rev. Lett.* 2008, *100* (11). https://doi.org/10.1103/PhysRevLett.100.116104.

(55) Ataca, C.; Şahin, H.; Ciraci, S. Stable, Single-Layer MX_2 Transition-Metal Oxides and Dichalcogenides in a Honeycomb-like Structure. *J. Phys. Chem. C* 2012, *116* (16), 8983–8999. https://doi.org/10.1021/jp212558p.

(56) Prabhu, M. K.; Boden, D.; Rost, M. J.; Meyer, J.; Groot, I. M. N. Structural Characterization of a Novel Two-Dimensional Material: Cobalt Sulfide Sheets on Au(111). *J. Phys. Chem. Lett.* 2020, *11* (21), 9038–9044. https://doi.org/10.1021/acs.jpclett.0c02268.

Chapter 2

Experimental Methods

2.0 The ReactorSTM setup

All the experiments presented in this thesis were carried out in the ReactorSTM ultra-high vacuum (UHV) setup shown in Figure 1.[1] The ReactorSTM has three stainless steel chambers which house the high-pressure scanning tunneling microscope (STM), a combined low-energy electron diffraction (LEED) - Auger electron spectroscopy (AES) apparatus, an X-ray photoelectron spectroscopy (XPS) system and the sample preparation facilities.

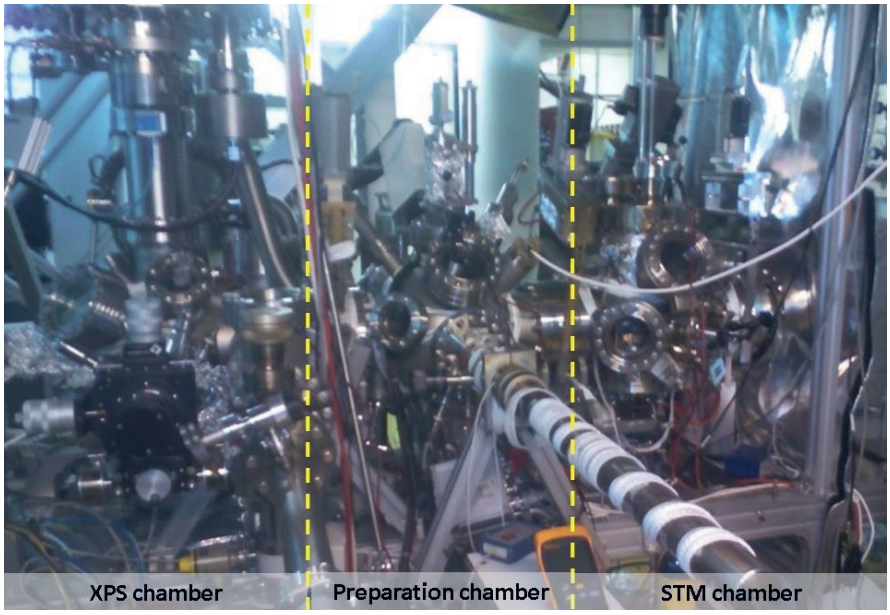

Figure 1: A photograph of the ReactorSTM setup.

The high-pressure STM is housed in the first chamber, the sample preparation and LEED/AES are housed in the second chamber called the "preparation chamber" and the XPS is in the third chamber. A transfer arm is used to move the sample between the chambers without air exposure. All the three chambers are independently pumped by ion pumps and are maintained at UHV conditions. The preparation chamber has a commercial sputtering gun, an e-beam evaporator and leak valves for dosing gases such as Ar, H_2, O_2, and H_2S. For reaching high local pressures of oxygen, the respective leak valve is attached to a doser which can be extended to reach very close to the surface of the sample. The sample heating is carried out using radiation and e-beam heating via a filament of thoriated-tungsten placed at the back of the sample inside the sample holder. Furthermore, there is also a load-lock system for transferring the samples from air into the UHV without breaking the vacuum.

2.0.1 Scanning tunneling microscope (STM)

Figure 2 shows the schematic with the essential components of a scanning tunneling microscope. An atomically sharp tip made of a wire of tungsten or Pt-Ir alloy, which is used as the probe, is attached to a piezoelectric scanner. The piezo electric scanner has orthogonal transducers along the X, Y, and Z directions each with a separate electronic connection. Application of a suitable voltage at each of these connections can be used to actuate the piezo, and hence the tip, in the three Cartesian directions. With the help of a coarse motor and by the application of a voltage along the Z direction, the atomically sharp tip is brought within a few angstroms of the sample of interest. Thereafter, a voltage is applied between the tip and sample to establish a tunneling junction. By applying a saw-tooth voltage input at X and a ramp input at Y, the tip can be moved in a raster manner across the surface. A preamplifier is used to boost the tunneling current signal which is then sent to a feedback system. The feedback system calculates the error in the tunneling current with respect to a user-decided set point. Using this error, the feedback acts on the Z voltage to reduce the error and maintain the tunneling current. Thus, by recording the tunneling current in a raster manner, a spatial map of the local density of states (LDOS) can be generated. This map is plotted on the computer screen as the STM image. The entire STM assembly has to be vibrationally isolated from the surroundings as electron tunneling is a very sensitive phenomenon. Such a vibrational isolation is achieved by suspending the rigid STM assembly on an eddy-current damping system. STM is a very robust technique than can be operated from near absolute zero to several hundred kelvin temperatures, in vacuum and high-pressure of gases, in liquids and electrochemical environments as long as there is a conducting sample to study. A detailed description of an STM can be found elsewhere.[2]

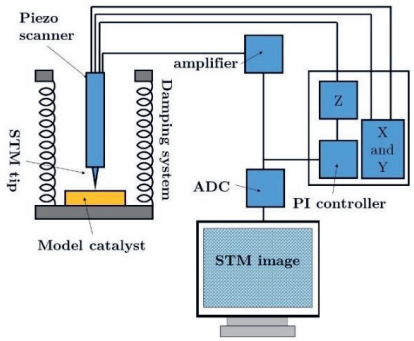

Figure 2. Schematic of a scanning tunneling microscope

The tunneling current I is a function of the applied voltage V, location z, local density of states ρ, mass of electron m, work function of the material φ and Planck constant h. This is represented by the equation:

$$I \propto V \rho e^{\frac{-4\pi z\sqrt{2m\varphi}}{h}} \tag{2.1}$$

Near the Fermi level, this equation can be written as:

$$I \propto V \rho_s e^{-1.025 z\sqrt{\varphi}} \tag{2.2}$$

Thus, there is a direct proportionality between I and applied voltage V. I exponentially decays ($\sim e^{-2.292}$ for $\varphi = 5$ eV) with the tip-sample distance z. Therefore, small changes in the tip-sample distance result in large variations in the tunneling current. The feedback system makes use of this property to apply the corrections in the Z voltage to maintain the tunneling current. As is evident from Equation 2.2, a conducting surface is necessary to have a finite ρ_s and a non-zero I.[2,3]

2.0.2 High-pressure STM

Heterogeneous catalysis is driven by surface reactions and therefore, understanding the surface structure of the catalyst is necessary for establishing the structure-activity relationships. A large number of catalytic processes use a catalysts that involve metal or metal sulfide nanoparticles supported on a metal oxide surface. Being one of the few techniques which are sensitive to the surface at the atomic level and one that does not impose limitations at the fundamental level when bridging the pressure gap, STM is an ideal technique to study model catalysts at industrially relevant conditions and resolve many of the unsolved problems of catalysis.[1,4]

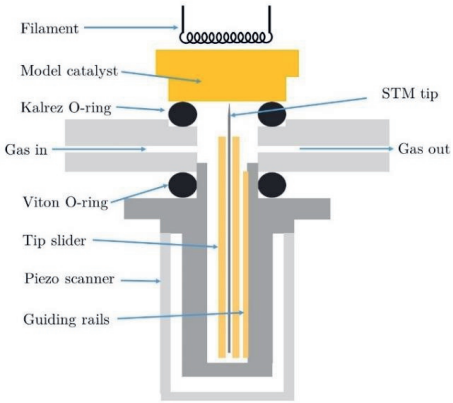

Figure 3. Schematic of the high-pressure STM for studying model catalysts at industrially relevant conditions based on Herbschleb et al.[1]

Figure 3 shows the schematic cross section of the high-pressure STM used in the studies presented in this thesis. The high-pressure STM assembly consists of a combination of the STM itself, the reactor volume, and the sample holder. The construction of the STM is such that the volume of the reactor formed by pressing the sample holder against the STM is 50 µL. The reactor is sealed vacuum tight from the rest of the assembly and the UHV components by two chemically inert elastomer O-rings as shown in Figure 3. The lower seal in Figure 3 is made up of Viton while the upper seal between the

sample and the STM is made up of Kalrez. The use of these O-rings limits the operating temperature to 600 K. The hat-shaped sample of interest is electrically isolated from the sample holder and has a filament mounted at its rear for radiative heating. K-type thermocouples welded on to the sample allow for direct temperature measurement. A set of bellows are used to press the sample, the Kalrez O-ring, and the STM together to establish a closed reactor cell. Capillary-size channels are present in the reactor volume to allow for the flow of gases. The channels are directly connected to a dedicated gas cabinet and a quadrupole mass spectrometer to control and monitor the flow of gases. A total operating pressure of up to 6 bar is possible. For establishing the tunneling junction, a single piezo tube is used for both the coarse Z approach and the raster scanning motion. The STM tip is placed within a gold-coated stainless-steel holder which is actuated by an SmCo magnet against a pair of gold-coated rails to allow for optimum stick-slip behavior and chemical inertness of these metallic parts. The magnet is chosen such that the force generated by the magnet overcomes the static friction between the tip holder and the guiding rails. A set of video-rate scanning electronics allows for the acquisition of the STM images at up to ~1 image/second with a resolution of 256 x 256 square pixels. Typically, operando STM images are acquired at 512 x 512 square pixel resolution with an acquisition time of 10-20 seconds.[1,5,6]

A typical experiment with the high-pressure STM starts with the preparation of the model catalyst in the preparation chamber according to the desired recipe. Meanwhile, the gas dosing system is baked out at ~423 K for several hours under the flow of Ar gas to remove any residual gasses and impurities. The prepared model catalyst is then loaded into the STM by the means of a transfer arm. At this stage, the Kalrez O-ring is placed on the reactor with the help of a wobble stick. The bellows of the reactor and the damping system are then actuated to close the gap between the reactor and the model catalyst. This ensures that the Kalrez O-ring makes a vacuum-tight contact with the sample and the reactor body as is shown in Figure 3. The gas dosing system is designed such that the closed reactor volume, thus formed, may either be maintained at UHV or be pressurized with the reaction gasses without breaking the UHV outside the reactor volume. In this manner, only the model catalyst, the STM tip, the slider and the Kalrez O-ring are exposed to the reaction gasses. In order to reach the desired operating conditions, the reactor is initially pressurized with the reaction gasses to up to 0.1 bar. Thereafter, the temperature of the sample is increased at a rate of at most 10 K/min to the desired value. A slow heating rate is used in order to ensure that the thermal gradient within the Kalrez O-ring is gradual so that failure of the O-ring may be avoided. Once the operating temperature is reached, the system is allowed to stabilize for at least 60 minutes. Thereafter, the reactor is pressurized at the rate of 0.01 bar per minute to the desired operating pressure with the reaction gasses. The system is then allowed to stabilize for at least 60 minutes before commencing the scan. During the time that is taken to go from UHV condition to the industrial reaction conditions, changes that occur on the model catalyst cannot be observed as the imaging is commenced only after several hours, when the system is thoroughly stabilized. However, the long term effects of the reaction gasses on the catalyst morphologies can be observed with the high-pressure STM. Furthermore, after the system is stabilized, the processes which occur on the time scale of a few seconds or more may also be imaged with the high-pressure STM if sufficiently fast image acquisition rates are used.

2.1 X-ray photoelectron spectroscopy

While the STM is excellent for atomic resolution of the surface of a model catalyst, it does not provide any direct chemical information and hence, should be supplemented by a technique which is surface sensitive and also provides chemical information. XPS works by the principle of the photoelectric effect and its probing depth is determined by the mean free path of the electrons in the sample. This allows for high surface sensitivity. There are four main processes which occur during XPS characterization: Excitation of the sample with X-ray photons, ejection of core-level electrons from the atoms present in the sample, interaction of these electrons with the atoms in the sample all the way to the surface leading to elastic and inelastic scattering, electrons leaving the sample at the surface and traversing through the vacuum to reach the detector. The schematic in Figure 4 describes the basic principle of operation of an XPS.[7] For a photon energy hν where ν is the frequency and h is the Plank constant, the kinetic energy of the ejected electron is given by:

$$E_{kin} = h\nu - E_{bin} - \varphi_a \qquad (2.3),$$

where φ_a is the work function of the analyzer and E_{bin} is the binding energy of the core electron. The photoelectron's kinetic energy depends on the interaction of the atoms with their nearest neighbors and hence, by measuring E_{kin}, we can obtain direct chemical information of the model catalyst.

Electrons generated by a tungsten filament in vacuum are accelerated on to an anode by applying a high voltage. The anode is typically made of Al or Mg. The incident high-energy electron beam generates core-level holes in the anode material. The relaxation of the electrons from the higher levels into the core hole leads to the emission of X-ray photons. The characteristics of these photons are described by the K-shell emission lines of the anode. Using a set of X-ray optics in a monochromator, the K_α emission line alone is selected and the other emission lines and Bremsstrahlung are filtered out.[8]

When the X-ray photons strike the model catalyst, core-level electrons of the atoms, which are excited by the X-rays, are ejected out. These ejected electrons interact strongly with the atoms they encounter along their path. The mean free path of electrons in solids is typically only about 7-10 atomic layers for electron energies varying from 100-1000 eV which are typically encountered in the XPS analysis.[9] Therefore, only those photoelectrons within the first 7-10 atomic layers below the surface of the model catalyst manage to reach the surface and escape into the vacuum.

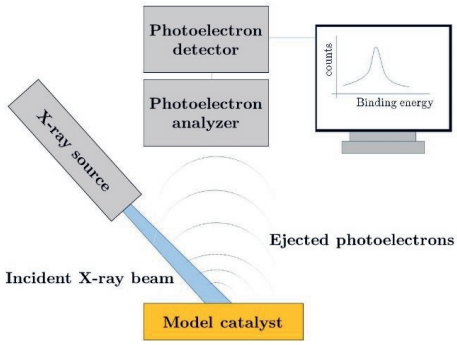

Figure 4. Schematic of the X-ray photoelectron spectroscopy apparatus

An electron analyzer captures these electrons and sorts them according to their kinetic energies. The analyzer typically performs the role of a band-pass filter for analyzing the incoming photoelectrons from the sample. The analyzer collects these photoelectrons and measures their intensity as a function of kinetic energy. Using Equation 2.3, a plot of binding energy vs intensity is generated. Analysis of the peaks in this plot gives information of the chemical state of the sample.[8]

2.2 Low-energy electron diffraction (LEED)

LEED is a powerful surface-sensitive technique for revealing the atomic structure of surfaces. Historically, LEED has been used to resolve the structure of a variety of metal and semiconductor surfaces and is an essential tool for structure determination in surface science.[10–12] LEED is particularly useful for this as it is sensitive to the actual positions of the atoms. In this study, LEED has been used to resolve the structure of 2D CoS_2 in Chapter 3.

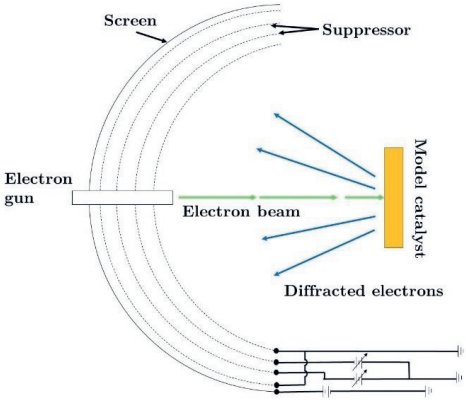

Figure 5. Schematic of the LEED apparatus based on Van Hove et al.[12]

The schematic of a typical LEED apparatus is shown in Figure 5. This apparatus consists of a 4-grid retarding field analyzer (RFA). The grids are hemispherical and concentric with the fluorescent screen on which the diffraction pattern is displayed. The electron gun is in the center through which a beam of electrons is accelerated and is incident on the sample. The electrons undergo diffraction by interacting with the surface atomic structure. The diffracted beam reflects back at the 4-grid RFA. The first grid is electrically grounded in order to maintain the region between the sample and the first grid field free. Negative potentials are applied to the second and the third grid to select diffracted electrons of a narrow energy range to be allowed to reach the fluorescent screen. The fourth grid is also grounded to ensure that the electrical fields from the fluorescent screen do not penetrate the region between the first and the fourth grid and disturb the band-filtering process of the second and the third grids. A large positive voltage (6-8 kV) is applied to the fluorescent screen to accelerate the filtered electrons and strike them against the screen and render the diffraction spots visible. By analyzing the diffraction pattern, the reciprocal-space lattice of the surface structure can be determined. From the reciprocal-space lattice, the real-space periodicity of the surface can be calculated. A detailed description of the LEED apparatus can be found elsewhere.[10–12]

2.3 References

(1) Herbschleb, C. T.; Van Der Tuijn, P. C.; Roobol, S. B.; Navarro, V.; Bakker, J. W.; Liu, Q.; Stoltz, D.; Cañas-Ventura, M. E.; Verdoes, G.; Van Spronsen, M. A.; Bergman, M.; Crama, L.; Taminiau, I.; Ofitserov, A.; Van Baarle, G. J. C.; Frenken, J. W. M. The ReactorSTM: Atomically Resolved Scanning Tunneling Microscopy under High-Pressure, High-Temperature Catalytic Reaction Conditions. *Rev. Sci. Instrum.* 2014, *85* (8). https://doi.org/10.1063/1.4891811.

(2) Chen, C. J. *Introduction to Scanning Tunneling Microscopy: Second Edition*; 2007; Vol. 9780199211. https://doi.org/10.1093/acprof:oso/9780199211500.001.0001.

(3) Kuk, Y.; Silverman, P. J. Scanning Tunneling Microscope Instrumentation. *Review of Scientific Instruments*. 1989, pp 165–180. https://doi.org/10.1063/1.1140457.

(4) Laegsgaard, E.; Österlund, L.; Thostrup, P.; Rasmussen, P. B.; Stensgaard, I.; Besenbacher, F. A High-Pressure Scanning Tunneling Microscope. *Rev. Sci. Instrum.* 2001, *72* (9), 3537–3542. https://doi.org/10.1063/1.1389497.

(5) Rost, M. J.; Crama, L.; Schakel, P.; Van Tol, E.; Van Velzen-Williams, G. B. E. M.; Overgauw, C. F.; Ter Horst, H.; Dekker, H.; Okhuijsen, B.; Seynen, M.; Vijftigschild, A.; Han, P.; Katan, A. J.; Schoots, K.; Schumm, R.; Van Loo, W.; Oosterkamp, T. H.; Frenken, J. W. M. Scanning Probe Microscopes Go Video Rate and Beyond. *Rev. Sci. Instrum.* 2005, *76* (5). https://doi.org/10.1063/1.1915288.

(6) Rost, M. J.; van Baarle, G. J. C.; Katan, A. J.; van Spengen, W. M.; Schakel, P.; van Loo, W. A.; Oosterkamp, T. H.; Frenken, J. W. M. Video-Rate Scanning Probe Control Challenges: Setting the Stage for a Microscopy Revolution. *Asian J. Control* 2009, *11* (2), 110–129. https://doi.org/10.1002/asjc.88.

(7) Pomeransky, A. A.; Khriplovich, I. B. *Equations of Motion of Spinning Relativistic Particle in External Fields*; 1999; Vol. 14. https://doi.org/10.1080/01422419908228843.

(8) Rivière, J. C. Surface Analysis. In *Handbook of Analytical Techniques*; 2008; Vol. 2–2, pp 851–949. https://doi.org/10.1002/9783527618323.ch27.

(9) Gall, D. Electron Mean Free Path in Elemental Metals. *J. Appl. Phys.* 2016, *119* (8). https://doi.org/10.1063/1.4942216.

(10) Held, G. Low-Energy Electron Diffraction (LEED). In *Surface and Thin Film Analysis: A Compendium of Principles, Instrumentation, and Applications, Second Edition*; 2011; pp 93–109. https://doi.org/10.1002/9783527636921.ch5.

(11) Jona, F.; Strozier, J. A.; Yang, W. S. Low-Energy Electron Diffraction for Surface Structure Analysis. *Reports Prog. Phys.* 1982, *45* (5), 527–585. https://doi.org/10.1088/0034-4885/45/5/002.

(12) VanHove, Michel A., Weinberg, William Henry, Chan, C.-M. *Low-Energy Electron Diffraction*; Ertl, G., Ed.; Springer-Verlag, 1986.

Chapter 3

Structural Characterization of a Novel 2D Material: Cobalt Sulfide Sheets on Au(111)

This chapter is based on:

Prabhu, M. K.; Boden, D.; Rost, M. J.; Meyer, J.; Groot, I. M. N. Structural Characterization of a Novel Two-Dimensional Material: Cobalt Sulfide Sheets on Au(111). J. Phys. Chem. Lett. 2020, 11, 21, 9038–9044

Abstract

Transition metal dichalcogenides (TMDCs) are a type of 2D materials widely investigated by both experimentalists and theoreticians, because of their unique properties. In the case of cobalt sulfide, density functional theory (DFT) calculations on freestanding S-Co-S sheets suggest there are no stable 2D cobalt sulfide polymorphs, whereas experimental observations clearly show TMDC-like structures on Au(111). In this study we resolve this disagreement by using a combination of experimental techniques and DFT calculations, considering the substrate explicitly. We find a 2D CoS_2 sheet with a CoS(0001)-like atomic structure on Au(111) that delivers excellent agreement between theory and experiment. Uniquely, this sheet exhibits a metallic character, contrary to most TMDCs, and exists due to the stabilizing interactions with the Au(111) substrate.

3.1 Introduction

Transition metal dichalcogenides (TMDCs) are a class of 2D materials that have been extensively researched over the last two decades, because of their unique chemical and mechanical properties for applications in (opto)electronics, biology, high-density storage, efficient energy harvesting, high-resolution imaging, and catalysis.[1–7] The scientific community has been on a quest to discover new TMDCs with unique properties to improve existing applications as well as to find completely new ones. Currently, the metals of groups 4 to 6 and those of group 10 are thoroughly investigated, because in the bulk, they form layered TMDCs held together by Van der Waals forces.[8] The weak Van der Waals forces enable mechanical or chemical exfoliation of 2D sheets from the bulk materials.[9]

Higher-quality single-layer TMDCs can also be synthesized by epitaxial growth on a suitable substrate, for example single-layer TMDCs of Mo,[10] W,[11] Ti,[12] Ta,[13] Zr,[14] Nb[15] and Hf.[16] Gold substrates are a preferred choice to grow many of these single-layer TMDCs as the high chalcogen affinity of gold can have a stabilizing effect.[17] Consequently, in order to properly investigate the existence and specific properties of potential TMDCs, interactions with the support must be considered.

Theoretical methods, such as density functional theory (DFT), are a powerful tool to predict new TMDC candidates with unique properties. However, the support is often not considered, which causes a major discrepancy between calculations and reality and limits the scope of the predictions. For instance, Ataca et al.[18] investigated most of the transition metals for their ability to form TMDCs using freestanding sheets in vacuum. They found that cobalt sulfide does not form stable TMDC sheets. This stands in disagreement with some experimental work by Kibsgaard et al.[19], who show TMDC-like cobalt sulfide sheets are formed on Au(111) after exposing cobalt nanoparticles to H_2S.

In this work we demonstrate that, when including the Au(111) substrate explicitly in our DFT calculations, excellent agreement between experiment and theory can be achieved for 2D cobalt sulfide. We obtain an atomic model for the cobalt sulfide sheets which nicely fits with our experimental results from scanning tunneling microscope (STM), low-energy electron diffraction (LEED) and X-ray photoelectron spectroscopy (XPS). Our structure, which is similar to bulk-terminated CoS(0001), improves the model suggested by Kibsgaard et al.[19]. In addition, the methodology used in our research could potentially be applied to other earth-abundant transition metals such as Fe, Ni, and Cu in order to explore the existence of other novel 2D materials.

3.2 Experimental details

All experiments were carried out in the *ReactorSTM*[20] in ultra-high vacuum (UHV) mode. An Au(111) single crystal was prepared by repeated cycles of sputter cleaning with Ar^+ ions (1.5 keV) and annealing to 873 K. Two-dimensional cobalt sulfide was grown by depositing cobalt in an H_2S atmosphere of 2×10^{-6} mbar onto the clean Au(111) single crystal maintained at 410 K. Thereafter, the sample was annealed to 650 K for 20 minutes and cooled down within 10 minutes to 473 K in the H_2S atmosphere. Lastly the sample was cooled down to 300 K within 120 minutes in UHV.

All STM imaging was performed with a tunneling current of ∼100 pA and a sample voltage of −1 V with the sample held at room temperature in UHV. To enhance the visibility of the details, we display

the STM images with a line-by-line background subtraction. Note, however, that the height profiles are obtained from STM images with planar background filtering on the entire image ensuring a correctly connected 2D surface. All post-processing is carried out using in-house developed software (*CAMERA* v4.3.5) as well as *WSXM*.[21] LEED experiments were performed using a commercial *Omicron SPECTALEED*. The diffraction images were obtained with a *Canon EOS50D* camera using manual focusing and a 30-second exposure time. The LEED images shown here were contrast-enhanced further in RAW format without any other processing. The XPS spectra were measured using the SPECS-Phoibos system with a *HSA 3500* hemispherical analyzer. A monochromator was used to select Al K-alpha radiation with a 1486.7 eV excitation energy and an incidence angle of 54.6 degrees was used. The spectra of S 2*p* and Co 2*p* were acquired with a pass energy of 20 eV and integrated 25 times to improve the signal-to-noise ratio. After acquisition, a Shirley background was subtracted using the *CASA XPS* software. To calculate the stoichiometry of 2D cobalt sulfide, the peak areas were corrected for their relative sensitivity factors.[22]

3.3 Computational Details

All DFT calculations were performed with the Vienna Ab Initio Simulation Package (VASP, version 5.2)[23–26] in combination with the Atomic Simulation Environment (ASE, version 3.19)[27] for generating input and analyzing output files. After having verified that spin-polarization is not relevant for CoS (bulk structure) and CoS_2 (bulk structure) consistent with earlier results,[28] the non-spin-polarized formulation of the PBE exchange correlation functional[29] has been used for all the surface calculations.

The Kohn-Sham orbitals were expanded into a plane-wave basis set with a cut-off energy of 300 eV, and ion-electron interactions were described by the projector-augmented wave method (PAW dataset 52 from 2012[30,31]). 12 × 12 × 12, 7 × 7 × 7 and 9 × 9 × 9 Monkhorst-Pack k-point grids[32] have been used for the aforementioned CoS, CoS_2 and fcc-Au bulk structures, respectively, resulting in the equilibrium lattice constants $a_{CoS}^{DFT} = 3.35$ Å (with $a_{CoS}^{DFT} / c_{CoS}^{DFT} = 2/3$), $a_{CoS2}^{DFT} = 5.49$ Å, and $a_{Au}^{DFT} = 4.16$ Å. This is in good agreement with the corresponding experimental values $a_{CoS}^{exp} = 3.38$ Å (with $a_{Au}^{exp} / c_{Au}^{exp} = 2/3$)[33], $a_{CoS2}^{exp} = 5.54$ Å[34] and $a_{Au}^{exp} = 4.07$ Å[35] which is expected for the PBE functional.[36] Despite this good agreement, differences between experimental and theoretical lengths remain, therefore in this work all distances discussed concern experimental values unless explicitly stated otherwise. Surface structures were based on a relaxed four-layer slab model for unreconstructed Au(111) with surface lattice constant $a_{Au(111)}^{DFT} = \frac{\sqrt{2}}{2} a_{Au}^{DFT}$. For the ensuing relaxations of the large-scale cobalt sulfide overlayer structures the bottom three gold layers were frozen. For all these calculations a maximum force threshold of 10^{-3} eV/ Å has been used, together with a vacuum distance of ≥ 8 Å and Monkhorst-Pack[32] k-point grids corresponding to at least 13 x 13 x 1 k-points in the primitive Au(111) unit cell. STM images have been simulated according to the Tersoff-Hamann approach[37] as implemented in the HIVE-STM software package[38] by plotting a surface of constant density of states within 0.05 eV of the reported bias voltage.

3.4 Results and discussions

Figure 1a shows the STM image of large 2D cobalt sulfide sheets grown on Au(111). The terraces of Au(111) no longer show the typical herringbone reconstruction after exposure to H_2S (see the SI). An identical distorted herringbone reconstruction of Au(111) upon exposure to H_2S has been observed in the experiments of Kibsgaard et al.[19] and also in low-coverage thiol[39–41] and hexabromobenzene[42] adsorption experiments performed by other research groups. Upon flash annealing to 673 K in UHV, the typical herringbone reconstruction is partially restored while the cobalt sulfide sheets remain intact (see SI). Furthermore, the height line A indicated in Figure 1a and shown in Figure 1b reveals that the cobalt sulfide sheet has an average thickness of 2.43 Å with corrugations of ± 0.2 Å in comparison to the experimental Au-Au step height of 2.32 Å.

The 2D cobalt sulfide grows as large pristine sheets into and out of the step edges of Au(111). The boundary-line of the 2D cobalt sulfide sheets has a curved shape along the Au-cobalt sulfide interface and the 2D cobalt sulfide step edge. Analysis of the contact angles between the line interfaces at the two triple points of the cobalt sulfide sheets reveals a mirror symmetry (see SI). The corresponding triple points of different cobalt sulfide sheets however, have surprisingly the same contact angles irrespective of the size of the sheets. This shows that the interfacial tension at the triple points of the interfaces are responsible for the observed shape of the cobalt sulfide islands. We think that the mirror symmetry arises from different edge terminations at the two triple points, however, further investigations into the interactions at the Au and 2D cobalt sulfide line interface are beyond the scope of this work.

The cobalt sulfide sheets have a hexagonal structure in their basal plane which has been further resolved in Figure 1c. This hexagonal structure consists of a rhombus-shaped unit cell marked in blue with six bright spots along its edges. This unit cell has a side length of 1.97 nm, which corresponds to 7 Au-Au inter-atomic distances. We therefore classify this structure as a (7x7) cobalt sulfide structure with respect to Au(111). This (7x7) structure is further demonstrated by the LEED pattern of the cobalt sulfide sheets shown in Figure 1d. The bright spots encircled in blue arise from the bare Au(111) surface. The small satellite spots expected for Au(111) are reduced to spot-broadening (see inset, 1d) due to the aforementioned modification of the herringbone reconstruction caused by the exposure to hydrogen sulfide. The smaller spots can be attributed to the Co sulfide sheets and show a hexagonal (7x7) symmetry with respect to the Au(111) spots in agreement with the STM results. The rhombus-shaped unit cell consists of two triangular halves, as indicated by a green dotted line in the inset of Figure 1c. One of the triangular halves (upper right one) has a higher relative contrast than the other (lower left one), causing the contrast to alternate in a hexagonal pattern. Additionally, the vertices of the rhombus-shaped unit cell appear dark in the STM image. Atomic resolution in Figure 1c reveals that the distances between the bright spots in the top layer of the cobalt sulfide of ~3.3 Å are similar to what was found by Kibsgaard et al.[19], who attributed this pattern to a sheet-like structure similar to $Co_3S_4(111)$.

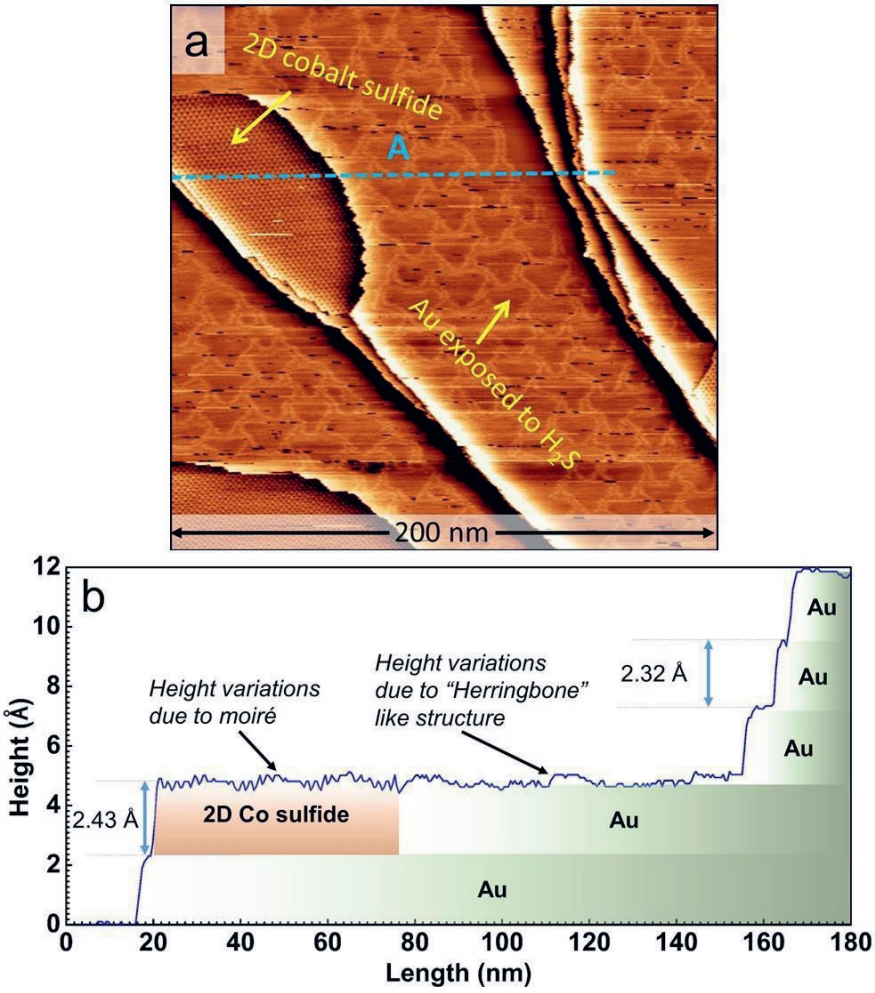
a
2D cobalt sulfide
A
Au exposed to H_2S
200 nm
b
Height variations due to moiré
Height variations due to "Herringbone" like structure
2.32 Å
2.43 Å
2D Co sulfide
Au
Au
Au
Au
Height (Å)
Length (nm)
0
2
4
6
8
10
12
0
20
40
60
80
100
120
140
160
180

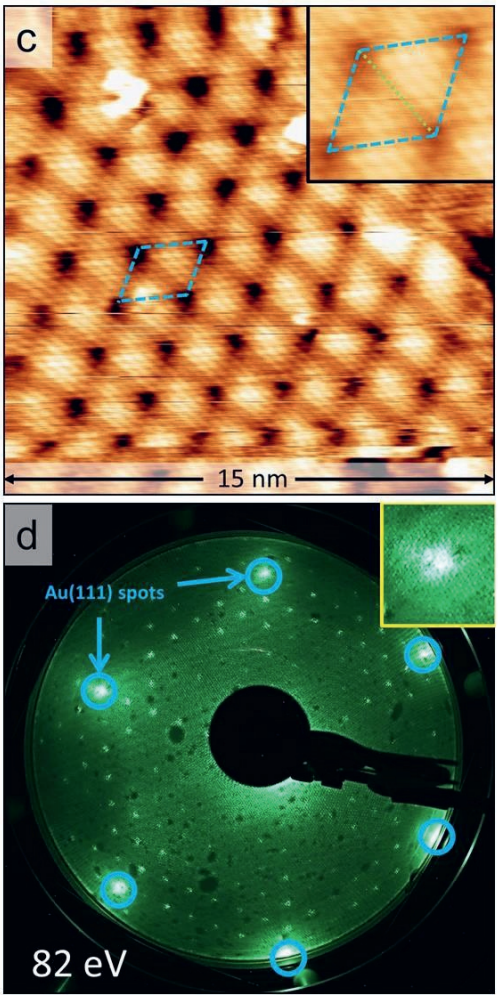

Figure 1: 2D cobalt sulfide supported on Au(111); (a) Large-scale STM image showing single-layer cobalt sulfide sheets. A modified reconstruction of Au(111) due to H_2S exposure with a long-range hexagonal arrangement is seen on the steps of gold. The respective phases are marked in the Figure. (b) Measured height profile along the blue dashed line marked A in (a). (c) Atomically-resolved STM image of the 2D cobalt sulfide. The rhombus-shaped unit cell is shown in blue with the two triangular halves demarcated by a green dotted line and enlarged in the inset for increased clarity. Image acquired at sample voltage of -0.7 V. (d) LEED pattern of cobalt sulfide sheets on Au(111) with an incident energy of 82 eV. The diffraction spots of the Au(111) surface are indicated by blue circles. Inset shows a zoom-in of the Au spot which shows that the spots due to herringbone reconstruction are reduced to spot broadening.

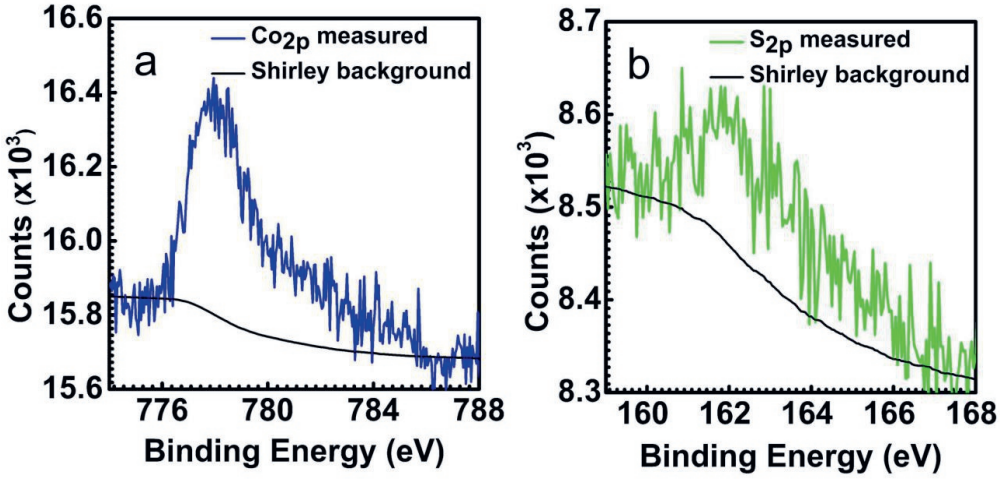

Figure 2: XPS spectra of 2D cobalt sulfide supported on Au(111) after flash annealing to 673 K to remove sulfur species adsorbed on the Au(111) terraces. (a) Co $2p_{3/2}$. (b) S $2p$.

To determine the stoichiometry of the cobalt sulfide sheets, the sample was flash annealed to 673 K in UHV in order to desorb the sulfur species on the Au(111) terraces. After this step, XPS spectra were measured (shown in Figure 2). The relative areas of the Co $2p_{3/2}$ and S $2p$ peaks were corrected by the surface relative sensitivity factors[22] to determine the Co : S ratio. Our measurements show a ratio of Co : S = 1 : 2.09 suggesting that the sheets are of the form CoS_2(see SI for details), while an approximate ratio of Co : S = 1 : 2.7 has been reported by Kibsgaard et al. using Auger electron spectroscopy.[19]

We used the experimental findings in this work and that of Kibsgaard et al. along with DFT calculations to arrive at an atomic model. A logical first structure is a sheet based on $Co_3S_4(111)$, as this is one of the most common bulk-terminated, hexagonal, cobalt sulfide surfaces reported in literature.[43] The experimental unit cell of $Co_3S_4(111)$ is 6.65 Å$\times$ 6.65 Å and the lateral S-S distance is 3.3 Å, which matches with the distance of 3.3 Å between the bright spots in the STM image in Figure 1c.[43] As discussed previously, the unit cell from LEED and STM corresponds to 7 $\times$ 7 gold atoms, which is only ~1.3% smaller than the experimental size of 3 $\times$ 3 $Co_3S_4(111)$ unit cells. To create a model for the cobalt sulfide sheet on gold, the top S-Co-S layers of a 3 $\times$ 3 $Co_3S_4(111)$ supercell are fitted onto a 7 $\times$ 7 Au(111) surface. As shown in Figure 3a, this results in an S-Co-S "sandwich" structure with a Co : S = 3 : 8 stoichiometry that is very similar to what was suggested by Kibsgaard et al.[19]. However, this $Co_3S_4(111)$-like structure proved unstable during relaxation with DFT. The simulated STM image of the resulting "rearranged" $Co_3S_4(111)$-like sheet shown in Figure 3b and the experimental STM image in Figure 1c showed no similarities. For details of the DFT relaxation, see the SI.

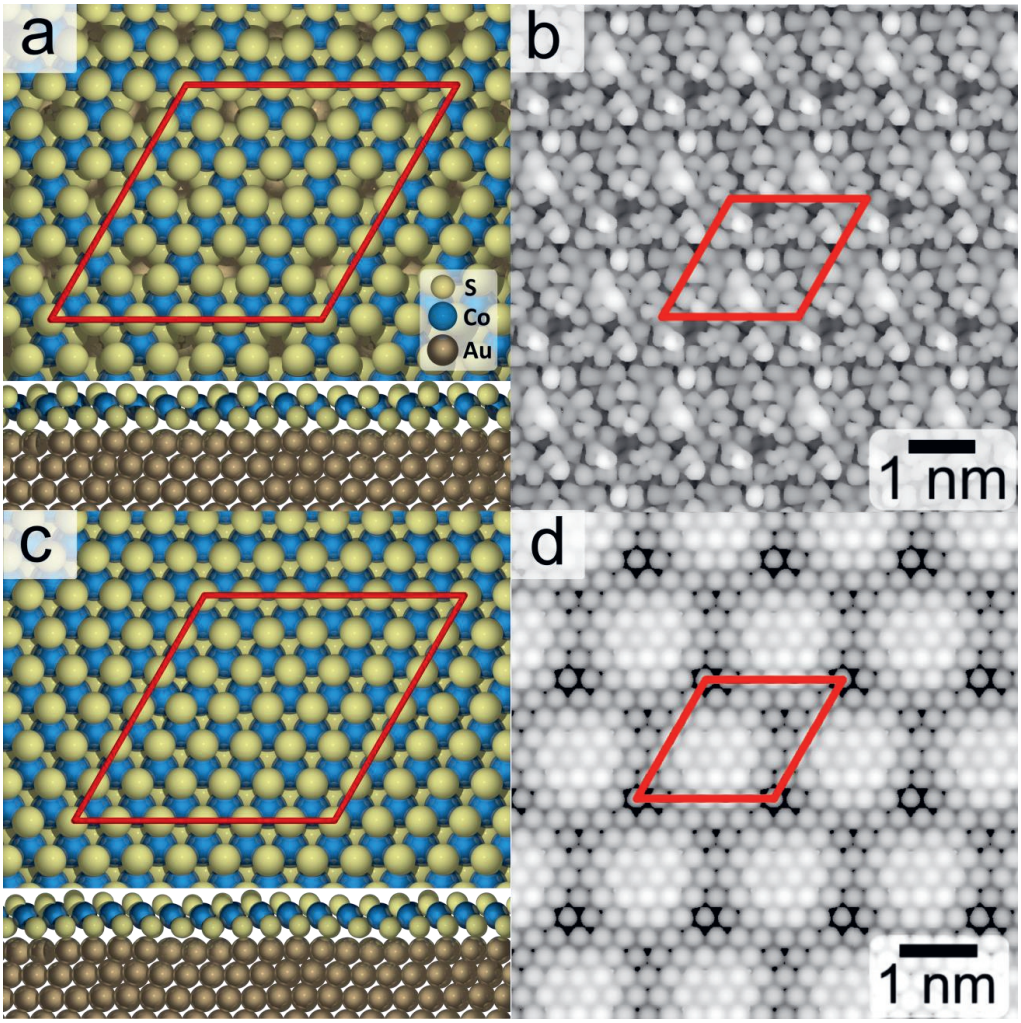

Figure 3: Schematic models of 7×7 overlayer structures on Au(111) comprised of (a) Co_3S_4(111)-like and (c) CoS(0001)-like S-Co-S sheets, each with a top (side) view in the upper (lower) part of the image. (b, d) Simulated STM images of the structures resulting from relaxation of (a) and (c), respectively. Both images were simulated using the Tersoff-Hamann method with a bias-potential of -0.3 V. The contrast has been adjusted for better comparison with Figure 1c. The unit cells in (a)-(d) are indicated in red.

CoS(0001) is another bulk-terminated cobalt sulfide surface having a hexagonal unit cell with an experimental unit cell size of 3.38 ˚A × 3.38 ˚A.[33] This means a 6 × 6 supercell of bulk-terminated CoS(0001) is ∼2.9% larger than the experimentally found unit cell of the cobalt sulfide sheet in Figure 1c. A schematic model of the CoS(0001)-like 2D CoS_2 sheet on Au(111) is shown in Figure 3c. It is very similar to the Co_3S_4(111)-like sheet, however, there are no holes in the Co layer, resulting in a Co : S = 1 : 2 stoichiometry. This matches the experimentally determined Co : S ratio of 1 : 2.09 more closely than the Co_3S_4(111)-like sheet. Furthermore, the 2D CoS_2 sheet remains stable during relaxation with DFT and the simulated STM image shown in Figure 3d reproduces most of the key features in the experimental STM image in Figure 1c. We note that the simulated STM images have a significantly higher resolution than is achievable in an STM experiment because no tunneling integral is included accounting for the finite tip size. Comparison of the bond distances in Table 1 reveals that the bond distances within the CoS(0001)-like 2D CoS_2 sheet remain similar to experimental values found in both bulk Co_3S_4 and CoS after relaxation with DFT, especially considering the known disparity stemming from the approximations in the DFT functional as discussed in the Computational Details section.

Because 6 lateral S-S distances in the 2D CoS_2 sheet are equivalent to 7 Au-Au distances along the Au(111) surface, a moiré pattern forms during relaxation with DFT featuring the striking bright and dark triangles seen in the STM images (1c), as well as the darker spots at the vertices. When the sulfur in the bottom layer sits close to the top of the underlying Au atom, it is slightly elevated (up to 0.5 Å) compared to the sulfur atom near the hollow or bridge sites, as is clearly visible in Figure 4. This causes a small corrugation in the entire cobalt sulfide sheet, which is exaggerated in the top sulfur layer. This leads to the brighter and darker areas in the STM images displayed in Figure 1c and Figure 3d.

Table 1: Average bond distances from the structure shown in Figure 3(c) after relaxation compared to corresponding bond distances in bulk cobalt sulfides and thiols on Au(111). Theoretically and experimentally obtained values are indicated with *T* and *E*, respectively

Structure	$d_{Au\text{-}S}$ (Å)	$d_{Co\text{-}S\ (bottom)}$ (Å)	$d_{Co\text{-}S(top)}$ (Å)	$d_{Co\text{-}Co}$ (Å)
CoS(0001)-like 2D CoS_2 sheet/Au(111) *T*	2.57	2.24	2.25	3.43
Bulk Co_3S_4[43,44] *E*	-	2.27	2.27	3.33
Bulk CoS[33] *E*	-	2.33	2.33	3.37
Thiols[45,46] *T*	2.63 (0.18)	-	-	-

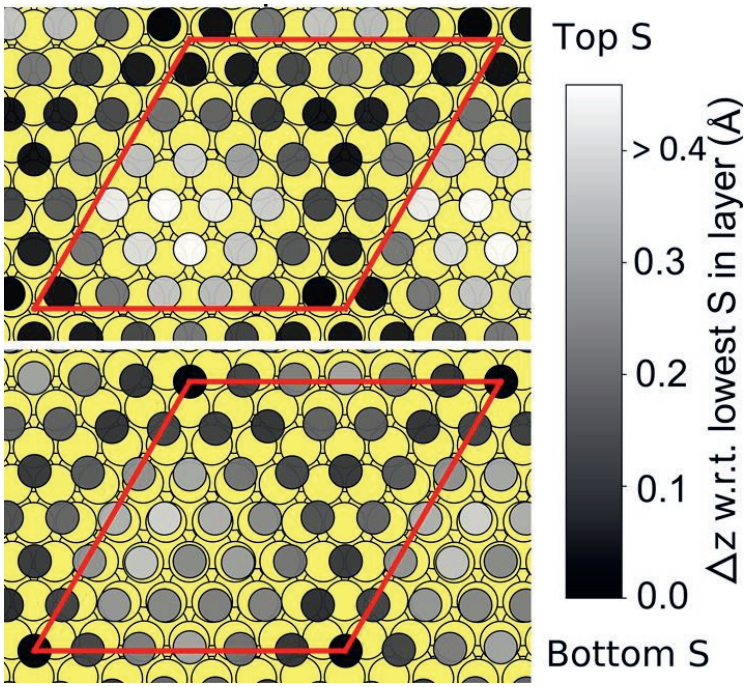

Figure 4: The positions of the sulfur atoms in the top and bottom basal planes of the cobalt sulfide sheet from Figure 3c. The gold atoms are shown in yellow, while the height of the sulfur atoms relative to the lowest atom in each respective layer is indicated in gray scale. The unit cell is displayed as a red rhombus. The height variation in the bottom layer of sulfur atoms due to the lattice mismatch with gold is exaggerated in the top layer. Comparison with Figure 3d indicates the distinct pattern can be explained by height variations of atoms in the top layer, rather than any electronic effect.

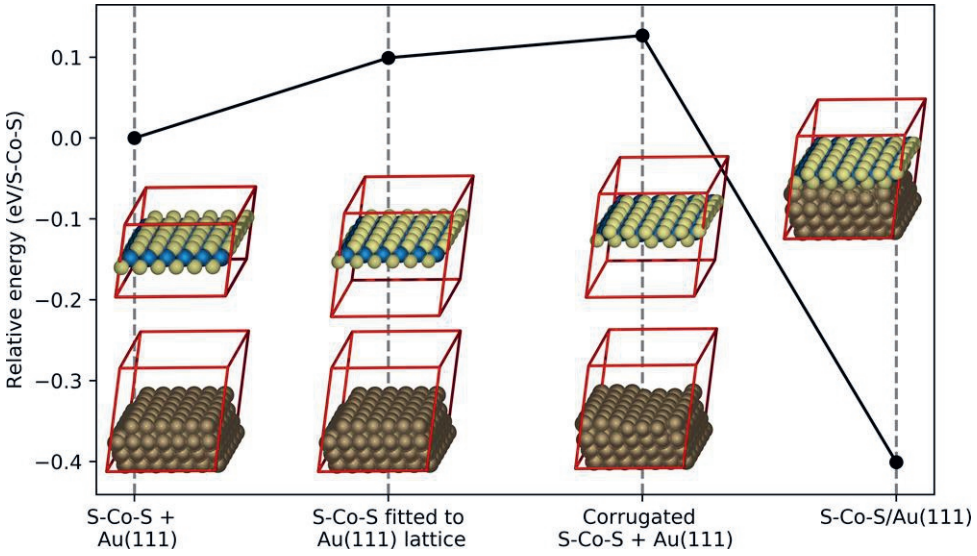

Figure 5: Decomposition of the interaction energy for the cobalt sulfide sheet and Au(111) as obtained from DFT calculations. Energies are per S-Co-S unit, with the separated Au(111) slab and freestanding S-Co-S film in equilibrium geometry shown in the leftmost inset defining the energy zero. Further from left to right: Separated Au(111) slab and freestanding S-Co-S film compressed by 1% to coincide with 7/6 Au(111) surface lattice constants, same as before but additionally including the interfacial corrugation of the structure where the S-Co-S film and Au(111) are in contact, which is finally the case in the rightmost relaxed 7x7 S-Co-S overlayer structure on Au(111) (i.e. same structure as schematically depicted in Figure 3c).

Unlike MoS_2 and TiS_2, no layered bulk structure has been reported for Co sulfide, whereby the interaction between layers consists of Van der Waals forces only, has been reported for cobalt sulfide. The cobalt sulfide bulk structure that most closely resembles MoS_2 and TiS_2 is the previously discussed CoS bulk structure. However, single-layer cobalt sulfide sheets cannot be obtained by exfoliation of a CoS crystal, because the layers are held together by covalent bonds.[17] Nevertheless, we demonstrate that 2D CoS_2 sheets with an S-Co-S structure can be synthesized on Au(111). Figure 5 shows that the interaction energy of the 2D CoS_2 sheet with the Au(111) surface is -0.40 eV per sulfur atom in the bottom layer according to our DFT calculations. This is very similar to the strong Au-S bond of thiols chemisorbed on Au(111),[45,46] as also further corroborated by the similarities in the bond lengths (see Table 1). The substantial interaction between gold and the 2D CoS_2 sheet can also be discerned from the band structure and the (projected) densities of states available in the SI, which also reveals the metallic nature of the 2D CoS_2 sheet. The formation of 2D CoS_2 sheets on the Au(111) surface may be facilitated by the strong interaction between sulfur and gold, despite the presence of Co. This interaction appears covalent in nature, since there is almost no net charge transfer between the gold and the cobalt sulfide sheet (see SI for more details).

In summary, we show that two-dimensional cobalt sulfide forms on Au(111) with a S-Co-S structure. The formation of 2D cobalt sulfide on Au(111) is facilitated by strong Au-S interactions. The nature of the electronic interaction of cobalt sulfide with the Au(111) substrate is similar to that of MoS_2, however, unlike MoS_2, cobalt sulfide does not have a band gap. Since most TMDCs are semiconductors, cobalt sulfide stands out in this regard which opens up possibilities for novel applications. In the case of 2D cobalt sulfide on Au(111), theory and experiment only agree when the substrate is considered explicitly in DFT calculations. This means that, when looking for potential new 2D materials, reliance solely on gas-phase calculations is not sufficient and a more complete approach is required.

3.5 References

(1) Jariwala, D.; Sangwan, V. K.; Lauhon, L. J.; Marks, T. J.; Hersam, M. C. Emerging Device Applications for Semiconducting Two-Dimensional Transition Metal Dichalcogenides. *ACS Nano*. 2014, pp 1102–1120. https://doi.org/10.1021/nn500064s.

(2) Chhowalla, M.; Shin, H. S.; Eda, G.; Li, L. J.; Loh, K. P.; Zhang, H. The Chemistry of Two-Dimensional Layered Transition Metal Dichalcogenide Nanosheets. *Nature Chemistry*. 2013, pp 263–275. https://doi.org/10.1038/nchem.1589.

(3) Geim, A. K.; Grigorieva, I. V. Van Der Waals Heterostructures. *Nature*. 2013, pp 419–425. https://doi.org/10.1038/nature12385.

(4) Lightcap, I. V.; Kosel, T. H.; Kamat, P. V. Anchoring Semiconductor and Metal Nanoparticles on a Two-Dimensional Catalyst Mat. Storing and Shuttling Electrons with Reduced Graphene Oxide. *Nano Lett.* 2010, *10* (2), 577–583. https://doi.org/10.1021/nl9035109.

(5) Fan, Z.; Yan, J.; Zhi, L.; Zhang, Q.; Wei, T.; Feng, J.; Zhang, M.; Qian, W.; Wei, F. A

Three-Dimensional Carbon Nanotube/Graphene Sandwich and Its Application as Electrode in Supercapacitors. *Adv. Mater.* 2010, *22* (33), 3723–3728. https://doi.org/10.1002/adma.201001029.

(6) Yin, Z.; Zhu, J.; He, Q.; Cao, X.; Tan, C.; Chen, H.; Yan, Q.; Zhang, H. Graphene-Based Materials for Solar Cell Applications. *Advanced Energy Materials*. 2014. https://doi.org/10.1002/aenm.201300574.

(7) Gong, Y.; Lin, J.; Wang, X.; Shi, G.; Lei, S.; Lin, Z.; Zou, X.; Ye, G.; Vajtai, R.; Yakobson, B. I.; Terrones, H.; Terrones, M.; Tay, B. K.; Lou, J.; Pantelides, S. T.; Liu, Z.; Zhou, W.; Ajayan, P. M. Vertical and In-Plane Heterostructures from WS_2 /MoS_2 Monolayers. *Nat. Mater.* 2014, *13* (12), 1135–1142. https://doi.org/10.1038/nmat4091.

(8) Manzeli, S.; Ovchinnikov, D.; Pasquier, D.; Yazyev, O. V.; Kis, A. 2D Transition Metal Dichalcogenides. *Nature Reviews Materials*. 2017. https://doi.org/10.1038/natrevmats.2017.33.

(9) Geim, A. K. Nobel Lecture: Random Walk to Graphene. *Rev. Mod. Phys.* 2011, *83* (3), 851–862. https://doi.org/10.1103/RevModPhys.83.851.

(10) Grønborg, S. S.; Ulstrup, S.; Bianchi, M.; Dendzik, M.; Sanders, C. E.; Lauritsen, J. V.; Hofmann, P.; Miwa, J. A. Synthesis of Epitaxial Single-Layer MoS_2 on Au(111). *Langmuir* 2015, *31* (35), 9700–9706. https://doi.org/10.1021/acs.langmuir.5b02533.

(11) Dendzik, M.; Michiardi, M.; Sanders, C.; Bianchi, M.; Miwa, J. A.; Grønborg, S. S.; Lauritsen, J. V.; Bruix, A.; Hammer, B.; Hofmann, P. Growth and Electronic Structure of Epitaxial Single-Layer WS_2 on Au(111). *Phys. Rev. B - Condens. Matter Mater. Phys.* 2015, *92* (24). https://doi.org/10.1103/PhysRevB.92.245442.

(12) Biener, M. M.; Biener, J.; Friend, C. M. Novel Synthesis of Two-Dimensional TiS_2 Nanocrystallites on Au(111). *J. Chem. Phys.* 2005, *122* (3). https://doi.org/10.1063/1.1826054.

(13) Kolekar, S.; Bonilla, M.; Ma, Y.; Diaz, H. C.; Batzill, M. Layer- and Substrate-Dependent Charge Density Wave Criticality in 1T-$TiSe_2$. *2D Mater.* 2018, *5* (1). https://doi.org/10.1088/2053-1583/aa8e6f.

(14) Tsipas, P.; Tsoutsou, D.; Fragkos, S.; Sant, R.; Alvarez, C.; Okuno, H.; Renaud, G.; Alcotte, R.; Baron, T.; Dimoulas, A. Massless Dirac Fermions in $ZrTe_2$ Semimetal Grown on InAs(111) by van Der Waals Epitaxy. *ACS Nano* 2018, *12* (2), 1696–1703. https://doi.org/10.1021/acsnano.7b08350.

(15) Stan, R. M.; Mahatha, S. K.; Bianchi, M.; Sanders, C. E.; Curcio, D.; Hofmann, P.; Miwa, J. A. Epitaxial Single-Layer NbS_2 on Au(111): Synthesis, Structure, and Electronic Properties. *Phys. Rev. Mater.* 2019, *3* (4). https://doi.org/10.1103/PhysRevMaterials.3.044003.

(16) Tsoutsou, D.; Aretouli, K. E.; Tsipas, P.; Marquez-Velasco, J.; Xenogiannopoulou, E.; Kelaidis, N.; Aminalragia Giamini, S.; Dimoulas, A. Epitaxial 2D $MoSe_2$ ($HfSe_2$) Semiconductor/2D $TaSe_2$ Metal van Der Waals Heterostructures. *ACS Appl. Mater. Interfaces* 2016, *8* (3), 1836–1841. https://doi.org/10.1021/acsami.5b09743.

(17) Sørensen, S. G.; Füchtbauer, H. G.; Tuxen, A. K.; Walton, A. S.; Lauritsen, J. V. Structure and Electronic Properties of in Situ Synthesized Single-Layer MoS_2 on a Gold Surface. *ACS Nano* 2014, *8* (7), 6788–6796. https://doi.org/10.1021/nn502812n.

(18) Ataca, C.; Şahin, H.; Ciraci, S. Stable, Single-Layer MX_2 Transition-Metal Oxides and Dichalcogenides in a Honeycomb-like Structure. *J. Phys. Chem. C* 2012, *116* (16), 8983–8999. https://doi.org/10.1021/jp212558p.

(19) Kibsgaard, J.; Morgenstern, K.; Lægsgaard, E.; Lauritsen, J. V.; Besenbacher, F. Restructuring of Cobalt Nanoparticles Induced by Formation and Diffusion of Monodisperse Metal-Sulfur Complexes. *Phys. Rev. Lett.* 2008, *100* (11). https://doi.org/10.1103/PhysRevLett.100.116104.

(20) Herbschleb, C. T.; Van Der Tuijn, P. C.; Roobol, S. B.; Navarro, V.; Bakker, J. W.; Liu, Q.; Stoltz, D.; Cañas-Ventura, M. E.; Verdoes, G.; Van Spronsen, M. A.; Bergman, M.; Crama, L.; Taminiau, I.; Ofitserov, A.; Van Baarle, G. J. C.; Frenken, J. W. M. The ReactorSTM: Atomically Resolved Scanning Tunneling Microscopy under High-Pressure, High-Temperature Catalytic Reaction Conditions. *Rev. Sci. Instrum.* 2014, *85* (8). https://doi.org/10.1063/1.4891811.

(21) Horcas, I.; Fernández, R.; Gómez-Rodríguez, J. M.; Colchero, J.; Gómez-Herrero, J.; Baro, A. M. WSXM: A Software for Scanning Probe Microscopy and a Tool for Nanotechnology. *Rev. Sci. Instrum.* 2007, *78* (1). https://doi.org/10.1063/1.2432410.

(22) Wagner, C. D. Sensitivity Factors for XPS Analysis of Surface Atoms. *J. Electron Spectros. Relat. Phenomena* 1983, *32* (2), 99–102. https://doi.org/10.1016/0368-2048(83)85087-7.

(23) Kresse, G.; Hafner, J. Ab Initio Molecular Dynamics for Liquid Metals. *Phys. Rev. B* 1993, *47* (1), 558–561. https://doi.org/10.1103/PhysRevB.47.558.

(24) Kresse, G.; Hafner, J. Ab Initio Molecular-Dynamics Simulation of the Liquid-Metalamorphous- Semiconductor Transition in Germanium. *Phys. Rev. B* 1994, *49* (20), 14251–14269. https://doi.org/10.1103/PhysRevB.49.14251.

(25) Kresse, G.; Furthmüller, J. Efficiency of Ab-Initio Total Energy Calculations for Metals and Semiconductors Using a Plane-Wave Basis Set. *Comput. Mater. Sci.* 1996, *6* (1), 15–50. https://doi.org/10.1016/0927-0256(96)00008-0.

(26) Kresse, G.; Furthmüller, J. Efficient Iterative Schemes for Ab Initio Total-Energy Calculations Using a Plane-Wave Basis Set. *Phys. Rev. B - Condens. Matter Mater. Phys.* 1996, *54* (16), 11169–11186. https://doi.org/10.1103/PhysRevB.54.11169.

(27) Hjorth Larsen, A.; JØrgen Mortensen, J.; Blomqvist, J.; Castelli, I. E.; Christensen, R.; Dułak, M.; Friis, J.; Groves, M. N.; Hammer, B.; Hargus, C.; Hermes, E. D.; Jennings, P. C.; Bjerre Jensen, P.; Kermode, J.; Kitchin, J. R.; Leonhard Kolsbjerg, E.; Kubal, J.; Kaasbjerg, K.; Lysgaard, S.; Bergmann Maronsson, J.; Maxson, T.; Olsen, T.; Pastewka, L.; Peterson, A.; Rostgaard, C.; SchiØtz, J.; Schütt, O.; Strange, M.; Thygesen, K. S.; Vegge, T.; Vilhelmsen, L.; Walter, M.; Zeng, Z.; Jacobsen, K. W. The Atomic Simulation Environment - A Python Library for Working with Atoms. *Journal of Physics Condensed Matter*. 2017. https://doi.org/10.1088/1361-648X/aa680e.

(28) Feng, Z. Y.; Yang, Y.; Zhang, J. M. The Structural, Electronic and Magnetic Properties of CoS2 under Pressure. *Solid State Commun.* 2018, *273*, 60–65. https://doi.org/10.1016/j.ssc.2018.02.010.

(29) Perdew, J. P.; Burke, K.; Ernzerhof, M. Generalized Gradient Approximation Made Simple. *Phys. Rev. Lett.* 1996, *77* (18), 3865–3868. https://doi.org/10.1103/PhysRevLett.77.3865.

(30) Blöchl, P. E. Projector Augmented-Wave Method. *Phys. Rev. B* 1994, *50* (24), 17953–17979. https://doi.org/10.1103/PhysRevB.50.17953.

(31) Joubert, D. From Ultrasoft Pseudopotentials to the Projector Augmented-Wave Method. *Phys. Rev. B - Condens. Matter Mater. Phys.* 1999, *59* (3), 1758–1775. https://doi.org/10.1103/PhysRevB.59.1758.

(32) Monkhorst, H. J.; Pack, J. D. Special Points for Brillouin-Zone Integrations. *Phys. Rev. B* 1976, *13* (12), 5188–5192. https://doi.org/10.1103/PhysRevB.13.5188.

(33) Alsén, N. Röntgenographische Untersuchung Der Kristallstrukturen von Magnetkies, Breithauptit, Pentlandit, Millerit Und Verwandten Verbindungen. *Gff* 1925, *47* (1), 19–72. https://doi.org/10.1080/11035892509443177.

(34) Nowack, E.; Schwarzenbach, D.; Hahn, T. Charge Densities in CoS_2 and NiS_2 (Pyrite Structure). *Acta Crystallogr. Sect. B* 1991, *47* (5), 650–659. https://doi.org/10.1107/S0108768191004871.

(35) Davey, W. P. Precision Measurements of the Lattice Constants of Twelve Common Metals. *Phys. Rev.* 1925, *25* (6), 753–761. https://doi.org/10.1103/PhysRev.25.753.

(36) Schimka, L.; Gaudoin, R.; Klimeš, J.; Marsman, M.; Kresse, G. Lattice Constants and Cohesive Energies of Alkali, Alkaline-Earth, and Transition Metals: Random Phase Approximation and Density Functional Theory Results. *Phys. Rev. B - Condens. Matter Mater. Phys.* 2013, *87* (21). https://doi.org/10.1103/PhysRevB.87.214102.

(37) Tersoff, J.; Hamann, D. R. Theory of the Scanning Tunneling Microscope. *Phys. Rev. B* 1985, *31* (2), 805–813. https://doi.org/10.1103/PhysRevB.31.805.

(38) Vanpoucke, D. E. P.; Brocks, G. Formation of Pt-Induced Ge Atomic Nanowires on Pt/Ge(001): A Density Functional Theory Study. *Phys. Rev. B - Condens. Matter Mater. Phys.* 2008, *77* (24). https://doi.org/10.1103/PhysRevB.77.241308.

(39) Fitts, W. P.; White, J. M.; Poirier, G. E. Low-Coverage Decanethiolate Structure on Au(111): Substrate Effects. *Langmuir* 2002, *18* (5), 1561–1566. https://doi.org/10.1021/la0107650.

(40) Liu, Y. F.; Yang, Y. C.; Lee, Y. L. Assembly Behavior and Monolayer Characteristics of OH-Terminated Alkanethiol on Au(111): In Situ Scanning Tunneling Microscopy and Electrochemical Studies. *Nanotechnology* 2008, *19* (6). https://doi.org/10.1088/0957-4484/19/6/065609.

(41) Darling, S. B.; Rosenbaum, A. W.; Wang, Y.; Sibener, S. J. Coexistence of the $(23 \times \sqrt{3})$ Au(111) Reconstruction and a Striped Phase Self-Assembled Monolayer. *Langmuir* 2002, *18* (20), 7462–7468. https://doi.org/10.1021/la020334x.

(42) Huang, H.; Tan, Z.; He, Y.; Liu, J.; Sun, J.; Zhao, K.; Zhou, Z.; Tian, G.; Wong, S. L.; Wee, A. T. S. Competition between Hexagonal and Tetragonal Hexabromobenzene Packing on Au(111). *ACS Nano* 2016, *10* (3), 3198–3205. https://doi.org/10.1021/acsnano.5b04970.

(43) Lundqvist, D.; Westgren, A. Röntgenuntersuchung Des Systems CoS. *Zeitschrift für Anorg. und Allg. Chemie* 1938, *239* (1), 85–88. https://doi.org/10.1002/zaac.19382390110.

(44) Knop, O.; Reid, K. I. G.; Sutarno; Nakagawa, Y. Chalkogenides of the Transition Elements. VI. X-Ray, Neutron, and Magnetic Investigation of the Spinels Co_3O_4, $NiCo_2O_4$, Co_3S_4, and $NiCo_2S_4$. *Can. J. Chem.* 1968, *46* (22), 3463–3476. https://doi.org/10.1139/v68-576.

(45) Franke, A.; Pehlke, E. First-Principles Study of 1,4-Butanedithiol Molecules and Radicals Adsorbed on Unreconstructed Au(111) and Au(100). *Phys. Rev. B - Condens. Matter Mater. Phys.* 2010, *81* (7). https://doi.org/10.1103/PhysRevB.81.075409.

(46) Franke, A.; Pehlke, E. Adsorption and Diffusion of SCH_3 Radicals and $Au(SCH_3)_2$ Complexes on the Unreconstructed Au(111) Surface in the Submonolayer Coverage Regime. *Phys. Rev. B - Condens. Matter Mater. Phys.* 2009, *79* (23). https://doi.org/10.1103/PhysRevB.79.235441.

Chapter 3 – Supporting Information

1. Au(111) exposed to H_2S

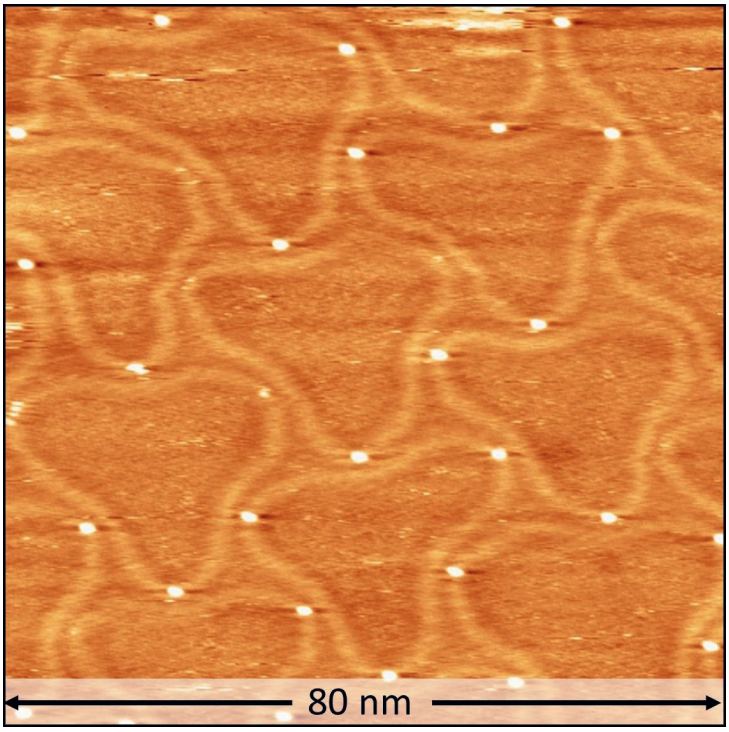

` Figure S1: Modified herringbone reconstruction of Au(111) after exposure to H_2S

The (111) surfaces of metals like Au, Pt and Ir have a tendency to exhibit higher surface atom density than the bulk. In case of Au(111), this shows as the well-known herringbone reconstruction.[S1] When this surface is exposed to H_2S, formation of surface sulfur species causes the herringbone reconstruction to relax and adopt a new structure as shown in S1. This new structure consists of a pair of mirrored 3-point stars arranged as a hexagonal array. A super-saturated Pt gas-phase environment has been observed to induce a similar reconstruction on a clean Pt(111) surface.[S2-S5] This reconstruction of Pt(111) consists of double lines which form star-like features similar to the one observed in our sample. These stars form a network with hexagonal symmetry over large areas of the terrace similar to the reconstruction observed in Figure S1. One key difference is that, in the case of Pt(111), the stars are observed to meet while in the case of Au(111) exposed to H_2S, the double lines do not meet. The Pt(111) surface also shows this behavior in the presence of adatoms such as Co,[S6,S7] Cr[S8] and Cu.[S9]

2. 2D CoS_2 sheets of various sizes supported on Au(111)

At the triple points, the Au(111) step energy is balanced against the step energy of 2D CoS_2 and the Au(111)-2D CoS_2 interfacial energy. This follows from the Young's equation of interfacial tensions,

$$\gamma_{\text{Au step}} = \gamma_{\text{2D } CoS_2 \text{ step}} \cdot \cos\theta + \gamma_{\text{Au-2D } CoS_2 \text{ line interface}} \cdot \cos\varphi \tag{S1}$$

where θ and φ are the respective interfacial angles and γ is the interfacial tension ofthe respective interface at the triple points. We make an assumption that the interfacial tensions are homogeneous in the vicinity of the triple points and hence ignore the torque term (i.e. $d\gamma/d\theta$). For a rigorous quantitative analysis, the torque terms may need to be considered. Figure S2 shows that the corresponding interfacial angles of the two triple points of a 2D CoS_2 sheet display a mirror symmetry. For example, the Au step and the Au-2D CoS_2 line interface has an angle of $158 \pm 0.5^\circ$ at one triple point and $122 \pm 0.5^\circ$ at the other. Such a mirror symmetry could be explained by considering that the 2D CoS_2 step could have different terminations at the two triple points. Further investigations into these phenomena are beyond the scope of this work.

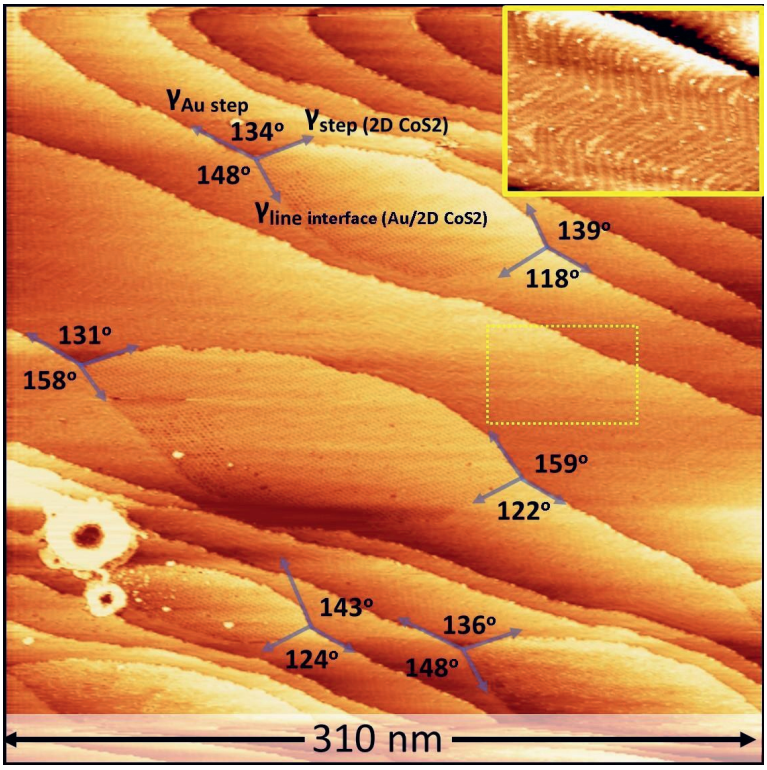

Figure S2: STM images of 2D CoS_2 / Au(111) after flash annealing to 673 K in UHV. The XPS spectra in Figure 2 were measured on this surface. Note the different contact angles at the two triple points of the Au-CoS_2 interface. The herringbone reconstruction, a characteristic of a clean Au(111) surface, is partially restored due to the desorption of most of the sulfur species after the flash annealing (see inset). Bright circular features seen on the lower left corner are debris from the tip as a result of pulsing. Inset shows a zoom-in of the yellow rectangular area.

3. XPS spectra

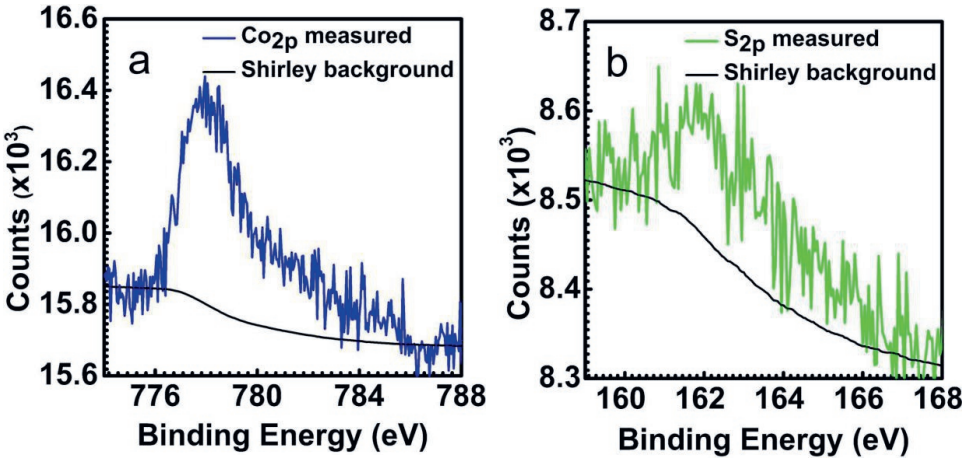

Figure S3: XPS spectra of 2D CoS_2 supported on Au(111) after flash annealing to 673 K to remove sulfur species adsorbed on the Au(111) terraces. (a) Co $2p_{3/2}$. (b) S $2p$.

a. Area under Co $2p_{3/2}$ spectrum = 22923 eV$\times$ counts

R.S.F. of Co $2p_{3/2}$ = 2.8

Contribution of Co taking into account the R.S.F. = $\frac{22983}{2.8}$= 8186.79 eV$\times$ counts;

b. Area under S $2p$ spectrum = 6336 eV$\times$ counts

R.S.F. of S $2p$ = 0.37

Contribution of S taking into account the R.S.F. = $\frac{6336}{0.37}$ = 17124.32 eV$\times$ counts

c. Ratio of Co : S = 8186.79 : 17124.32 $\approx$ 1 : 2.09.

4. TMDC-like structure in sulfur-terminated $Co_3S_4(111)$

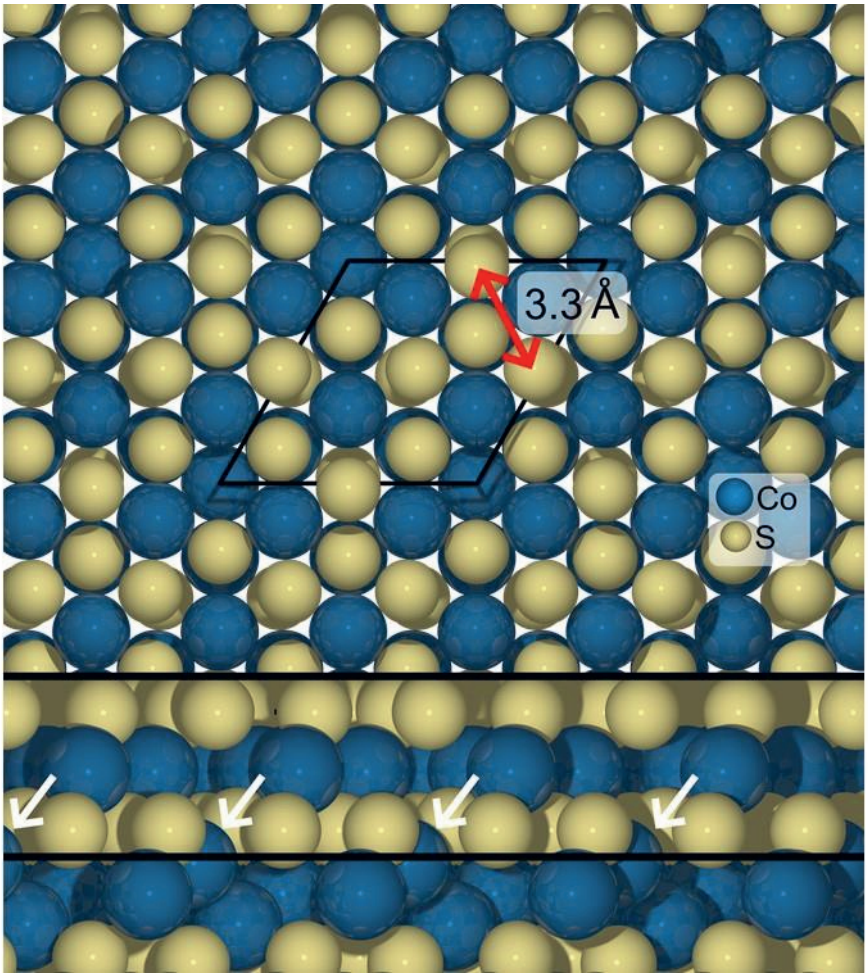

Figure S4: Atomic-scale model for sulfur-terminated $Co_3S_4(111)$ from Lundqvist, D. and Westgren[S11]. Cobalt atoms are shown in blue, while the sulfur atoms are shown in yellow. Top: Top view of the $Co_3S_4(111)$ surface. The hexagonal unit cell of 6.65 A x 6.65 A is indicated in black, however the periodicity of the topmost sulfur layer is half as much(3.33 A, as indicated by the red arrow). Bottom: Side view. The atoms that make up an S-Co-S "sandwich" that form the $Co_3S_4(111)$-cobalt sulfide sheets discussed in this work are enclosed by black lines. The cobalt atoms indicated by white arrows are not part of the proposed structure, resulting in a Co : S = 3 : 8 stoichiometry and visible "holes" in the cobalt layer (see main text).

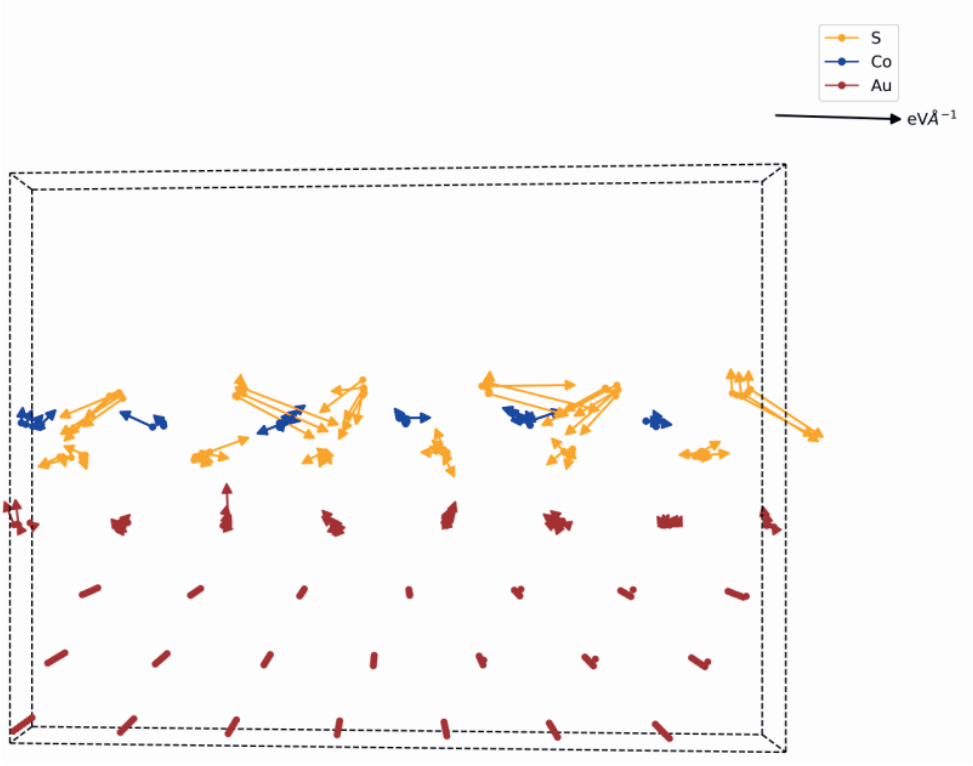

Figure S5: The forces on the atoms in a Co_3S_4(111)-like sheet on Au(111) as suggested by Kibsgaard et al.[S10] at the initial step of the geometry optimization. The length and direction of the arrows are proportional to the magnitude of force. Only forces on the Au atoms in the topmost layer are shown, since the layers below have been frozen in bulk positions. The colors indicate Co (blue), S (orange), and Au (red) respectively.

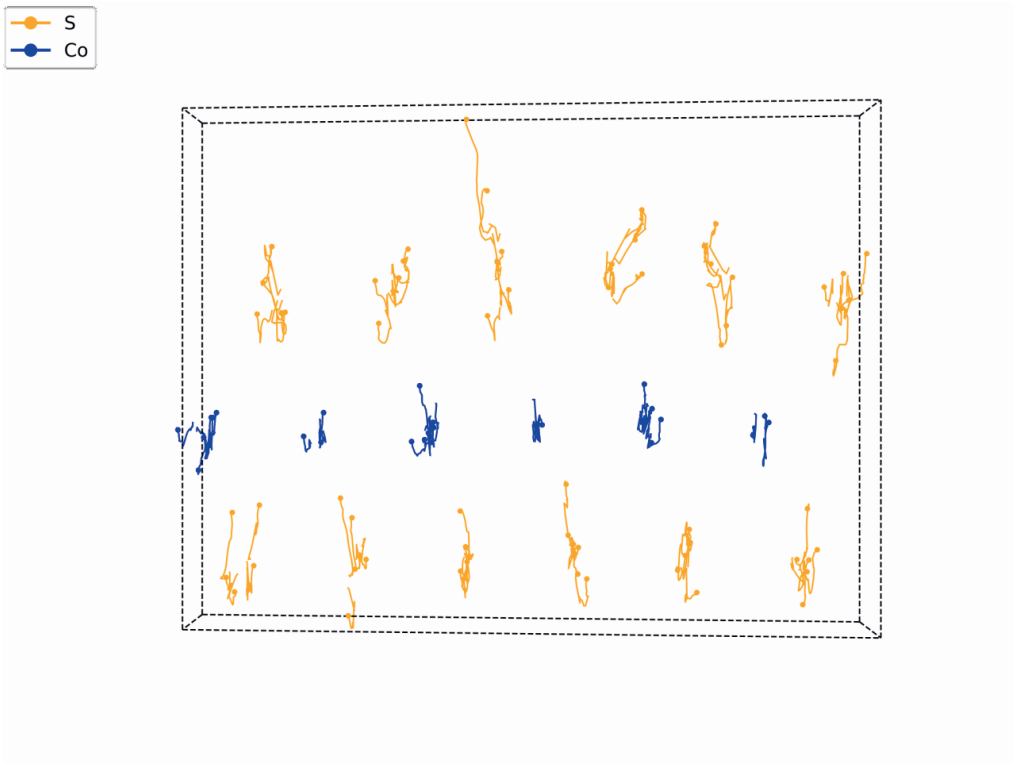

Figure S6: Geometry optimization trajectory for the Co (blue) and S (orange) atoms of a $Co_3S_4(111)$-like sheet on Au(111) as suggested by Kibsgaard et al.[S10] (corresponding to Fig- ure S5). The final position of the atoms is indicated by a circle. The atoms of the Au(111) slab are omitted for the sake of clarity.

The structure suggested by Kibsgaard et al. [S10] consists of a S-Co-S sheet based on $Co_3S_4(111)$, as illustrated schematically in Figure S4. However, our DFT calculations reveal that this structure is not stable. Figure S5 shows that there are large forces on the atoms in the initial step of the geometry optimization. Consequently, the relaxation yields a final structure where the atoms have been significantly displaced from their initial positions as shown in Figure S6.

5. TMDC-like structure in CoS(0001)

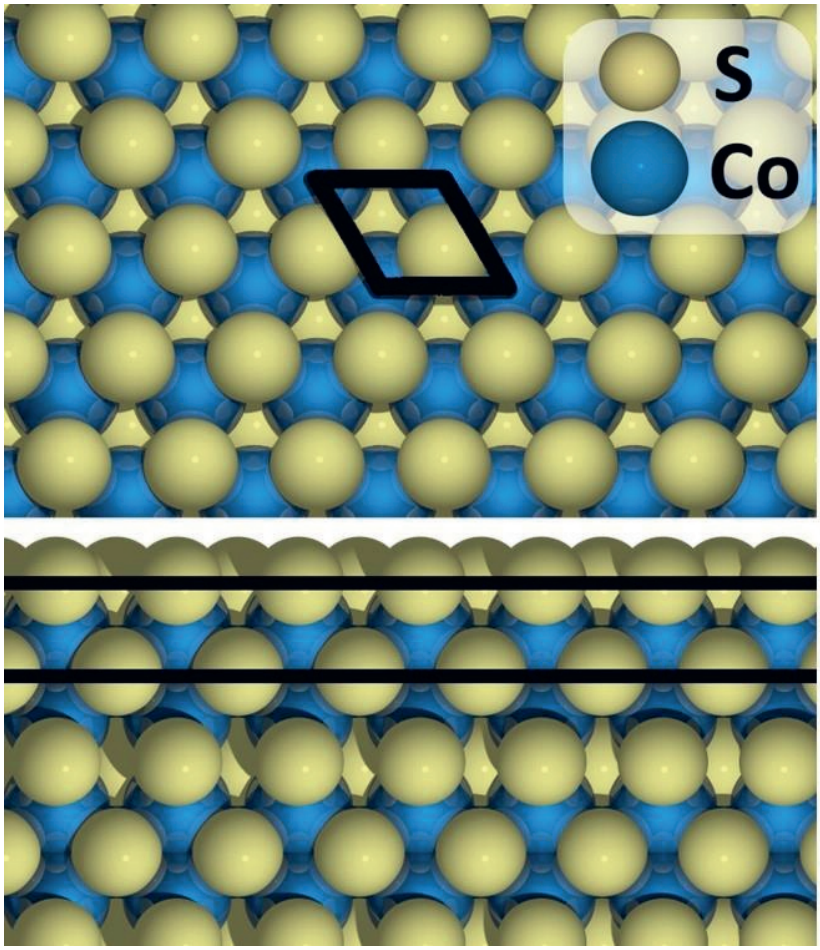

Figure S7: Atomic-scale model for sulfur-terminated CoS(0001). Cobalt atoms are shown in blue, while the sulfur atoms are shown in yellow. Top: Top-down view of the CoS(0001) surface. The hexagonal unit cell of is indicated in black. The experimental lattice constants a_{CoS}^{exp}= 3.38 Å (with a_{Au}^{exp} / c_{Au}^{exp} = 2/3) agree well with those obtained from DFT calculations a_{CoS}^{DFT}= 3.35 Å (with a_{CoS}^{DFT} / c_{CoS}^{DFT} = 2/3). Bottom: Side view.[S12] The atoms that make up the S-Co-S "sandwich" that served as the inspiration for the CoS(0001)-like 2D CoS_2 sheets discussed in this work are enclosed by black lines.

6. Density of states and band structure of 2D CoS_2/Au(111)

In order to compare the electronic band structure of 2D CoS_2 overlayers with large unit cells to freestanding film equivalents and unreconstructed Au(111), we unfold the bands onto the largest surface Brillouin zone according to the method suggested by Popescu and Zunger[S14] as implemented in the BandUp package.[S13,S15] Consistent with STM experiments, in which scanning was possible even at very low bias voltages, the projected densities of states (PDOS) presented in Figure S8 show that the CoS_2 is metallic in contrast to well-studied TMDCs such as e.g. MoS_2. The PDOS also show that both Co and S contribute to the metallic nature of the 2D CoS_2 sheet. In Figure S8, the band structure of the supported CoS(0001)-like 2D CoS_2 sheet on Au(111) from Figure 3c is unfolded and compared to that of the corresponding freestanding 2D CoS_2 sheet as well as a bare Au(111) slab. The 2D CoS_2 states seem strongly affected by the Au at the $\bar{\Gamma}$ point, near the Fermi level, where the bands become more diffuse and hybridize with the nearby gold d-band. The 2D CoS_2 band that is affected the most (indicated by white arrows) exhibits a large p_z-character, indicating hybridization between the p_z-orbital of the sulfur and the d-band of the gold. The hybridization of the 2D CoS_2 states with the d-band of Au is similar to what is reported for MoS_2 sheets on Au(111).[S16]

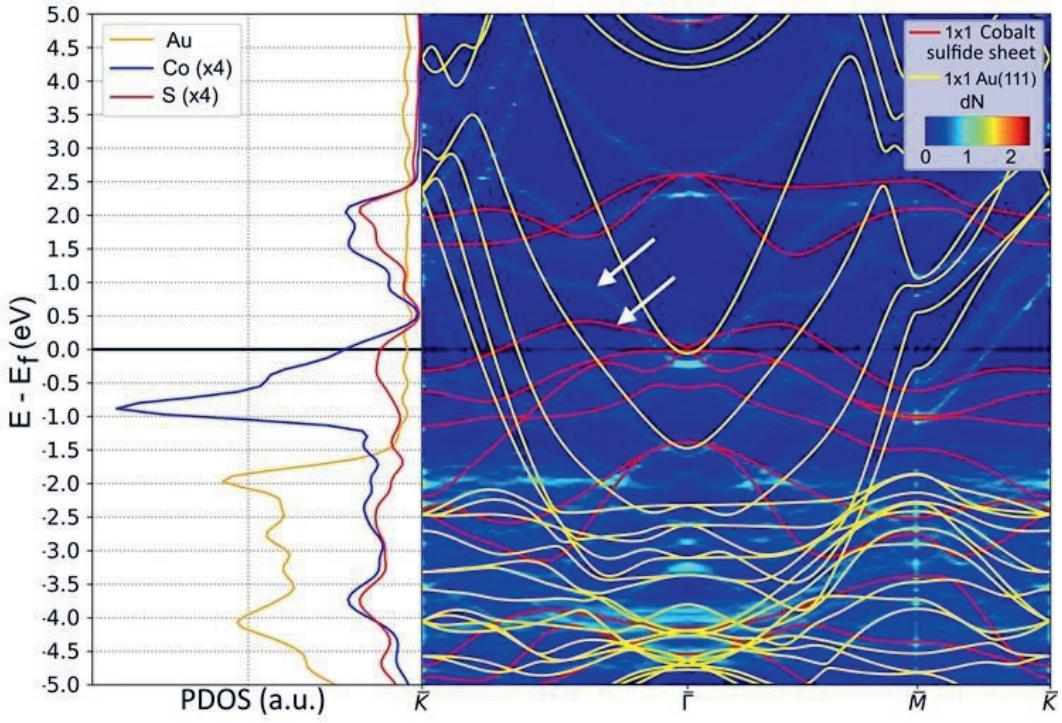

Figure S8: Electronic structure of the CoS(0001)-like 2D CoS_2/Au(111) structure in Figure 3c. Left: Density of states projected on Au (orange), Co (blue), and S (red) atoms. The PDOS of Co and S are multiplied by a factor of 4 for ease of viewing. Right: Comparison of the band structure of gas-phase and Au(111)-supported 2D CoS_2 sheets. The bands of the 2D CoS_2 / Au(111) overlayer structure from Figure 3c are unfolded onto the Brillouin zone of a freestanding CoS(0001)-like 2D CoS_2 film with its much smaller primitive unit cell (background, indicated by color scaleS13). For comparison, the band structure of the latter and the Au(111) slab are shown by the red and yellow lines, respectively. Strong band- hybridization near the $\bar{\Gamma}$ point due to the interaction with the gold surface is indicated by white arrows.

7. Charge analysis

The Bader charges of the corrugated 2D CoS_2 sheet on an Au(111) slab, in vacuum, and of the relaxed sheet in vacuum are compiled in table S1. There is very little difference between the Bader charges of the 2D CoS_2 sheet on the gold substrate and a free-standing 2D CoS_2 sheet (in vacuum), which implies there is little charge transfer between the gold substrate and the 2D CoS_2 sheet. A lack of charge transfer between the sheet and gold indicates their interaction is not ionic in nature. The change in charge density due to the interaction between the CoS_2 sheet and gold substrate is displayed in Figure S9. There is a visible charge depletion near the S- and Au atoms (indicated by red isosurfaces) and there is a charge accumulation in between the S- and Au atoms (indicated by green isosurfaces). This charge accumulation, which is characteristic of covalent-type bonding, is even more obvious in Figure S10, which displays the charge density difference due to the adsorption of the 2D CoS_2 sheet on Au(111) integrated over the surface (xy-) plane.

Table S1: Average Bader charges[S17–S20] for the (relaxed and thus corrugated) 2D CoS_2 on Au(111), the free-standing 2D CoS_2 sheet with the same corrugation as on Au(111), and the free-standing relaxed CoS_2. The average charge accumulation of the sulfur atoms at the bottom of the 2D CoS_2 sheet towards Au(111) and at its top, S_{bottom} and S_{top} respectively, is given separately. Lowest and highest charges are listed in parenthesis.

Element	Average (minimum / maximum) Bader charges (e)				
	CoS_2 sheet on Au(111)		corrugated CoS_2 sheet		CoS_2 sheet
Co	+0.60	(+0.60 / +0.62)	+0.53	(+0.53 / +0.54)	+0.59
S_{bottom}	–0.36	(-0.30 / -0.43)	–0.30	(-0.27 / -0.33)	–0.29
S_{top}	–0.33	(-0.31 / -0.35)	–0.30	(-0.28 / -0.32)	–0.29

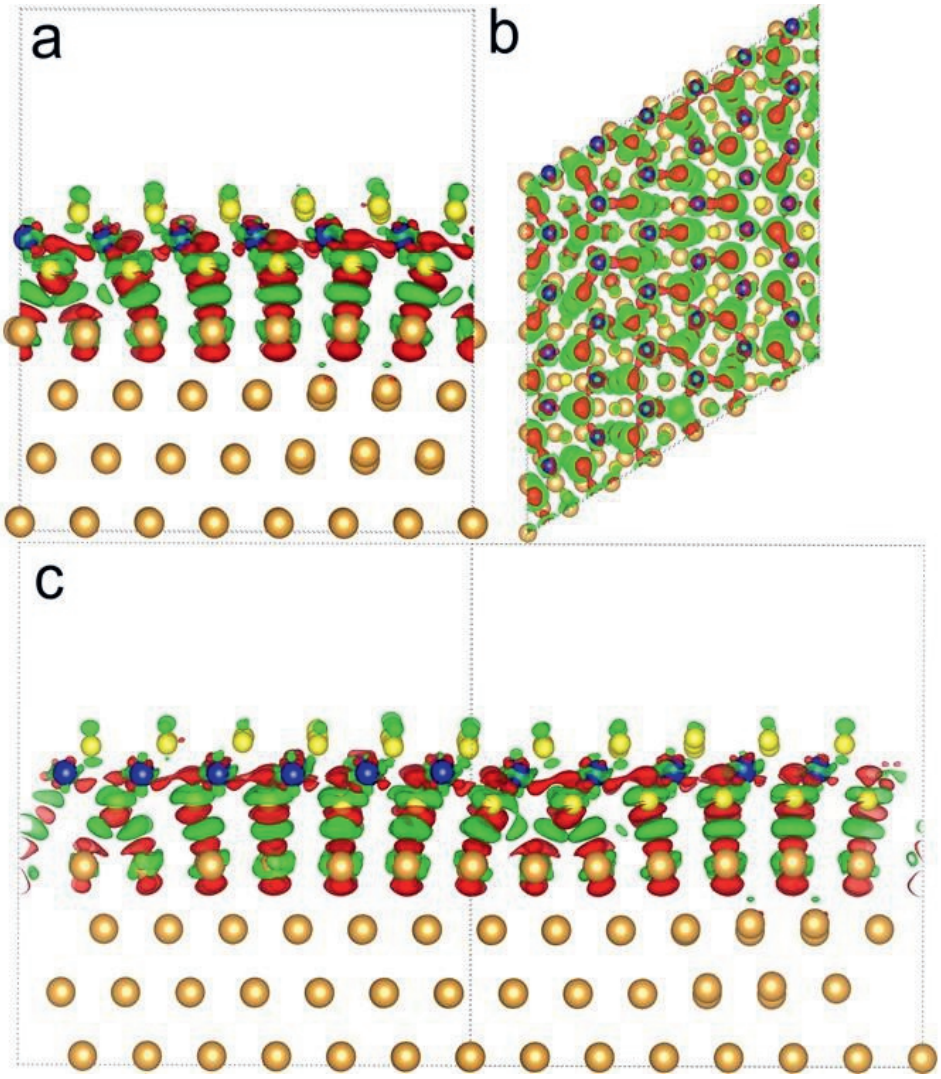

Figure S9: Change in charge density due to interaction between CoS(0001)-like CoS_2 sheet and Au(111) slab. a: Side view. b: Top view c: Side view, rotated by 60°. Gold, cobalt and sulfur atoms are indicated by orange, blue and yellow spheres respectively. A green surface indicates an area of charge accumulation in the combined CoS_2/Au(111), compared to the gas phase, while a red surface indicates an area of charge depletion.

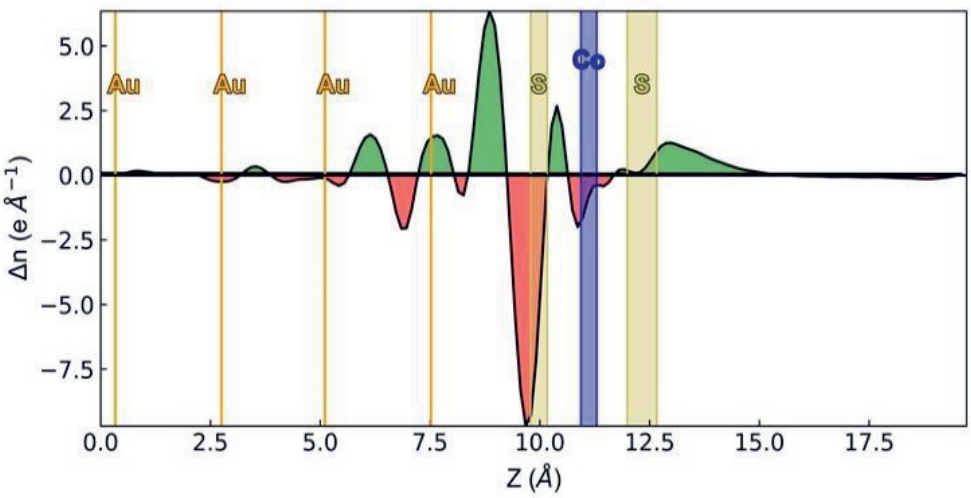

Figure S10: Change in charge density due to interaction between the 2D CoS_2 sheet and Au(111) slab, integrated over the surface (*xy*-) plane. A correction for the dipole intro- duced by the finite periodic cell size in the direction perpendicular to the surface (*z*-direction), resembling that of Neugebauer and Scheffler[S21] is used to avoid unphysical artefacts in the charge density difference. Green indicates charge accumulation, while red indicates charge depletion. The *z*-positions of gold, cobalt and sulfur atoms are marked in orange, blue and yellow respectively. The height variations in the cobalt and sulfur atoms, due to the moire pattern, are indicated in blue and yellow.

8. Van-der-Waals corrections

The influence of van-der-Waals (vdW) forces on the structures was examined by using the D3-method developed by Grimme et al.[S22] on top of our DFT calculations based on the PBE functional, the results of which are presented in the main article.

The adsorption energy of the 2D CoS_2 sheet on Au(111) is -0.98 eV per S-Co-S with PBE+D3, compared to -0.40 eV with PBE (see Figure 5 in the main text). Such a likely overbind- ing has been observed frequently with C_6-correction methods like D3 (see e.g. McNellis et al. [S23]). More importantly, relaxation with PBE+D3 leads to increased corrugation for the structure from Figure 3c. The moire pattern matches the moire pattern obtained using PBE, as demonstrated by the excellent match between Figure S11 and Figure 4 in the main text. Altogether, this is consistent with the bonding to the surface being dominated by covalent interactions between the gold substrate and the sulfur atoms of the 2D CoS_2 structure as analyzed in the previous section 7.

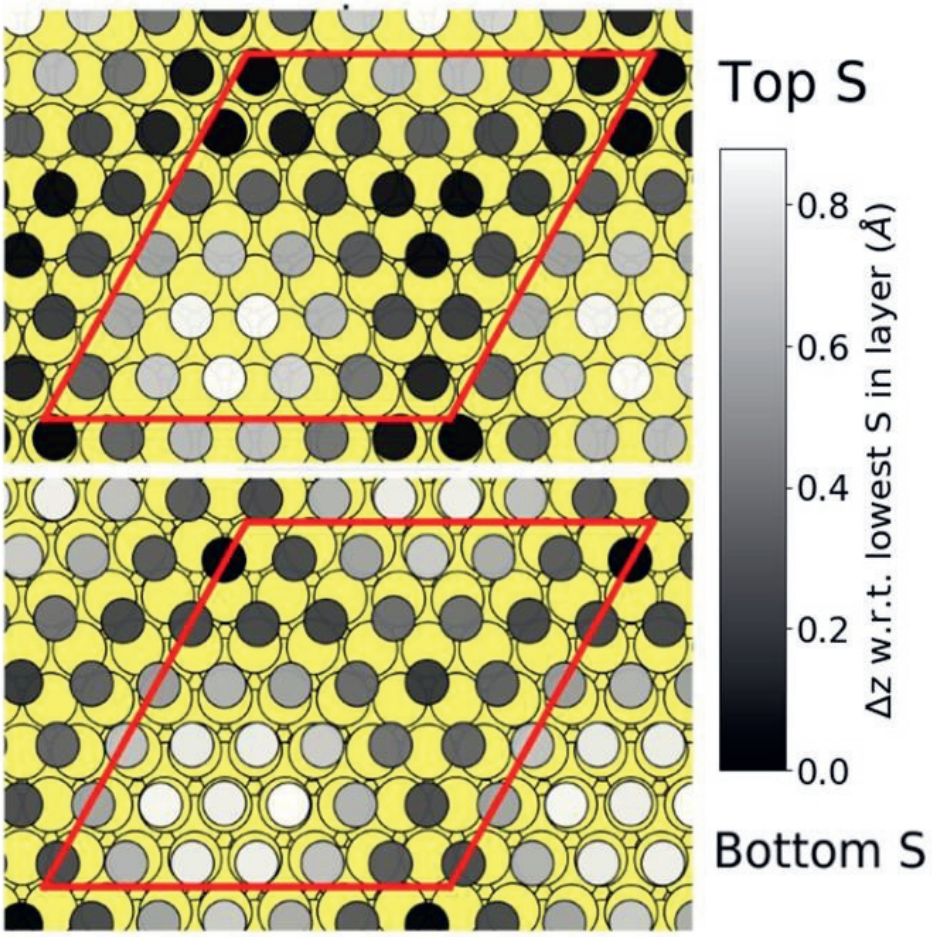

Figure S11: The positions of the sulfur atoms in the top and bottom basal planes of the CoS_2 sheet from Figure 3c. The gold atoms are shown in yellow, while the height of the sulfur atoms relative to the lowest atom in each respective layer is indicated in gray scale. The unit cell is displayed as a red rhombus. The moire pattern looks qualitatively the same as the pattern in Figure 4 in the main text, although the curvature is much stronger.

References

(S1) Chen, W.; Madhavan, V.; Jamneala, T.; Crommie, M. F. Scanning Tunneling Mi- croscopy Observation of an Electronic Superlattice At the Surface of Clean Gold. *Phys. Rev. Lett.* 1998, *80*, 1469–1472.

(S2) Bott, M.; Hohage, M.; Michely, T.; Comsa, G. Pt(111) Reconstruction Induced by Enhanced Pt Gas-phase Chemical Potential. *Phys. Rev. Lett.* 1993, *70*, 1489–1492.

(S3) Hohage, M.; Michely, T.; Comsa, G. Pt(111) Network Reconstruction: Structure, Growth and Decay. *Surf. Sci.* 1995, *337*, 249 – 267.

(S4) Teichert, C.; Hohage, M.; Michely, T.; Comsa, G. Nuclei of the Pt(111) Network Reconstruction Created by Single Ion Impacts. *Phys. Rev. Lett.* 1994, *72*, 1682–1685.

(S5) Sandy, A. R.; Mochrie, S. G. J.; Zehner, D. M.; Gr¨bel, G.; Huang, K. G.; Gibbs, D. Reconstruction of the Pt(111) Surface. *Phys. Rev. Lett.* 1992, *68*, 2192–2195.

(S6) Gr¨tter, P.; D¨rig, U. T. Growth of Vapor-deposited Cobalt Films on Pt(111) Studied by Scanning Tunneling Microscopy. *Phys. Rev. B* 1994, *49*, 2021–2029.

(S7) Gr¨tter, P.; D¨rig, U. Quasidendritic Growth of Co Induced by Localized Reconstruc- tion of Pt(111). *Surf. Sci.* 1995, *337*, 147 – 152.

(S8) Lanping, Z.; Ek, J.; Diebold, U. Highly Ordered Nanoscale Surface Alloy Formed Through Cr-induced Pt(111) Reconstruction. *Phys. Rev. B* 1998, *57*, R4285–R4288.

(S9) Holst, B.; Nohlen, M.; Wandelt, K.; Allison, W. Observation of an Adlayer-driven Substrate Reconstruction in Cu-Pt(111). *Phys. Rev. B* 1998, *58*, R10195–R10198.

(S10) Kibsgaard, J.; Morgenstern, K.; Lægsgaard, E.; Lauritsen, J. V.; Besenbacher, F. Re-structuring of Cobalt Nanoparticles Induced by Formation and Diffusion of Monodis- perse Metal-sulfur Complexes. *Phys. Rev. Lett.* 2008, *100*, 2–5.

(S11) Lundqvist, D. and Westgren, A. Rontgenuntersuchung Des Systems Co-S. *Z. Anorg.*

Allg. Chem. 1936, *48*, 85–88.

(S12) Alsen, N. Rontgenographische Untersuchung Der Kristallstrukturen Von Magnetkies, Breithauptit, Pentlandit, Millerit Und Verwandten Verbindungen. *GFF* 1925, *47*, 19–72.

(S13) Medeiros, P. V. C.; Stafstrom, S.; Bjork, J. Effects of Extrinsic and Intrinsic Perturba- tions on the Electronic Structure of Graphene: Retaining an Effective Primitive Cell Band Structure by Band Unfolding. *Phys. Rev. B* 2014, *89*, 041407.

(S14) Popescu, V.; Zunger, A. Extracting E Versus K Effective Band Structure from Super- cell

Calculations on Alloys and Impurities. *Phys. Rev. B* 2012, *85*, 085201.

(S15) Medeiros, P. V. C.; Tsirkin, S. S.; Stafstrom, S.; Bjork, J. Unfolding Spinor Wave Functions and Expectation Values of General Operators: Introducing the Unfolding- density Operator. *Phys. Rev. B* 2015, *91*, 041116.

(S16) Bruix, A.; Miwa, J. A.; Hauptmann, N.; Wegner, D.; Ulstrup, S.; Grønborg, S. S.; Sanders, C. E.; Dendzik, M.; Grubisic ˇabo, A.; Bianchi, M.; Lauritsen, J. V.; Khaje- toorians, A. A.; Hammer, B.; Hofmann, P. Single-layer MoS_2 on Au(111): Band Gap Renormalization and Substrate Interaction. *Phys. Rev. B* 2016, *93*, 1–10.

(S17) Henkelman, G.; Arnaldsson, A.; J´nsson, H. "A Fast and Robust Algorithm for Bader Decomposition of Charge density". *Comput. Mater. Sci.* 2006, *36*, 354 – 360.

(S18) Sanville, E.; Kenny, S. D.; Smith, R.; Henkelman, G. Improved Grid-based Algorithm for Bader Charge Allocation. *J. Comput. Chem.* 2007, *28*, 899–908.

(S19) Tang, W.; Sanville, E.; Henkelman, G. A Grid-based Bader Analysis Algorithm with- out Lattice Bias. *J. Phys.: Condens. Matter* 2009, *21*, 084204.

(S20) Yu, M.; Trinkle, D. R. Accurate and Efficient Algorithm for Bader Charge Integration. *J. Chem. Phys.* 2011, *134*, 064111.

(S21) Neugebauer, J.; Scheffler, M. Adsorbate-substrate and Adsorbate-adsorbate Interac- tions of Na and K Adlayers on Al(111). *Phys. Rev. B* 1992, *46*, 16067–16080.

(S22) Grimme, S.; Antony, J.; Ehrlich, S.; Krieg, H. A Consistent and Accurate Ab Ini- tio Parametrization of Density Functional Dispersion Correction (DFT-D) for the 94 Elements H-pu. *J. Chem. Phys.* 2010, *132*, 154104.

(S23) McNellis, E. R.; Meyer, J.; Reuter, K. Azobenzene At Coinage Metal Surfaces: Role of Dispersive Van Der Waals Interactions. *Phys. Rev. B* 2009, *80*, 205414.

Chapter 4

Simultaneous sulfidation of Mo and Co oxides supported on Au(111)

This chapter is based on :

Prabhu, M. K.; Groot, I. M. N. Simultaneous sulfidation of Mo and Co oxides supported on Au(111), Phys. Chem. Chem. Phys. ***2021****,23, 8403-8412*

Abstract

In this chapter, we present the results of a study carried out to investigate the simultaneous sulfidation of Co and Mo oxide nanoparticles on Au(111) as a synthesis strategy to prepare a model catalyst for hydrodesulfurization (HDS). We make use of scanning tunneling microscopy and X-ray photoelectron spectroscopy to track the changes in chemistry and morphology through the synthesis of a mixed Mo and Co oxide precursor and the sulfidation to the respective sulfides. We investigated the effects of temperature and the duration of sulfidation on the completeness of the sulfidation process. Our study shows that the formation of MoS_2 with the CoMoS edge is not affected by the time or the temperature of sulfidation. However, the yield of the Co-promoted MoS_2 slabs is limited by the formation of large clusters due to the spreading of Mo and Co oxide phases upon sulfidation. Complete sulfidation of the mixed oxide precursor to Co-promoted MoS_2 can be accelerated by increasing the sulfidation temperature to 730 K due to the thermally activated nature of Mo oxide sulfidation. Thus, we demonstrate that using a mixed Mo and Co oxide precursor as a starting point for Co-promoted MoS_2 phase for fundamental catalysis studies is a viable strategy.

4.1 Introduction

Graphite-like layered materials such as the transition metal dichalcogenides (TMDC) have garnered a lot of attention from the scientific community over the last decade.[1] The atomic structure of TMDCs consists of a layer of metal atoms sandwiched between two layers of chalcogen(S, Se or Te) atoms resulting in an MX_2-type stoichiometry. In the bulk, such molecular layers are held together by van der Waals forces. Like graphene from graphite, single-layer (SL) TMDCs can be exfoliated from the bulk.[2] The most widely studied among SL TMDCs include MoS_2 and WS_2.[3] SL MoS_2 has a direct band gap unlike its bulk counterpart and has found applications in a variety of fields such as electronics[4], biochemistry[5], efficient energy harvesting and storage[6,7] and catalysis.[8]

In many of these applications, nanosheets of SL MoS_2 deposited on substrates like Au(111)[9,10], highly-oriented pyrolytic graphite[11] and TiO_2(110)[12–14] are employed. Typically, these nanosheets are doped with foreign metal atoms such as Co or Ni to enhance their properties, for instance, the catalytic activity. Such doped SL MoS_2 slabs have been widely used in catalytic applications such as hydrodesulfurization (HDS)[15,16], CO_2 hydrogenation[17] and in fuel cell electrodes.[18,19] The SL Co- or Ni-promoted MoS_2 for these applications is usually grown by wet chemical methods[16], chemical vapor deposition (CVD)[20], thermal decomposition[21] or physical vapor deposition (PVD).[22,23] PVD in particular is useful for producing high quality promoted SL MoS_2 slabs and thus, has been the choice method for synthesizing the Co-promoted MoS_2 for fundamental research. The PVD method makes use of a mixture of metallic Co and Mo nanoparticles as the precursor. The metal nanoparticles being highly reactive, readily form promoted MoS_2 slabs in the presence of a chalcogen containing reactive gas such as H_2S.[23] In many of the industrially relevant synthesis strategies such as the wet impregnation method, however, the precursor to form the promoted MoS_2 nanoparticles, for instance, Co-promoted MoS_2, is a mixture of the respective oxides: Mo oxide and Co oxide. As an example, the HDS catalyst containing Co-promoted MoS_2 can be formed by sulfiding a mixture of MoO_3 and Co_3O_4 nanoparticles.[24,25] The transformation of the metal oxide nanoparticles to metal sulfide can show more complex behavior than the respective metal nanoparticles because of the reducibility of the oxides and the metal oxidation state dependent susceptibility towards sulfidation.[26–28] From the point of view of real catalysts used in the industry, it is important to understand the process of sulfiding a mixture of Mo and Co oxide nanoparticles in order to control the morphology of the Co-promoted MoS_2 slabs.

Molybdenum oxides have been studied on supports such as Au(111)[28–32], highly-oriented pyrolytic graphite (HOPG)[33], NiAl[34] and TiO_2(110).[35] The typical preparation methods used in these studies involve direct sublimation of MoO_3 powder, oxidation of Mo clusters, or CVD-like processes involving carbonyl complexes of Mo with NO_2 as the oxidizing agent. Additionally, the prior work carried out in our group[34] demonstrates a method of directly depositing Mo oxides from a source containing Mo metal. Co oxide has been synthesized by oxidizing Co nanoclusters on substrates like Ag(111)[36], Pt(111)[37,38] and Au(111).[39–44] This method produces pristine Co oxide slabs containing Co^{2+} and Co^{3+} depending on the oxygen background pressure used; higher O_2 pressures resulting in higher oxidation state of the metal atom. The Co oxide slabs thus formed, are known to have layered Co-O or O-Co-O-type structures. The oxidation and the reduction of these slabs have also been observed.[36,42,43]

Recently, sulfidation of MoO_3 supported on Au(111) was studied using a scanning tunneling microscope (STM) and X-ray photoelectron spectroscopy (XPS).[28] It was shown that the progressive annealing of the PVD-grown MoO_3 results in the reduction of Mo^{6+} to lower oxidation states, thus forming sub-stoichiometric Mo oxides. This causes morphological changes in the nanoparticles. Extensive sulfidation with H_2S was found to be necessary to form SL MoS_2 slabs as the oxide phase readily undergoes reduction and oxygen-sulfur exchange to form a stable oxysulfide phase, thereby hindering the complete sulfidation. It was observed that the sulfidation to MoS_2 was most efficient when Mo remained predominantly in its highest oxidation state, namely, Mo^{6+}. The sulfidation of aforementioned cobalt oxide slabs on the other hand, have not been studied so far. The sulfidation to Co_9S_8 and Co_3S_4 have been observed in sorbents containing Co_3O_4 supported on TiO_2.[45] However, fundamental studies involving sulfidation of cobalt oxides have predominantly been performed in conjunction with Mo oxide nanoparticles as a method to synthesize catalysts for HDS.[21,46–48] Furthermore, extensive studies in the last decade have shown that STM is a very powerful technique for directly observing the incorporation of Co atoms in the MoS_2 phase.[22,23,49]

In this chapter, we aim to gain insights into the sulfidation of a mixture of Co and Mo oxide precursor. Particularly, we investigate the formation of the Co-promoted MoS_2 phase. In order to do this, we first synthesize a precursor containing nanoparticles of Mo and Co oxides on an Au(111) substrate. Thereafter, the mixed oxide precursor is sulfided using hydrogen sulfide at 650 K for 25 to 90 minutes and at 730 K for 25 minutes in order to investigate the effects of time and temperature on the completeness of the sulfidation process and the formation of the Co-promoted MoS_2 phase. Using a combination of STM and XPS, we observe the formation of large clusters containing the 2D CoS_2 and the Co-promoted MoS_2 phases as well as individual SL Co-promoted MoS_2 nanoclusters. The results presented in this study show that by using a mixed oxide precursor as a starting point, the Co-promoted MoS_2 phase can be synthesized, albeit with a low yield due to the kinetically-hindered sulfidation of Mo oxide.

4.2 Experimental Methods

4.2.1 Substrate cleaning

The experiments described in this Chapter were carried out in the ReactorSTM setup.[50] The Au(111) single crystal was purchased from Surface Preparation Laboratory and cleaned with cycles of sputtering and annealing. Sputter cleaning with Ar^+ was performed under an argon atmosphere of $1x10^{-6}$ mbar and with an ion energy of 1.5 keV. The Au(111) single crystal was then annealed to 850 K using radiative heating for 45 minutes to obtain atomically flat gold terraces. The cleanliness was checked with XPS and STM until impurities were below the detection limits.

4.2.2 Deposition of Co and Mo oxides

Deposition of the Mo and Co oxides was performed using an Oxford EGCO4 e-beam evaporator. In the case of Mo oxide, the Mo rod was heated to ~1100 K in an oxygen atmosphere of $1x10^{-5}$ mbar. At

this temperature the vapor pressure of metallic Mo is negligible. However, the Mo^{6+} oxide formed on the Mo rod sublimes and deposits onto the sample held at 300 K. By maintaining the O_2 background pressure low, formation of Mo^{6+} on the rod can be controlled and therefore we can suppress the sublimation of Mo oxide polymers and ensure that small nanoparticles of Mo oxide are formed. The sample was then annealed to 500 K for 20 minutes while maintaining the background oxygen pressure. A doser was used to increase the local O_2 pressure near the sample ($>10^{-4}$ mbar) to suppress the reduction of Mo oxides to lower oxidation states. Subsequently, the sample was cooled to 300 K under the same O_2-rich atmosphere.

Cobalt oxide was grown by depositing metallic cobalt at 300 K in an O_2 atmosphere of $1x10^{-6}$ mbar followed by annealing at 600 K for 30 minutes while maintaining the oxygen background. The sample was cooled to room temperature in the same oxygen atmosphere. This recipe has been adapted from literature and is known to grow layered cobalt oxides on Au(111).[36,44]

4.2.3 Sulfidation

Sulfidation of the mixed Mo and Co oxide samples was carried out in an H_2S atmosphere of $2.5x10^{-6}$ mbar. Separate identical samples were prepared for investigating the effects of sulfidation at 650 K for 25 to 90 minutes and at 730 K for 25 minutes. In this manner, we aim to gain insights into the effects of the duration and the temperature of sulfidation. All the samples were cooled after sulfidation to 473 K maintaining the H_2S background after which the sample was allowed to cool to 300 K in ultra-high vacuum (UHV).

4.2.4 Scanning tunneling microscopy

Scanning tunneling microscopy was performed at room temperature using the UHV mode of the ReactorSTM. Tips were prepared from polycrystalline Pt-Ir 90-10 wire purchased from Goodfellow without further processing. Constant current scans were performed using LPM video-rate scanning electronics described in detail elsewhere.[51,52] Image processing was performed with a combination of home-developed Camera software and WSxM.[53,54] Most common normal filtering was used to obtain a correctly connected surface in order to calculate the height profiles. No other further processing was performed on the images reported in this Chapter.

4.2.5 X-ray photoelectron spectroscopy (XPS)

The XPS measurements were performed in a SPECS Phoibos system equipped with an XRM50 X-ray source set to the Al K-alpha line used along with a monochromator to excite the sample with a beam spot of 0.4 mm diameter at 55^{o} incidence. The acceleration voltage was set to 10 kV and a power of 250 W was used for all the measurements. The HSA3500 hemispherical analyzer with a pass energy of 30 eV was used to analyze the photoemission. The Au 4f peak set to 84.0 eV was used to calibrate the XPS spectra obtained. The number of integrations was set to 20. The data thus obtained, were characterized and quantified using CASA-XPS and XPSPEAK41 software with relative sensitivity factors for surfaces.[55] Gaussian-Leorentzian (35) curves were used for peak fitting using a Newton-Raphson algorithm after applying a Shirley background subtraction. For Mo 3d spectra, doublets with

a spacing of 3.15 eV due to the spin-orbit splitting of the Mo 3d signal were used for peak fitting each of the components arising from Mo and while a singlet was used for the S 2s component. The parameters used for peak fitting are tabulated in Table 1. The peak positions of the components were obtained from previously reported literature work.[28,31,56–59]

Table 1: XPS peak fitting parameters of the Mo 3d and Co $2p_{3/2}$ spectra

Component for Co $2p_{3/2}$	**Peak position (eV)**	**Component for Mo 3d**	**Peak position (eV)**
Co^{2+} oxide	780	Mo^{6+} oxide	233.1*
Co^{2+} oxide satellite 1	782	Mo^{5+} oxide	231.5*
Co^{2+} oxide satellite 2	785.4	Mo^{4+} oxide	230.6*
Co^{2+} oxide satellite 3	786.4	Mo^{4+} sulfide	229.2*
Co^{3+} oxide	779.5	Mo metal	228.1*
Co^{3+} oxide satellite 1	780.8	S 2s	226
Co^{3+} oxide satellite 2	782.1		
Co^{3+} oxide satellite 3	785.1		
Co^{3+} oxide satellite 4	789.4		
Co metal	778.3		
Co metal satellite 1	781.3		
Co metal satellite 2	783.3		
CoS_2	778.1		
CoS_2 satellite 1	781.1		
CoS_2 satellite 2	783.1		

*Peak positions are of the $3d_{5/2}$ component

4.3 Results

In order to prepare a mixed Mo and Co oxide precursor, we start with the growth of Co oxide slabs on Au(111). After the deposition of ~0.05 monolayers (ML) Co in an O_2 atmosphere followed by oxidation of the Co nanoparticles at 600 K, the Au(111) surface is covered with slabs of cobalt oxide (see Figure 1a) which are 6-10 nm in size. The slabs are atomically flat and have a truncated hexagonal shape. Most of the slabs of cobalt oxide have a measured height of 4.1 Å (see Figure 1b) while some of them have a height of 1.9 Å. We observed that the later was formed mostly around the step edges of Au(111). Additionally, the Co oxide slabs have a diffuse hexagonal pattern (inset Figure 1a) on their basal plane. We identify this as a moiré structure due to lattice mismatch with the underlying Au(111) surface. The moiré structures of the cobalt oxide slabs which are 4.1 Å high have a rotation of ~6° with respect to that of the slabs which are 1.9 Å high (see supporting information, Figure S1). All these observations match nicely with those of Walton et al.[44] who have shown with combined STM experiments and DFT calculations that Co oxide slabs grow as a layered -Co-O structure on Au(111). According to their experiments, Co oxide slabs with -Co-O-Co-O structure have measured heights of 4 Å on gold, while single -Co-O layer slabs have 1.7 Å heights. They have, however, observed a higher

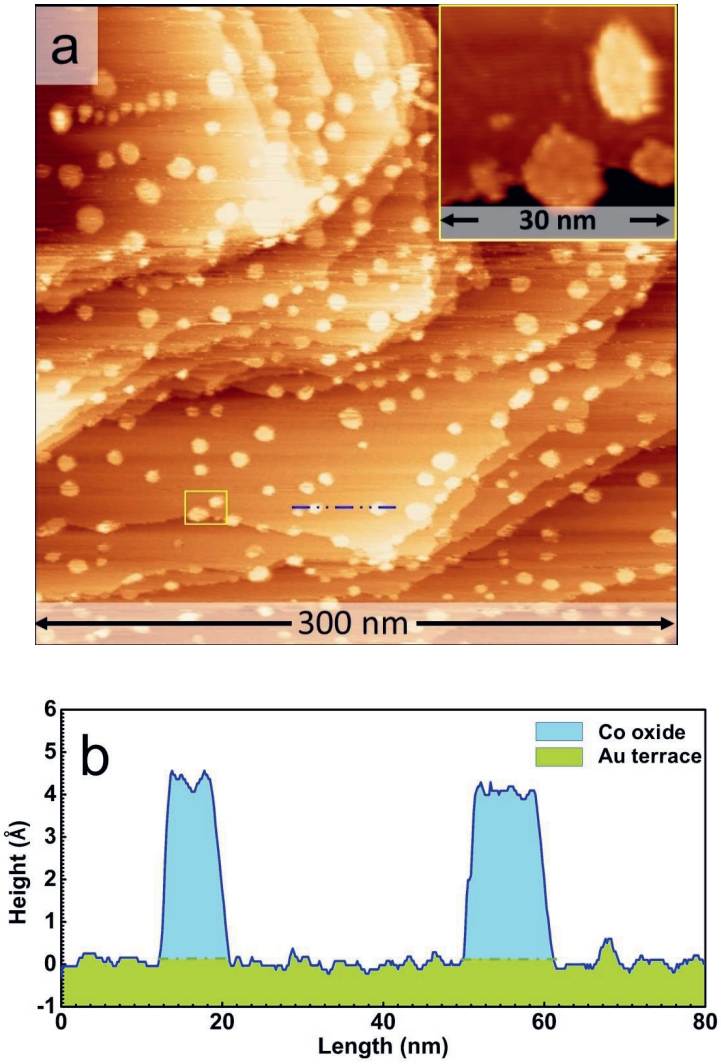

Figure 1:a) Large-scale STM image of Co oxide slabs on Au(111) obtained at sample voltage = -1.6 V, tunneling current = 150 pA. The inset shows the zoom-in of the region marked in yellow. The hexagonal moiré structure of the Co oxide slabs is clearly visible. b) Measured height along the blue dash-double dotted line in Figure 1a.

density of SL Co-O islands contrary to our experiment where the majority are 4.1 Å high. This disagreement could be due to the higher amount of Co deposited during synthesis in this study.

Mo oxide nanoparticles were grown on the sample containing Co oxide slabs supported on Au(111) by the direct deposition technique detailed in the experimental methods. Mo oxide was grown until ~0.05 ML Mo was detected on the sample using the XPS such that an Mo:Co ratio of ~1:1 could be achieved and Mo and Co together had a total coverage of ~10% of a monolayer on Au(111). This particular value was chosen because the typical techniques reported in literature for growing 2-3 nm slabs of Co-promoted MoS_2 involve the use of at most ~0.1 ML of metallic Co and Mo.[23] Our recipe resulted in the formation of Mo oxide nanoparticles with a 3D morphology (see Figure 2a). Most of the Mo oxide particles had a measured height of 9.5-11 Å (Figure 2b). Some Mo oxide nanoparticles were measured to have a height of 5.5-6 Å. The growth mode and the morphologies of Mo oxides deposited on Au(111) depends on the type of precursor used, the temperature of oxidation and the oxidizing agent.[30–32] Therefore, comparing the Mo oxide morphologies from our STM images with those from other Mo oxide synthesis methods on Au(111) reported in literature becomes difficult. To investigate the effects of Co oxide slabs on the Mo oxide morphology, we deposited Mo oxide nanoparticles directly on a clean Au(111) (see supporting information, Figure S2) in a separate experiment. We observed that the Mo oxide nanoparticles grown on clean Au(111) also have identical morphologies and measured STM heights, suggesting that the Mo oxide morphology is largely unaffected by the presence of Co oxide slabs on Au(111). However, we cannot rule out the possibility of some Mo oxide nanoparticles nucleating over a cobalt oxide slab. The Co oxide slabs, on the other hand, were observed to undergo changes in their morphology all of which can be attributed to the exposure to higher oxygen pressures ($>1\text{x}10^{-5}$ mbar) during the Mo oxide synthesis. The Co oxide slabs largely retained the truncated hexagonal shape but were observed to grow in height. We observed the presence of Co oxide slabs of 3 Å, 4 Å and 5 Å heights post-annealing (see supporting information, Figure S3). The previously grown SL Co oxide slabs of 2 Å height were not observed anymore after the synthesis of Mo oxides. Fester et al.[43] have observed that –Co-O- type Co oxide slabs exposed to higher oxygen pressures undergo systematic oxidation from Co^{2+} to Co^{3+} which results in the formation of -O-Co-O type slabs with measured height of 2.9 Å in their experiment. We propose that the Co oxide slabs measured with heights of 3 Å and 5 Å are single and multilayer stacks (O-Co-O-Co-O) respectively, each containing Co^{3+}, while those slabs with heights of 4 Å are likely the unconverted double Co-O layer slabs with Co^{2+}. It is also possible that some of the multilayer slabs consist of both Co^{2+} and Co^{3+} layers leading to an overall mixed oxidation state of Co.

The mixed Co and Mo oxide sample thus prepared, was chosen as the precursor for sulfidation using H_2S ($1\text{x}10^{-6}$ mbar). Figure 3a shows the large-scale STM image after the sulfidation at 650 K for 25 minutes. We observed the formation of two types of structures on the Au(111) surface post-sulfidation: a) large clusters of ~50 nm size, b) small hexagonal slabs. The large clusters consist of three phases (see Figure 3a) with the outer two phases marked 1 and 2 in Figure 3a being atomically flat while the inner phase marked 3 being atomically rough. Phase 1 and 2 were often observed to encapsulate the phase 3 as seen in Figure 3a. The small hexagonal slabs are discussed later in this chapter.

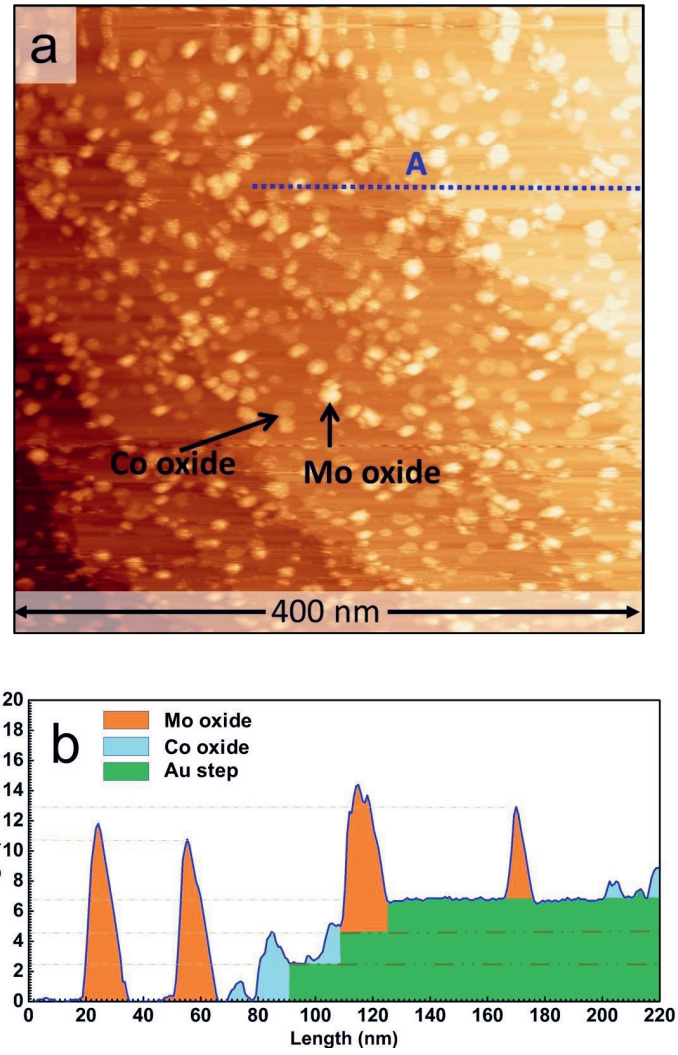

Figure 2: a) Large-scale STM image of Mo oxide nanoparticles deposited on the Au(111) sample containing Co oxide slabs, sample voltage = -1.5 V, tunneling current = 150 pA. b) Measured height along the blue dashed line marked A in Figure 2a.

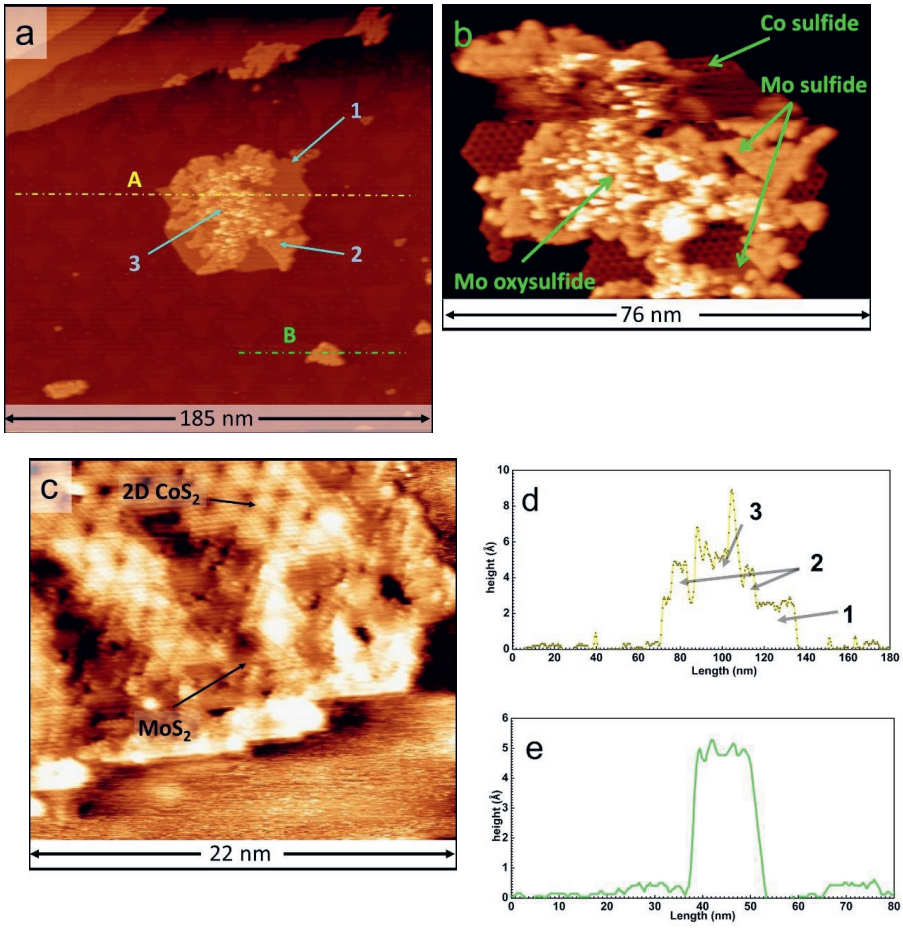

Figure 3:a) Large-scale STM image of the simultaneously sulfided Co and Mo oxides on the Au(111) substrate. Phase 1,2 and 3 are marked in the Figure; b) zoom-in of a large cluster containing the three phase. The MoS_2, 2D CoS_2, and partially sulfided Mo oxide phases are marked; c) Atom-resolved STM image of the defective MoS_2 phase in one of the large clusters; d, e) Measured height along the blue dashed lines marked A and B respectively in Figure 3a. The respective layers in Figure 3a and 3c have been marked as 1) 2D CoS_2 2) MoS_2 slabs 3) Partially sulfided Mo oxide. All of STM images in Figure 3 were acquired at sample voltage = -1.2 V and tunneling current = 200 pA.

Phase 1 has a low contrast in the STM image and has a hexagonal superstructure on its basal plane (see Figure 3b and 3c). This phase has a measured height of 2.4±0.2 Å (Figure 3d). We identify this phase as a SL 2D-CoS_2 sheet with an S-Co-S layered structure and the hexagonal super structure being a moiré pattern due to lattice mismatch with Au(111). The detailed structural characterization of this phase has been carried out in Chapter 3 and elsewhere in the literature.[60] Phase 2 has an intermediate contrast in the STM image in comparison to Phase 1 and 3. Additionally, its basal plane shows irregular contrast variations. We identify this layer as an MoS_2 slab which is not fully crystalline. These contrasts variations are attributed to the presence of a large number of defects which are resolved further in the atom-resolved STM image in Figure 3c. SL MoS_2 slabs on gold are reported to have a measured height of 2±0.3 Å.[9] However, we measure a height of 4.5±0.2 Å for the MoS_2 slabs present in phase 2 (see Figure 3d and 3e) suggesting the presence of a double layer. It is also possible that the second MoS_2 layer is supported over a layer of 2D CoS_2 sheet. The innermost phase marked 3, which has atomic roughness, is very likely an Mo oxysulfide phase. Reducible oxides of metals such as Mo, Ti and Ce are known to readily undergo O-S exchange even in vacuum pressures of H_2S.[28,61] Therefore, it is unlikely that any of the pure Mo oxides survive the annealing step in the presence of H_2S. Furthermore, prior experiments involving the sulfidation of Mo oxides supported on gold have shown that an intermediate oxysulfide phase can form during the sulfidation of the Mo oxide phase.[28]

Thus, the sulfidation carried out at 650 K for 25 minutes resulted in a partial conversion of the oxide phase and the formation of defective MoS_2 slabs. We devised two strategies to enhance the yield of the Mo and Co sulfide phase. For this, identical precursors of mixed Mo and Co oxide nanoparticles as in Figure 2a were prepared. In the first strategy, we increased the time of sulfidation systematically to up to 90 minutes. In the second, we increased the sulfidation temperature to 730 K while maintaining the time of sulfidation to 25 minutes. XPS was used to check for the completeness of the sulfidation process and STM images were acquired thereafter.

Figure 4a and 4b show the Co $2p_{3/2}$ and Mo 3d XPS spectra respectively, which were acquired for the samples after the initial synthesis of Co oxide slabs supported on Au(111), deposition of Mo oxide on the sample containing Co oxide supported on Au(111), and after 25 minutes of sulfidation at 650 K, 50 minutes of sulfidation at 650 K, 90 minutes of sulfidation at 650 K, and 25 minutes of sulfidation at 730 K. The Co $2p_{3/2}$ spectrum (Figure 4a) of the initially grown Co oxide slabs on Au(111) consists of contributions of a high-spin Co oxide and a Co metal component. The Co oxide component shows a broad main peak at 780 eV with a shoulder at 782 and 785.4 eV. Furthermore, a broad satellite feature at 786.4 eV is also detected. These observations are in agreement with prior experimental reports of –Co-O- type Co oxide slabs supported on Au(111)[42] and in line with our interpretation of the STM image in Figure 1a. The presence of Co metal component indicates that there is very likely Co that is alloyed with gold and is present in the sub-surface region as we do not observe any metallic Co phase in the STM images. After the deposition of Mo oxide, the main peak of the Co $2p_{3/2}$ spectrum shows a 0.6 eV shift towards higher binding energy at 780.6 eV (see Figure 4a). Peak fitting shows contributions from Co^{3+} oxide, Co^{2+} oxide as well as a minor contribution from Co metal. Figure 4a shows that the contribution from the Co^{2+} oxide and the Co metal component decreases significantly while the Co^{3+} component is dominant which suggests an oxidation of some of the Co^{2+} to Co^{3+}. This supports our observations from the STM images in Figure 2a which suggest a partial oxidation of the Co^{2+} slabs into slabs containing Co^{3+} oxide. Similar observations were also reported in the work of

Fester et al..[42,43] We note that the presence of CoOOH in the Co oxide slabs cannot be ruled out as its reference spectrum also has similar features to those of Co^{3+} oxide.[56] We, however, did not consider this component in our peak fitting. The Mo 3d spectrum of the Mo oxide deposited on the sample containing Co oxide slabs supported on Au(111) shows the presence of predominantly Mo^{6+} and Mo^{5+} oxidation states.[24,28] The higher local pressure of oxygen attained with the usage of a doser ensures that extensive thermal reduction of Mo oxides as in the work of Salazar et al.[28] is greatly suppressed.

Upon sulfidation, for all the conditions used, the Co $2p_{3/2}$ main peak shifts to lower binding energy at 778.1 eV, indicating a conversion to the sulfide. The satellite feature also shifts to 783.1 eV and is consistent with the reference spectra of 2D CoS_2 on Au(111)[60] and other supports.[24] Components from the Co^{2+} and Co^{3+} oxide were not observed for all the sulfided samples. This suggests that the sulfidation is complete within the first 25 minutes at 650 K itself. This is also in agreement with our observation of a pristine 2D CoS_2 phase in the STM images (phase 1, Figure 3a). The Mo 3d spectrum, on the other hand, shows a progressive shift to the Mo^{4+} oxidation state with increasing sulfidation time. Additionally a component at 226 eV of the S 2s signal is also detected. The Mo^{4+} and the S 2s features are attributed to the formation of MoS_2. The S 2s also likely has some contribution from sulfur adsorbed on Au(111) due to H_2S exposure. Furthermore, it is also possible that some of the Mo^{4+} component arises due to incomplete sulfidation and reduction of Mo oxide in the presence of H_2S. Some contributions from the Mo^{5+} and Mo^{6+} components are also detected. These components are attributed to Mo oxide phases that are not completely sulfided (phase 3, Figure 3a) and likely are present as an oxysulfide. After 90 minutes of sulfidation, the Mo 3d spectrum shows only the Mo^{4+} component characteristic of pristine MoS_2 [28] indicating complete sulfidation of Mo. However, traces of the incompletely sulfide phase were observed in the STM images obtained after 90 minutes of sulfidation at 650 K (see supporting information, Figure S4). After sulfidation at 730 K for 25 minutes, the Mo 3d spectrum shows only the Mo^{4+} and S 2s features characteristic of MoS_2 suggesting a complete conversion to MoS_2. For the corresponding O 1s and S 2p spectra, we refer to the supporting information, Figure S5.

Table 2: Ratio and coverage of Co and Mo determined from the XPS spectra in Figure 4

	Co: Mo	**Co coverage (ML)***	**Mo coverage (ML)***
Co oxide / Au(111)		0.061	
Mo oxide + Co oxide	0.98	0.055	0.056
sulfidation 650 k 25 min	1.05	0.061	0.058
sulfidation 650 k 50 min	1.02	0.062	0.061
sulfidation 650 k 90 min	1.04	0.059	0.057
sulfidation 730 k 25 min	0.83	0.042	0.050

*with respect to Au(111), ML = monolayers

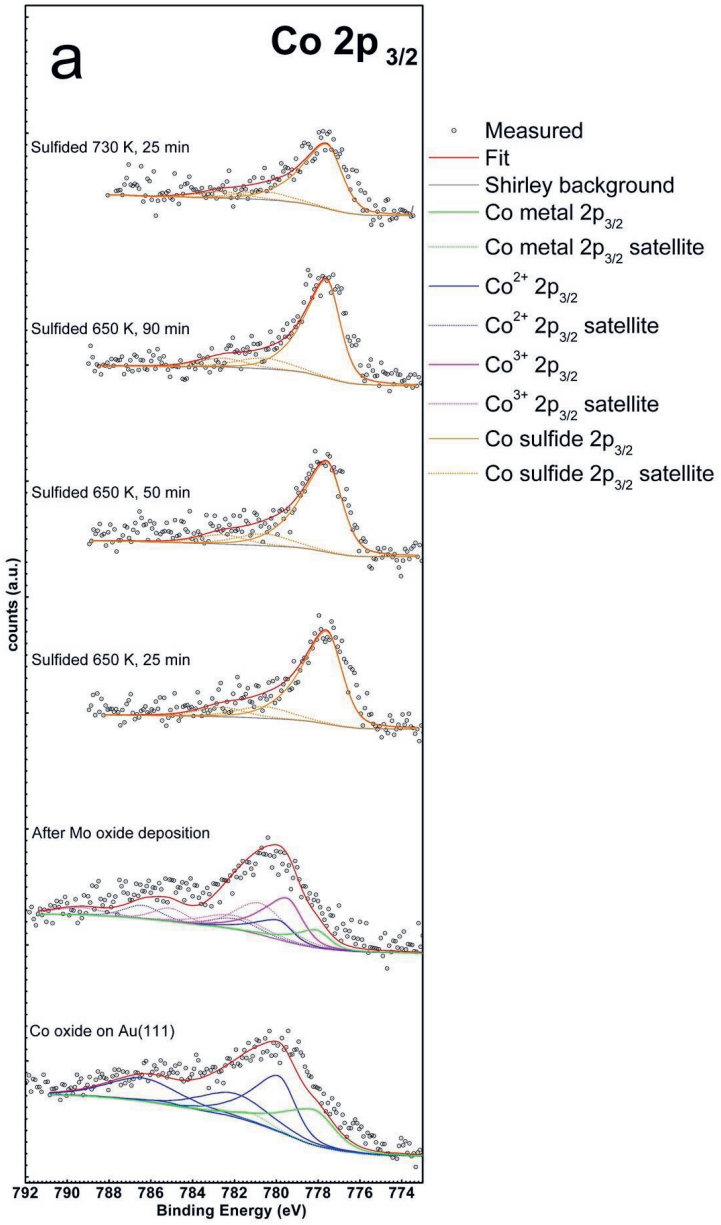
a
Co 2p 3/2
Sulfided 730 K, 25 min
Sulfided 650 K, 90 min
Sulfided 650 K, 50 min
Sulfided 650 K, 25 min
After Mo oxide deposition
Co oxide on Au(111)
counts (a.u.)
792 790 788 786 784 782 780 778 776 774
Binding Energy (eV)
Measured
Fit
Shirley background
Co metal 2p3/2
Co metal 2p3/2 satellite
Co2+ 2p3/2
Co2+ 2p3/2 satellite
Co3+ 2p3/2
Co3+ 2p3/2 satellite
Co sulfide 2p3/2
Co sulfide 2p3/2 satellite

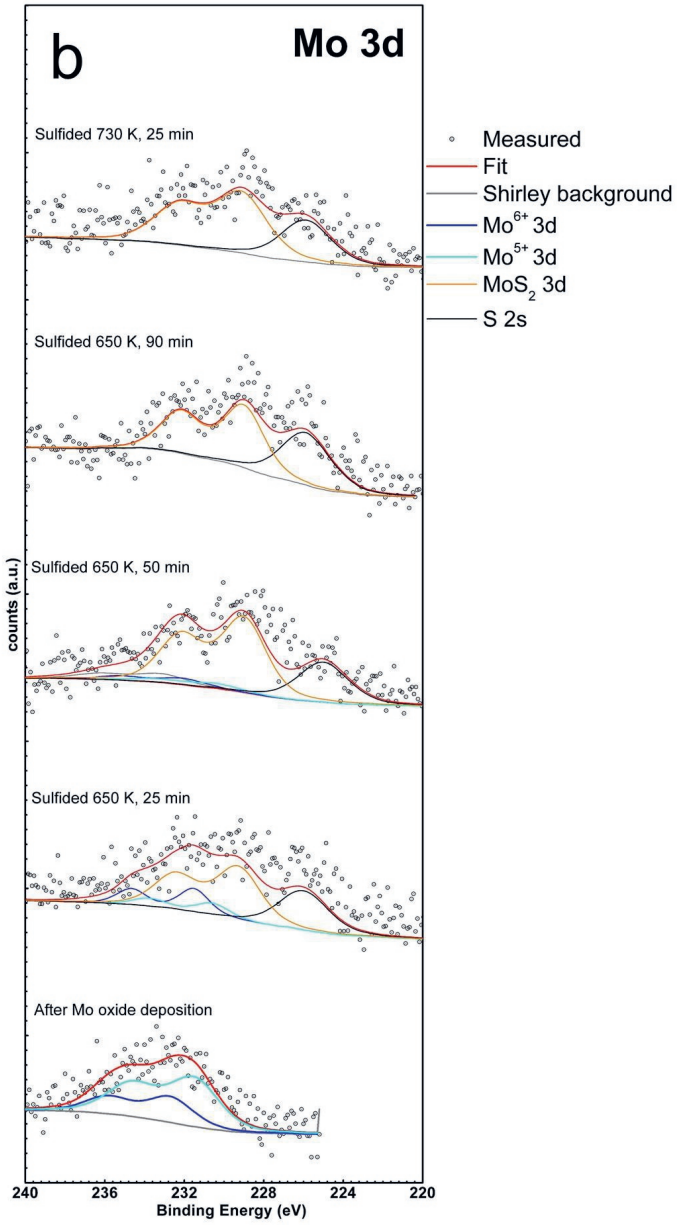

Figure 4: a,b) XPS spectra of Co $2p_{3/2}$ and Mo 3d regions respectively at various stages of oxide precursor synthesis and subsequent sulfidation.

We note that because of our ultimate aim of synthesizing small nanoclusters of the Co-promoted MoS_2 phase for catalytic studies, low coverages of Mo and Co are used in the experiments presented in this study. Therefore, it is only expected that the signal-to-noise ratio in the XPS data is low because of which there is greater uncertainty in the peak fitting used. However, due to the significant morphological changes occurring during the sulfidation process, it is important to obtain chemical information of our samples to gain more insights. Given the chemically blind nature of the STM and its inability to quantitatively probe the sub-surface, information on the coverages of Co and Mo obtained from the XPS is still very useful due to its ability to simultaneously probe the surface and the sub-surface atomic layers. The Co:Mo ratio and the coverages of the Co and Mo were estimated from the XPS spectra by taking into account the relative sensitivity factors of Co and Mo (see Table 2). The oxidic precursor containing the Co oxide slabs has a measured Co coverage of 0.061 ML. After the deposition of Mo oxide nanoparticles to 0.056 ML, the coverage of Co decreases to 0.055 ML. We attribute this decrease to a slight attenuation of the XPS signal of Co due to the Mo oxide growing over some of the Co oxide slabs. After sulfidation for 25 minutes at 650 K, we observe that the Co coverage is restored to the initial value of 0.061 ML while the Mo coverage only increases marginally resulting in a Co:Mo ratio of 1.05:1. This is a direct consequence of the morphological changes observed in the STM wherein both the Co and Mo oxides sulfide and spread on the surface to form large 2D clusters. The Co:Mo ratio as well as the coverages of Mo and Co remain constant with increasing time of sulfidation within the limits of the minute differences between the initial precursors prepared for each of the sulfidation experiments and the inherent uncertainty due to the lower signal-to-noise ratio in the XPS data. After sulfidation at 730 K for 25 minutes, however, we observe a significant decrease in the Co:Mo ratio as well as a decrease in the coverages of Co and Mo. We attribute this change to the increased tendency of Co and Mo oxides to reduce and alloy with Au at 730 K due to the surface of Au(111) being more sulfur-deficient than at 650 K. This leads to a partial lifting of the herringbone reconstruction and the formation of vacancy islands on the Au surface (see SI, Figure S4b).

In all of the sulfided samples studied in this chapter, individual SL slabs with a truncated hexagonal shape were also observed to form(Figure 5a). We identify these slab as the Co-promoted MoS_2 slabs. It is also known that MoS_2 slabs without the Co-promoter atoms adopt a fully triangular shape under sulfur-rich conditions that are used in this study. This is because the Mo-terminated edge is thermodynamically more favorable than the S-terminated edge for a pristine MoS_2 slab under S-rich conditions.[49] Incorporation of Co atoms into the S edge leads to thermodynamic stability and hence, the Co-promoted MoS_2 slabs adopt a hexagonal or truncated hexagonal shape displaying both the Mo- and S-terminated edges (see SI, Figure S6). Thus, the formation of hexagonal slabs under the sulfiding conditions used in our study is a signature of Co being incorporated into the S edges of the MoS_2 slabs.[49] Figure 5b shows the zoom in of a Co-promoted MoS_2 slab. It is known from prior STM experiments on MoS_2 that it is the sulfur atoms that are imaged as bright protrusions in the basal plane.[9] In Figure 5b, we observe that the penultimate row of protrusions along the edges of the Co-promoted MoS_2 slabs appear brighter than those in the basal plane. This feature is attributed to the electronic effects due to the 1D metallic edge states called as Brim sites.[9,49] In the past, a combination of STM experiments and DFT calculations has been used to show that the registry of the ultimate row of protrusions along the edges of a Co-promoted MoS_2 slabs with respect to the basal plane can be used to identify the type and the sulfur saturation of the edges.[49] In Figure 5b, the rows of atoms in the basal plane have been marked with green lines as a guide for the eyes. We observe that along

one of the edges, the bright protrusions are in registry with the basal plane protrusions. This is the signature of a 100% sulfur-saturated Co-substituted S edge.[49] On the adjacent edge, however, the edge protrusions are clearly out of registry with respect to the line of protrusions in the basal plane. This edge is identified as the 100% sulfur-saturated Mo-terminated edge in agreement with the work of Grønborg et al..[49] Figure 5c shows an atom-resolved STM image of a large cluster containing the MoS_2 and the 2D CoS_2 phase, measured after sulfidation for 90 minutes at 650 K. Based on the same method of edge identification, we identify the presence of Co-substituted S edge and the Mo-terminated edge in the MoS_2 phase (phase 2, Figure 3a) as well. This observation shows that the Co-substituted S edge is formed not only in the hexagonal SL Co-promoted MoS_2 slabs, but also in the MoS_2 phase present in the larger clusters as well.

4.4 Discussion

We have studied the process of growing a mixed Mo and Co oxide precursor and the subsequent transformation to Mo and Co sulfide through sulfidation with H_2S. We have carried out the sulfidation at 650 K for 25 to up to 90 minutes and at 730 K for 25 minutes. Our objective has been to gain insights into the process of oxide to sulfide conversion to form the Co-promoted MoS_2 phase.

Our results from XPS and STM show that there is a strong preference for the sulfidation of Co oxide. This is evident from the complete conversion of the Co oxide within the first 25 minutes of sulfidation. The sulfidation of Mo oxide on the other hand, is observed to be thermally activated. The sulfidation process is accompanied by a change in morphology from well-distributed nanoparticles and slabs to large clusters containing multiple phases. The formation of large clusters after the sulfidation process from a precursor containing oxide nanoparticles of Co and Mo can be driven by two factors, namely, the temperature and the presence of sulfur species. Annealing the oxidic precursor containing the Mo and Co oxides to 600 K in the absence of H_2S causes clustering of the Mo oxide phases (see SI, Figure S7). This clustering is accompanied by reduction of the Mo oxide phase as can be seen in the Mo 3d spectra in SI. Mo^{6+} oxide is known to undergo reduction to Mo^{5+} and Mo^{4+} states at temperatures above 600 K even in mild oxygen backgrounds ($\leq 1x10^{-6}$ mbar).[28,31,59] This thermal reduction is typically accompanied by a tendency to form large atomically flat clusters due to the underlying thermally activated cluster diffusion process.[29,31,59] The cobalt oxide slabs, on the other hand, are observed to be stable such heat treatments up to 650 K. However, in the presence of sulfur, diffusion of Co is known to be greatly enhanced due to the formation of Co-sulfur complexes even at 300 K.[62] Therefore, the observed morphological changes are very well in agreement with previous experimental reports.

Our STM experiments also show that the formation of the SL Co-promoted MoS_2 slabs with truncated hexagonal shape is not affected by the temperature or the duration of sulfidation as they are observed to form in all the sulfide samples studied in this chapter. Additionally, formation of the MoS_2 phase in the large clusters with the Co-substituted S edge is not hindered by the slower sulfidation of Mo oxide. However, the yield of individual SL Co-promoted MoS_2 slabs is significantly less than what would be obtained if the respective metallic precursors were used as a starting point such as in the recipes reported in literature.[23] This is mainly due to the tendency of the mixed oxide precursor to spread and form large clusters in the presence of sulfur and at elevated temperature, which then leads to differential sulfidation of the Co and Mo oxide phases in the cluster, thereby, reducing the yield of

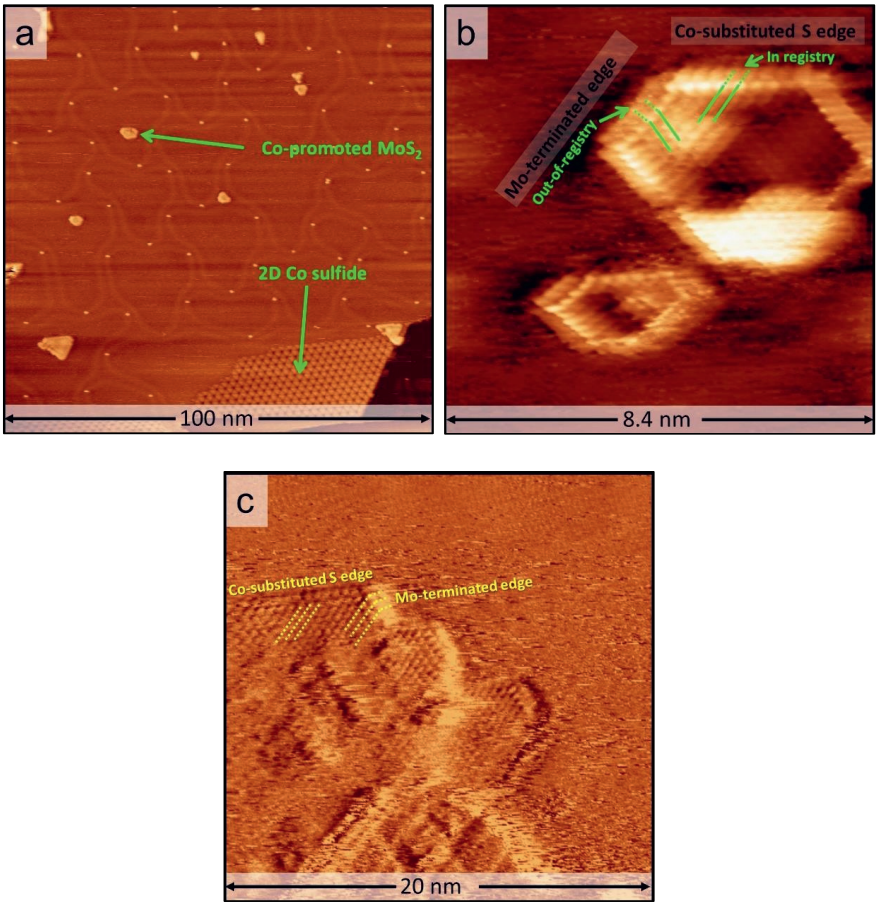

Figure 5:a) Large-scale STM image showing hexagonal MoS_2 slabs formed because of Co incorporation into the S edge, sample voltage = -1 V, tunneling current = 150 pA; b) Atom-resolved STM image of hexagonal Co-promoted MoS_2 slabs showing the Mo-terminated and the Co-substituted S edges, sample voltage = -0.5 V, tunneling current = 200 pA; ;c) Atom-resolved STM image of the MoS_2 slabs in the large clusters (phase 2), sample voltage = -0.35 V, tunneling current = 900 pA.

the Co-promoted MoS_2 phase. The Mo oxide phase that is not fully sulfided, is encapsulated by the 2D CoS_2 and the MoS_2 slabs as can be seen in the STM images presented in this chapter. This could create additional barriers for the sulfur atoms to diffuse into the partially converted Mo oxide phase. This is quite in contrast to the previously reported synthesis strategies that involve Au(111)-supported metallic Co and Mo nanoparticles as the precursor wherein, the nanoparticles readily sulfide and form Co-promoted MoS_2 slabs due to the absence of the oxysulfide phase.[23,49] Despite the low yield, we show that using a precursor with mixed Mo and Co oxides is a viable strategy to synthesize the Co-promoted MoS_2 phase in order to carry out fundamental studies relevant for fields such as catalysis. One possible strategy to increase the yield of individual Co-promoted MoS_2 slabs could involve starting with a precursor containing other ratios Mo and Co. Another solution may lay in the use of model supports like TiO_2(110) that interact strongly with Co and Mo oxides, and thus, prevent large clusters from forming.

4.5 Conclusions

Starting with a mixture of Mo and Co oxide nanoparticles on Au(111), we have investigated the process of their sulfidation using STM and XPS. We have shown that it is possible to synthesis SL Co-promoted MoS_2 slabs using this mixed oxide precursor independent of the temperature and duration of the sulfidation process. We have also shown that due to the tendency to reduce and spread on the surface, the Mo and Co oxides form large clusters that contain the MoS_2, 2D CoS_2 and likely an incompletely sulfided Mo oxide phase depending on the temperature and duration of the sulfidation. The MoS_2 slabs in these large clusters also have Co atoms incorporated in their S edges. Thus, we have shown that sulfiding a mixture of Co and Mo oxide nanoparticles is a feasible strategy to synthesize Co-promoted MoS_2 for fundamental catalysis studies, especially those for hydrodesulfurization.

.

4.6 References

(1) Liu, B.; Abbas, A.; Zhou, C. Two-Dimensional Semiconductors: From Materials Preparation to Electronic Applications. *Advanced Electronic Materials*. 2017, p 1700045. https://doi.org/10.1002/aelm.201700045.

(2) Bissett, M. A.; Worrall, S. D.; Kinloch, I. A.; Dryfe, R. A. W. Comparison of Two-Dimensional Transition Metal Dichalcogenides for Electrochemical Supercapacitors. *Electrochim. Acta* 2016, *201*, 30–37. https://doi.org/10.1016/j.electacta.2016.03.190.

(3) Manzeli, S.; Ovchinnikov, D.; Pasquier, D.; Yazyev, O. V.; Kis, A. 2D Transition Metal Dichalcogenides. *Nature Reviews Materials*. 2017, p 17033. https://doi.org/10.1038/natrevmats.2017.33.

(4) Lembke, D.; Bertolazzi, S.; Kis, A. Single-Layer MoS_2 Electronics. *Acc. Chem. Res.* 2015, *48* (1), 100–110. https://doi.org/10.1021/ar500274q.

(5) Yin, W.; Yan, L.; Yu, J.; Tian, G.; Zhou, L.; Zheng, X.; Zhang, X.; Yong, Y.; Li, J.; Gu, Z.; Zhao, Y. High-Throughput Synthesis of Single-Layer MoS_2 Nanosheets as a near-Infrared Photothermal-Triggered Drug Delivery for Effective Cancer Therapy. *ACS Nano* 2014, *8* (7), 6922–6933. https://doi.org/10.1021/nn501647j.

(6) Feng, J.; Graf, M.; Liu, K.; Ovchinnikov, D.; Dumcenco, D.; Heiranian, M.; Nandigana, V.; Aluru, N. R.; Kis, A.; Radenovic, A. Single-Layer MoS_2 Nanopores as Nanopower Generators. *Nature* 2016, *536* (7615), 197–200. https://doi.org/10.1038/nature18593.

(7) Wu, W.; Wang, L.; Li, Y.; Zhang, F.; Lin, L.; Niu, S.; Chenet, D.; Zhang, X.; Hao, Y.; Heinz, T. F.; Hone, J.; Wang, Z. L. Piezoelectricity of Single-Atomic-Layer MoS_2 for Energy Conversion and Piezotronics. *Nature* 2014, *514* (7253), 470–474. https://doi.org/10.1038/nature13792.

(8) Li, Y.; Li, Y. L.; Araujo, C. M.; Luo, W.; Ahuja, R. Single-Layer MoS_2 as an Efficient Photocatalyst. *Catal. Sci. Technol.* 2013, *3* (9), 2214–2220. https://doi.org/10.1039/c3cy00207a.

(9) Helveg, S.; Lauritsen, J. V.; Lægsgaard, E.; Stensgaard, I.; Nørskov, J. K.; Clausen, B. S.; Topsøe, H.; Besenbacher, F. Atomic-Scale Structure of Single-Layer MoS_2 Nanoclusters. *Phys. Rev. Lett.* 2000, *84* (5), 951–954. https://doi.org/10.1103/PhysRevLett.84.951.

(10) Grønborg, S. S.; Ulstrup, S.; Bianchi, M.; Dendzik, M.; Sanders, C. E.; Lauritsen, J. V.; Hofmann, P.; Miwa, J. A. Synthesis of Epitaxial Single-Layer MoS_2 on Au(111). *Langmuir* 2015, *31* (35), 9700–9706. https://doi.org/10.1021/acs.langmuir.5b02533.

(11) Kibsgaard, J.; Lauritsen, J. V.; Lægsgaard, E.; Clausen, B. S.; Topsøe, H.; Besenbacher, F. Cluster-Support Interactions and Morphology of MoS_2 Nanoclusters in a Graphite-Supported Hydrotreating Model Catalyst. *J. Am. Chem. Soc.* 2006, *128* (42), 13950–13958. https://doi.org/10.1021/ja0651106.

(12) Liu, H.; Li, Y.; Xiang, M.; Zeng, H.; Shao, X. Single-Layered MoS2 Directly Grown on Rutile TiO_2(110) for Enhanced Interfacial Charge Transfer. *ACS Nano* 2019, *13* (5), 6083–6089. https://doi.org/10.1021/acsnano.9b02608.

(13) Galhenage, R. P.; Yan, H.; Rawal, T. B.; Le, D.; Brandt, A. J.; Maddumapatabandi, T. D.; Nguyen, N.; Rahman, T. S.; Chen, D. A. MoS_2 Nanoclusters Grown on TiO_2: Evidence for New Adsorption Sites at Edges and Sulfur Vacancies. *J. Phys. Chem. C* 2019, *123* (12), 7185–7201. https://doi.org/10.1021/acs.jpcc.9b00076.

(14) Kibsgaard, J.; Clausen, B. S.; Topsøe, H.; Lægsgaard, E.; Lauritsen, J. V.; Besenbacher, F. Scanning Tunneling Microscopy Studies of TiO_2-Supported Hydrotreating Catalysts: Anisotropic Particle Shapes by Edge-Specific MoS_2-Support Bonding. *J. Catal.* 2009, *263* (1), 98–103. https://doi.org/10.1016/j.jcat.2009.01.016.

(15) Topsøe, H.; Clausen, B. S.; Candia, R.; Wivel, C.; Mørup, S. In Situ Mössbauer Emission Spectroscopy Studies of Unsupported and Supported Sulfided CoMo Hydrodesulfurization Catalysts: Evidence for and Nature of a CoMoS Phase. *J. Catal.* 1981, *68* (2), 433–452. https://doi.org/10.1016/0021-9517(81)90114-7.

(16) Dai, X.; Du, K.; Li, Z.; Liu, M.; Ma, Y.; Sun, H.; Zhang, X.; Yang, Y. Co-Doped MoS_2 Nanosheets with the Dominant CoMoS Phase Coated on Carbon as an Excellent Electrocatalyst for Hydrogen Evolution. *ACS Appl. Mater. Interfaces* 2015, *7* (49), 27242–27253. https://doi.org/10.1021/acsami.5b08420.

(17) Nieskens, D. L. S.; Ferrari, D.; Liu, Y.; Kolonko, R. The Conversion of Carbon Dioxide and Hydrogen into Methanol and Higher Alcohols. *Catal. Commun.* 2011, *14* (1), 111–113. https://doi.org/10.1016/j.catcom.2011.07.020.

(18) Escalera-López, D.; Niu, Y.; Yin, J.; Cooke, K.; Rees, N. V.; Palmer, R. E. Enhancement of the Hydrogen Evolution Reaction from Ni-MoS_2 Hybrid Nanoclusters. *ACS Catal.* 2016, *6* (9), 6008–6017. https://doi.org/10.1021/acscatal.6b01274.

(19) Deng, J.; Li, H.; Xiao, J.; Tu, Y.; Deng, D.; Yang, H.; Tian, H.; Li, J.; Ren, P.; Bao, X. Triggering the Electrocatalytic Hydrogen Evolution Activity of the Inert Two-Dimensional MoS_2 Surface via Single-Atom Metal Doping. *Energy Environ. Sci.* 2015, *8* (5), 1594–1601. https://doi.org/10.1039/c5ee00751h.

(20) Okamoto, Y. A Novel Preparation-Characterization Technique of Hydrodesulfurization Catalysts for Cleaner Fuels. *Catal. Today* 2008, *132* (1–4), 9–17. https://doi.org/10.1016/j.cattod.2007.12.030.

(21) Menart, M. J.; Hensley, J. E.; Costelow, K. E. Thermal Decomposition of Bulk K-$CoMoS_x$ Mixed Alcohol Catalyst Precursors and Effects on Catalyst Morphology and Performance. *Appl. Catal. A Gen.* 2012, *437–438*, 36–43. https://doi.org/10.1016/j.apcata.2012.06.010.

(22) Byskov, L. S.; Nørskov, J. K.; Clausen, B. S.; Topsøe, H. Edge Termination of MoS_2 and CoMoS Catalyst Particles. *Catal. Letters* 2000, *64* (2–4), 95–99. https://doi.org/10.1023/a:1019063709813.

(23) Lauritsen, J. V.; Kibsgaard, J.; Olesen, G. H.; Moses, P. G.; Hinnemann, B.; Helveg, S.; Nørskov, J. K.; Clausen, B. S.; Topsøe, H.; Lægsgaard, E.; Besenbacher, F. Location and Coordination of Promoter Atoms in Co- and Ni-Promoted MoS_2-Based Hydrotreating Catalysts. *J. Catal.* 2007, *249* (2), 220–233. https://doi.org/10.1016/j.jcat.2007.04.013.

(24) Leliveld, R. G.; Van Dillen, A. J.; Geus, J. W.; Koningsberger, D. C. The Sulfidation of γ-Alumina and Titania Supported (Cobalt)Molybdenum Oxide Catalysts Monitored by EXAFS. *J. Catal.* 1997, *171* (1), 115–129. https://doi.org/10.1006/jcat.1997.1783.

(25) Qian, W.; Ishihara, A.; Aoyama, Y.; Kabe, T. Sulfidation of Nickel- and Cobalt-Promoted Molybdenum-Alumina Catalysts Using a Radioisotope 35S-Labeled H_2S Pulse Tracer Method. *Appl. Catal. A Gen.* 2000, *196* (1), 103–110. https://doi.org/10.1016/S0926-860X(99)00454-8.

(26) Kobayashi, M.; Flytzani-Stephanopoulos, M. Reduction and Sulfidation Kinetics of Cerium Oxide and Cu-Modified Cerium Oxide. *Ind. Eng. Chem. Res.* 2002, *41* (13), 3115–3123. https://doi.org/10.1021/ie010815w.

(27) Chen, C. J.; Chiang, R. K. Sulfidation of Rock-Salt-Type Transition Metal Oxide Nanoparticles as an Example of a Solid State Reaction in Colloidal Nanoparticles. *Dalt. Trans.* 2011, *40* (4), 880–885. https://doi.org/10.1039/c0dt00906g.

(28) Salazar, N.; Beinik, I.; Lauritsen, J. V. Single-Layer MoS_2 Formation by Sulfidation of Molybdenum Oxides in Different Oxidation States on Au(111). *Phys. Chem. Chem. Phys.* 2017, *19* (21), 14020–14029. https://doi.org/10.1039/c7cp00958e.

(29) Guimond, S.; Göbke, D.; Sturm, J. M.; Romanyshyn, Y.; Kuhlenbeck, H.; Cavalleri, M.; Freund, H. J. Well-Ordered Molybdenum Oxide Layers on Au(111): Preparation and Properties. *J. Phys. Chem. C* 2013, *117* (17), 8746–8757. https://doi.org/10.1021/jp3113792.

(30) Biener, M. M.; Friend, C. M. Heteroepitaxial Growth of Novel MoO_3 Nanostructures on Au(1 1 1). *Surf. Sci.* 2004, *559* (2–3), 173–179.

(31) Song, Z.; Cai, T.; Chang, Z.; Liu, G.; Rodriguez, J. A.; Hrbek, J. Molecular Level Study of the Formation and the Spread of MoO_3 on Au (111) by Scanning Tunneling Microscopy and X-Ray Photoelectron Spectroscopy. *J. Am. Chem. Soc.* 2003, *125* (26), 8059–8066. https://doi.org/10.1021/ja034862m.

(32) Biener, M. M.; Biener, J.; Schalek, R.; Friend, C. M. Growth of Nanocrystalline MoO_3 on Au(111) Studied by in Situ Scanning Tunneling Microscopy. *J. Chem. Phys.* 2004, *121* (23), 12010–12016. https://doi.org/10.1063/1.1808422.

(33) Uetsuka, H.; Onishi, H.; Ikeda, S.; Harada, Y.; Sakama, H.; Sakashita, Y. Atomic Force Microscope Observation of MoS_2 Particles Synthesized on Mica, MoS_2, and Graphite. *e-Journal Surf. Sci. Nanotechnol.* 2003, *1*, 80–83. https://doi.org/10.1380/ejssnt.2003.80.

(34) Mom, R. V.; Rost, M. J.; Frenken, J. W. M.; Groot, I. M. N. Tuning the Properties of Molybdenum Oxide on Al_2O_3/NiAl(110): Metal versus Oxide Deposition. *J. Phys. Chem. C* 2016, *120* (35), 19737–19743. https://doi.org/10.1021/acs.jpcc.6b06040.

(35) Haber, J.; Nowak, P.; Stoch, J. Molybdenum Oxide Monolayers at the Rutile (110) Surface Studied by Electrochemical and XPS Methods. *Bull. Polish Acad. Sci. Chem.* 1997, *45* (2), 139–149.

(36) Fester, J.; Bajdich, M.; Walton, A. S.; Sun, Z.; Plessow, P. N.; Vojvodic, A.; Lauritsen, J. V. Comparative Analysis of Cobalt Oxide Nanoisland Stability and Edge Structures on Three Related Noble Metal Surfaces: Au(111), Pt(111) and Ag(111). *Top. Catal.* 2017, *60* (6–7), 503–512. https://doi.org/10.1007/s11244-016-0708-6.

(37) De Santis, M.; Buchsbaum, A.; Varga, P.; Schmid, M. Growth of Ultrathin Cobalt Oxide Films on Pt(111). *Phys. Rev. B - Condens. Matter Mater. Phys.* 2011, *84* (12), 125430.

(38) Entani, S.; Kiguchi, M.; Saiki, K. Fabrication of Polar CoO(111) Thin Films on Pt(111). In *Surface Science*; 2004; Vol. 566–568, pp 165–169.

(39) Sebastian, I.; Heiler, M.; Meinel, K.; Neddermeyer, H. Growth of Epitaxial Layers of Co and CoO on Au(111). *Appl. Phys. A Mater. Sci. Process.* 1998, *66*, 525–528. https://doi.org/10.1007/s003390051195.

(40) Li, M.; Altman, E. I. Shape, Morphology, and Phase Transitions during Co Oxide Growth on Au(111). *J. Phys. Chem. C* 2014, *118* (24), 12706–12716. https://doi.org/10.1021/jp411375w.

(41) Li, M.; Altman, E. I. Cluster-Size Dependent Phase Transition of Co Oxides on Au(111). *Surf. Sci.* 2014, *619*, 6–10. https://doi.org/10.1016/j.susc.2013.09.029.

(42) Fester, J.; Sun, Z.; Rodríguez-Fernández, J.; Walton, A.; Lauritsen, J. V. Phase Transitions of Cobalt Oxide Bilayers on Au(111) and Pt(111): The Role of Edge Sites and Substrate Interactions. *J. Phys. Chem. B* 2018, *122* (2), 561–571. https://doi.org/10.1021/acs.jpcb.7b04944.

(43) Fester, J.; Walton, A.; Li, Z.; Lauritsen, J. V. Gold-Supported Two-Dimensional Cobalt Oxyhydroxide (CoOOH) and Multilayer Cobalt Oxide Islands. *Phys. Chem. Chem. Phys.* 2017, *19* (3), 2425–2433. https://doi.org/10.1039/c6cp07901f.

(44) Walton, A. S.; Fester, J.; Bajdich, M.; Arman, M. A.; Osiecki, J.; Knudsen, J.; Vojvodic, A.; Lauritsen, J. V. Interface Controlled Oxidation States in Layered Cobalt Oxide Nanoislands on Gold. *ACS Nano* 2015, *9* (3), 2445–2453. https://doi.org/10.1021/acsnano.5b00158.

(45) Chung, J. Bin; Chung, J. S. Desulfurization of H_2S Using Cobalt-Containing Sorbents at Low Temperatures. *Chem. Eng. Sci.* 2005, *60* (6), 1515–1523. https://doi.org/10.1016/j.ces.2004.11.002.

(46) Sanders, A. F. H.; De Jong, A. M.; De Beer, V. H. J.; Van Veen, J. A. R.; Niemantsverdriet, J. W. Formation of Cobalt-Molybdenum Sulfides in Hydrotreating Catalysts: A Surface Science Approach. *Appl. Surf. Sci.* 1999, *144–145*, 380–384. https://doi.org/10.1016/S0169-4332(98)00831-9.

(47) Coulier, L.; De Beer, V. H. J.; Van Veen, J. A. R.; Niemantsverdriet, J. W. On the Formation

of Cobalt-Molybdenum Sulfides in Silica-Supported Hydrotreating Model Catalysts. *Top. Catal.* 2000, *13* (1–2), 99–108. https://doi.org/10.1023/a:1009037006529.

(48) Leliveld, R. G.; Van Dillen, A. J.; Geus, J. W.; Koningsberger, D. C. A Mo-K Edge XAFS Study of the Metal Sulfide-Support Interaction in (Co)Mo Supported Alumina and Titania Catalysts. *J. Catal.* 1997, *165* (2), 184–196. https://doi.org/10.1006/jcat.1997.1480.

(49) Grønborg, S. S.; Salazar, N.; Bruix, A.; Rodríguez-Fernández, J.; Thomsen, S. D.; Hammer, B.; Lauritsen, J. V. Visualizing Hydrogen-Induced Reshaping and Edge Activation in MoS_2 and Co-Promoted MoS_2 Catalyst Clusters. *Nat. Commun.* 2018, *9* (1), 1–11.

(50) Herbschleb, C. T.; Van Der Tuijn, P. C.; Roobol, S. B.; Navarro, V.; Bakker, J. W.; Liu, Q.; Stoltz, D.; Cañas-Ventura, M. E.; Verdoes, G.; Van Spronsen, M. A.; Bergman, M.; Crama, L.; Taminiau, I.; Ofitserov, A.; Van Baarle, G. J. C.; Frenken, J. W. M. The ReactorSTM: Atomically Resolved Scanning Tunneling Microscopy under High-Pressure, High-Temperature Catalytic Reaction Conditions. *Rev. Sci. Instrum.* 2014, *85* (8), 83703. https://doi.org/10.1063/1.4891811.

(51) Rost, M. J.; van Baarle, G. J. C.; Katan, A. J.; van Spengen, W. M.; Schakel, P.; van Loo, W. A.; Oosterkamp, T. H.; Frenken, J. W. M. Video-Rate Scanning Probe Control Challenges: Setting the Stage for a Microscopy Revolution. *Asian J. Control* 2009, *11* (2), 110–129.

(52) Rost, M. J.; Crama, L.; Schakel, P.; Van Tol, E.; Van Velzen-Williams, G. B. E. M.; Overgauw, C. F.; Ter Horst, H.; Dekker, H.; Okhuijsen, B.; Seynen, M.; Vijftigschild, A.; Han, P.; Katan, A. J.; Schoots, K.; Schumm, R.; Van Loo, W.; Oosterkamp, T. H.; Frenken, J. W. M. Scanning Probe Microscopes Go Video Rate and Beyond. *Rev. Sci. Instrum.* 2005, *76* (5), 053710. https://doi.org/10.1063/1.1915288.

(53) Horcas, I.; Fernández, R.; Gómez-Rodríguez, J. M.; Colchero, J.; Gómez-Herrero, J.; Baro, A. M. WSXM: A Software for Scanning Probe Microscopy and a Tool for Nanotechnology. *Rev. Sci. Instrum.* 2007, *78* (1), 013705. https://doi.org/10.1063/1.2432410.

(54) Horcas, I.; Fernández, R.; Gómez-Rodríguez, J. M.; Colchero, J.; Gómez-Herrero, J.; Baro, A. M. WSXM: A Software for Scanning Probe Microscopy and a Tool for Nanotechnology. *Rev. Sci. Instrum.* 2007, *78* (1), 013705. https://doi.org/10.1063/1.2432410.

(55) Wagner, C. D. Sensitivity Factors for XPS Analysis of Surface Atoms. *J. Electron Spectros. Relat. Phenomena* 1983, *32* (2), 99–102. https://doi.org/10.1016/0368-2048(83)85087-7.

(56) Biesinger, M. C.; Payne, B. P.; Grosvenor, A. P.; Lau, L. W. M.; Gerson, A. R.; Smart, R. S. C. Resolving Surface Chemical States in XPS Analysis of First Row Transition Metals, Oxides and Hydroxides: Cr, Mn, Fe, Co and Ni. *Appl. Surf. Sci.* 2011, *257* (7), 2717–2730. https://doi.org/10.1016/j.apsusc.2010.10.051.

(57) van Haandel, L.; Smolentsev, G.; van Bokhoven, J. A.; Hensen, E. J. M.; Weber, T. Evidence of Octahedral Co–Mo–S Sites in Hydrodesulfurization Catalysts as Determined by Resonant Inelastic X-Ray Scattering and X-Ray Absorption Spectroscopy. *ACS Catal.* 2020, *10* (19), 10978–10988. https://doi.org/10.1021/acscatal.0c03062.

(58) Bremmer, G. M.; van Haandel, L.; Hensen, E. J. M.; Frenken, J. W. M.; Kooyman, P. J. The Effect of Oxidation and Resulfidation on (Ni/Co)MoS_2 Hydrodesulfurisation Catalysts. *Appl. Catal. B Environ.* 2019, *243*, 145–150. https://doi.org/10.1016/j.apcatb.2018.10.014.

(59) Deng, X.; Quek, S. Y.; Biener, M. M.; Biener, J.; Kang, D. H.; Schalek, R.; Kaxiras, E.; Friend, C. M. Selective Thermal Reduction of Single-Layer MoO_3 Nanostructures on Au(1 1 1). *Surf. Sci.* 2008, *602* (6), 1166–1174. https://doi.org/10.1016/j.susc.2008.01.014.

(60) Prabhu, M. K.; Boden, D.; Rost, M. J.; Meyer, J.; Groot, I. M. N. Structural Characterization of a Novel Two-Dimensional Material: Cobalt Sulfide Sheets on Au(111). *J. Phys. Chem. Lett.* 2020, *11* (21), 9038–9044. https://doi.org/10.1021/acs.jpclett.0c02268.

(61) Hebenstreit, E. L. D.; Hebenstreit, W.; Diebold, U. Adsorption of Sulfur on TiO_2(110) Studied with STM, LEED and XPS: Temperature-Dependent Change of Adsorption Site Combined with O-S Exchange. *Surf. Sci.* 2000, *461* (1–3), 87–97. https://doi.org/10.1016/S0039-6028(00)00538-0.

(62) Kibsgaard, J.; Morgenstern, K.; Lægsgaard, E.; Lauritsen, J. V.; Besenbacher, F. Restructuring of Cobalt Nanoparticles Induced by Formation and Diffusion of Monodisperse Metal-Sulfur Complexes. *Phys. Rev. Lett.* 2008, *100* (11), 116104. https://doi.org/10.1103/PhysRevLett.100.116104.

Chapter 4 - Supporting information

1. Moiré structure of Co oxide

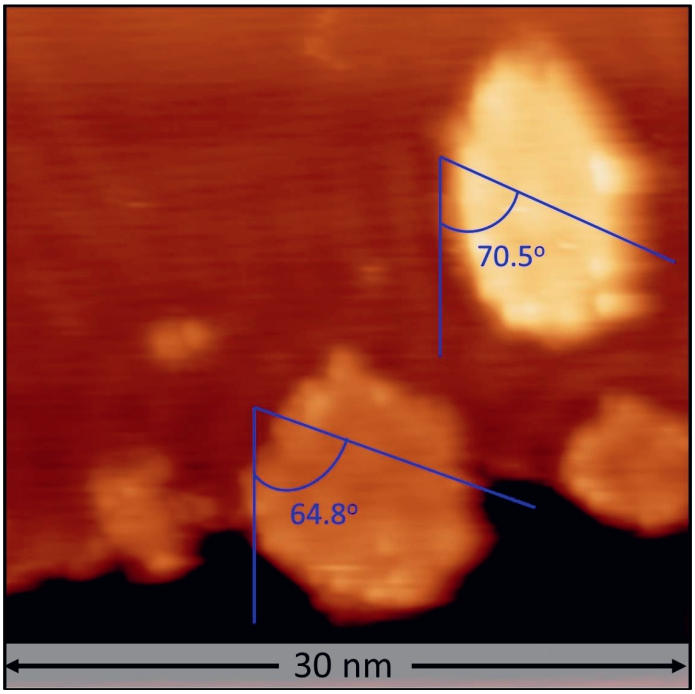

Figure S1: Angle measurement of the hexagonal moiré pattern on single- and double-layer Co-O type Co oxide slabs, tunneling current = 200 pA, sample voltage = -1.2 V. We measure a difference of ~6° in the direction of the moiré pattern of the higher slabs compared to the lower ones.

2. Synthesis of Mo oxide nanoparticles on Au(111)

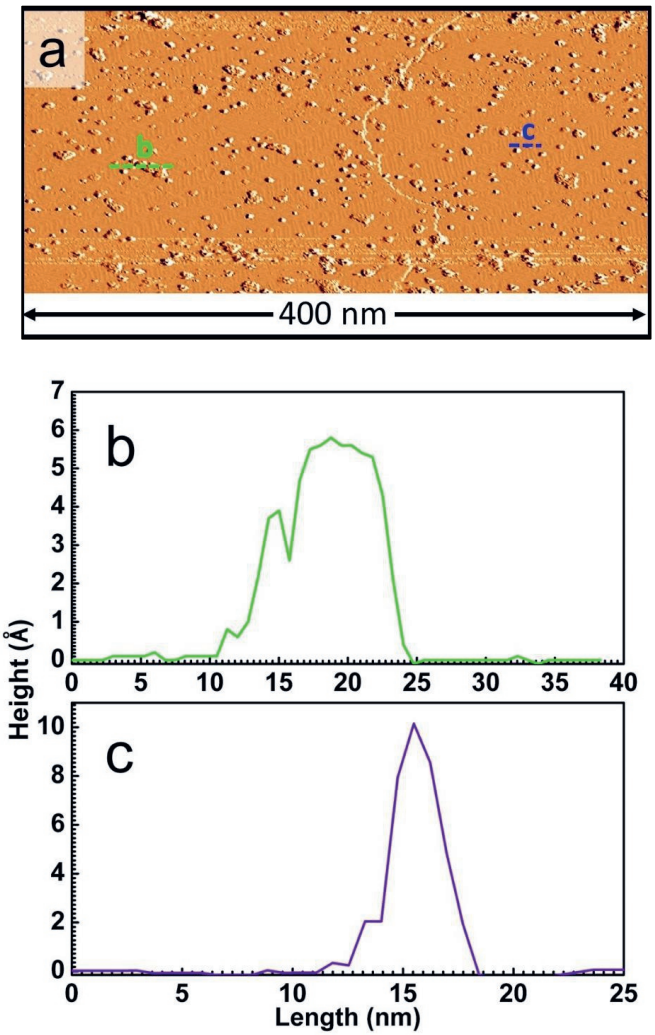

Figure S2: a) Large-scale STM image of Mo oxide nanoparticles on Au(111), sample voltage = -1.8 V, tunneling current = 200 pA. For clarity, the image is shown with a differential filter. The nanoparticles are grown by the direct deposition method described in the experimental section; b) measured height along line marked 'b' in Figure S2a; c) measured height along line marked 'c' in Figure S2a.

3. Measured STM heights of Co and Mo oxide nanoparticles supported on Au(111)

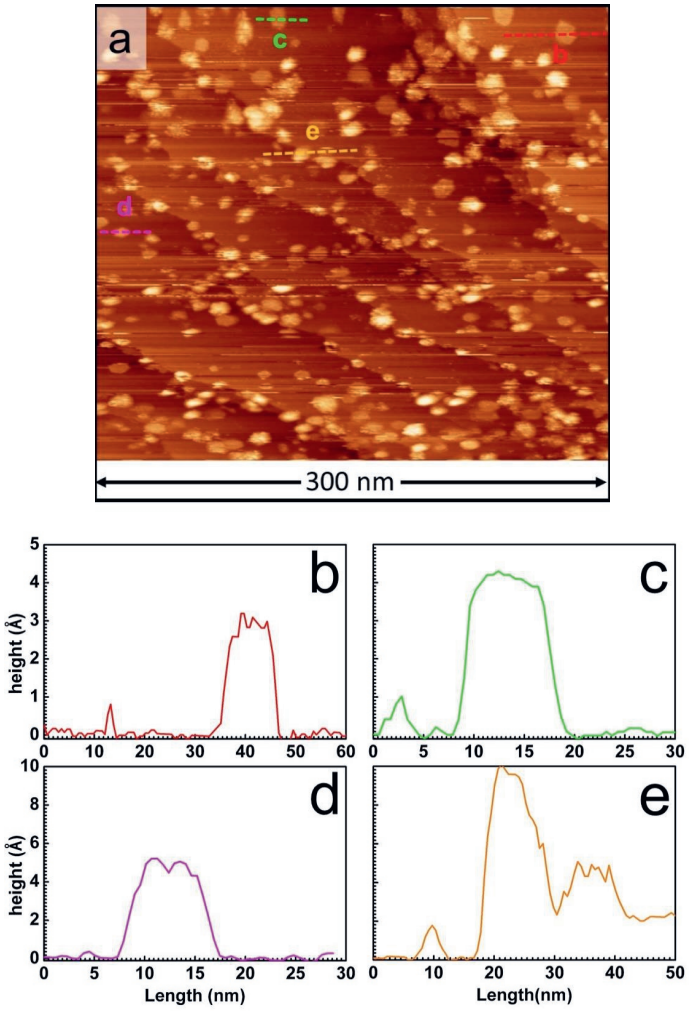

Figure S3: Mo and Co oxide nanoparticles on Au(111), sample voltage = -1.7 V, tunneling current = 150 pA; a) Large-scale STM image obtained at 300 K in UHV; b-d) Measured heights of Co oxide slabs along the dashed lines in Figure S3a with the respective colors, showing heights of 3 Å, 4 Å and 5 Å respectively; e) Measured height of an Mo oxide nanoparticle along the orange dashed line in Figure S3a showing a height of 10 Å.

4. Effect of increasing the duration of sulfidation and the temperature

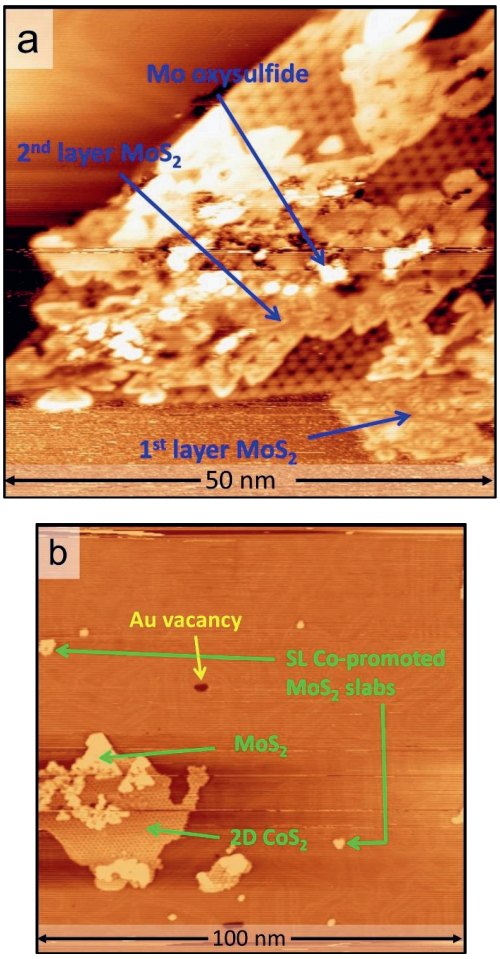

Figure S4: STM images after sulfidation of a mixture of Mo and Co oxides on Au(111), sample voltage = -1 V, tunneling current = 100 pA; a) at 650 K for 90 minutes, b) at 730 K for 25 minutes.

5. S 2p and O 1s XPS spectra

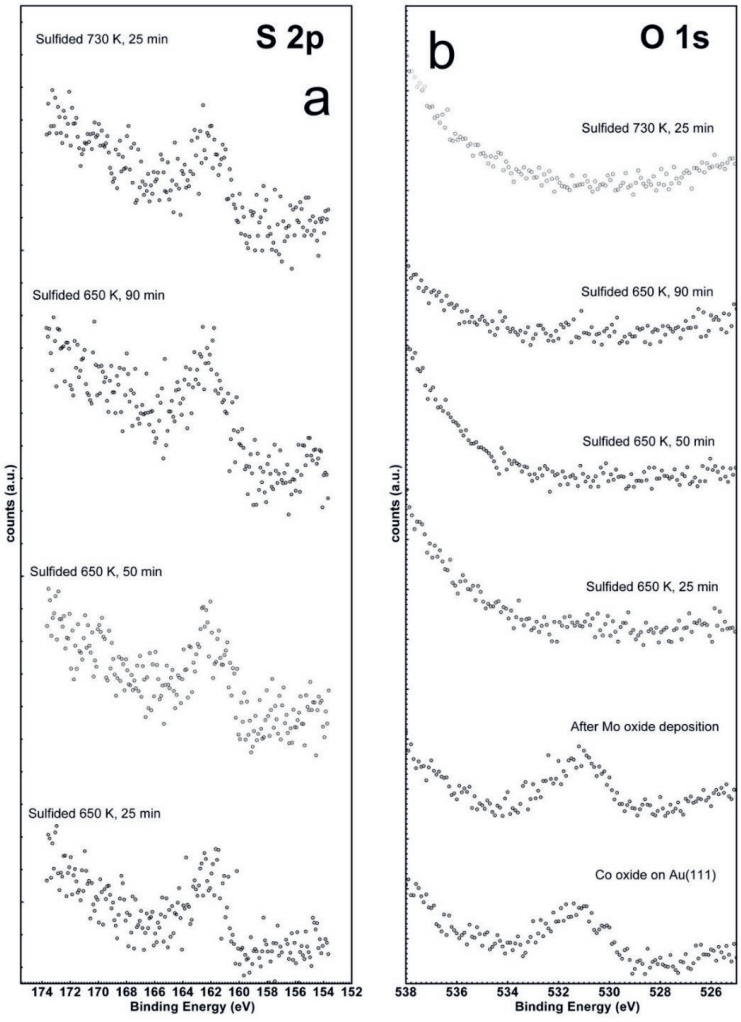

Figure S5:a,b) XPS spectra of S 2p and O 1s regions respectively at various stages of the oxide precursor synthesis and subsequent sulfidation.

6. Atomic model of the Co-promoted MoS_2 slab

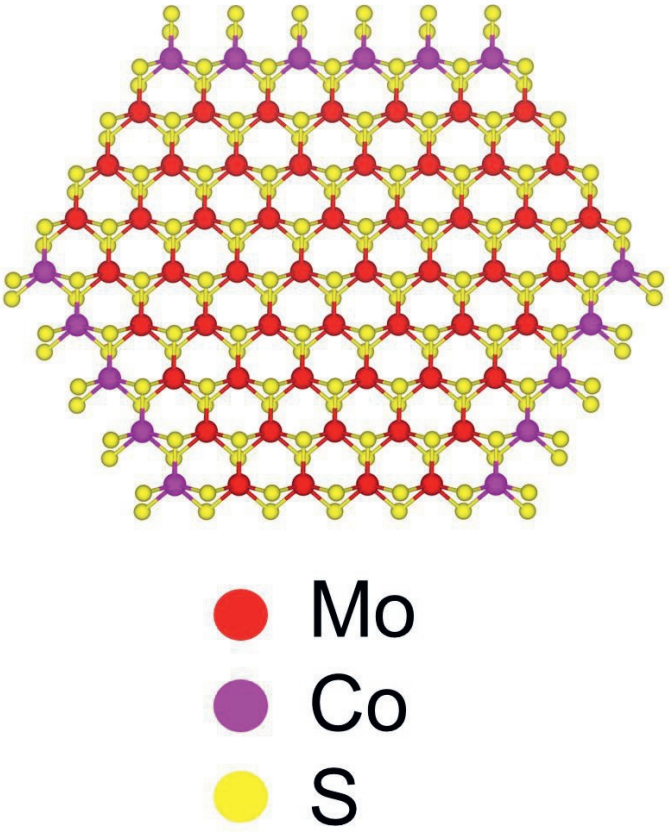

Figure S6: Atomic model of a Co-promoted MoS_2 slab.

7. Mixed Co and Mo oxide precursor heated in the absence of H_2S

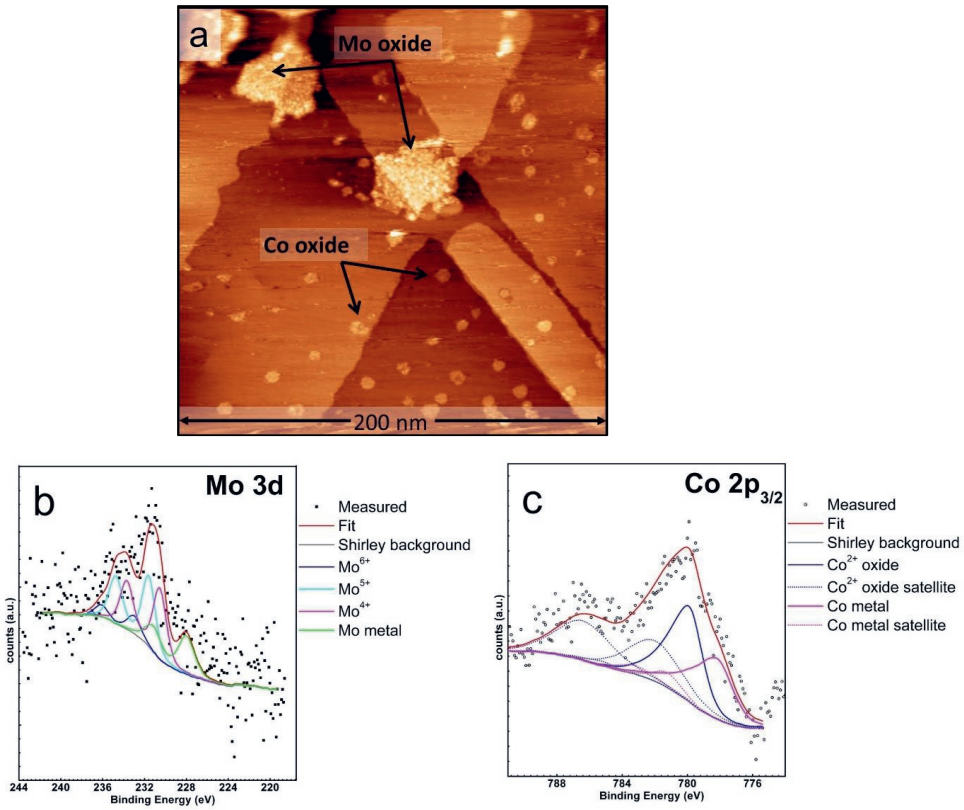

Figure S7: a) Large-scale STM image of a precursor containing Co oxide and Mo oxide slabs (as in Figure 2a) annealed at 650 K in a $5x10^{-7}$ mbar O_2 atmosphere, sample voltage = -1.5 V, tunneling current = 100 pA; b) Mo 3d XPS spectra of the sample in Figure S7a; c) Co $2p_{3/2}$ XPS spectra of the sample in Figure S7a.

Chapter 5

Low-temperature synthesis strategy for MoS_2 slabs supported on TiO_2(110)

This chapter is based on:
Prabhu, M. K.; Groot, I. M. N. Low-Temperature Synthesis Strategy for MoS_2 Slabs Supported on TiO_2(110), Surfaces ***2020****, 3(4), 605-621*

Abstract:

MoS_2 supported on oxides like TiO_2 has a broad range of applications. The atomic structure of this system is therefore, very useful to study. Previous research work in this area has made use of high-temperature synthesis methods to gain atomic-level insights for important applications such as catalysis, while the industrial synthesis strategy predominantly makes use of a low-temperature synthesis method. In this chapter, we investigate a low-temperature synthesis strategy for MoS_2 slabs supported on rutile TiO_2(110). Using scanning tunneling microscopy and X-ray photoelectron spectroscopy, we demonstrate that not only flat MoS_2 slabs with irregular shapes but also MoS_x stripes with coordinatively unsaturated Mo atoms are also formed. Furthermore, this work shows that for atomic structural characterization of MoS_2/TiO_2 and similar oxide-supported systems grown by low-temperature synthesis methods, the surface structure of the support becomes highly relevant and cannot be ignored.

5.1 Introduction

Nanostructured MoS_2/TiO_2 composites have attracted a lot of interest as a model system for applications in electronics[1–3], photovoltaics[4], electrocatalysis[5] and heterogeneous catalysis[6], combining a transition metal dichalcogenide (TMDC) and a wide-bandgap semiconductor. In particular, the promoted MoS_2/TiO_2 system is widely applied in industry to perform hydrodesulfurization (HDS) and reduce the global SO_x emissions.[7–9] More recently, the MoS_2/TiO_2 system has also found application as an efficient hydrogen evolution reaction (HER) catalyst.[10]

Despite the widespread applications, many fundamental properties of the MoS_2-TiO_2 system, especially those relevant for catalysis, such as the atomic structure and reactivity of the edges, are disputed due to the difficulty of resolving the edge structure with sufficient contrast in conventional characterization techniques such as electron microscopy.[11,12] Recent studies on model systems have attempted to tackle some of these challenges using scanning tunneling microscope (STM) and X-ray photoelectron spectroscopy (XPS). For instance, Kibsgaard et al.[6] have shown that the morphology of MoS_2 slabs supported on rutile $TiO_2(110)$ depends on the atomic structure of the $TiO_2(110)$ surface and the synthesis temperature. The MoS_2 slabs grown using physical vapor deposition (PVD) at 900 K are hexagonal, while at 950 K, elongated particles are formed. Galhenage et al.[13] have investigated the effects of exposure of $MoS_2/TiO_2(110)$ grown by PVD at 950 K to various gas environments such as D_2, CO and methanol. The MoS_2 slabs grown on $TiO_2(110)$ by alternative strategies, like chemical vapor deposition (CVD), have shown efficient excitonic separation between the MoS_2 and TiO_2 phases and hence, better photocatalytic activity.[14] In all these studies, MoS_2 is grown at temperatures above 900 K and thermodynamically favorable pristine MoS_2 slabs with well-defined edges and the basal planes lying flat on the $TiO_2(110)$ surface are observed.

In industrially relevant systems such as a HDS catalyst however, MoS_2 is typically grown at much lower temperatures between 573-673 K using wet chemical procedures.[15–17] The transmission electron microscopy (TEM) studies of MoS_2 grown at low-temperatures on various facets of rutile and anatase TiO_2 have shown the presence of "edge-on" supported MoS_2 slabs.[18,19] The X-ray absorption fine structure (XAFS) studies of the Mo K-edge of MoS_2 slabs grown on $TiO_2(110)$ at lower temperature have indicated the presence of MoS_2 clusters with Mo being in five-fold coordination or less.[20,21] Such unsaturated Mo atoms were assigned to small MoS_2 clusters potentially growing as stripes on the TiO_2 surface.[20] On the contrary, the prior STM-based studies on $MoS_2/TiO_2(110)$ fabricated by the high-temperature synthesis procedure have not observed the formation of any such structures. Given the sensitivity of the MoS_2 morphology to the synthesis temperature, it is important to synthesize MoS_2 on the TiO_2 surface at lower temperatures in order to gain atomic level insights, especially those relevant for industrial HDS. However, such attempts are complicated by the reactivity of the $TiO_2(110)$ substrate towards sulfur. Studies performed by other groups have shown that, depending on the temperature and the coverage, sulfur can form a plethora of structures by binding to five-fold coordinated surface Ti atoms, by replacement of the surface bridging oxygen atoms or by replacement of the near-surface in-plane oxygen atoms.[22–25] Such complications are conveniently avoided at higher temperatures as the sulfur desorbs from the $TiO_2(110)$ surface.

In this chapter, we report a synthesis procedure to grow MoS_2 on rutile $TiO_2(110)$ at a catalytically relevant low temperature of 650 K. We start with depositing Mo nanoparticles on a clean $TiO_2(110)$

surface. The Mo nanoparticles are thereafter, sulfided using H_2S as the sulfiding agent. We make use of STM and XPS to study the morphology of MoS_2. We show that our synthesis procedure yields irregular shaped MoS_2 slabs with their basal planes lying flat on the substrate and "edge-on" MoS_x stripes forming as elongated structures aligned along the $[1\bar{1}0]$ direction of the $TiO_2(110)$ substrate. At higher initial Mo coverage, we obtain predominantly multilayered MoS_2 slabs with their basal planes lying flat on the substrate. Furthermore, we show that all these structures adhere to a (3x1) lattice on the $TiO_2(110)$ surface formed by adsorption of sulfur. Additionally, we present possible atomic models supported by our experimental results to explain our findings for future theoretical work.

5.2 Materials and Methods

All the experiments were carried out in the ReactorSTM setup.[26] A polished rutile $TiO_2(110)$ crystal was purchased from Surface Preparation Laboratory, Zaandam, the Netherlands. The $TiO_2(110)$ crystal was cleaned by repeated cycles of sputtering and annealing. The sputtering was performed using Ar^+ with an ion energy of 1.5 keV and annealing was performed at 873 K for 10 min in the presence of O_2 at $2x10^{-6}$ mbar. Heating and cooling rates of 10 K/minute were maintained to prevent cracks in the crystals due to thermal shock. The ultimate cleaning cycle involved annealing in ultra-high vacuum (UHV) at 900 K for 10 min to generate atomically flat $TiO_2(110)$ terraces. The cleanliness was checked with XPS and STM until impurities were below the detection limits. The $TiO_2(110)$ crystal turned light blue after this cleaning procedure due to the slight bulk reduction in UHV generating oxygen vacancies which act as color centers.

Mo metal was deposited from an Mo rod using an Oxford EGCO4 e-beam evaporator with the TiO_2 substrate held at 300 K. Coverages of Mo were checked using XPS and samples with 0.25, 0.49 and 0.61 ML Mo nanoparticles were prepared as precursors for the sulfidation process. The coverage of the Mo nanoparticles was calculated from the XPS spectra by comparing the peak areas of Mo 3d and Ti 2p signals after correcting for the relative sensitivity factors.[27] The sulfidation was carried out by heating the samples to 650 K for 45 minutes in a H_2S atmosphere of $1x10^{-3}$ mbar. Thereafter, the samples were cooled to room temperature in UHV.

Scanning tunneling microscopy was performed at room temperature using the UHV mode of the ReactorSTM. Polycrystalline Pt-Ir 90-10 wires purchased from Goodfellow were cut and used as STM tips without further processing. Constant-current scans were performed using LPM video-rate scanning electronics described in detail elsewhere.[28,29] Home-developed Camera software and WSxM were used for STM image processing.[30,31] Most-common normal filtering was used to obtain a correctly connected surface in order to calculate the height profiles. Line-by-line background subtraction was used otherwise for the ease of viewing. No other processing was performed on the STM images reported in this Chapter.

The XPS measurements were performed in a SPECS Phoibos system equipped with an XRM50 X-ray source set to the Al K-alpha line used along with a monochromator to excite the sample with a beam spot of 0.4 mm diameter at 54.6° incidence. The acceleration voltage was set to 10 kV and a power of 250 W was used for all the measurements. The HSA3500 hemispherical analyzer with a pass energy of 30 eV was used to analyze the photoemission. The bulk Ti 2p peak set to 458.5 eV was used to calibrate the XPS spectra obtained.[32] The calibration was further checked using a separate clean Au(111) single crystal by confirming the peak position of Au 4f at 84 eV. The number of integrations was set to 20.

The data thus obtained, were characterized and quantified using CASA-XPS and with relative sensitivity factors reported in the literature.[27] The XPSPEAK41 software was used for peak fitting the Mo 3d and S 2p spectra. The Mo 3d and S 2p peaks were fit using a mixed Gaussian-Lorentzian (65-35) curves. Shirley background subtraction was applied and a non-linear least squares method was used for peak fitting. The Mo 3d spectrum was fit with components for Mo (228.0 eV), MoO_x (228.7 eV) and MoO_2 (229.8 eV) for the Mo nanoparticles and MoS_2 (229.2 eV), MoS_x (228.8 eV, 228.3 eV) and the S 2s (226.2 eV) component for the Mo sulfide samples. The MoS_x has two components arising from 5-fold and 4-fold coordinated Mo atoms. The S 2p spectra were fit with components for S^{2-} (161.8 eV) and bridging S_2^{2-} (163.1 eV) doublets separated by 3.15 eV and 1.16 eV, respectively. These binding energies are tabulated in Table 1 and they are based on previous experiments reported in literature.[33–40]

Table 1: XPS binding energies for various components used for peak fitting.

Components	**Mo metal**	**MoO_x**	**MoO_2**	**MoS_2**
Binding energy (eV)	228.0	228.7	229.8	229.2
ΔBE (eV)	3.15	3.15	3.15	3.15
Components	MoS_x	S 2s	S^{2-} 2p	S_2^{2-}2p
Binding energy (eV)	228.3, 228.8	226.2	161.8	163.1
ΔBE* (eV)	3.15		1.16	1.16

* $\Delta BE(3d) = BE\ 3d_{5/2} - BE\ 3d_{3/2}$; $\Delta BE(2p) = BE\ 2p_{3/2} - BE\ 2p_{1/2}$

5.3 Results and Discussion

A clean $TiO_2(110)$ surface with atomic steps produced by our cleaning procedure is shown in Figure 1a. The height of steps (Figure 1b) is measured to be 3.19 Å and it is very close to the monoatomic step height 3.24 Å of $TiO_2(110)$.[41] The terraces show bright and dark rows along the [001] direction (Figure 1c, 1d) characteristic of a slightly reduced UHV-annealed $TiO_2(110)$ surface.[22,41–43] The bright rows in Figure 1c are attributed to the Ti^{4+} atoms with five-fold coordination and the dark rows are attributed to the bridging oxygen atoms of the rutile $TiO_2(110)$ atomic structure.[44] Figure 1d shows that the presence of dark spots on the bright rows of the (1x1) structure. These features have been interpreted as sub-surface oxygen vacancy sites in a previous study.[43] The bright features on the dark rows which are expected for surface oxygen defects are not imaged here.[43–45] The Pt-Ir tips are known to be prone to a tip state where these features are not imaged and the appearance of the dark features are enhanced.[43] The bright features observed in Figure 1d are likely due to residual -OH groups on the surface.[45]

Mo metal was deposited onto the clean $TiO_2(110)$ surface by physical vapor deposition from an Mo rod as detailed in the experimental methods. Figure 2a shows the large-scale STM image of the Mo nanoparticles supported on the $TiO_2(110)$ surface grown to a coverage of 0.25 ML of Mo. The Mo nanoparticles are observed to nucleate randomly on the $TiO_2(110)$ terraces and are 1.8-3.2 Å high (Figure 2b). Some nanoparticles of 4-5 Å height are also observed. The Mo nanoparticles uniformly cover the $TiO_2(110)$ surface and preference for any nucleation site was not observed. Furthermore, the Mo 3d XPS

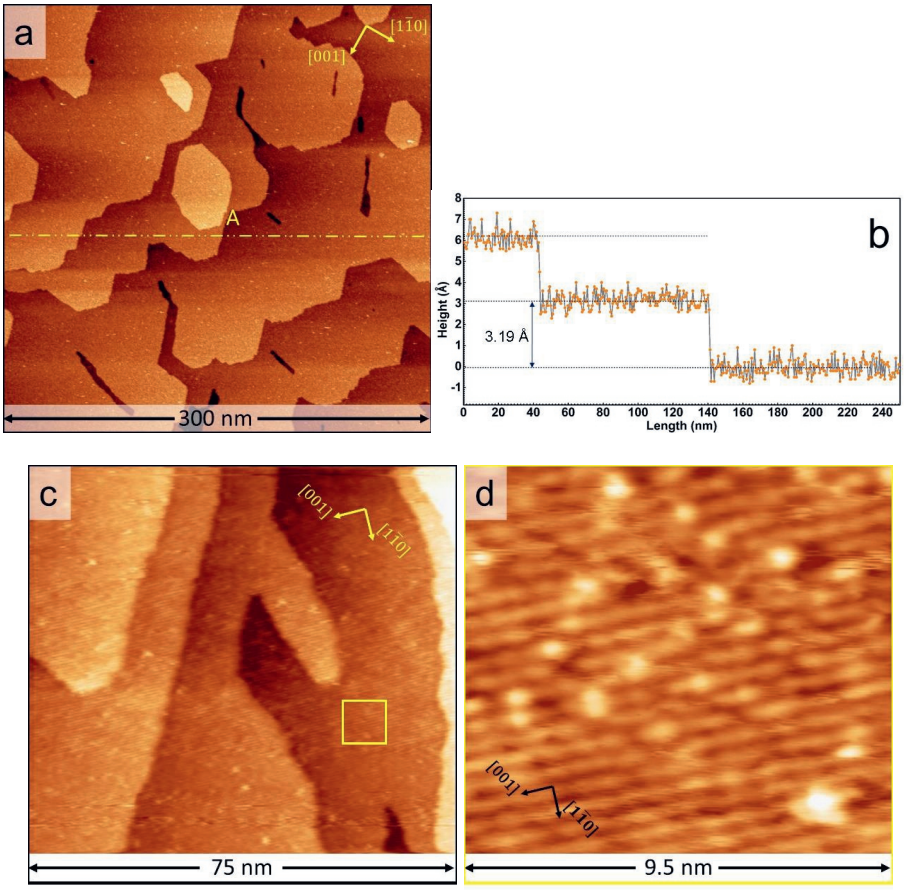

Figure 1: a) Large-scale STM image of a clean TiO_2(110) surface after sputtering and annealing in UHV at 900 K; sample voltage = +2.2 V, tunneling current = 150 pA. b) Height along line A in Figure 1a shows the measured step height of clean TiO_2(110) is 3.19 Å. c) Zoom in of the TiO_2(110) surface showing the alternating bright and dark rows characteristic of the (1x1) structure of slightly reduced rutile titania. d) Zoom-in of the area denoted by the yellow square in Figure 1c.

spectrum (Figure 2c) shows a peak at 228.8 eV which is less than the expected 229.2 eV for Mo^{4+} suggesting that the particles have an overall oxidation state of less than 4. Peak fitting shows the presence of Mo^{4+} as well as a sub-stoichiometric Mo oxide component suggesting that the particles are of the form MoO_{2-x}. The lack of a preferred nucleation site and the spontaneous partial oxidation of Mo nanoparticles on the $TiO_2(110)$ surface suggests a very strong substrate-overlayer interaction. Such a strong Mo-$TiO_2(110)$ interaction has been observed in the previous studies on this system.[33–36,46,47] The nature of interaction between metal nanoparticles and the TiO_2 surface has been found to depend on the initial heat of adsorption of oxygen on the respective metal nanoparticle in comparison to the initial heat of reduction of TiO_2. In the case of Mo, the heat of absorption of oxygen is greater than the heat of reduction of TiO_2. Therefore, the transfer of oxygen from the surface to the Mo nanoparticles leading to their partial oxidation is thermodynamically favorable.[47] The Mo nanoparticles thus formed, are known to have an oxidation state of less than 4, as observed in our experiment. Similar behavior is also observed for reactive metals with high heat of oxygen adsorption such as Re, Al, Hf, Cr, and Mn supported on TiO_2.[48–50] Growing Mo nanoparticles to higher coverages, for instance, to 0.49 ML leads to an increase in their metallicity, as is evident from the overall 0.4 eV shift of the Mo 3d spectrum to lower binding energy(see SI, Figure S1). The peak fits also show a non-zero contribution from metallic Mo signature at 228.0 eV. This increase in the metallicity of Mo is attributed to the kinetic limitations of oxygen diffusion from the bulk TiO_2 to Mo nanoparticles and was observed in the previous studies as well.[33]

The Mo nanoparticles thus prepared, were sulfided at 650 K in a H_2S atmosphere of $1x10^{-3}$ mbar, as detailed in the experimental methods. Figures 3a and 3b show large-scale STM images of MoS_2 slabs on $TiO_2(110)$ formed after the sulfidation process. Upon sulfidation, the atomically-flat structures with a dark relative contrast and a bright rim along their perimeter are formed. We identify these structures as MoS_2 slabs with their basal planes lying flat on the TiO_2 (110) support and refer to them as "basal-bonded" MoS_2 slabs in the rest of this chapter. These MoS_2 slabs are of 3-5 nm size and predominantly have an irregular shape (Figures 3b and 3c). The "basal-bonded" MoS_2 slabs, despite their irregular shape, appear to be slightly elongated along the $[1\bar{1}0]$ direction. This is in contrast to the MoS_2 slabs grown by the high-temperature synthesis methods used in prior studies where highly elongated particles with well-defined edges aligned along both the [001] and $[1\bar{1}0]$ directions were observed.[6,13] Kibsgaard et al.[6], in particular, observed a strong dependence of the shape of the MoS_2 slabs on the synthesis temperature. The irregular edge shapes of the "basal-bonded" MoS_2 in our experiments are likely driven by the strong interaction of Mo nanoparticles with the $TiO_2(110)$ substrate as well as the adsorption of S on $TiO_2(110)$ which, in turn, strongly depends on the temperature.[22–25,51] Atomic resolution of the basal planes of the "basal-bonded" MoS_2 slabs show an interatomic distance of 3.13 Å (see Figure 3d) which matches well with the reported S-Mo-S distance of 3.15 Å of the (0001) basal plane of single-layer (SL) MoS_2 slabs.[52] This further shows that the "basal-bonded" MoS_2 slabs grown in this experiment are crystalline in nature. Atomic resolution along the edges was, however, difficult to obtain due to the low conductivity of the titania substrate. Furthermore, the tendency for rapid tip changes due to the mobile sulfur species present on the sample made it difficult to maintain the tip state required for the atomic resolution of the MoS_2 basal planes.

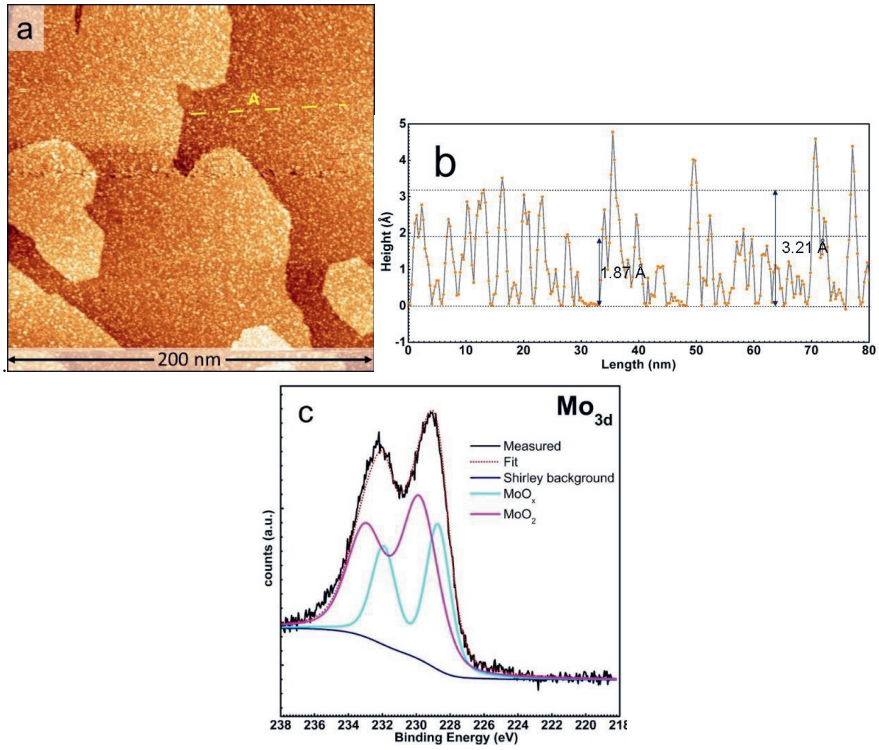

Figure 2: a) Large-scale STM image of Mo nanoparticles supported on TiO_2(110) grown by physical vapor deposition at 300 K; sample voltage = +2.2 V, tunneling current = 200 pA. The Mo coverage is 0.25 ML as determined from XPS. b) Measured height along the line marked A in Figure 2a. c) Mo 3d XPS spectrum of the Mo nanoparticles supported on TiO_2(110).

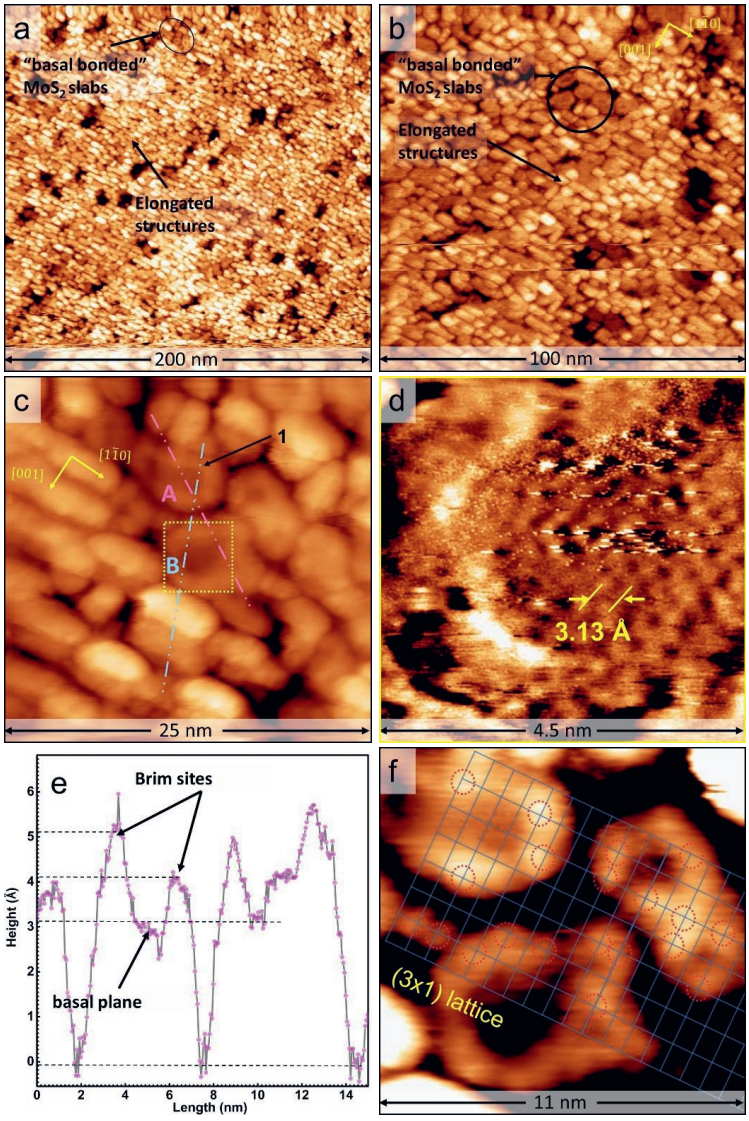

Figure 3: a, b) Large-scale STM images of MoS_2 slabs supported on TiO_2(110) obtained with a sample voltage = +2.1 V and tunneling current = 150 pA. The coverage of Mo determined from XPS is 0.25 ML. c) Zoomed-in STM image showing MoS_2 slabs supported on TiO_2(110). d) Atom-resolved STM image of the "basal-bonded" MoS_2 slab within the area marked by the yellow dotted square in Figure 3c. e) Measured height along the line marked A in Figure 3c, (Measured height along the line B is discussed later in Figure 5a). f) A (3x1) lattice superimposed on the "basal-bonded" MoS_2 slabs in Figure 3c. The red dotted circles show the locations where the bright corner sites match the (3x1) lattice.

The observed bright rim along the periphery of the MoS_2 slabs was attributed to the electronic effects of one-dimensional metallic states on the edges of the MoS_2 slabs called Brim sites.[53] The bright rim of "basal-bonded" MoS_2 slabs supported on TiO_2(110) is, however, more diffuse as compared to MoS_2 on metallic supports like Au(111). These Brim sites were also observed on MoS_2 slabs grown on TiO_2 at 900 K.[6] The measured height along the line marked A in Figure 3c (shown in Figure 3e) shows that the "basal-bonded" MoS_2 slabs have the edge protrusions measured up to 5.1±0.1 Å high while the basal planes are measured to be 3.3±0.2 Å high which is close to the theoretical S-Mo-S distance of 3.15 Å. However, the SL MoS_2 slabs with measured height of up to 4.7 Å were reported in previous studies.[6,13] The measured height of MoS_2 is strongly influenced by electronic effects due to the chemical state of the tip, applied sample voltage, MoS_2-TiO_2 interactions as well as the conductivity of the substrate which in turn is influenced by the cleaning procedure and fate of the substrate due to the inevitable sulfur-TiO_2 chemical reactions at the lower synthesis temperature used in our experiment. Therefore, the comparison of our measured heights with previous literature reports becomes difficult. Since nearly all of the "basal-bonded" MoS_2 slabs have the same relative contrast with respect to the TiO_2(110) steps, we conclude that the synthesis procedure yields predominantly SL "basal-bonded" MoS_2 slabs. Furthermore, we observe that there are two types of Brim sites with a measured height difference of ~1 Å. This is attributed to the Mo- and S- terminated edges of the MoS_2 slabs having slightly different electron densities at the respective Brim sites. Furthermore, the electron density at these Brim sites was found to have maxima (bright spots) at the corner sites of the irregular "basal-bonded" MoS_2 slabs. Analysis of the locations of these corner sites of nearby "basal-bonded" MoS_2 slabs showed that the bright spots were located at positions which were integral multiples of ~6.2 Å along the $[1\bar{1}0]$ direction and ~8.9 Å along the [001] direction, thus fitting a (3x1) TiO_2(110) lattice (see Figure 3f) strongly suggesting that these bright spots are related to bonding of the MoS_2 slabs with the substrate, likely through an edge sulfur atom. Theoretical calculations using density functional theory (DFT) on the influence of the substrate interactions are necessary to correctly assign the edge terminations.

Increasing the initial coverage of Mo nanoparticles to 0.49 ML followed by sulfidation also formed "basal-bonded" MoS_2 slabs. However, the slabs were observed to merge along at least one of their edges and thus, forming effectively larger-size MoS_2 slabs. This effect can be seen in Figure 4a and is better resolved in Figure 4b. The "basal-bonded" MoS_2 slabs thus formed, retain their irregular shape and also have an atomically-flat basal plane with a dark relative contrast. However, we also observed the formation of a significant number of slabs with a brighter contrast in the basal plane. Heightlines along the basal planes of these slabs show a measured height of ~5.8 Å suggesting the formation of a second layer (see SI, Figure S2). Upon further increasing the coverage of Mo nanoparticles to 0.61 ML followed by sulfidation, the MoS_2 slabs are predominantly "basal-bonded" and are multilayered, as is evident from their STM contrasts (see Figure 4c). As the substrate is already completely covered at this Mo coverage, determining the number layers of "basal-bonded" MoS_2 slabs from the STM images becomes difficult. However, a layer-by-layer growth of the MoS_2 slabs is evident from our experiments up to a coverage of 0.61 ML Mo.

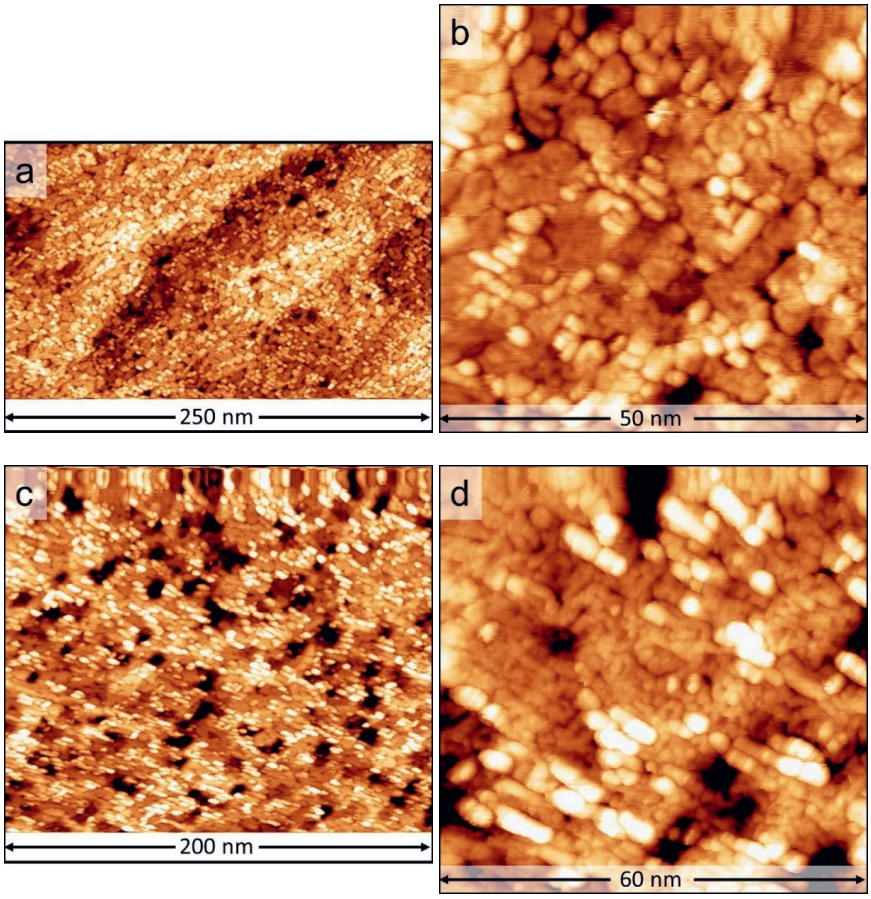

Figure 4: a, b) STM images of MoS_2 slabs supported on TiO_2(110) obtained with a sample voltage = +2.2 V and tunneling current = 150 pA. The coverage of Mo determined from XPS is 0.49 ML. c, d) MoS_2 slabs supported on TiO_2(110) obtained with a sample voltage = +2.2 V and tunneling current = 200 pA. The coverage of Mo determined from XPS is 0.61 ML.

In addition to the "basal-bonded" MoS_2 slabs, we also observe the formation of several elongated structures aligned along the [1$\bar{1}$0] direction for all the coverages of Mo nanoparticles presented in this work. These elongated structures have both intermediate and bright relative contrasts with respect to the "basal-bonded" MoS_2 slabs as seen in the large-scale STM images in Figures 3a, 4a and 4c. These structures have not been observed to form in the previous studies that use high temperature for the synthesis of MoS_2 on TiO_2 at 900 K and 950 K. The measured height along the line marked B in Figure 3c over one such elongated structures is shown in Figure 5a. The elongated structures were measured to have a height of 7.2±0.2 Å for the intermediate contrast ones and 11.7±0.4 Å for the bright contrast ones. Additionally, the elongated structures are 3-5 nm in length and are formed without a preferred

location as is seen from their uniform distribution on the TiO_2(110) steps in Figure 4a. Furthermore, these elongated structures are resolved further into a row of bright spots separated by 6.2±0.1 Å (see Figure 5b). The elongated structures typically consist of 2-4 of such rows separated by 8.6±0.2 Å (see Figure 5b and 5c). These distances fit well with a (3x1) TiO_2(110) lattice suggesting that strong substrate interactions are present and likely play a key role in the formation of these structures. We also observed that the number density of the elongated structures decreases sharply with increasing the Mo coverage from 0.25 to 0.49 ML but only decreases slightly with further increasing the Mo coverage to 0.61 ML (see SI, Figure S3). However, we also observe that the elongated structures always have a higher STM contrast than that of the "basal-bonded" MoS_2 slabs irrespective of the number of layers of MoS_2 grown, suggesting a more metallic nature of the elongated structures. For example, in the case of Mo coverage of 0.25 ML, a relative height difference of up to 8.3±0.4 Å (see Figure 5a) is measured between the elongated structures and the basal planes of nearby "basal-bonded" MoS_2 slabs, while in the case of Mo coverage of 0.61 ML, a height difference of 7.4±0.2 Å (see SI, Figure S2) is measured. However, one may expect that the geometric effect growing multiple layers of "basal-bonded" MoS_2 slabs eventually offsets the electronic effects of an adjacent, more metallic elongated structure and, therefore, the contrast difference between the MoS_2 phase and the elongated structures should decrease with increasing coverage of Mo. The measured height difference however, contradicts this expectation. This observation can, however, be explained by the vertical growth of the elongated structures with respect to the TiO_2 substrate.

The Mo 3d and S 2p spectra of all the sulfided samples are shown in Figure 6. After sulfidation, irrespective of the coverage, all the Mo 3d spectra show a doublet with peaks at 229.2 eV and 232.3 eV which are identified as those of MoS_2 and a shoulder at 226.1 eV which is identified as the expected S 2s feature. The Mo 3d doublets were fit based on the interpretations by Bruix et al.[37]. The observed Mo 3d signal has no components of Mo^{5+} and Mo^{6+} states suggesting complete conversion to MoS_2 and no residual Mo oxysulfides within the detection limits of the XPS measurements. This matches very well with our STM observations. Furthermore, the data also suggest the presence of sub-stoichiometric MoS_x due to non-zero components at 228.7 eV and 228.3 eV. These two components have been assigned by Bruix et al. to coordinatively unsaturated Mo atoms bound to sulfur, such as the edge Mo atoms of an MoS_2 slab. Such coordinatively unsaturated Mo atoms have a lower oxidation state than that of the Mo atoms in the basal plane of an MoS_2 slab and hence, a lower binding energy signal in XPS. Upon increasing the coverage of Mo from 0.25 to 0.49 ML, it is observed that the MoS_2 : MoS_x ratio increases. But further increase of Mo coverage to 0.61 ML does not change this relative ratio significantly, as it is seen in Table 2. The S 2p peak shows a slight red-shift from 162.2 eV to 162 eV upon increasing the coverage of Mo. The corresponding S 2s spectra also show this behavior. Furthermore, the S 2p peak for low coverage MoS_2 shows an asymmetry on the higher binding energy side of the peak. Fitting is performed with components for S^{2-} and S_2^{2-}[38–40,54] The S_2^{2-} states are attributed to the presence of double S atoms on the edges of the MoS_2 slabs.[39,40] Our fits indicate an increase in the S^{2-}:S_2^{2-} ratio (see Table 2) upon increasing the Mo coverage to 0.49 ML, but the ratio remains the same within experimental errors upon further increase of the amount of Mo. This observation also corresponds to the changes in the MoS_2:MoS_x ratio observed from the Mo 3d spectra. Furthermore, the Mo:S ratio remains fairly constant at ~1:2.2 upon increasing the coverage of Mo. The ratio of 1:2.2 is very close to the expected value of 1:2 for MoS_2. The extra sulfur is attributed to the adsorption of S on TiO_2. The component for these

sulfur atoms could not be satisfactorily resolved in the peak fits for S 2p due to overlap with the S_2^{2-} component.[24]

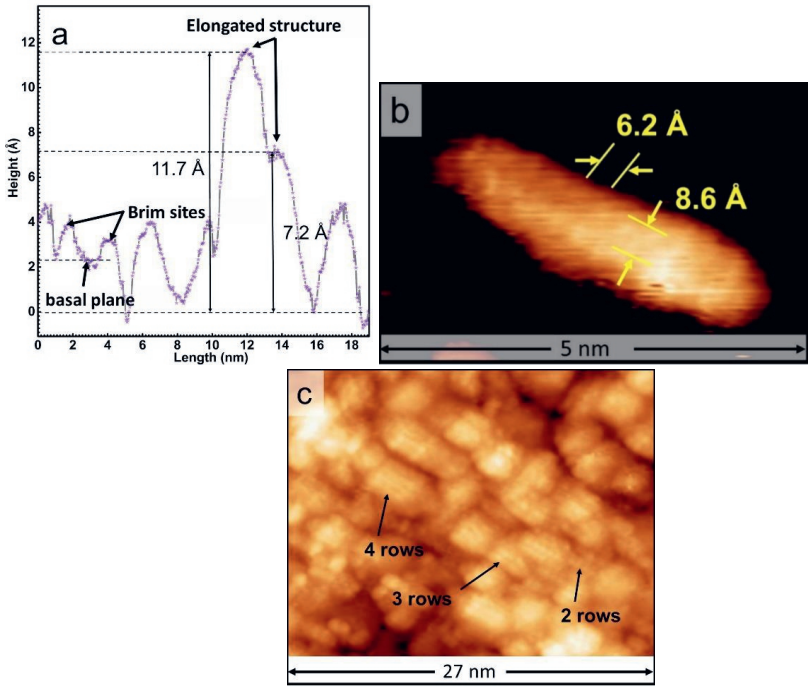

Figure 5: a) Measured height along the line marked B in Figure 3c over the elongated structures, b) Zoom-in of an elongated structure at high contrast resolving rows of bright spots. The STM image is obtained with a sample voltage = +2.2 V and tunneling current = 400 pA. The coverage of Mo determined from XPS is 0.25 ML. c) STM image showing the elongated structures formed as 2-4 rows.

In order to gain insights into the fate of the TiO_2(110) support after the sulfidation of the Mo nanoparticles, the STM images of the sample obtained after sulfiding 0.25 ML Mo nanoparticles were analyzed at high contrast to highlight the substrate (see SI, Figure S4). A characteristic (3x1) structure on the substrate that is identical to the well-known (3x1) sulfur adsorption structure of TiO_2(110) was observed to form on the exposed areas of the TiO_2 support.[22,24] It is expected that the exposure to H_2S at elevated temperatures drastically changes the surface structure of the TiO_2(110) surface. The extensive studies on S-TiO_2 interactions in the past have shown that the interaction is very complex and can result in a wide variety of structures depending on the S coverage and temperature of adsorption.[22–25,51,55,56] For instance, at room temperature, sulfur adsorbs on the exposed titanium atoms (five-fold coordinated) of TiO_2(110) but does not form ordered structures. When the temperature is increased to 573 K, the bridging oxygen atoms are systematically replaced by sulfur which eventually forms a (3x1) ordered structure. At 673 K, the in-plane oxygen atoms are also replaced by sulfur atom pairs, forming an ordered

(3x3) and ultimately, a (4x1) structure.[23,24] Typically, the TiO_2(110) surface has multiple structures co-existing depending on the sulfur coverage at that given temperature as has been demonstrated by STM and low-energy electron diffraction (LEED) experiments.[24] Based on these studies, at 650 K, the temperature used for MoS_2 synthesis in our experiments, the formation of (3x3) and (4x1) domains is expected on TiO_2(110). We did not observe such structures in any of the STM images where the substrate is exposed. Instead, only a (3x1) structure associated with a slightly lower coverage of sulfur was observed to form on the exposed areas of the substrate. This can be explained by considering the presence of the overlayer of partially oxidized Mo nanoparticles which can act as a sulfur sink and compete with TiO_2 for the sulfur atoms thereby resulting in an effectively lower sulfur coverage on the TiO_2 substrate, since Mo nanoparticles have a higher affinity for sulfur. Therefore, a (3x1) structure, corresponding to a lower sulfur coverage, is likely to form. We also point out that (3x1) domains are also formed at elevated temperatures as have been observed in previous experiments.[24]

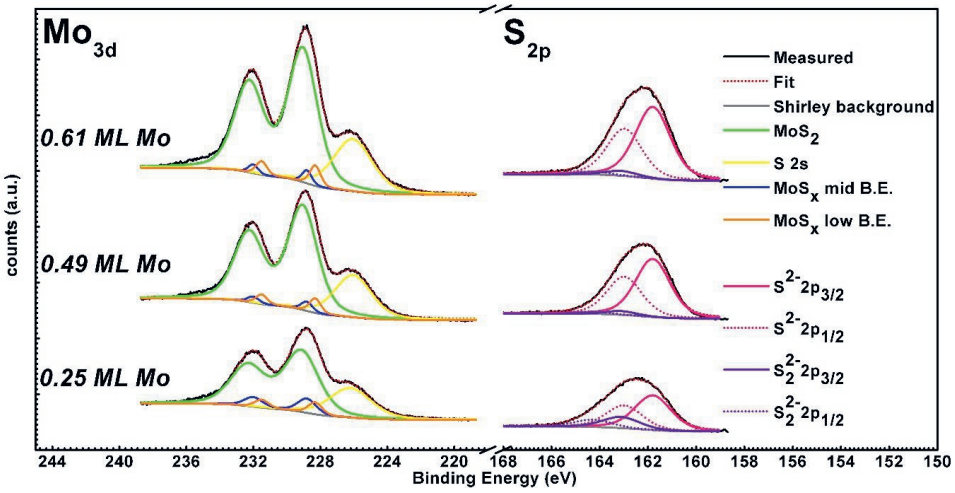

Figure 6: Mo 3d and S 2p XPS spectra of MoS_2 slabs supported on TiO_2(110) at various initial coverages of Mo.

Given our observation that the bright spots on the "basal-bonded" MoS_2 slabs confirm to a (3x1) lattice, we propose that the overall curved structure of the MoS_2 slabs is due to interactions of the edges with the (3x1) S adsorption structure on TiO_2(110). This is not surprising as prior studies have shown that the morphology and stoichiometry of Mo sulfides strongly depend on the interactions with the support.[57–61] Taking into account the observation that the "basal-bonded" MoS_2 slabs are oriented along the $[1\bar{1}0]$ direction, we present a possible atomic model to account for our experimental findings. We take the case of the "basal-bonded" MoS_2 slab marked 1 in Figure 3c. The proposed atomic model for this MoS_2 slab is shown in Figure 7a. In our model, a pair of opposite edges of the MoS_2 slab with S- and Mo-terminations are oriented along the $[1\bar{1}0]$ direction of the TiO_2(110) surface with the (3x1) sulfur structure. The terminating S atoms along these edges interact with both the five-fold and four-fold coordinated Ti atoms of the (3x1) structure. The S-S distance in the basal plane of MoS_2 is 3.15 Å which

matches well with the distance of 6.2 Å of the alternate Ti rows in the (3x1) structure of TiO_2(110) facilitating an MoS_2 edge - substrate Ti interaction for every alternating S atom of the MoS_2 edges. This may also be visualized by considering alternating lower edge S atoms lying close to the TiO_2(110) surface as belonging to the (3x1) TiO_2(110) structure. Furthermore, the STM images of all the "basal-bonded" MoS_2 slabs show that the corner sites of the slabs appear very bright, suggesting a high metallicity of these sites. Similar bright corner sites have been observed in Ni-promoted MoS_2 slabs supported on gold where some slabs adopt a curved shape with corner sites having coordinatively unsaturated Ni and Mo atoms.[53] The edge sites in these experiments have coordination numbers less than 5. Furthermore, the XAFS studies of promoted and unpromoted MoS_2 catalysts supported on TiO_2 showed that, for small MoS_2 slabs, Mo atoms tend to have coordination numbers between 4-5.5 resulting in sulfur-deficient edge terminations which are stabilized by bonding to the TiO_2 substrate.[20,21] We propose that the terminating corner sites in the "basal-bonded" MoS_2 slabs in our experiments are formed due to an unsaturated Mo atom of less than 6 coordination number. The conformation of the MoS_2 slab to the (3x1) sulfur structure likely stabilizes these coordinatively unsaturated Mo sites. As a comparison, we overlay the particle marked 1 in Figure 3c over our atomic model (see SI, Figure S5). A visual comparison clearly shows a close match between the locations of the bright spots in the STM image and locations of coordinatively unsaturated Mo corner sites in our atomic model.

Table 2: Ratio between various components of the XPS spectra in Figure 6.

Mo coverage (ML)	Mo:S	MoS_2:MoS_x	S^{2-}:S_2^{2-}
0.25	1:2.31	1:0.241	1:0.329
0.49	1:2.22	1:0.096	1:0.056
0.61	1:2.24	1:0.093	1:0.062

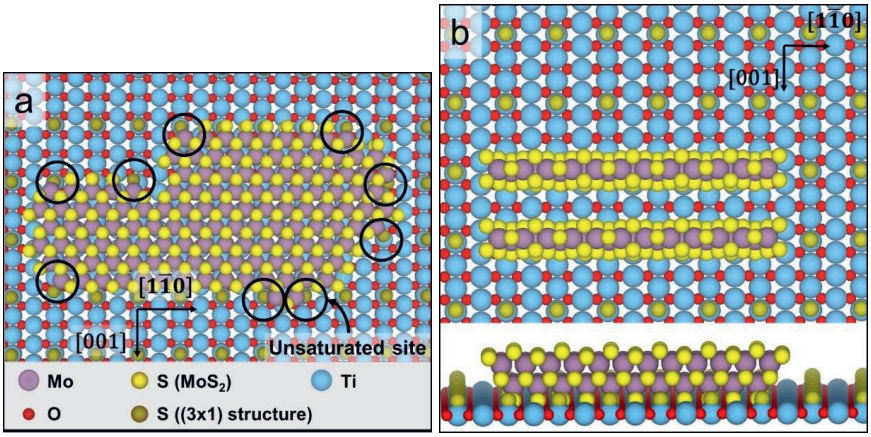

Figure 7: a) Possible atomic model of the "basal-bonded" MoS_2 slab supported on TiO_2(110) with a (3x1) structure due to S adsorption, b) Possible atomic model of "edge-on" MoS_x stripes supported on TiO_2(110) with a (3x1) structure due to S adsorption.

In addition to the "basal-bonded" MoS_2 slabs, the elongated structures are also oriented along the $[1\bar{1}0]$ direction of the TiO_2 substrate. Furthermore, these structures have rows of bright spots that also closely fit a (3x1) lattice suggesting strong substrate interactions. We first consider the possibility of the elongated structures being formed by S atoms reacting with the TiO_2(110) substrate. The well-known (4x1) structure of sulfur on TiO_2(110) also has a similar geometry, albeit with the rows of bright spots separated by 3.2 Å.[24] The previous experiments on S-TiO_2(110) interactions showed that the measured height difference of this structure with respect to areas of the substrate with the (3x1) structure is, however, only about 0.5 Å in contrast to the 7.2±0.2 Å and 11.7±0.4 Å measured for the elongated structures in our experiments. The excess sulfur atoms are also not known to form any ordered structures on TiO_2(110) at 650 K. Thus, we rule out the possibility that the elongated structures are formed by sulfur atoms alone. Leliveld et al.[20,21] have observed the formation of small MoS_2 clusters on a TiO_2 support with only 4-15 Mo atoms per slabs with most of the Mo in likely bonding with the substrate. They have suggested the formation of linear chains of MoS_2 oriented along the $[1\bar{1}0]$ direction of rutile TiO_2 as a possible candidate structure. Chen et al.[62] and Uetsuka et al.[19] have observed the edge-on coupling of MoS_2 slabs to anatase TiO_2 surfaces. Uetsuka et al.[18], in another study, also reported the formation of edge-on coupled MoS_2 slabs on rutile TiO_2(110) when pure H_2S was used as a sulfiding agent using high-resolution transmission electron microscopy (HRTEM) experiments. Furthermore, many MoS_x-type molybdenum sulfides are known to form striped phases on suitable substrates.[59,61] We consider the possibility of the elongated structures in our experiments being Mo sulfide stripes. From the STM images of the sample obtained after sulfiding 0.25 ML Mo nanoparticles, we estimated that the coverage of Mo present in the "basal-bonded" MoS_2 slabs is only 0.11±0.02 ML (see SI, S6) in contrast to the 0.25 ML calculated from the XPS spectra. Prior experiments of Mo on TiO_2 showed that the diffusion of Mo into the bulk of TiO_2 is negligible as the process is thermodynamically not favorable.[34,36] We therefore conclude that the missing Mo is present on the surface and attribute this Mo to the elongated structures observed in the STM images. Furthermore, the observation that the elongated structures are more metallic suggests that they are likely composed of unsaturated Mo atoms, for instance, as MoS_x structures with $1<x<2$.

Based on these observations from the STM and XPS data, we attempt to arrive at a possible atomic model for the elongated structures. We first consider the possibility of MoS_2 stripes formed with their (0001) basal plane parallel to the TiO_2 (110) surface. This may be visualized as a 1D "basal-bonded" MoS_2 slab. We expect such an orientation of MoS_2 stripes to be highly unlikely due to the high energy cost of such a morphology in comparison to a 2D slab containing the same number of Mo atoms. An alternative possibility is that stripes are formed with an "edge-on" orientation such that one of their edges are directly bonded to the TiO_2 support (see Figure 7b) and with the (0001) plane being perpendicular to the TiO_2(110) surface. Considering the closely matching lattice constants of MoS_2 and TiO_2(110) along the $[1\bar{1}0]$ direction, it is likely that the S edge is bonded to the TiO_2 surface such that alternate sulfur positions match with the location of an S atom of the (3x1) structure, hence the observed periodicity in the STM images. Such "edge-on" MoS_2 stripes growing on adjacent rows of the (3x1) structure could appear as the group of 2 to 5 rows observed in the STM images. The observed STM contrasts of the row of bright spots (such as in Figure 4b) could be due to the structure of the Mo-terminated edge of the "edge-on" MoS_2 stripe that is oriented upwards towards vacuum (see Figure 7b). Based on our assignment of these stripes to the MoS_x signal in XPS, majority of the Mo atoms in such a stripe, including those on the edges, will be unsaturated. An example of such an unsaturated Mo edge

is shown in our model with alternating S^{2-} and S_2^{2-} units. The elongated structures which appear with a higher contrast and have a measured height of 11.7±0.4 Å (see Figure 3c) in the STM images can be explained by the formation of a second -Mo-S layer over the "edge-on" MoS_2 stripe. The height difference of ~4 Å matches closely with the theoretical distance of 3.2 Å. One also cannot rule out the electronic effects of charge transfer due to chemical bonding with the substrate. Thus, the "edge-on" MoS_x stripes described in our model predominantly consist of Mo in less than the ideal coordination number of 6. The presence of under-coordinated Mo atoms leads to an increased metallicity of these MoS_x stripes, thus explaining the higher contrasts in the STM images in comparison to that of the "basal-bonded"MoS_2 slabs. In fact, our observation that the number density of the elongated structures decreases upon increasing the amount of Mo from 0.25 to 0.49 ML, but remains relatively the same upon increasing the amount of Mo further up to 0.61 ML is in direct correlation with the XPS observations of the change in the MoS_2:MoS_x and S^{2-}:S_2^{2-} ratios, and can be fully explained by considering the elongated structures as unsaturated "edge-on" MoS_x stripes as in our atomic model. Given the correlations between our proposed atomic models and the STM and XPS data, these models could be good candidate structures for future theoretical research using DFT calculations. This, however, is outside the scope of this current work.

5.5 Conclusions

We have presented a low-temperature synthesis strategy for MoS_2 slabs supported on TiO_2(110) using partially oxidized Mo nanoparticles as a precursor. We have studied the MoS_2 slabs using STM and XPS and have proposed possible atomic models. When MoS_2 is grown by similar low-temperature synthesis methods on single-crystal metal substrates like Au(111) with weak interactions, only the "basal-bonded" MoS_2 slabs with the thermodynamically favored edges have been observed to form. In particular, the MoS_2 – Au system has been used to study the many well-known remarkable properties of SL MoS_2 slabs. A similar effect is achieved by growing MoS_2 at high-temperatures on TiO_2 where the sulfur-substrate interactions are circumvented due to extensive desorption of S. The low-temperature synthesis method presented in this work is very relevant for fields such as catalysis where this system is synthesized industrially at similar low-temperatures and is widely used to produce cleaner fuels. In particular, our work shows that the reaction of the substrate with sulfur needs to be taken into account for atomic structural characterization. Furthermore, the lower temperature not only leads to the formation of flat MoS_2 slabs with irregular shapes (thermodynamically less favorable), but also to MoS_x stripes with large number of coordinatively unsaturated Mo atoms which are likely very reactive.

5.6 References

(1) Zeng, H.; Dai, J.; Yao, W.; Xiao, D.; Cui, X. Valley Polarization in MoS_2 Monolayers by Optical Pumping. *Nat. Nanotechnol.* 2012, *7* (8), 490–493. https://doi.org/10.1038/nnano.2012.95.

(2) Chhowalla, M.; Shin, H. S.; Eda, G.; Li, L. J.; Loh, K. P.; Zhang, H. The Chemistry of Two-Dimensional Layered Transition Metal Dichalcogenide Nanosheets. *Nature Chemistry.* 2013, pp 263–275. https://doi.org/10.1038/nchem.1589.

(3) Jariwala, D.; Sangwan, V. K.; Lauhon, L. J.; Marks, T. J.; Hersam, M. C. Emerging Device Applications for Semiconducting Two-Dimensional Transition Metal Dichalcogenides. *ACS Nano.* 2014, pp 1102–1120. https://doi.org/10.1021/nn500064s.

(4) K., S.; J., A.; S., H.; M., N.; R., S. G.; S., P.; C., M.; K., H. One-Step Fabrication of Ultrathin Layered 1T@2H Phase MoS_2 with High Catalytic Activity Based Counter Electrode for Photovoltaic Devices. *J. Mater. Sci. Technol.* 2020, *51*, 94–101. https://doi.org/10.1016/j.jmst.2020.01.024.

(5) Zhang, G.; Liu, H.; Qu, J.; Li, J. Two-Dimensional Layered MoS_2: Rational Design, Properties and Electrochemical Applications. *Energy and Environmental Science*. 2016, pp 1190–1209. https://doi.org/10.1039/c5ee03761a.

(6) Kibsgaard, J.; Clausen, B. S.; Topsøe, H.; Lægsgaard, E.; Lauritsen, J. V.; Besenbacher, F. Scanning Tunneling Microscopy Studies of TiO_2-Supported Hydrotreating Catalysts: Anisotropic Particle Shapes by Edge-Specific MoS_2-Support Bonding. *J. Catal.* 2009, *263* (1), 98–103. https://doi.org/10.1016/j.jcat.2009.01.016.

(7) Brunet, S.; Mey, D.; Pérot, G.; Bouchy, C.; Diehl, F.; On the Hydrodesulfurization of FCC Gasoline: A Review. *Applied Catalysis A: General*. 2005, pp 143–172. https://doi.org/10.1016/j.apcata.2004.10.012.

(8) Song, C.; Ma, X. New Design Approaches to Ultra-Clean Diesel Fuels by Deep Desulfurization and Deep Dearomatization. In *Applied Catalysis B: Environmental*; 2003; Vol. 41, pp 207–238. https://doi.org/10.1016/S0926-3373(02)00212-6.

(9) Somorjai, G. A.; De Beer, V. H. J. Structure and Function of The Catalyst and The Promoter In Co-Mo Hydrodesuifurization Catalysts. *Catal. Rev.* 1989, *31* (1–2), 1–41. https://doi.org/10.1080/01614948909351347.

(10) Liu, C.; Wang, L.; Tang, Y.; Luo, S.; Liu, Y.; Zhang, S.; Zeng, Y.; Xu, Y. Vertical Single or Few-Layer MoS_2 Nanosheets Rooting into TiO_2 Nanofibers for Highly Efficient Photocatalytic Hydrogen Evolution. *Appl. Catal. B Environ.* 2015, *164*, 1–9. https://doi.org/10.1016/j.apcatb.2014.08.046.

(11) Kooyman, P. J.; Hensen, E. J. M.; De Jong, A. M.; Niemantsverdriet, J. W.; Van Veen, J. A. R. The Observation of Nanometer-Sized Entities in Sulphided Mo-Based Catalysts on Various Supports. *Catal. Letters* 2001, *74* (1–2), 49–53. https://doi.org/10.1023/A:1016632130625.

(12) Shido, T.; Prins, R. Why EXAFS Underestimated the Size of Small Supported MoS_2 Particles. *J. Phys. Chem. B* 1998, *102* (43), 8426–8435. https://doi.org/10.1021/jp982322j.

(13) Galhenage, R. P.; Yan, H.; Rawal, T. B.; Le, D.; Brandt, A. J.; Maddumapatabandi, T. D.; Nguyen, N.; Rahman, T. S.; Chen, D. A. MoS_2 Nanoclusters Grown on TiO_2: Evidence for New Adsorption Sites at Edges and Sulfur Vacancies. *J. Phys. Chem. C* 2019, *123* (12), 7185–7201. https://doi.org/10.1021/acs.jpcc.9b00076.

(14) Liu, H.; Li, Y.; Xiang, M.; Zeng, H.; Shao, X. Single-Layered MoS_2 Directly Grown on Rutile TiO_2(110) for Enhanced Interfacial Charge Transfer. *ACS Nano* 2019, *13* (5), 6083–6089. https://doi.org/10.1021/acsnano.9b02608.

(15) Coulier, L.; De Beer, V. H. J.; Van Veen, J. A. R.; Niemantsverdriet, J. W. On the Formation of Cobalt-Molybdenum Sulfides in Silica-Supported Hydrotreating Model Catalysts. *Top. Catal.* 2000, *13* (1–2), 99–108. https://doi.org/10.1023/a:1009037006529.

(16) Sanders, A. F. H.; De Jong, A. M.; De Beer, V. H. J.; Van Veen, J. A. R.; Niemantsverdriet, J. W. Formation of Cobalt-Molybdenum Sulfides in Hydrotreating Catalysts: A Surface Science Approach. *Appl. Surf. Sci.* 1999, *144–145*, 380–384. https://doi.org/10.1016/S0169-4332(98)00831-9.

(17) Escobar, J.; Toledo, J. A.; Cortés, M. A.; Mosqueira, M. L.; Pérez, V.; Ferrat, G.; López-Salinas, E.; Torres-García, E. Highly Active Sulfided CoMo Catalyst on Nano-Structured TiO2. In *Catalysis Today*; 2005; Vol. 106, pp 222–226. https://doi.org/10.1016/j.cattod.2005.07.136.

(18) Uetsuka, H.; Onishi, H.; Harada, Y.; Sakama, H.; Sakashita, Y. Microscope Observation of MoS_2 Nanoparticles Synthesized on Rutile TiO_2 Single Crystals. *e-Journal Surf. Sci. Nanotechnol.* 2004, *2*, 32–37. https://doi.org/10.1380/ejssnt.2004.32.

(19) Uetsuka, H.; Onishi, H.; Ikeda, S.; Harada, Y.; Sakama, H.; Sakashita, Y. Atomic Force Microscope Observation of MoS_2 Particles Synthesized on Mica, MoS_2, and Graphite. *e-Journal Surf. Sci. Nanotechnol.* 2003, *1*, 80–83. https://doi.org/10.1380/ejssnt.2003.80.

(20) Leliveld, R. G.; Van Dillen, A. J.; Geus, J. W.; Koningsberger, D. C. A Mo-K Edge XAFS Study of the Metal Sulfide-Support Interaction in (Co)Mo Supported Alumina and Titania Catalysts. *J. Catal.* 1997, *165* (2), 184–196. https://doi.org/10.1006/jcat.1997.1480.

(21) Leliveld, R. G.; Van Dillen, A. J.; Geus, J. W.; Koningsberger, D. C. The Sulfidation of γ Alumina and Titania Supported (Cobalt)Molybdenum Oxide Catalysts Monitored by EXAFS. *J. Catal.* 1997, *171* (1), 115–129. https://doi.org/10.1006/jcat.1997.1783.

(22) Hebenstreit, E. L. D.; Hebenstreit, W.; Diebold, U. Structures of Sulfur on TiO_2(110) Determined by Scanning Tunneling Microscopy, X-Ray Photoelectron Spectroscopy and Low-Energy Electron Diffraction. *Surf. Sci.* 2001, *470* (3), 347–360. https://doi.org/10.1016/S0039-6028(00)00849-9.

(23) Ventrice, C. A.; Hite, D. A.; Sprunger, P. T.; Hebenstreit, E. L. D.; Hebenstreit, W.; Diebold, U.; Geisler, H.; Thornburg, S. N. Sulfur on (Formula Presented) Studied with Resonant Photoemission. *Phys. Rev. B - Condens. Matter Mater. Phys.* 2001, *64* (11). https://doi.org/10.1103/PhysRevB.64.115418.

(24) Hebenstreit, E. L. D.; Hebenstreit, W.; Diebold, U. Adsorption of Sulfur on TiO_2(110) Studied with STM, LEED and XPS: Temperature-Dependent Change of Adsorption Site Combined with O-S Exchange. *Surf. Sci.* 2000, *461* (1–3), 87–97. https://doi.org/10.1016/S0039-6028(00)00538-0.

(25) Hrbek, J.; Rodriguez, J. A.; Dvorak, J.; Jirsak, T. Sulfur Adsorption and Reaction with a TiO_2(110) Surface: O⇔Exchange and Sulfide Formation. *Collect. Czechoslov. Chem. Commun.*

2001, *66* (8), 1149–1162. https://doi.org/10.1135/cccc20011149.

(26) Herbschleb, C. T.; Van Der Tuijn, P. C.; Roobol, S. B.; Navarro, V.; Bakker, J. W.; Liu, Q.; Stoltz, D.; Cañas-Ventura, M. E.; Verdoes, G.; Van Spronsen, M. A.; Bergman, M.; Crama, L.; Taminiau, I.; Ofitserov, A.; Van Baarle, G. J. C.; Frenken, J. W. M. The ReactorSTM: Atomically Resolved Scanning Tunneling Microscopy under High-Pressure, High-Temperature Catalytic Reaction Conditions. *Rev. Sci. Instrum.* 2014, *85* (8). https://doi.org/10.1063/1.4891811.

(27) Wagner, C. D. Sensitivity Factors for XPS Analysis of Surface Atoms. *J. Electron Spectros. Relat. Phenomena* 1983, *32* (2), 99–102. https://doi.org/10.1016/0368-2048(83)85087-7.

(28) Rost, M. J.; Crama, L.; Schakel, P.; Van Tol, E.; Van Velzen-Williams, G. B. E. M.; Overgauw, C. F.; Ter Horst, H.; Dekker, H.; Okhuijsen, B.; Seynen, M.; Vijftigschild, A.; Han, P.; Katan, A. J.; Schoots, K.; Schumm, R.; Van Loo, W.; Oosterkamp, T. H.; Frenken, J. W. M. Scanning Probe Microscopes Go Video Rate and Beyond. *Rev. Sci. Instrum.* 2005, *76* (5). https://doi.org/10.1063/1.1915288.

(29) Rost, M. J.; van Baarle, G. J. C.; Katan, A. J.; van Spengen, W. M.; Schakel, P.; van Loo, W. A.; Oosterkamp, T. H.; Frenken, J. W. M. Video-Rate Scanning Probe Control Challenges: Setting the Stage for a Microscopy Revolution. *Asian J. Control* 2009, *11* (2), 110–129. https://doi.org/10.1002/asjc.88.

(30) Horcas, I.; Fernández, R.; Gómez-Rodríguez, J. M.; Colchero, J.; Gómez-Herrero, J.; Baro, A. M. WSXM: A Software for Scanning Probe Microscopy and a Tool for Nanotechnology. *Rev. Sci. Instrum.* 2007, *78* (1). https://doi.org/10.1063/1.2432410.

(31) Horcas, I.; Fernández, R.; Gómez-Rodríguez, J. M.; Colchero, J.; Gómez-Herrero, J.; Baro, A. M. WSXM: A Software for Scanning Probe Microscopy and a Tool for Nanotechnology. *Rev. Sci. Instrum.* 2007, *78* (1). https://doi.org/10.1063/1.2432410.

(32) Atuchin, V. V.; Kesler, V. G.; Pervukhina, N. V.; Zhang, Z. Ti 2p and O 1s Core Levels and Chemical Bonding in Titanium-Bearing Oxides. *J. Electron Spectros. Relat. Phenomena* 2006, *152* (1–2), 18–24. https://doi.org/10.1016/j.elspec.2006.02.004.

(33) Domenichini, B.; Pétigny, S.; Blondeau-Patissier, V.; Steinbrunn, A.; Bourgeois, S. Effect of the Surface Stoichiometry on the Interaction of Mo with TiO_2(110). *Surf. Sci.* 2000, *468* (1–3), 192–202. https://doi.org/10.1016/S0039-6028(00)00816-5.

(34) Blondeau-Patissier, V.; Lian, G. D.; Domenichini, B.; Steinbrunn, A.; Bourgeois, S.; Dickey, E. C. Molybdenum Thin-Film Growth on Rutile Titanium Dioxide (110). *Surf. Sci.* 2002, *506* (1–2), 119–128. https://doi.org/10.1016/S0039-6028(02)01383-3.

(35) Prunier, J.; Domenichini, B.; Li, Z.; Møller, P. J.; Bourgeois, S. A Photoemission Study of Molybdenum Hexacarbonyl Adsorption and Decomposition on TiO_2(1 1 0) Surface. *Surf. Sci.* 2007, *601* (4), 1144–1152. https://doi.org/10.1016/j.susc.2006.12.009.

(36) Domenichini, B.; Petukhov, M.; Rizzi, G. A.; Sambi, M.; Bourgeois, S.; Granozzi, G. Epitaxial Growth of Molybdenum on TiO_2(110). *Surf. Sci.* 2003, *544* (2–3), 135–146. https://doi.org/10.1016/j.susc.2003.07.013.

(37) Bruix, A.; Füchtbauer, H. G.; Tuxen, A. K.; Walton, A. S.; Andersen, M.; Porsgaard, S.; Besenbacher, F.; Hammer, B.; Lauritsen, J. V. In Situ Detection of Active Edge Sites in Single-Layer MoS_2 Catalysts. *ACS Nano* 2015, *9* (9), 9322–9330. https://doi.org/10.1021/acsnano.5b03199.

(38) Weber, T.; Muijsers, J. C.; Van Wolput, J. H. M. C.; Verhagen, C. P. J.; Niemantsverdriet, J. W. Basic Reaction Steps in the Sulfidation of Crystalline MoO_3 to MoS_2, as Studied by X-Ray Photoelectron and Infrared Emission Spectroscopy. *J. Phys. Chem.* 1996, *100* (33), 14144–14150. https://doi.org/10.1021/jp961204y.

(39) Bremmer, G. M.; Van Haandel, L.; Hensen, E. J. M.; Frenken, J. W. M.; Kooyman, P. J. Instability of $NiMoS_2$ and $CoMoS_2$ Hydrodesulfurization Catalysts at Ambient Conditions: A Quasi in Situ High-Resolution Transmission Electron Microscopy and X-Ray Photoelectron Spectroscopy Study. *J. Phys. Chem. C* 2016, *120* (34), 19204–19211. https://doi.org/10.1021/acs.jpcc.6b06030.

(40) Bremmer, G. M.; van Haandel, L.; Hensen, E. J. M.; Frenken, J. W. M.; Kooyman, P. J. The Effect of Oxidation and Resulfidation on (Ni/Co)MoS_2 Hydrodesulfurisation Catalysts. *Appl. Catal. B Environ.* 2019, *243*, 145–150. https://doi.org/10.1016/j.apcatb.2018.10.014.

(41) Diebold, U. Structure and Properties of TiO_2 Surfaces: A Brief Review. *Appl. Phys. A Mater. Sci. Process.* 2003, *76* (5), 681–687. https://doi.org/10.1007/s00339-002-2004-5.

(42) Diebold, U.; Li, M.; Dulub, O.; Hebenstreit, E. L. D.; Hebenstreit, W. The Relationship between Bulk and Surface Properties of Rutile TiO_2(110). In *Surface Review and Letters*; 2000; Vol. 7, pp 613–617. https://doi.org/10.1016/S0218-625X(00)00052-X.

(43) Diebold, U.; Lehman, J.; Mahmoud, T.; Kuhn, M.; Leonardelli, G.; Hebenstreit, W.; Schmid, M.; Varga, P. Intrinsic Defects on a TiO_2(110)(1 × 1) Surface and Their Reaction with Oxygen: A Scanning Tunneling Microscopy Study. *Surf. Sci.* 1998, *411* (1–2), 137–153. https://doi.org/10.1016/S0039-6028(98)00356-2.

(44) Diebold, U.; Anderson, J. F.; Ng, K. O.; Vanderbilt, D. Evidence for the Tunneling Site on Transition-Metal Oxides: TiO_2(110). *Phys. Rev. Lett.* 1996, *77* (7), 1322–1325. https://doi.org/10.1103/PhysRevLett.77.1322.

(45) Li, M.; Hebenstreit, W.; Diebold, U.; Tyryshkin, A. M.; Bowman, M. K.; Dunham, G. G.; Henderson, M. A. The Influence of the Bulk Reduction State on the Surface Structure and Morphology of Rutile TiO_2(110) Single Crystals. *J. Phys. Chem. B* 2000, *104* (20), 4944–4950. https://doi.org/10.1021/jp9943272.

(46) Berkó, A.; Magony, A.; Szökõ, J. Characterization of Mo Deposited on a TiO_2(110) Surface by

Scanning Tunneling Microscopy and Auger Electron Spectroscopy. *Langmuir* 2005, *21* (10), 4562–4570. https://doi.org/10.1021/la046826m.

(47) Kitchin, J. R.; Barteau, M. A.; Chen, J. G. A Comparison of Gold and Molybdenum Nanoparticles on TiO_2(1 1 0) 1 × 2 Reconstructed Single Crystal Surfaces. *Surf. Sci.* 2003, *526* (3), 323–331. https://doi.org/10.1016/S0039-6028(02)02679-1.

(48) Campbell, C. T. Metal Films and Particles on Oxide Surfaces: Structural, Electronic and Chemisorptive Properties. *J. Chem. Soc. - Faraday Trans.* 1996, *92* (9), 1435–1445. https://doi.org/10.1039/ft9969201435.

(49) Diebold, U.; Pan, J. M.; Madey, T. E. Ultrathin Metal Films on TiO_2(110): Metal Overlayer Spreading and Surface Reactivity. *Surf. Sci.* 1993, *287–288* (PART 2), 896–900. https://doi.org/10.1016/0039-6028(93)91095-7.

(50) Diebold, U.; Pan, J. M.; Madey, T. E. Ultrathin Metal Film Growth on TiO_2(110): An Overview. *Surf. Sci.* 1995, *331–333* (PART B), 845–854. https://doi.org/10.1016/0039-6028(95)00124-7.

(51) Rodriguez, J. A.; Hrbek, J.; Chang, Z.; Dvorak, J.; Jirsak, T.; Maiti, A. Importance of O Vacancies in the Behavior of Oxide Surfaces: Adsorption of Sulfur on (Formula Presented). *Phys. Rev. B - Condens. Matter Mater. Phys.* 2002, *65* (23), 1–12. https://doi.org/10.1103/PhysRevB.65.235414.

(52) Helveg, S.; Lauritsen, J. V.; Lægsgaard, E.; Stensgaard, I.; Nørskov, J. K.; Clausen, B. S.; Topsøe, H.; Besenbacher, F. Atomic-Scale Structure of Single-Layer MoS_2 Nanoclusters. *Phys. Rev. Lett.* 2000, *84* (5), 951–954. https://doi.org/10.1103/PhysRevLett.84.951.

(53) Lauritsen, J. V.; Kibsgaard, J.; Olesen, G. H.; Moses, P. G.; Hinnemann, B.; Helveg, S.; Nørskov, J. K.; Clausen, B. S.; Topsøe, H.; Lægsgaard, E.; Besenbacher, F. Location and Coordination of Promoter Atoms in Co- and Ni-Promoted MoS_2-Based Hydrotreating Catalysts. *J. Catal.* 2007, *249* (2), 220–233. https://doi.org/10.1016/j.jcat.2007.04.013.

(54) Han, X.; Tong, X.; Liu, X.; Chen, A.; Wen, X.; Yang, N.; Guo, X. Y. Hydrogen Evolution Reaction on Hybrid Catalysts of Vertical MoS_2 Nanosheets and Hydrogenated Graphene. *ACS Catal.* 2018, *8* (3), 1828–1836. https://doi.org/10.1021/acscatal.7b03316.

(55) Rodriguez, J. A.; Chaturvedi, S.; Kuhn, M.; Hrbek, J. Reaction of H_2S and S_2 with Metal/Oxide Surfaces: Band-Gap Size and Chemical Reactivity. *J. Phys. Chem. B* 1998, *102* (28), 5511–5519. https://doi.org/10.1021/jp9815208.

(56) Hartmann, N.; Biener, J.; Madix, R. J. Monitoring the Interaction of Sulfur Dioxide with a TiO_2(1 1 0) Surface at 300 K by Scanning Tunneling Microscopy. *Surf. Sci.* 2002, *505*, 81–92. https://doi.org/10.1016/S0039-6028(02)01099-3.

(57) Le, D.; Sun, D.; Lu, W.; Aminpour, M.; Wang, C.; Ma, Q.; Rahman, T. S.; Bartels, L. Growth of Aligned Mo_6S_6 Nanowires on Cu(111). *Surf. Sci.* 2013, *611*, 1–4.

https://doi.org/10.1016/j.susc.2012.12.016.

(58) Tiwari, R. K.; Yang, J.; Saeys, M.; Joachim, C. Surface Reconstruction of MoS_2 to Mo_2S_3. *Surf. Sci.* 2008, *602* (15), 2628–2633. https://doi.org/10.1016/j.susc.2008.06.006.

(59) Sun, D.; Lu, W.; Le, D.; Ma, Q.; Aminpour, M.; Alcántara Ortigoza, M.; Bobek, S.; Mann, J.; Wyrick, J.; Rahman, T. S.; Bartels, L. An MoS_x Structure with High Affinity for Adsorbate Interaction. *Angew. Chemie - Int. Ed.* 2012, *51* (41), 10284–10288. https://doi.org/10.1002/anie.201205258.

(60) Kibsgaard, J.; Tuxen, A.; Levisen, M.; Lægsgaard, E.; Gemming, S.; Seifert, G.; Lauritsen, J. V.; Besenbacher, F. Atomic-Scale Structure of Mo_6S_6 Nanowires. *Nano Lett.* 2008, *8* (11), 3928–3931. https://doi.org/10.1021/nl802384n.

(61) Bao, Y.; Yang, M.; Tan, S. J. R.; Liu, Y. P.; Xu, H.; Liu, W.; Nai, C. T.; Feng, Y. P.; Lu, J.; Loh, K. P. Substoichiometric Molybdenum Sulfide Phases with Catalytically Active Basal Planes. *J. Am. Chem. Soc.* 2016, *138* (42), 14121–14128. https://doi.org/10.1021/jacs.6b09042.

(62) Chen, G.; Song, X.; Guan, L.; Chai, J.; Zhang, H.; Wang, S.; Pan, J.; Tao, J. Defect Assisted Coupling of a MoS_2/TiO_2 Interface and Tuning of Its Electronic Structure. *Nanotechnology* 2016, *27* (35). https://doi.org/10.1088/0957-4484/27/35/355203.

Chapter 5 - Supporting Information

1. Comparison of $Mo/TiO_2(110)$ precursors at Mo coverages of 0.25 ML and 0.49 ML

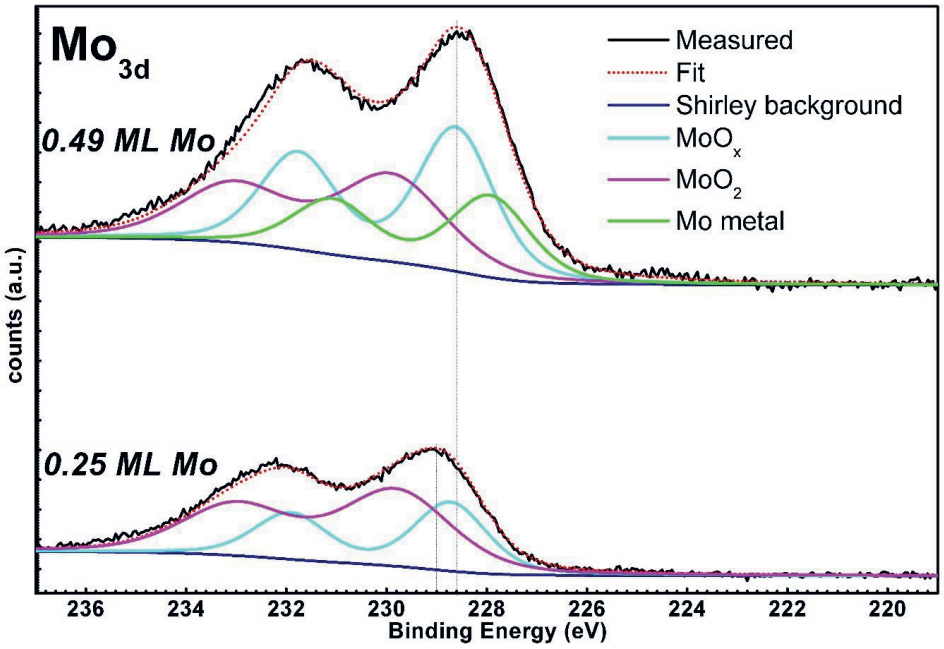

Figure S1: Mo 3d spectra of Mo nanoparticles supported on $TiO_2(110)$ at initial Mo overages of 0.25 ML and 0.49 ML

2. MoS_2 slabs grown on TiO_2(110) at Mo coverages of 0.49 and 0.61 ML

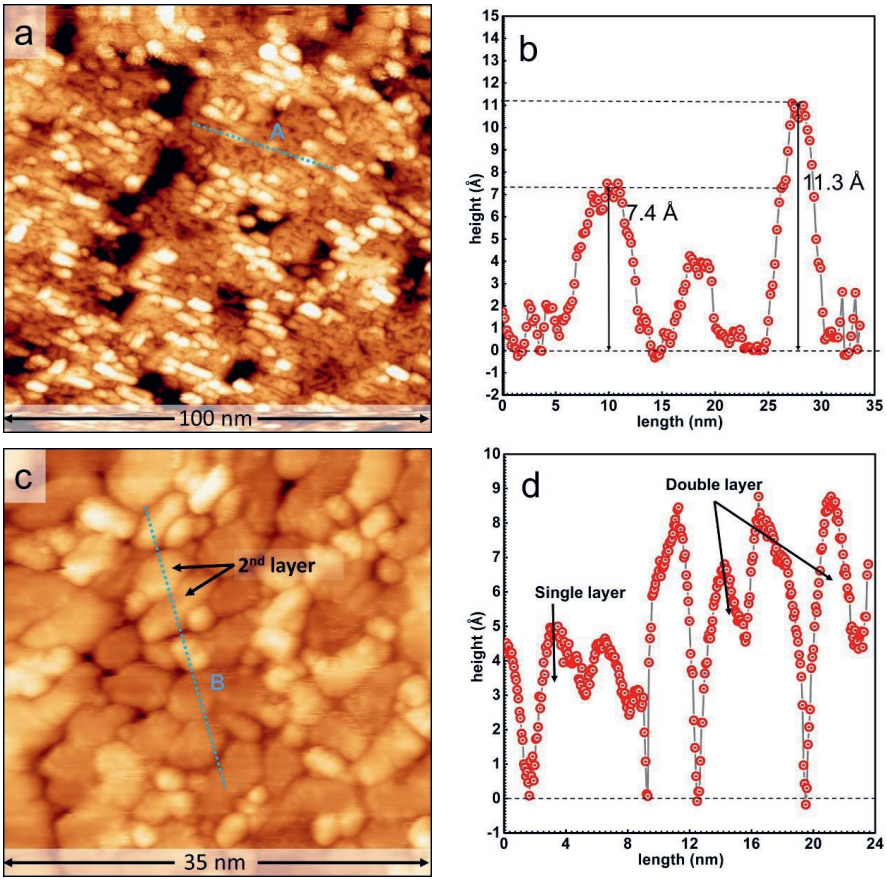

Figure S2: a) Large-scale STM image of MoS_2 supported on TiO_2(110) obtained with a sample voltage = +2.2 V and tunneling current = 250 pA. The coverage of Mo is 0.61 ML. b) Measured height along the line marked A in Figure S2a. c) Large-scale STM image of MoS_2 supported on TiO_2(110) obtained with a sample voltage = +2.1 V and tunneling current = 300 pA. The coverage of Mo is 0.49 ML. d) Measured height along the line marked B in Figure S2c.

3. Estimation of the number density of the elongated structures from STM images

Table S3. Table for estimation of the projected coverages of the elongated structures from STM images of various locations of the samples

absolute Mo coverage from XPS	Area fraction - elongated structure
0.25	0.44±0.02
0.49	0.32±0.04
0.61	0.29±0.03

The number of elongated structures per unit area of the substrate is proportional to the projected area fractions as measured from the STM images, taking into account the elongated structures with both the intermediate and bright STM contrasts. Estimation of the projected area fraction of the elongated structures requires statistical averaging of the number of pixels over large substrate areas. For this, STM images of various areas of substrate totaling to ~2 μm^2 for each of the three Mo coverages were analyzed. Using the Gwyddion 2.47 software, masks were drawn over areas occupied by the elongated structures. The statistically averaged area coverages of the elongated structures are mentioned in Table S3.

4. STM images of the exposed areas of the TiO_2(110) substrate

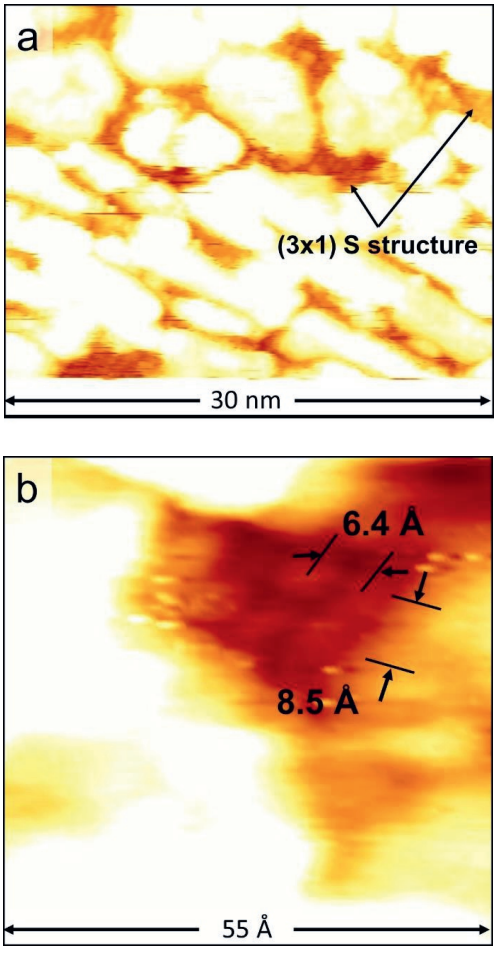

Figure S4: a) High-contrast STM image highlighting the exposed TiO_2(110) substrate with the (3x1) sulfur structure; obtained with a sample voltage = +2.3 V and tunneling current = 500 pA. b) Zoom-in of a (3x1) structure near the edge of a "basal-bonded" MoS_2 slab.

5. Atomic model of "basal-bonded" MoS_2 slabs

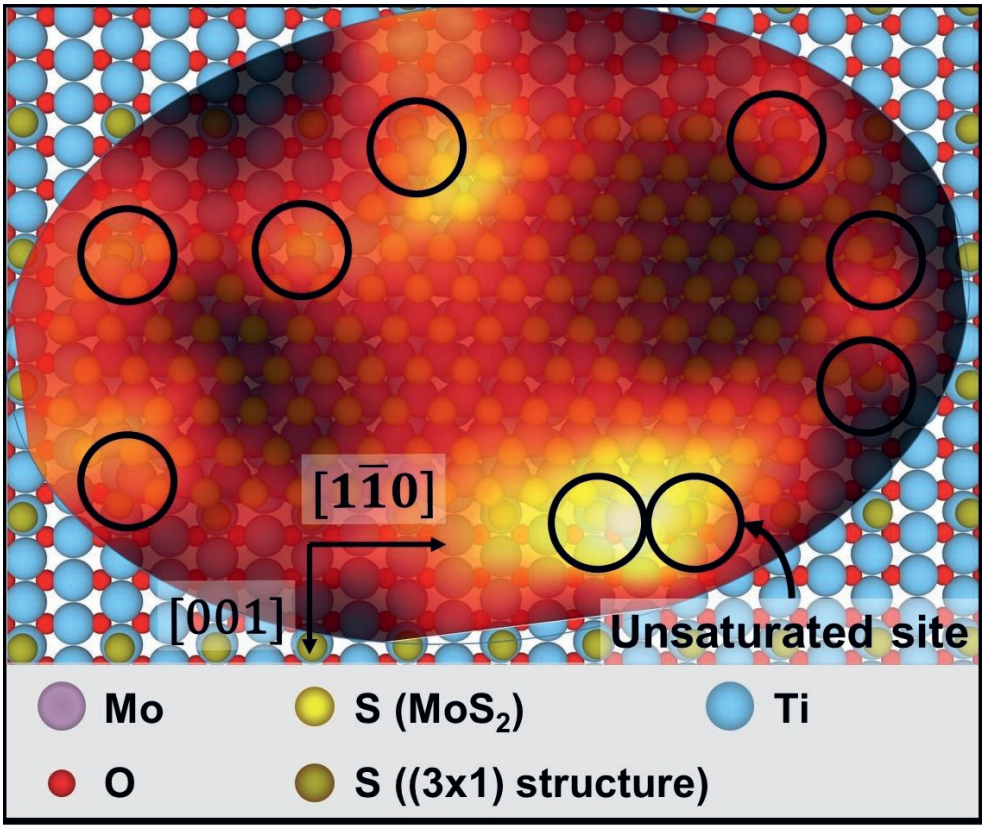

Figure S5: Atomic model of a "basal-bonded" MoS_2 slab from Figure 7a with the STM image of the slab marked 1 in Figure 3c superimposed. Note the close match between the bright spots and the coordinatively unsaturated corner Mo sites marked with black circles.

6. Estimation of Mo coverage from the STM images

In order to estimate the amount of Mo present in the "basal-bonded" MoS_2 slabs, the statistically averaged projected area needs to be determined. For this purpose, we make use of the same method as in S3, but mask the areas occupied by the MoS_2 slabs instead. Analyzing an area of 1.25 μm^2, we obtain:

Projected area fraction of the "basal-bonded" MoS_2 slabs = 0.117 *(measured from the masking)*

Area occupied by MoS_2 slabs for every (100 x 100) nm^2 of TiO_2(110)

= 1170 nm^2

Side length of a hexagon of the same area = $\{(1170)\ \mathrm{x}\ \frac{2}{3\sqrt{3}}\}^{1/2}$ (*assuming that the MoS_2 slabs are perfectly hexagonal)*

= 21.23 nm

= 21.23/0.315 Mo atoms, *(S-Mo-S distance in MoS_2 is 0.315 nm.)*

~ 67 atoms

Therefore, number of Mo atoms in MoS_2 for every (100 x 100) nm^2 of TiO_2

= $\frac{3\sqrt{3}}{2}$ x 67^2 *(area of a regular hexagon)*

= 11805 atoms

Number of Ti atoms for every (100 x 100) nm^2 of TiO2

= $(\frac{100}{0.298})$ x $(\frac{100}{0.32})$ where 0.298 and 0.32 nm are the experimentally measured Ti-Ti distances of the TiO_2(110) unit cell [22][40-42].

= 104865 atoms

Since for low coverage, nearly all MoS_2 slabs are single-layer, coverage of Mo in "basal-bonded" MoS_2; = 11805/104865

= 0.113 ML

< 0.25 ML estimated from XPS data.

Chapter 6

In Situ Observation of a CoMoS Model Hydrodesulfurization Catalyst at Industrially-Relevant Conditions Using the ReactorSTM

Abstract

In this Chapter, the first direct observations of Co-promoted MoS_2 (CoMoS) slabs under industrially-relevant hydrodesulfurization (HDS) conditions using the ReactorSTM are presented. CoMoS slabs supported on Au(111) show new edge structures when imaged under 100% H_2 and 100% CH_3SH atmospheres. However, during the desulfurization of CH_3SH, we observe a dynamically evolving edge structure on the low index Co-substituted S edges of the CoMoS slabs. Furthermore, we also report the formation of curved CoMoS slabs with high index edge terminations under the HDS conditions. Additionally, mass transport along the edges of the larger CoMoS slabs results in the formation of highly irregular edges. XPS analysis shows that the mass transport likely is due to the migration of Co atoms from the CoMoS slabs into the 2D CoS_2 phase. Our experimental observations emphasize the importance of studying a complex catalyst such as Co-promoted MoS_2 during the catalysis process. The results presented in this work open up avenues for more fundamental research on HDS including theoretical modelling with DFT calculations.

6.1 Introduction

Hydrodesulfurization (HDS) is the process of selectively removing sulfur from fractionated crude oil using a catalyst and hydrogen. The most widely used catalyst for this purpose is based on MoS_2, a transition metal dichalcogenide (TMDC). Typically, Co and Ni are used as promoters to enhance the activity of the catalyst. Such TMDC based catalysts have a broad spectrum HDS activity and have met the commercial fuel's residual sulfur standards of up to ~100 ppm for over the last 100 years.[1] However, the regulations on SO_x emissions worldwide have become significantly more stringent in the last decade. To meet the future sulfur emission thresholds, the residual sterically-hindered aromatic sulfides also must be removed.[2] The current TMDC catalysts are not very active towards desulfurizing such refractory sulfur compounds.[1] To design a more efficient HDS catalyst, however, the much needed atomic-level understanding of the catalyst for establishing the structure-activity relationships is currently lacking. For instance, despite being a well-established process in the industry, the precise working mechanism as well as the atomic structure of the working HDS catalyst is still under considerable scientific discussion.

In the last two decades, a lot of work has been done to gain atomic-level insights into the Co-promoted MoS_2 catalysts. It has been established that the active sites lay on the edges of the Co-promoted MoS_2 slabs with the promoter Co atoms being incorporated into the S-terminated edges of the S-Mo-S sandwich MoS_2 slabs.[3-6] Such Co-incorporated MoS_2 slabs are also known as CoMoS slabs (see Figure 1). Several islands of single-layer (SL) and multi-layer CoMoS slabs are known to exist on the industrial catalyst, as has been observed with electron microscopy techniques.[7,8] While the atomic structure of the CoMoS slabs has been studied in detail, the atomic structure of the edges of these slabs during the hydrodesulfurization process is still unknown. Directly observing the HDS catalysts in action is necessary to gain atomic-level insights necessary for designing better catalysts in order to meet the demands of the ever-growing stringent regulations on sulfur emissions.[9]

Several attempts have been made in the recent past to gain such atomic-level understanding of pristine and promoted MoS_2 slabs at near-industrial conditions using techniques such as X-ray absorption fine structure (XAFS)[4,10–14], transmission electron microscopy (TEM)[15], X-ray diffraction (XRD)[10,16], X-ray photoelectron spectroscopy (XPS)[17], Raman spectroscopy[18,19], neutron scattering[20] and importantly, scanning tunneling microscope (STM).[21,22] Especially the recent work by Mom et al.[22] using the ReactorSTM[23] bridges the pressure gap with the industrial catalysts and reports direct observations of the edges of a non-promoted MoS_2 model catalyst under hydrodesulfurization conditions. Their work shows that active edge sites of the MoS_2 slab adapt to the sulfur, hydrogen, and hydrocarbon coverages depending on the gas environment. For Co-promoted MoS_2 slabs, the work carried out by Grønborg et al.[21] investigates the effects of a reducing atmosphere on the Co-substituted edges of a CoMoS slab. However, their work has a pressure gap of 7 orders of magnitude with respect to the industrial HDS conditions. Furthermore, the possible effects of the interactions of organic molecules with the Co-substituted edges are not investigated in their work.

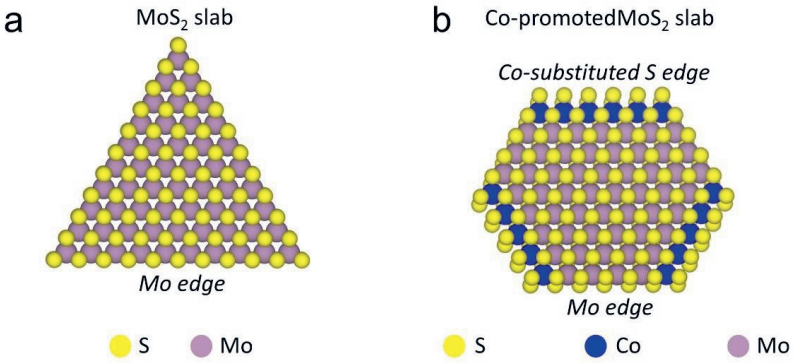

Figure 1: a) Atomic model of a pristine MoS_2 slab with the Mo-terminated edges. b) Atomic model of a CoMoS slab with the 100% S coverage Mo-terminated and Co-substituted S edges. The models are based on the reference number 21.

In this work, we present the first observations of the Co-promoted MoS_2 model catalyst under industrially-relevant HDS conditions using the ReactorSTM. We have prepared a model catalyst containing the CoMoS slabs supported on an Au(111) substrate. We study this model catalyst both in UHV as well as in situ under industrially relevant conditions for HDS. Under the desulfurizing gas mixture of CH_3SH and H_2, we observe that the structure of the Co-substituted edge changes with time whereas in pure H_2 and pure CH_3SH, the edge structure remains static. The desulfurizing gas condition also causes the transformation of hexagonal CoMoS slabs into slabs with curved edges signifying the presence of high index terminations which have not been observed in prior low pressure experiments. Additionally, we also observe the mass transport of Co atoms from the CoMoS slabs into the 2D CoS_2 phase. Our experiments demonstrate that it is very important to observe a complex catalyst like the CoMoS nanoclusters under industrially relevant catalytic conditions.

6.2 Experimental Methods

All the experiments were carried out in the ReactorSTM setup.[23] We use the same crystal cleaning procedure as presented in Chapter 3 and 4 presented of this thesis. Briefly, a polished Au(111) single crystal was purchased from the Surface Preparation Laboratory (SPL), Zaandam, the Netherlands. The crystal was cleaned by repeated cycles of sputtering and annealing until impurities were no longer detected by XPS and STM. Sputtering was performed using Ar^+ with an ion energy of 1.5 keV and annealing was performed using radiative heating at 873 K for 10 minutes in ultra-high vacuum (UHV).

For growing the CoMoS slabs on Au(111), we used the well-known Aarhus recipe.[21] First, MoS_2 slabs were grown on the Au(111) surface by depositing Mo from an Oxford EGCO4 evaporator in a H_2S atmosphere of $2x10^{-6}$ mbar with the sample held at 400 K. Thereafter, annealing was performed at 650 K under the same H_2S atmosphere to synthesize the pristine MoS_2 slabs which act as seeds for growing

the CoMoS slabs subsequently. The sample was then cooled to 400 K in the same H_2S background over 30 minutes. At this stage, co-deposition of Mo and Co was performed followed by annealing to 650 K for 20 minutes while maintaining the H_2S background. This step allows for the Co atoms to be incorporated into the MoS_2 slabs. The model catalyst containing CoMoS slabs, thus synthesized, was cooled in the H_2S background to 450 K over 45 minutes and thereafter, to 300 K in UHV over 150 minutes.

Scanning tunneling microscopy was performed with the ReactorSTM using both the UHV mode and the high-pressure mode. STM tips were prepared by cutting polycrystalline Pt-Ir 90-10 wires purchased from Goodfellow without further processing. Constant-current scans were performed using LPM video-rate scanning electronics described in detail elsewhere.[24,25] Home-developed Camera software and WSxM were used for STM image processing.[26,27] Line-by-line background subtraction was used for the ease of viewing the STM images. Line-by-line differential filtering was used to view the edge registry if necessary. All of the UHV scans were carried out at room temperature.

For the high-pressure STM imaging, the model catalyst consisting of CoMoS slabs supported on Au(111) was loaded into the STM assembly and a Kalrez seal was placed between the sample and the reactor. Thereafter, the bellows of the reactor were actuated to close the reactor and establish the closed volume for introducing the reaction gasses. The CoMoS model catalyst was studied under three gasses: 1 bar H_2, 0.1 bar CH_3SH and a desulfurization mixture containing H_2 and CH_3SH. Ar N5.0, H_2 N5.0 and CH_3SH N2.8 (dimethylsulfide and dimethyldisulfide are the primary impurities) were procured from Westfalen AG. The gas purity was confirmed using a mass spectrometer before use. The gas lines were flushed with Ar and baked out at 423 K for 12 hours to remove any residual reactants and volatiles before commencing all experiments presented in this chapter. All high-pressure STM measurements were carried out at 510 K. A temperature of 510 K was chosen as this is within the typical range of temperatures under which HDS is carried out in the industry.[9,28]

For observing the model catalyst under 1 bar H_2, the STM's reactor was first pressurized up to 0.1 bar with H_2 and thereafter, the temperature was raised to 510 K with a heating rate of 2 K/min. After this step, the system was allowed to reach thermal steady-state for 90 minutes in order to minimize the thermal drift while scanning with the STM. Finally, the hydrogen pressure was raised to 1 bar at a rate of 0.01 bar/min. After the system was allowed to reach steady-state for 180 minutes, the STM scanning was commenced.

For observing the reduced model catalyst under CH_3SH, the reactor was pressurized to 0.1 bar H_2 at 300 K. Thereafter, the temperature was raised to 510 K at a heating rate of 2 K/min. Once the thermal steady-state was reached, the reactor pressure was gradually raised to 1 bar while maintaining the temperature. The model catalyst was then allowed to reduce for 120 minutes under 1 bar H_2 at 510 K. After the reduction, the total pressure was reduced to 0.1 bar and the gas composition changed from 100 % H_2 to 100 % CH_3SH while maintaining the temperature at 510 K. A mass spectrometer was used to analyze the exhaust gases and ensure that all the residual hydrogen was pumped away. Thereafter, the system was allowed to reach steady-state for 180 minutes and the STM scanning was commenced.

For imaging the CoMoS slabs under HDS conditions, a freshly prepared CoMoS model catalyst was reduced under 1 bar H_2 at 510 K using the procedure mentioned in the previous paragraph. Thereafter, desulfurizing conditions were reached by introducing CH_3SH in the gas stream. The molar flow rate of the gas stream was selected to ensure a residence time of ~1s in the reactor so that the product build up, if any, is negligible. A variety of H_2:CH_3SH ratios have been used to image the CoMoS slabs. These conditions are detailed in Table 1. For each of the conditions, only after the system was allowed to reach steady-state for 180 minutes, the STM scanning was commenced.

For the post-HDS UHV measurements, the total pressure was reduced to 0.1 bar and the model catalyst was allowed to cool down to 373 K under the flow of gasses for 15 minutes. After this step, the gasses were pumped away and the model catalyst was brought under UHV conditions and allowed to cool to room temperature over 120 minutes. Thereafter, the STM scanning was commenced.

The XPS spectra were obtained using a commercial SPECS Phoibos system equipped with an XRM50 X-ray source set to the Al K-alpha line and a HSA3500 hemispherical analyzer with a pass energy of 30 eV. A monochromator was used to separate the satellite peaks and the sample was excited with a 54.6° incidence. An acceleration voltage of 10 kV and a power of 250 W was used for all the measurements. Calibration of the XPS spectra was performed by setting the bulk Au 4f peak of the clean Au(111) substrate to 84.0 eV. The number of integrations was set to 30 in order to have sufficient signal-to-noise ratio. CASA-XPS software was used for quantification and XPSPEAK41 software was used for the peak fitting. Relative sensitivity factors for surface were obtained from literature.[29] Shirley background subtraction was performed for all the spectra and a Newton-Raphson method was used for convergence. The XPS spectra were fit using mixed Gaussian-Lorentzian (65-35) curves. For the Mo 3d signal, a doublet separated by 3.15 eV was used. For the Co $2p_{3/2}$ peaks, an asymmetric Gaussian-Lorentzian sum function was used to fit the main component. The Mo 3d spectra were fit with components for Mo^{4+} in MoS_2 at 229.2 eV, reduced MoS_2 at 228.8 eV and 228.3 eV for 5-fold and 4-fold coordinated Mo atoms respectively and the S 2s component at 226.2 eV. The Co $2p_{3/2}$ spectra were fit with components for Co in the metallic Co sulfide phase and Co in the CoMoS phase. Co in the metallic Co sulfide phase is fit with a main asymmetric peak at 778.1 eV, and two satellites at 781.1 eV and 783.1 eV. The Co in the CoMoS phase was fit with a main asymmetric peak at 778.6 eV and two satellites at 781.6 eV and 783.6 eV. These binding energies are tabulated in Table 2. All the signature peak positions are based on previously reported literature work.[11,15,17,30]

Table 1: Hydrodesulfurization gas conditions used for high-pressure STM measurements

Temperature (K)	Total pressure (bar)	H_2 partial pressure (bar)	CH_3SH partial pressure (bar)	H_2:CH_3SH
510 K	1	0.9	0.1	9:1
510 K	0.3	0.15	0.15	1:1
510 K	0.6	0.45	0.15	3:1
510 K	0.6	0.515	0.085	6:1

Table 2: XPS binding energies for various components used for peak fitting.

Components	MoS_2	Reduced MoS_2 (4-fold)	Reduced MoS_2 (5-fold)	S 2s
Binding energy (eV)	229.2	228.3	228.8	226.2
ΔBE* (eV)	3.15	3.15	3.15	
Components	Co sulfide main	Co sulfide sat. 1**	Co sulfide sat. 2**	S 2s –CH_3S
Binding energy (eV)	778.1	781.1	783.1	226.9
Components	Co (CoMoS) main	Co (CoMoS) sat. 1**	Co (CoMoS) sat. 2**	
Binding energy (eV)	778.6	781.6	783.6	

* $\Delta BE(3d) = BE\ 3d_{5/2} - BE\ 3d_{3/2}$; ** sat. stands for satellite

6.3 Results and Discussions

Figure 2 shows a large-scale STM image of MoS_2 slabs grown on Au(111) by the recipe detailed in the experimental methods. The MoS_2 slabs are observed to have a triangular shape. The slabs exhibit this shape because Mo-terminated edges of MoS_2 are thermodynamically more stable than the S-terminated edges under the sulfur-rich conditions used during the synthesis.[31–34] The MoS_2 slabs have a measured height of 1.8 Å which is close to the experimentally measured height of 2±0.3 Å of SL MoS_2 slabs supported on Au(111) at similar sample voltages (see SI, Figure S1).[31] In addition to the MoS_2 slabs, the Au(111) terraces exhibit a 'distorted' herringbone reconstruction due to the exposure to H_2S during the synthesis procedure. A similar effect on the Au(111) surface due to H_2S exposure has been observed in Chapter 3 and also reported in the literature.[31–35] We use the MoS_2 supported on Au(111) sample as a precursor to synthesize the Co-promoted MoS_2 model catalyst.

Figure 3a and 3b show the large-scale STM images of CoMoS slabs synthesized by the co-deposition technique detailed in the experimental methods. The CoMoS slabs are observed to have a hexagonal shape, in contrast to the triangular shape of the non-promoted MoS_2 in the precursor. This is because the growth of the MoS_2 slabs in the presence of Co adatoms causes the Co to be incorporated into the S-terminated edges.[5] The incorporation of Co atoms causes the S-terminated edges to become thermodynamically stable under the sulfur-rich synthesis conditions.[5,21,36] Therefore, the CoMoS slabs exhibit a hexagonal shape. Additionally, large atomically-flat islands of SL Co sulfides like 2D CoS_2 are also observed to form. The structural characterization of the 2D CoS_2 sheets on Au(111) has been reported in Chapter 3 of this thesis and elsewhere in literature.[35] Such Co sulfide sheets have also been observed to form in the previous studies on CoMoS model catalysts as byproducts of the synthesis recipe.[5,21,36]

Figure 3c shows an atom-resolved STM image of the CoMoS slabs. From the previous STM experiments on MoS_2 slabs supported on Au(111), it is known that the sulfur atoms are imaged as the bright protrusions on the basal plane at the filled-state scanning conditions used.[31] Furthermore, the penultimate line of protrusions preceding the edges of the CoMoS slabs is observed to be bright in comparison to the protrusions on the basal plane. This bright feature is attributed to the presence of 1-D metallic states along the edges called as Brim sites.[5,31] In the prior work carried out on MoS_2 and

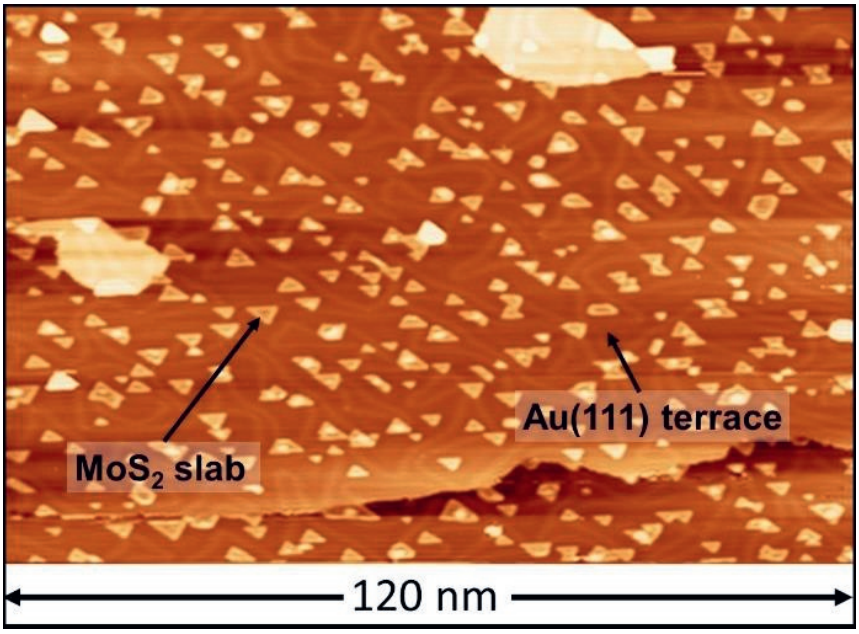

Figure 2: Large-scale STM image of MoS_2 slabs supported on Au(111) acquired in UHV at room temperature with sample voltage = -1 V and tunneling current = 200 pA. Some Au islands are also observed to form during the MoS_2 synthesis.

Co-promoted MoS_2 model catalysts, the registry of the edge protrusions with respect to those of the basal plane has been directly correlated with the sulfur saturation of the edges.[21,22] Figure 3d shows the zoom-in of the area marked by the green dotted rectangle in Figure 3c. The bright protrusions associated with the basal plane sulfur atoms have been superimposed with a hexagonal lattice for the ease of identifying the edge registry. The hexagonal lattice is drawn by connecting the experimentally measured protrusions so that locally, any distortions due to thermal drift or creep in the piezo scanner can be accounted for. Along one of the edges, the observed edge protrusions deviate from their expected position and are clearly out-of-registry with respect to the basal plane. The registry shift along this edge is measured to be 21±2%. This matches very well with the signature of a 100% S saturated Mo-terminated edge of a CoMoS slab.[21,22] Therefore, we identify this edge as an Mo-terminated edge. On the adjacent edge, however, the edge protrusions are observed to be in registry but shifted away from their expected positions in the in-plane vertical direction from the edge by ~0.4 Å. The Brim sites along this edge have a higher contrast that those along the Mo-terminated edge suggesting a higher metallicity. These characteristics match very well with those of a 100% S Co-substituted S edge of a CoMoS slab.[21] The Co atoms along this edge are expected to be in a trigonal prismatic coordination and are stabilized by the interaction of the edge sulfur atoms with the Au(111) surface (see SI, Figure S1).[21]

As the next logical step towards reaching the HDS reaction conditions, the S-saturated CoMoS slabs must be imaged under industrially-relevant pressures of hydrogen and at a high temperature as reduction with H_2 is performed industrially to activate the CoMoS catalysts for HDS. Even at vacuum pressures, hydrogen treatment is known to reduce the Mo and Co-substituted edges of the CoMoS slabs and drastically change the edge structure.[21,22] A total pressure of 1 bar and a temperature of 510 K were selected in order to get close to the industrial reducing conditions. To image the Co-promoted MoS_2 model catalyst under H_2, the operating conditions were reached by following the procedures detailed in the experimental methods. Thereafter, the system was allowed to reach steady-state for 180 min before approaching with the STM tip and commencing the scanning.

Figure 4a shows a large-scale STM image of the CoMoS slabs supported on Au(111) acquired in situ under 1 bar H_2 and at 510 K. The CoMoS slabs are observed to retain their hexagonal shape at these conditions. This shows that both the Mo-terminated and Co-terminated edges are stable when reduced by hydrogen and the overall hexagonal shape observed under the UHV conditions is also the stable shape of the CoMoS slabs under 1 bar H_2 at 510 K. Additionally, all the CoMoS slabs retain the bright Brim sites along their periphery. Figure 4b shows an atom-resolved STM image of a CoMoS slab obtained in situ under 1 bar of H_2 at 510 K. The Brim sites along one of the edges are observed to be relatively brighter. Along this edge, the edge protrusions are in registry with the basal plane. The characteristics of this edge match well with the signatures of a reduced Co-substituted S edge with 50% S-atom saturation and adsorbed H.[21] The adjacent edge, however, has a relatively darker Brim. Furthermore, the edge protrusions along this edge are observed to be in registry with the basal plane, but with a 0.2 Å shift towards the edge along the vertical direction with respect to the edge. There is an excellent match with the characteristics of this edge and that of a reduced Mo-terminated edge

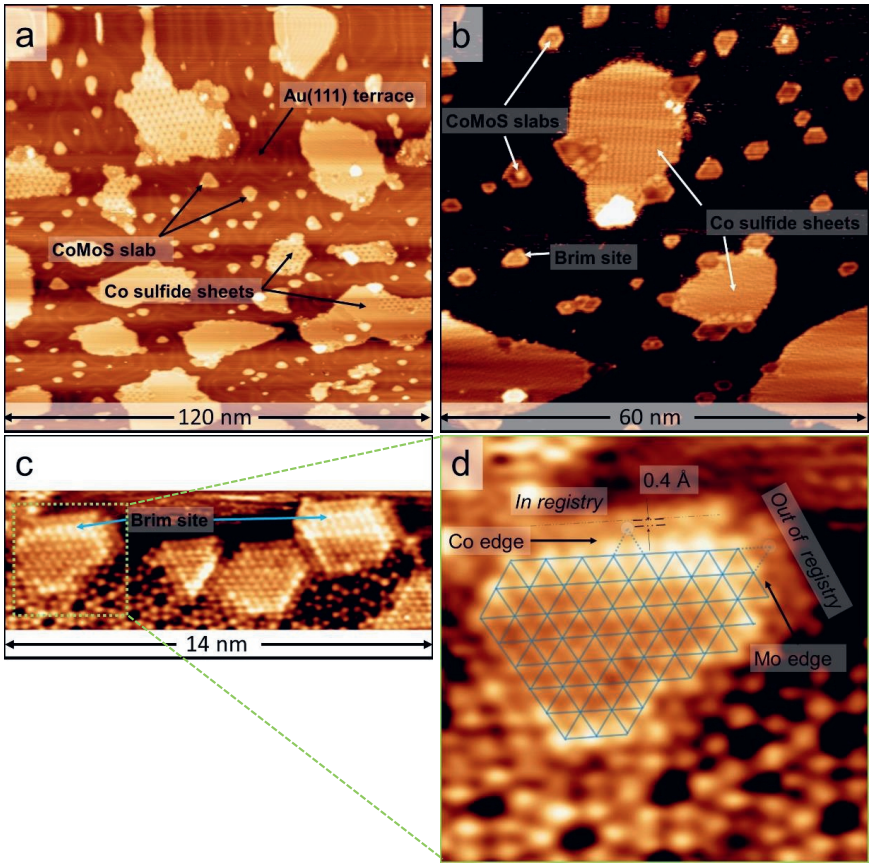

Figure 3: a,b) Large-scale STM images of CoMoS slabs supported on Au(111); sample voltage = -1 V, tunneling current = 200 pA. Figure 3b shows a high-contrast STM image highlighting the hexagonal CoMoS slabs. c) Atom-resolved STM image of CoMoS slabs supported on Au(111); sample voltage = -0.35 V, tunneling current = 300 pA. d) Zoom-in of the region marked by the green rectangle in Figure 3c. The blue dotted lines denote the expected positions of the edge protrusions.

with 50% S and adsorbed H which was observed in previous vacuum and high-pressure studies on a pristine MoS_2 and CoMoS model catalysts.[21,22]

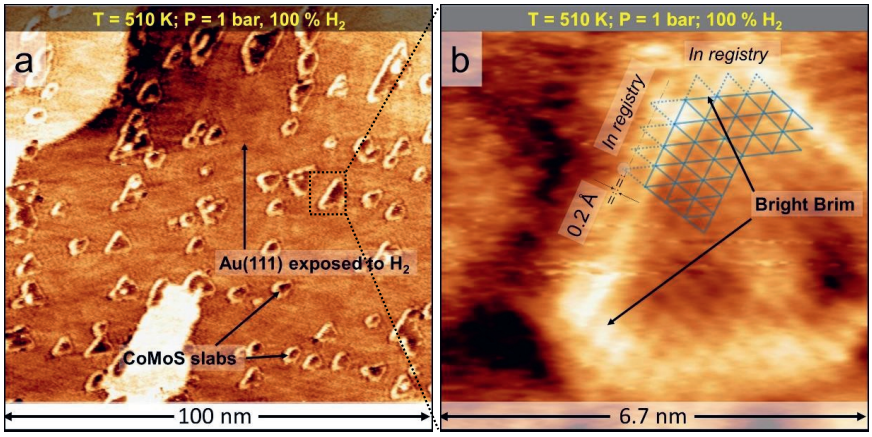

Figure 4: a) Large-scale STM image of CoMoS slabs supported on Au(111) measured in situ under H_2; total pressure = 1 bar, gas composition = 100% H_2, sample voltage = -1 V, tunneling current = 400 pA. b) Atom-resolved STM image of a CoMoS slab measured in situ under H_2; total pressure = 1 bar, gas composition = 100% H_2, sample voltage = -0.2 V, tunneling current = 600 pA.

Recently reported work on hydrogen-induced restructuring of CoMoS slabs[21] showed that, upon exposure to rough vacuum pressures of H_2 and at elevated temperatures, two types of Co-substituted S edges are formed. One of these edges has an intensely bright Brim, the edge protrusions are clearly visible in the STM images and are observed to be in registry with the basal plane protrusions. This edge was identified as a reduced Co-substituted S edge with adsorbed H atoms using pyridine adsorption experiments.[21] The adsorption of hydrogen was observed to lift the sulfur atoms that otherwise strongly interact with the Au(111) substrate and remain low. The other type of S edge, however, has the Brim sites quenched and the edge protrusions not very clearly visible in the STM images. This edge was found to not be reactive towards pyridine and was identified as a reduced Co-substituted S edge without adsorbed H. The edge S atoms on this type of edge lay low due to chemically bonding with the gold substrate.[21] Thus, the two types of Co-substituted edges could be identified by the brightness of the Brim sites upon reduction under vacuum pressures of hydrogen. Figure 4a clearly shows that all the CoMoS slabs observed at 510 K in situ under 1 bar H_2 retain the bright Brim associated with the Co- and Mo- terminated edges. The edges with quenched Brim sites were never observed in our experiment. This shows that, under 1 bar H_2 and at 510 K, all of the Mo terminated and Co-substituted S edges are not only reduced but also hydrogenated.

In order to ultimately image the CoMoS slabs under HDS conditions, it is also important to understand the structural and morphological changes occurring upon exposing the CoMoS slabs not only to H_2, but also to organosulfur molecules that need to be desulfurized. Methylthiol was chosen as a model desulfurization compound for three reasons. First, methylthiol is a very common organosulfur contaminant present in various fractions of processed crude oil.[1,9,37] Second, methylthiol is a gaseous organosulfur compound and is easier to handle in the ReactorSTM as compared to organosulfur liquids. Third, methylthiol being the simplest aliphatic thiol, only has one possible HDS reaction pathway and hence, complex side reactions can be circumvented.[38,39]

A fresh model catalyst containing CoMoS slabs supported on Au(111) was prepared and reduced at 510 K under 1 bar H_2 following the methodology detailed in the experimental methods. Thereafter, the gas composition was changed to 100 % CH_3SH with a total pressure of 0.1 bar and 510 K. The system was allowed to reach steady-state for 180 minutes before approaching with the STM tip and commencing the scan.

Figure 5a shows the STM image of CoMoS slabs reduced under 1 bar H_2 and then observed in situ under a 100% CH_3SH atmosphere at a pressure of 0.1 bar and temperature of 510 K. Under these conditions, the CoMoS slabs are observed to have three types of edges based on the Brim site contrast: edge with an intermediate-contrast Brim, edge with a quenched Brim and edge with a bright Brim. Figure 5b shows the zoom-in of the edge with an intermediate contrast Brim site. Comparison of the positions of the edge protrusions along this edge with respect to those of the basal plane shows that the edge protrusions are out-of-registry with a measured registry shift of 24±2 %. These features match very well with those of the Mo-terminated edges of pristine MoS_2 slabs when exposed to CH_3SH, as observed by Mom et al.[22] According to their work, the low activation barriers for the adsorption/desorption of CH_3SH on the Mo edge leads to fast adsorption/desorption kinetics and an overall time-averaged out-of-registry structure at the elevated temperature and pressure. Based on these characteristics, we identify this edge of the CoMoS slab with an out-of-registry edge structure and an intermediate contrast Brim as an Mo-terminated edge.

Figure 5c shows the zoom in of an edge of the CoMoS slab with a quenched Brim. The edge protrusions along this edge show a complex structure. Every alternate edge site has an intensely bright and diffuse protrusion which is in registry with the corresponding basal plane protrusions. Due to the diffuse nature of this protrusion, a minor registry shift if any, cannot be ruled out. On the site adjacent to the the diffuse feature, a relatively darker protrusion that has a registry shift of 17±1% of a unit cell towards the nearby diffuse bright protrusion is observed. We also note that the darker features were always observed to be on the same side of the bright feature on a given edge, suggesting that the features interact with each other along the edge. Additionally, the bright features are measured to be 0.2 Å further away from the edge than the adjacent darker features. In the work carried out by Mom et al.[22], a CH_3SH adsorption structure on a reduced Mo edge without time averaging was also modelled using DFT calculations. The simulated STM image of this structure showed a pair of a bright diffuse feature and a darker adjacent feature due to the formation of an –SH and adsorbed CH_3S- on adjacent sites respectively, identical to the ones observed in Figure 5c. It is very likely that the structure observed in Figure 5c is a similar CH_3SH adsorption structure. Additionally, low pressure molecular

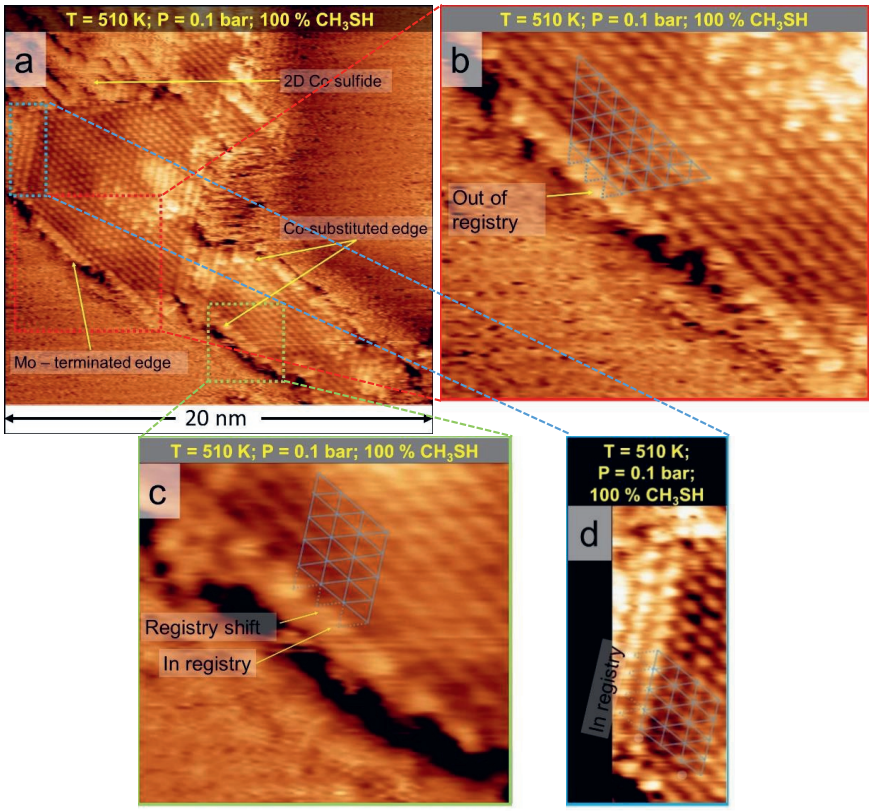

Figure 5: a) Atom-resolved STM image of CoMoS slabs measured in situ under 100% CH_3SH. b,c,d) Zoom-in of the areas marked red, green and blue respectively, in Figure 5a. The areas highlight the atomic structure of the three types of edges of the CoMoS slabs. All STM images are obtained under the following conditions: total pressure = 0.1 bar (100% CH_3SH), T = 510 K, sample voltage = -0.2 V, tunneling current = 0.9 nA.

adsorption experiments on CoMoS slabs with other organo sulfur compounds have shown the formation of paired edge features on the Co-substituted edge and the quenching of adjacent Brim sites similar to the one observed on the edge in Figure 5c.[40–44] We interprete the edge with quenched Brim and paired features on the edge (as in Figure 5c) to be a Co-substituted S edge which has adsorbed CH_3SH molecules. However, we note that in the model of CH_3SH adsorption presented in the work of Mom et al., the bright diffuse features were found to be in an out-of-registry configuration while the darker feature was observed to be in registry. This is in contrast to the edge structure in Figure 5c. This difference in the registry is attributed to the intrinsic structural differences between an Mo and a Co-substituted S edge. That we do not observe the time-averaged structure suggests that CH_3S- binds very strongly to a Co-substituted S edge. A possible candidate structure for this type of an edge is presented in the SI, Figure S2.

Figure 5d shows the zoom in of an edge with a bright Brim. The edge protrusions on this edge are measured to be in registry with the basal plane and appear identical to those of a 100% S Co-substituted S edge.[21] All the edges that have this structure were observed to be encapsulated by the 2D CoS_2 sheets. We note that the adjacent edge of the CoMoS was identified as an Mo-terminated edge in the previous paragraphs (Figure 5a and 5b). Based on the geometry arguments from the Wulff construction,[5] the edge in Figure 5d should therefore, be an S edge. However, none of the features observed on a Co-substituted S edge with a quenched Brim and adsorbed CH_3SH (as in Figure 5c) were observed on this edge. A possible explaination is that the edge sites on this edge are not available for CH_3SH adsorption as they are involved in atomic bonding with the edges of the 2D CoS_2 sheet.

Having observed the effect of methylthiol exposure on the CoMoS slabs, at this stage, we introduced H_2 into the gas stream while maintaining the partial pressure of CH_3SH and the sample temperature in order to transition into the HDS reaction conditions. A gas phase composition of 1:9 CH_3SH:H_2 at a total pressure of 1 bar and a temperature of 510 K was used to closely imitate the industrial HDS conditions. The precise steps undertaken to achieve the HDS reaction conditions are detailed in the experimental methods. The system was allowed to reach steady-state for 180 minutes before the STM scanning was commenced.

Figure 6a shows a large-scale STM image of the CoMoS slabs measured in situ under the HDS conditions (1:9 CH_3SH:H_2, 1 bar and 510 K). Under these conditions, the Au(111) support did not show the herringbone reconstruction. This effect is attributed to the presence of sulfur atoms formed by the dissociation of CH_3SH and the residual H_2S (<0.1 mbar).[22] In fact, a (1x1) structure of Au upon exposure to CH_3SH has been reported in the literature.[45] In order to avoid the formation of a CH_3SH self-assembled structure, the temperature during the measurement was always maintained above 500 K.

Under the HDS conditions, in addition to the hexagonal CoMoS slabs, a significant number of curved CoMoS slabs were observed to form (see Figure 6b). Additionally, the larger slabs were observed to also have irregular edges (see inset, Figure 6a). CoMoS slabs with such curved and irregular edges were observed to form only under the HDS conditions but not after the synthesis, reduction under H_2 or the exposure to CH_3SH. In the past, curved MoS_2 nanoclusters have only been observed with

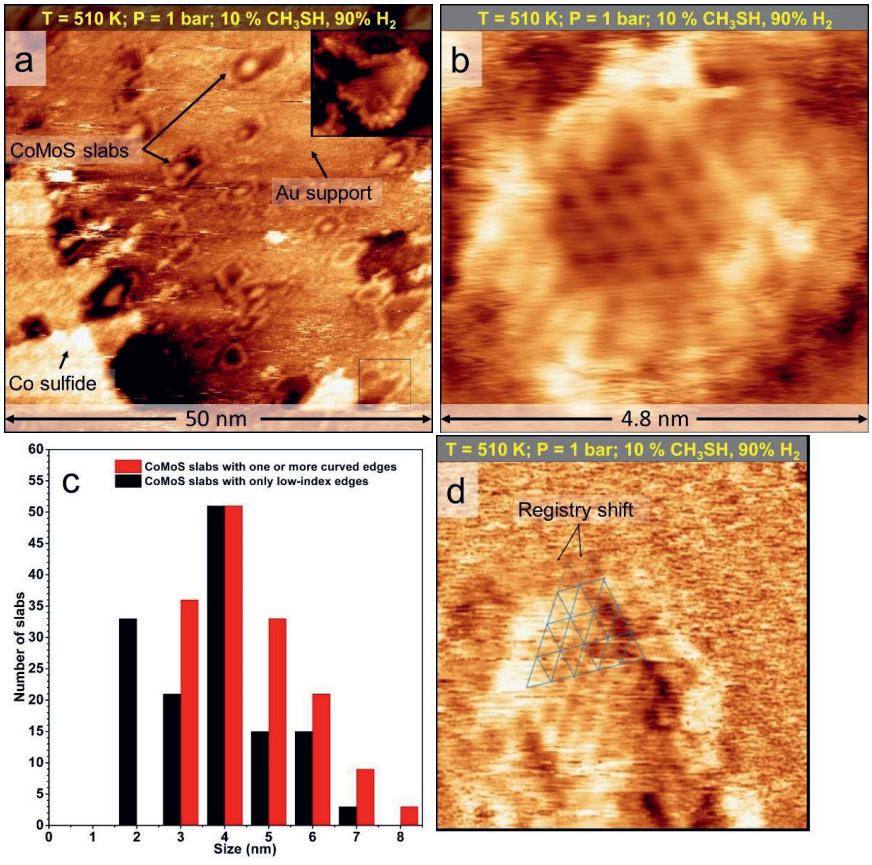

Figure 6: a) Large-scale STM image of CoMoS slabs supported on Au(111) acquired in situ under the HDS condition. The inset shows a zoom in of the CoMoS slab within the black rectangle.b) A CoMoS slab with a curved shape observed in situ under the HDS conditions. c) Statistics of the shape of the CoMoS slabs vs slab size obtained by analyzing large-scale STM images after 16 hours of HDS. d) Atom-resolved STM image with a differential filter showing the out-of-registry structure on the Mo-terminated edge. All the images are measured under the following conditions: total pressure = 1 bar (1:9 CH_3SH:H_2), T = 510 K, sample voltage = -0.2 V, tunneling current = 500 pA.

STM on NiMoS model catalysts supported on Au(111) and have been attributed to coordinatively unsaturated (CUS) Ni sites in the corner.[5] However, several electron microscopy experiments also report the observation of CoMoS slabs with curved edges on a carbon support.[7,8,46] They have suggested that the curved edges may be due to high index terminations such as the $(11\bar{2}0)$ termination resulting in highly undercoordinated Co atoms being exposed. An example of such a termination is shown in the SI, Figure S3. It is likely that such CUS sites involving Co atoms are formed under HDS conditions on the CoMoS slabs in our sample, causing them to adopt a curved shape. The analysis of the shape of 291 CoMoS slabs vs slabs size after 16 hours of HDS shows that 53 % of the CoMoS slabs have at least one curved edge (see Figure 6c). Slabs larger than 4 nm were observed to have a higher tendency to show curved edges while, slabs below the size of 2.5 nm did not show any curved edges. This observation suggests the role of size effects in the formation of the curved CoMoS slabs.

Figure 6d shows the atom-resolved STM image of a CoMoS slab observed during the desulfurization of CH_3SH. A differential filter has been applied for the ease of viewing the registry of the edge protrusions. The edge protrusions along one of the edges show a registry shift of 22±1% of a unit cell. Furthermore, this type of edge was observed to have a relatively more intense Brim (not seen in Figure 6d). The features of this edge match very well with those of a 38%S-CH_3SH Mo-terminated edge of an MoS_2 slab imaged during the desulfurization of methylthiol.[22] Therefore, we assign this edge as the Mo-terminated edge of the CoMoS slab. Based on the arguments from the Wulff construction,[5] the other set of edges are then interpreted as the Co-substituted S edge.

The Co-substituted S edges were observed to have relatively darker Brim sites. Furthermore, these edges also showed a time-varying structure under the HDS reaction conditions. In order to capture this changing edge structure, the hexagonal CoMoS slabs were repeatedly scanned with the STM to track the changes occuring on the edges. STM images were acquired 10 seconds apart to account for any thermal drift. Figure 7 shows the successive STM images of a CoMoS slab obtained under the HDS reaction condition. Over the time scale of seconds, several bright and diffuse features identical to those attributed to CH_3SH adsorption in Figure 5c, were observed to form and disappear on the Co-substituted S edges. The dynamic activity is clearly activated by the introduction of hydrogen in the gas stream as imaging the edge in CH_3SH alone showed a static edge structure (Figure 5c). These features are marked by the blue arrows in Figure 7a-h for the ease of viewing. In order to confirm that the observed activity was not isolated to the particular CoMoS slab, several other CoMoS slabs on various locations of the sample were also imaged under the HDS conditions (see SI, Figure S4). Additionally, the CoMoS slabs were also imaged using other tunneling conditions (V =-0.2 to -1V, I = 900 to 100 pA) to check if the observed dynamic activity may have been induced by the STM tip. All the slabs were observed to show the dynamic edge structure irrespective of the tunneling conditions. We also note that the darker features on the adjacent sites, as in Figure 5c, were not imaged here very likely due to tip effects. The STM image of CoMoS slabs acquired at 300 K in UHV immediately after the HDS reaction gasses were pumped away indeed confirmed the presence of the neighbouring darker features near the bright and diffuse features on the Co-substituted edge (see SI, Figure S5 and S6). Additionally, it was also observed that sustained atom-resolved image acquisition under the HDS conditions was difficult owing to the frequently changing tip-states. The likelihood of a change of the

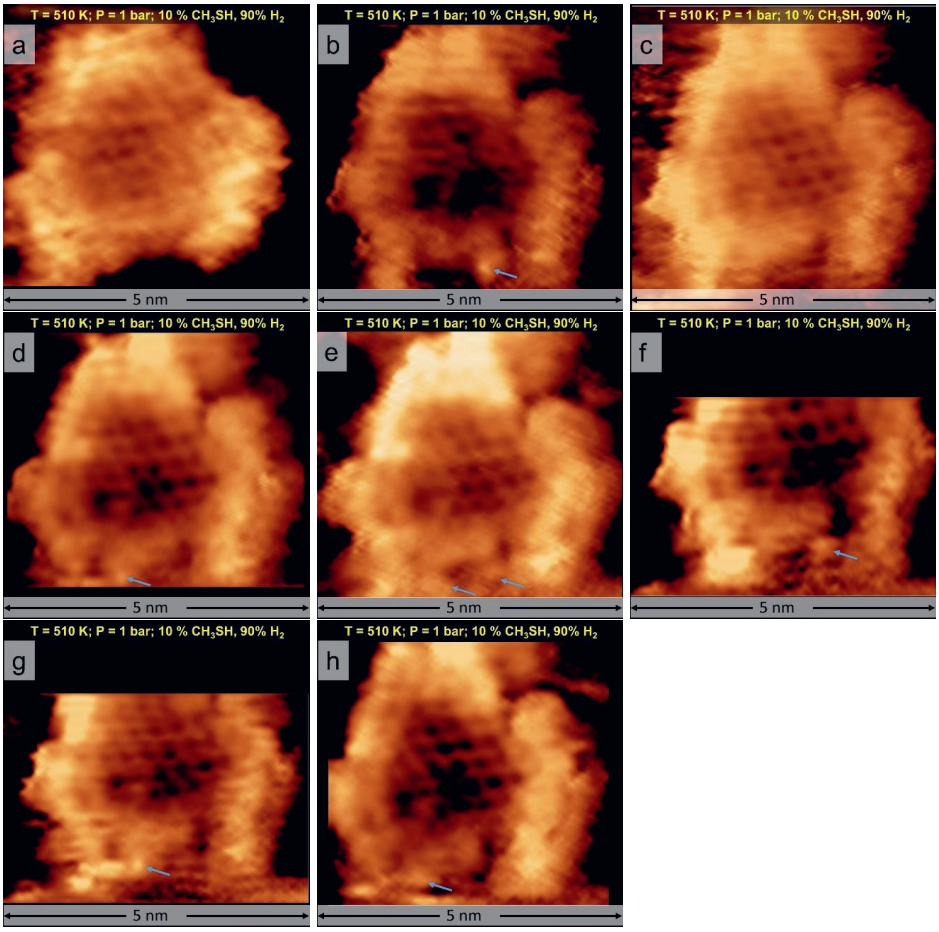

Figure 7: a-h) Successive STM images of a CoMoS slab measured 10 seconds apart under the HDS reaction conditions. The images have been acquired under the following conditions: total pressure = 1 bar (1:9 CH_3SH:H_2), T = 510 K, sample voltage = -0.2 V, tunneling current = 500 pA.

tip-state under the HDS reaction conditions was observed to be related to the hydrogen partial pressure; higher hydrogen partial pressure causing more frequent tip-state changes.

Since the changes of the tip-states were found to be related to the partial pressure of hydrogen, a lower hydrogen pressure could allow for better quality imaging. The desulfurization experiment was repeated for a CH_3SH:H_2 ratio of 1:1, 1:3 and 1:6 while maintaining the partial pressure of methylthiol close to 0.1 bar. The system was allowed to reach steady-state for 180 minutes before commencing the STM image acquisition for each of the experiments.

Figure 8 and 9 show the STM images of CoMoS slabs acquired at 510 K under HDS reaction gasses with the CH_3SH:H_2 ratio of 1:1 and 1:6 respectively. Successive STM images were recorded 14 seconds apart. The images thus prepared, were used to generate movies of CoMoS slabs observed in situ under the HDS reaction conditions (see SI, S7). For the ease of discussion, only the relevant frames are presented. A time-variant edge structure marked by the appearance/disappearance of the bright and diffuse edge protrusions identical to the one in Figure 7, was observed on the Brim-quenched Co-substituted S edges under both of the reaction conditions (see Figure 8 and Figure 9). Additionally, the contrast of the Brim sites was observed to be dependent on the occupation of the edge by the bright and diffuse features. For example, the Brim sites on the edge in the lower right corner of Figure 9a appear relatively darker and more disrupted when the number of the bright edge features on the edge increases, for instance, in Figure 9e. Furthermore, it is also observed that the corner sites of the Co-substituted edge have a higher tendency to be occupied by the bright and diffuse features.

In addition to the Mo-terminated and Co-substituted edges with well-defined low index terminations, a significant number of CoMoS slabs were also observed to have a highly irregular edges. The CoMoS slab in Figure 9 (see also SI, S7) shows such irregular edges. The shape of the irregular edges of the CoMoS slab was also observed to be time variant. Such irregular edges were observed to form under all of the HDS conditions studied in this work. The irregular edges were, however, not observed either in pure hydrogen, pure CH_3SH or after the synthesis procedure that involves annealing at 650 K in H_2S. Therefore, the effect of temperature, H_2, H_2S or CH_3SH independently can be ruled out. A likely explanation lies in the interaction of CH_3SH with the edges of the CoMoS slabs under the highly reducing conditions at elevated temperatures. The changing shape of the irregular edge could also be due to mass transport of atoms into and out of the edge. Larger CoMoS slabs are especially prone to this effect and were observed to always show such irregular edges suggesting that size effect likely plays a role. We also note that this effect was not observed on pristine MoS_2 slabs under similar hydrodesulfurization conditions in prior research work.[22] Therefore, it is evident that the formation of the irregular edges very likely involves the Co promoter atoms. Large-scale STM images acquired in UHV at room temperature immediately after the HDS reaction gasses were pumped away(see SI, Figure S6) revealed that these edge structures were static in the UHV scans further suggesting the combined role of the reaction gasses and elevated temperature.

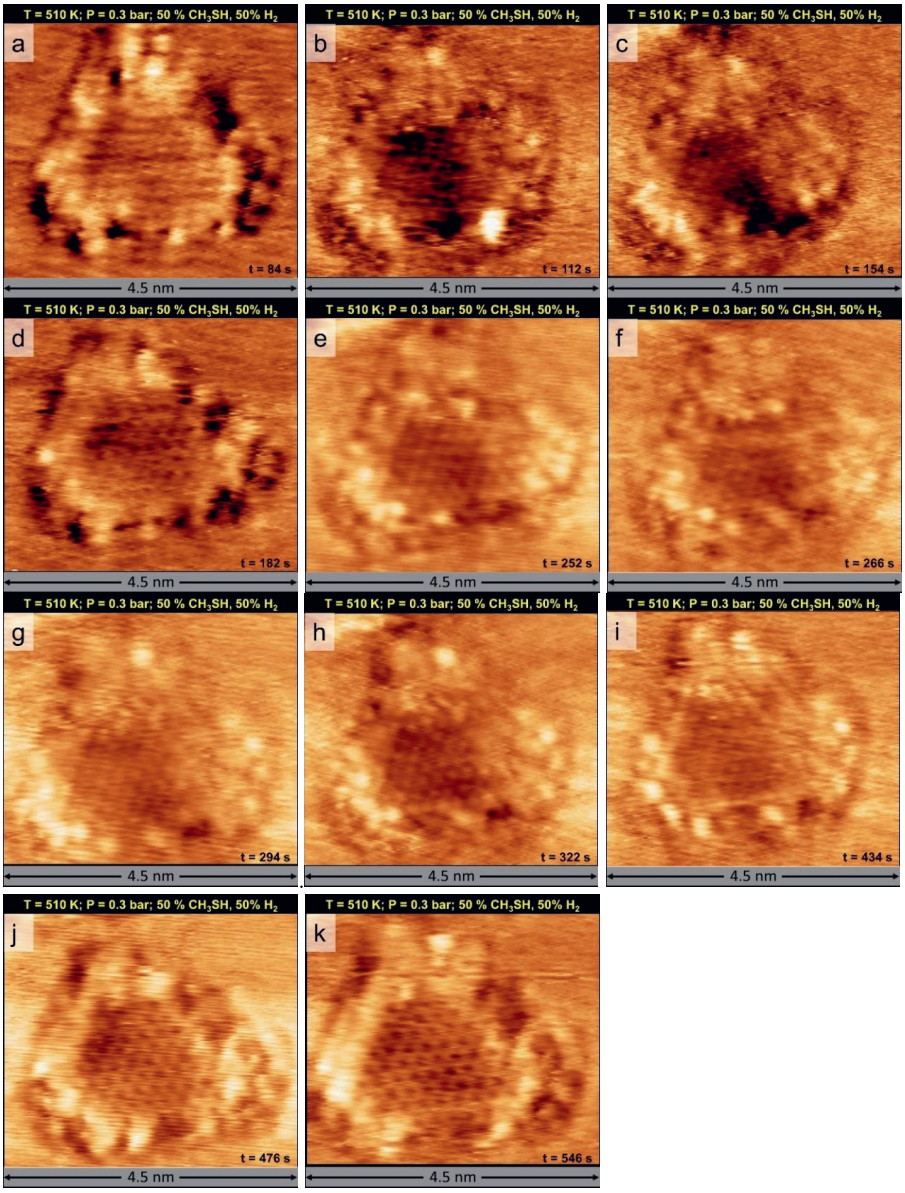

Figure 8: a-k) STM images of a CoMoS slab measured in situ during the hydrodesulfurization of methylthiol showing the dynamic activity along the edges with quenched Brim. The images have been acquired under the following conditions: total pressure = 0.3 bar (1:1 CH_3SH:H_2), T = 510 K, sample voltage = -0.2 V, tunneling current = 1.2 nA, acquisition time = 14 s/frame.

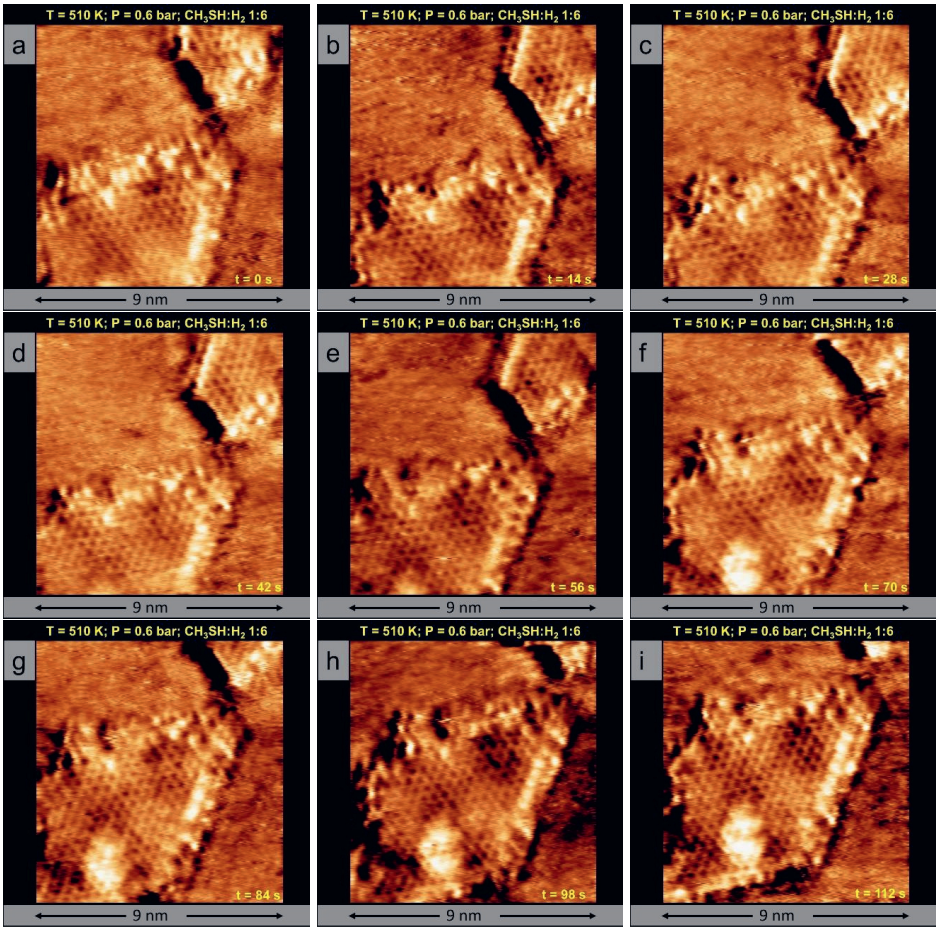

Figure 9: a-i) STM images of a CoMoS slab measured in situ during the hydrodesulfurization of methylthiol. The images have been acquired under the following conditions: total pressure = 0.6 bar (1:6 CH_3SH:H_2), T = 510 K, sample voltage = -0.2 V, tunneling current = 1.5 nA, acquisition time = 14 s/frame. Note the changing contrast of the Brim of the edge on the lower right corner with increasing occupancy of the bright and diffuse features from Figure 9a to 9e. The irregular edges are seen in Figure 9f to 9i.

Additionally, CoMoS slabs which are involved in bonding with the 2D CoS_2 sheets were also imaged under the HDS conditions. Figure 10 shows the STM images of a CoMoS slab in the vicinity of a 2D CoS_2 sheet obtained in situ under a total pressure of 0.6 bar(CH_3SH:H_2 1:3), at 510 K. In Figure 10a, the CoMoS slab is attached to the 2D CoS_2 sheet along the edge marked by the green arrow. With the progress of time, the overall shape of the 2D CoS_2 phase is observed to change. Furthermore, the CoMoS slab and the edge of the 2D CoS_2 sheet are observed to drift away from each other in the successive STM images. The changing shape of the edge of the 2D CoS_2 sheet further suggests that there is likely mass transport of Co atoms under HDS conditions.

To further investigate the hypothesis of Co mass transport, Mo 3d and Co $2p_{3/2}$ XPS spectra of the as-synthesized CoMoS slabs and that of the CoMoS slabs after 16 hours of HDS at 1 bar (CH_3SH:H_2 1:9) and 510 K were analyzed. The Mo 3d and Co $2p_{3/2}$ signatures were fit with components based on the fitting parameters detailed in the experimental methods. Figure 11a shows the Mo 3d spectra of an as-synthesized CoMoS model catalyst. The measured spectrum shows a doublet feature at 229.2 eV with a separation of 3.15 eV. This doublet consists predominantly of the Mo^{4+} component belonging to fully sulfur saturated MoS_2. This is expected due to the sulfur-rich conditions used for the synthesis. A small amount of CUS Mo component at 228.3 eV is also present. This feature is attributed to the traces of reduced Mo sites formed due to the presence of H_2 contaminant during the synthesis and in the UHV background. The shoulder at 226.3 eV is attributed to the S 2s signature characteristic of MoS_2. Figure 11b shows the corresponding Co $2p_{3/2}$ spectra of an as-synthesized CoMoS model catalyst. The Co $2p_{3/2}$ signature shows components from Co present in the Co sulfide phase at 778.1 eV and Co present in the CoMoS phase at 778.6 eV. Comparison of the areas of the two Co $2p_{3/2}$ components shows that 25.5 % of the total Co is present in the CoMoS phase (see Table 3). This is expected as an excess of Co is used in the synthesis recipe to ensure that all the MoS_2 slabs have Co-substituted S edges. Figure 11c and 11d show the Mo 3d and Co $2p_{3/2}$ spectra of the CoMoS slabs acquired in UHV after 16 hours of HDS. We note that both the spectra show a decrease in the overall intensity of the measured signal by ~50 % in comparison to those of Figure 11a and 11b. This decrease in intensity is attributed to the presence of polymer residue left behind by the Kalrez O-ring on the Au(111) substrate after the HDS experiment. This polymer residue covers a fraction of the region on the sample which is excited by the X-rays and hence, an overall decrease in the intensities of the Mo and Co signals is observed. We also note that this polymer residue is outside the scan area of the STM and cannot be observed in the STM images. The region of the sample excited by the X-rays is such that it only includes the area of the sample exposed to the gasses as well as the region that has the residue of the Kalrez polymer seal. Therefore, the Mo 3d and Co $2p_{3/2}$ signals measured after the HDS experiment can be attributed only to that region of the sample which has been exposed to the HDS reaction gasses. In Figure 11c, we observe that the Mo 3d spectra has components from Mo^{4+} belonging to MoS_2 at 229.2 eV as well as those of reduced Mo species at 228.3 eV and 228.8 eV. In comparison to the as-synthesized CoMoS slabs, the fraction of unsaturated Mo component increases from 3.6 % to 19.5 % of the total Mo signal after 16 hours of HDS. These features are attributed to the presence of unsaturated Mo edges of the CoMoS slabs formed due to the prevailing reducing conditions during HDS. The Co $2p_{3/2}$ spectra in Figure 11d shows a component of Co sulfide at 778.1 eV and that of Co in CoMoS phase at 778.6 eV. Furthermore, we also observe that only 9.9 % of the total Co is present

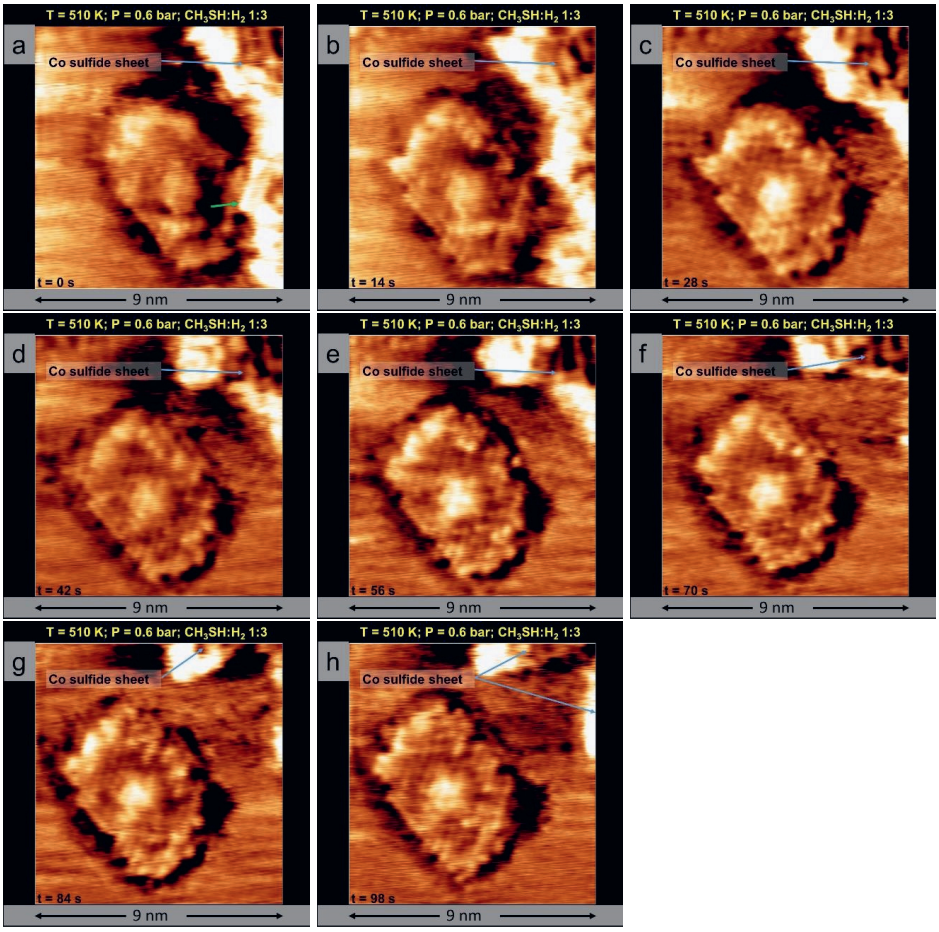

Figure 10: a-h) Successive STM images of a CoMoS slab measured in situ under HDS reaction conditions. The images have been acquired under the following conditions: total pressure = 0.6 bar (1:3 CH_3SH:H_2), T = 510 K, sample voltage = -0.2 V, tunneling current = 1.2 nA, acquisition time = 14 s/frame. The green arrow in Figure 10a indicates the edge of the CoMoS slab which is attached to the CoS_2 sheet. The CoMoS slab and the CoS_2 sheet diffuses away from each other. Note the changing shape of the edge of the CoS_2 phase.

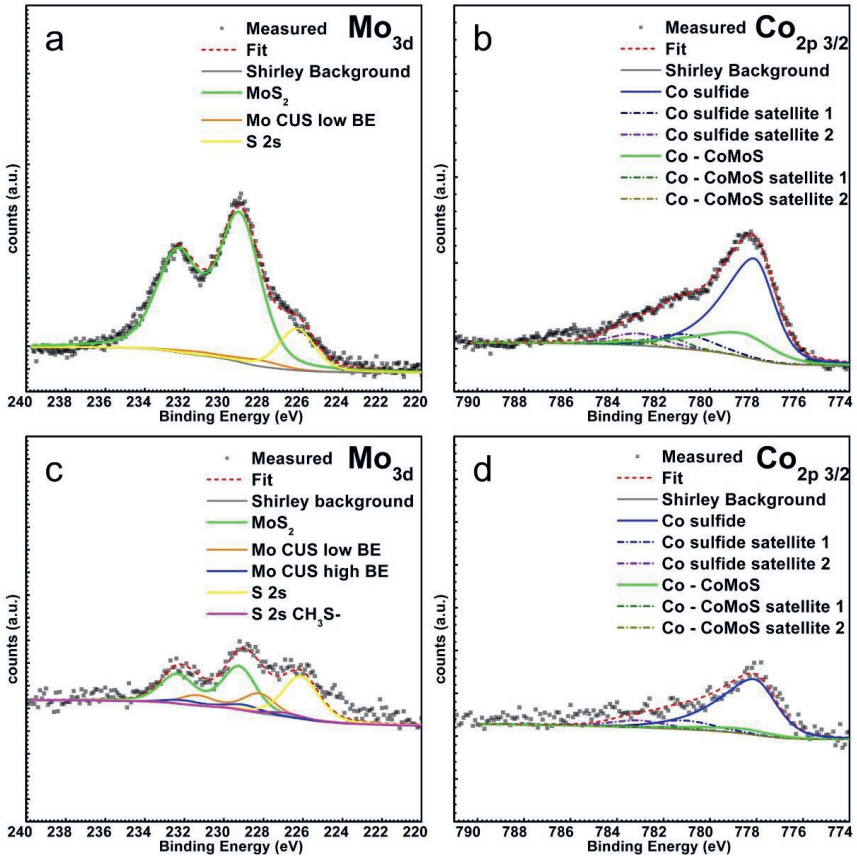

Figure 11: a,b) Mo 3d and Co $2p_{3/2}$ spectra of an as-synthesized Au(111)-supported CoMoS model catalyst. c,d) Mo 3d and Co $2p_{3/2}$ spectra of an Au(111)-supported CoMoS model catalyst after 16 hours of HDS at 1 bar (CH_3SH:H_2 1:9) and 510 K. The spectra are acquired in UHV.

Table 3: Ratio between various components of the XPS spectra in Figure 11

Conditions	Co : Mo	Mo CUS (%)	Co in CoMoS (%)	Co in Co sulfide (%)
As-synthesized	0.78	3.6	25.5	74.5
After HDS for 16 hours	0.80	19.5	9.9	90.1

in the CoMoS phase (see Table 3) as compared to the 25.5% for the as-synthesized CoMoS model catalyst. The decrease in the amount of Co in the CoMoS phase indicates an overall loss Co from the CoMoS edges. However, the Co:Mo ratio before and after the HDS experiment remains a constant at 0.8 (see Table 3), suggesting that the total amount of Co in the system has not changed. Therefore, the Co lost from the CoMoS edge must have migrated to the 2D CoS_2 phase. This observation supports the hypothesis that the irregular edges of the CoMoS slabs and 2D CoS_2 observed in the STM images acquired under the HDS conditions are likely caused by the migration of Co atoms. Such kinetic effects that are observed only under the HDS conditions, however, raise many questions.

First, what is the location of the Co promoter atoms during HDS? Given the changing shape of the edge due to Co mass transport, the location of the Co promoter atoms becomes uncertain. One possibility is that the Co atoms are also redistributed around such irregular edges, likely to sites that are equivalent to the S edge terminations of an MoS_2 slab. Theoretical work by Krebs et al. suggests that Co migration from the CoMoS edges should be thermodynamically favorable under HDS reaction conditions.[47] An irregular edge shape suggests that previously unknown high index terminations of the Co-substituted edge are possible under HDS conditions and also likely contribute to the overall HDS activity. Therefore, the low index Co-substituted edge terminations that have been widely studied in literature under vacuum pressure of gasses relevant for HDS, do not completely represent the CoMoS slabs under HDS conditions. Such kinetic effects might also explain why small hexagonal CoMoS slabs were observed to adopt a curved shape under the HDS conditions, such as in Figure 6b.

Second, what is the underlying process that causes the dynamic edge structure observed on the low index Co-substituted S edges during the desulfurization of methylthiol? From the work of Mom et al.[22] and Grønborg et al.[21], we know that the atomic structure of the Mo edges of a CoMoS slab not only depends on the equilibrium with the H_2 and H_2S in the gas phase, but also on the CH_3SH sorption kinetics and the C-S bond dissociation barriers on the respective edges. On the Mo edge, it is known that a 38 % S-CH_3SH edge structure is dominant due to the fast adsorption/desorption process of CH_3SH. The Co-substituted edges of the CoMoS slabs under 100% CH_3SH conditions showed an edge structure that is not time-averaged (see Figure 5c) likely due to the high desorption barrier for CH_3SH on the Co-substituted edge. If the C-S bond dissociation barriers on the Co-substituted edge are low, then it is possible that the appearance and disappearance of the bright features observed in Figure 7, 8 and 9 is due to the desulfurization process forming CH_4 and leaving behind an SH group which is imaged by the STM. The disappearance of the bright feature will then be due to the H_2S desorption process on the Co-substituted edge regenerating the active site for the next catalytic cycle. Turn over frequencies of around 0.1-10 s^{-1} are typically observed on highly optimized industrial HDS catalysts.[1,9,37] Even if the CoMoS slabs used in this experiment were just as active, the desulfurization process would only occur on a time scale that can be captured by the ReactorSTM.

Third, what is the mechanism of the Co transport from CoMoS slabs under the HDS conditions? A possible mechanism could be that under HDS conditions, attachment of methylthiol weakens the binding of Co to the edges of MoS_2 especially along the curved edges thereby, enhancing the Co diffusion. Enhanced diffusion of Co on Au(111) in the presence of H_2S even at vacuum pressures and

room temperature has been observed in previous experiments.[48] In general, gas phase molecules and adsorbates can profoundly affect the mass transport phenomena on a surface. The effect of gasses has been observed on the shapes of nanoparticles and islands[49,50], surface reconstructions[51,52], step morphologies[53], surface roughening[54–56] and segregation.[57–59] Many of these effects are attributed to a 'skyhook' effect where the surface diffusion coefficients are greatly enhanced in the presence of gas molecules.[60] Etching of the CoMoS basal plane by hydrogen could be yet another explanation. This explanation is not possible as we do not observe this effect in a pure hydrogen atmosphere. Furthermore, etching of the MoS_2 basal planes by hydrogen is known to occur only at temperatures > 700K which is far above the temperatures used in our experiments.[61–63] A third possible explanation is that of tip-sample interactions. If tip effects played a role, then the onset of the process with the progress of the STM scan would be observed. This, however, was not the case in our experiments as we observed CoMoS slabs with irregular edges irrespective of the scanning time and position on the sample. By the time the STM scans were commenced, the CoMoS slabs were already under HDS conditions for >4 hours. Furthermore, the conditions used for tunneling in the experiments presented in this work are similar to those used in previous literature reports involving MoS_2 and CoMoS slabs both in vacuum and at high-pressure conditions.[21,22,40,41,43,64] Prior work has not reported any tip-induced mass transport effects of Co or Mo from the CoMoS slab edges at these tunneling conditions. Furthermore, voltage pulsing has also been avoided while scanning over the CoMoS slabs under all the conditions presented in this work in order to prevent the effects of field-induced processes. Therefore, tip effects are highly unlikely to be the cause of the mass transport. However, why the mass transport is observed only on some of the edges of the CoMoS slabs is not known.

In this work, several new edge structures have been observed on the CoMoS slabs under synthesis, reducing, organosulfur exposure and desulfurizing conditions. We have interpreted the edge structures based on comparison with previous literature work. We note that more than one type of edge structure could give rise to identical STM images as has been observed by Mom et al.[22] Therefore, the edge structures and terminations assigned in this work need to be thoroughly investigated and verified by DFT calculations. Furthermore, theoretical studies on the interactions of Co atoms present in the edges of CoMoS slabs with the organosulfur molecules and hydrogen could provide insights into the observed mass transport of Co under the HDS conditions. Such mass transport effects possibly play a major role in catalyst deactivation that is observed in the industry. Furthermore, given our observation that the larger CoMoS slabs have a higher tendency to form irregular edges, future theoretical modelling of CoMoS slabs should be based on larger slab sizes.

6.4 Conclusions

In this work, we have presented the first in situ observation of CoMoS slabs supported on Au(111) using the ReactorSTM under industrially-relevant HDS reaction conditions. We have observed a variety of edge structures of the CoMoS slabs under sulfiding, reducing and desulfurizing conditions. Our work shows that the atomic structure of the edges of the CoMoS slabs is very sensitive to these gas conditions. The in situ STM movies acquired under HDS conditions show that the atomic structure of the edges of the CoMoS slabs is time variant. Additionally, we also observe the mass transport Co

atoms along the Co-substituted edges of the CoMoS slabs which causes the edges to appear highly irregular and contain high index terminations involving coordinatively-unsaturated Co atoms. Such high index edges have never been observed in the previous vacuum or low pressure studies. The results presented in this work open many avenues for future fundamental research on HDS through more experiments and DFT calculations. Furthermore, our findings greatly emphasize the need to perform fundamental studies on complex catalytic processes like HDS in situ under industrially-relevant conditions.

6.5 References

(1) Wu, G.; Yin, Y.; Chen, W.; Xin, F.; Lu, Y.; Qin, K.; Zhang, L.; Song, Y.; Li, M. Catalytic Kinetics for Ultra-Deep Hydrodesulfurization of Diesel. *Chem. Eng. Sci.* 2020, *214*. https://doi.org/10.1016/j.ces.2019.115446.

(2) Miller, J.; Jin, L. *Global Progress toward Soot-Free Diesel Vehicles in 2019*; 2019.

(3) de León, J. N. D.; Kumar, C. R.; Antúnez-García, J.; Fuentes-Moyado, S. Recent Insights in Transition Metal Sulfide Hydrodesulfurization Catalysts for the Production of Ultra Low Sulfur Diesel: A Short Review. *Catalysts*. 2019. https://doi.org/10.3390/catal9010087.

(4) Gaur, A.; Hartmann Dabros, T. M.; Høj, M.; Boubnov, A.; Prüssmann, T.; Jelic, J.; Studt, F.; Jensen, A. D.; Grunwaldt, J. D. Probing the Active Sites of MoS_2 Based Hydrotreating Catalysts Using Modulation Excitation Spectroscopy. *ACS Catal.* 2019, *9* (3), 2568–2579. https://doi.org/10.1021/acscatal.8b04778.

(5) Lauritsen, J. V.; Kibsgaard, J.; Olesen, G. H.; Moses, P. G.; Hinnemann, B.; Helveg, S.; Nørskov, J. K.; Clausen, B. S.; Topsøe, H.; Lægsgaard, E.; Besenbacher, F. Location and Coordination of Promoter Atoms in Co- and Ni-Promoted MoS_2-Based Hydrotreating Catalysts. *J. Catal.* 2007, *249* (2), 220–233. https://doi.org/10.1016/j.jcat.2007.04.013.

(6) Zhu, Y.; Ramasse, Q. M.; Brorson, M.; Moses, P. G.; Hansen, L. P.; Topsøe, H.; Kisielowski, C. F.; Helveg, S. Location of Co and Ni Promoter Atoms in Multi-Layer MoS_2 Nanocrystals for Hydrotreating Catalysis. *Catal. Today* 2016, *261*, 75–81. https://doi.org/10.1016/j.cattod.2015.08.053.

(7) Brorson, M.; Carlsson, A.; Topsøe, H. Carbon-Supported Hydrotreating Catalysts: Morphology of MoS_2, Co-MoS_2 and Ni-MoS_2 Nanoclusters as Observed by HAADF-STEM. In *ACS National Meeting Book of Abstracts*; 2006; Vol. 232.

(8) Brorson, M.; Carlsson, A.; Topsøe, H. The Morphology of MoS_2, WS_2, Co-Mo-S, Ni-Mo-S and Ni-W-S Nanoclusters in Hydrodesulfurization Catalysts Revealed by HAADF-STEM. *Catal. Today* 2007, *123* (1–4), 31–36. https://doi.org/10.1016/j.cattod.2007.01.073.

(9) Shafiq, I.; Shafique, S.; Akhter, P.; Yang, W.; Hussain, M. Recent Developments in Alumina Supported Hydrodesulfurization Catalysts for the Production of Sulfur-Free Refinery Products: A Technical Review. *Catal. Rev. - Sci. Eng.* 2020. https://doi.org/10.1080/01614940.2020.1780824.

(10) Rochet, A.; Baubet, B.; Moizan, V.; Pichon, C.; Briois, V. Co-K and Mo-K Edges Quick-XAS

Study of the Sulphidation Properties of Mo/Al_2O_3 and $CoMo/Al_2O_3$ Catalysts. *Comptes Rendus Chim.* 2016, *19* (10), 1337–1351. https://doi.org/10.1016/j.crci.2016.01.009.

(11) van Haandel, L.; Smolentsev, G.; van Bokhoven, J. A.; Hensen, E. J. M.; Weber, T. Evidence of Octahedral Co–Mo–S Sites in Hydrodesulfurization Catalysts as Determined by Resonant Inelastic X-Ray Scattering and X-Ray Absorption Spectroscopy. *ACS Catal.* 2020, *10* (19), 10978–10988. https://doi.org/10.1021/acscatal.0c03062.

(12) van Haandel, L.; Hensen, E. J. M.; Weber, T. High-pressure Flow Reactor for in Situ X-Ray Absorption Spectroscopy of Catalysts in Gas-Liquid Mixtures—A Case Study on Gas and Liquid Phase Activation of a $Co\text{-}Mo/Al_2O_3$ Hydrodesulfurization Catalyst. *Catal. Today* 2017, *292*, 51–57. https://doi.org/10.1016/j.cattod.2016.08.027.

(13) Chang, C. J.; Zhu, Y.; Wang, J.; Chen, H. C.; Tung, C. W.; Chu, Y. C.; Chen, H. M. In Situ X-Ray Diffraction and X-Ray Absorption Spectroscopy of Electrocatalysts for Energy Conversion Reactions. *J. Mater. Chem. A* 2020, *8* (37), 19079–19112. https://doi.org/10.1039/d0ta06656g.

(14) Tougerti, A.; Simon, P.; Desjacques, C.; Girardon, J. S.; Mazzanti, F.; Pipolo, S.; Trentesaux, M.; Cristol, S. Rethinking Electronic and Geometric Structures of Real Hydrodesulfurization Catalysts by in Situ Photon-In/Photon-Out Spectroscopy. *J. Phys. Chem. C* 2020, *124* (32), 17586–17598. https://doi.org/10.1021/acs.jpcc.0c03429.

(15) Bremmer, G. M.; Van Haandel, L.; Hensen, E. J. M.; Frenken, J. W. M.; Kooyman, P. J. Instability of $NiMoS_2$ and $CoMoS_2$ Hydrodesulfurization Catalysts at Ambient Conditions: A Quasi in Situ High-Resolution Transmission Electron Microscopy and X-Ray Photoelectron Spectroscopy Study. *J. Phys. Chem. C* 2016, *120* (34), 19204–19211. https://doi.org/10.1021/acs.jpcc.6b06030.

(16) Liu, X.; Hou, X.; Zhang, Y.; Yuan, H.; Hong, X.; Liu, G. In Situ Formation of CoMoS Interfaces for Selective Hydrodeoxygenation of P-Cresol to Toluene. *Ind. Eng. Chem. Res.* 2020, *59* (36), 15921–15928. https://doi.org/10.1021/acs.iecr.0c03589.

(17) Bruix, A.; Füchtbauer, H. G.; Tuxen, A. K.; Walton, A. S.; Andersen, M.; Porsgaard, S.; Besenbacher, F.; Hammer, B.; Lauritsen, J. V. In Situ Detection of Active Edge Sites in Single-Layer MoS_2 Catalysts. *ACS Nano* 2015, *9* (9), 9322–9330. https://doi.org/10.1021/acsnano.5b03199.

(18) Guerrero-Pérez, M. O.; Rojas, E.; Gutiérrez-Alejandre, A.; Ramírez, J.; Sánchez-Minero, F.; Fernández-Vargas, C.; Bañares, M. A. In Situ Raman Studies during Sulfidation, and Operando Raman-GC during Ammoxidation Reaction Using Nickel-Containing Catalysts: A Valuable Tool to Identify the Transformations of Catalytic Species. *Phys. Chem. Chem. Phys.* 2011, *13* (20), 9260–9267. https://doi.org/10.1039/c0cp02242j.

(19) Guerrero-Pérez, M. O.; Bañares, M. A. Observing Heterogeneous Cataysts While They Are Working: Operando Raman Spectroscopy. *Spectrosc. (Santa Monica)* 2012, *27* (10).

(20) Polo-Garzon, F.; Luo, S.; Cheng, Y.; Page, K. L.; Ramirez-Cuesta, A. J.; Britt, P. F.; Wu, Z. Neutron Scattering Investigations of Hydride Species in Heterogeneous Catalysis.

ChemSusChem. 2019, pp 93–103. https://doi.org/10.1002/cssc.201801890.

(21) Grønborg, S. S.; Salazar, N.; Bruix, A.; Rodríguez-Fernández, J.; Thomsen, S. D.; Hammer, B.; Lauritsen, J. V. Visualizing Hydrogen-Induced Reshaping and Edge Activation in MoS_2 and Co-Promoted MoS_2 Catalyst Clusters. *Nat. Commun.* 2018, *9* (1), 1–11.

(22) Mom, R. V.; Louwen, J. N.; Frenken, J. W. M.; Groot, I. M. N. In Situ Observations of an Active MoS_2 Model Hydrodesulfurization Catalyst. *Nat. Commun.* 2019, *10* (1). https://doi.org/10.1038/s41467-019-10526-0.

(23) Herbschleb, C. T.; Van Der Tuijn, P. C.; Roobol, S. B.; Navarro, V.; Bakker, J. W.; Liu, Q.; Stoltz, D.; Cañas-Ventura, M. E.; Verdoes, G.; Van Spronsen, M. A.; Bergman, M.; Crama, L.; Taminiau, I.; Ofitserov, A.; Van Baarle, G. J. C.; Frenken, J. W. M. The ReactorSTM: Atomically Resolved Scanning Tunneling Microscopy under High-Pressure, High-Temperature Catalytic Reaction Conditions. *Rev. Sci. Instrum.* 2014, *85* (8), 83703. https://doi.org/10.1063/1.4891811.

(24) Rost, M. J.; Crama, L.; Schakel, P.; Van Tol, E.; Van Velzen-Williams, G. B. E. M.; Overgauw, C. F.; Ter Horst, H.; Dekker, H.; Okhuijsen, B.; Seynen, M.; Vijftigschild, A.; Han, P.; Katan, A. J.; Schoots, K.; Schumm, R.; Van Loo, W.; Oosterkamp, T. H.; Frenken, J. W. M. Scanning Probe Microscopes Go Video Rate and Beyond. *Rev. Sci. Instrum.* 2005, *76* (5), 053710. https://doi.org/10.1063/1.1915288.

(25) Rost, M. J.; van Baarle, G. J. C.; Katan, A. J.; van Spengen, W. M.; Schakel, P.; van Loo, W. A.; Oosterkamp, T. H.; Frenken, J. W. M. Video-Rate Scanning Probe Control Challenges: Setting the Stage for a Microscopy Revolution. *Asian J. Control* 2009, *11* (2), 110–129.

(26) Horcas, I.; Fernández, R.; Gómez-Rodríguez, J. M.; Colchero, J.; Gómez-Herrero, J.; Baro, A. M. WSXM: A Software for Scanning Probe Microscopy and a Tool for Nanotechnology. *Rev. Sci. Instrum.* 2007, *78* (1), 013705. https://doi.org/10.1063/1.2432410.

(27) Horcas, I.; Fernández, R.; Gómez-Rodríguez, J. M.; Colchero, J.; Gómez-Herrero, J.; Baro, A. M. WSXM: A Software for Scanning Probe Microscopy and a Tool for Nanotechnology. *Rev. Sci. Instrum.* 2007, *78* (1), 013705. https://doi.org/10.1063/1.2432410.

(28) Brunet, S.; Mey, D.; Pérot, G.; Bouchy, C.; Diehl, F. On the Hydrodesulfurization of FCC Gasoline: A Review. *Applied Catalysis A: General.* 2005, pp 143–172. https://doi.org/10.1016/j.apcata.2004.10.012.

(29) Wagner, C. D. Sensitivity Factors for XPS Analysis of Surface Atoms. *J. Electron Spectros. Relat. Phenomena* 1983, *32* (2), 99–102. https://doi.org/10.1016/0368-2048(83)85087-7.

(30) Bremmer, G. M.; van Haandel, L.; Hensen, E. J. M.; Frenken, J. W. M.; Kooyman, P. J. The Effect of Oxidation and Resulfidation on (Ni/Co)MoS_2 Hydrodesulfurisation Catalysts. *Appl. Catal. B Environ.* 2019, *243*, 145–150. https://doi.org/10.1016/j.apcatb.2018.10.014.

(31) Helveg, S.; Lauritsen, J. V.; Lægsgaard, E.; Stensgaard, I.; Nørskov, J. K.; Clausen, B. S.; Topsøe, H.; Besenbacher, F. Atomic-Scale Structure of Single-Layer MoS_2 Nanoclusters. *Phys.*

Rev. Lett. 2000, *84* (5), 951–954. https://doi.org/10.1103/PhysRevLett.84.951.

(32) Bruix, A.; Lauritsen, J. V.; Hammer, B. Effects of Particle Size and Edge Structure on the Electronic Structure, Spectroscopic Features, and Chemical Properties of Au(111)-Supported MoS_2 Nanoparticles. *Faraday Discuss.* 2016, *188*, 323–343. https://doi.org/10.1039/c5fd00203f.

(33) Jaramillo, T. F.; Jørgensen, K. P.; Bonde, J.; Nielsen, J. H.; Horch, S.; Chorkendorff, I. Identification of Active Edge Sites for Electrochemical H_2 Evolution from MoS_2 Nanocatalysts. *Science (80-.).* 2007, *317* (5834), 100–102. https://doi.org/10.1126/science.1141483.

(34) Kibsgaard, J.; Chen, Z.; Reinecke, B. N.; Jaramillo, T. F. Engineering the Surface Structure of MoS_2 To Preferentially Expose Active Edge Sites ForÂ Electrocatalysis. *Nat. Mater.* 2012, *11* (11), 963–969. https://doi.org/10.1038/nmat3439.

(35) Prabhu, M. K.; Boden, D.; Rost, M. J.; Meyer, J.; Groot, I. M. N. Structural Characterization of a Novel Two-Dimensional Material: Cobalt Sulfide Sheets on Au(111). *J. Phys. Chem. Lett.* 2020, *11* (21), 9038–9044. https://doi.org/10.1021/acs.jpclett.0c02268.

(36) Byskov, L. S.; Nørskov, J. K.; Clausen, B. S.; Topsøe, H. Edge Termination of MoS_2 and CoMoS Catalyst Particles. *Catal. Letters* 2000, *64* (2–4), 95–99. https://doi.org/10.1023/a:1019063709813.

(37) Babich, I. V.; Moulijn, J. A. Science and Technology of Novel Processes for Deep Desulfurization of Oil Refinery Streams: A Review. *Fuel.* 2003, pp 607–631. https://doi.org/10.1016/S0016-2361(02)00324-1.

(38) Šarić, M.; Rossmeisl, J.; Moses, P. G. Modeling the Adsorption of Sulfur Containing Molecules and Their Hydrodesulfurization Intermediates on the Co-Promoted MoS_2 Catalyst by DFT. *J. Catal.* 2018, *358*, 131–140. https://doi.org/10.1016/j.jcat.2017.12.001.

(39) Prins, R.; Egorova, M.; Röthlisberger, A.; Zhao, Y.; Sivasankar, N.; Kukula, P. Mechanisms of Hydrodesulfurization and Hydrodenitrogenation. In *Catalysis Today*; 2006; Vol. 111, pp 84–93. https://doi.org/10.1016/j.cattod.2005.10.008.

(40) Salazar, N.; Schmidt, S. B.; Lauritsen, J. V. Adsorption of Nitrogenous Inhibitor Molecules on MoS_2 and CoMoS Hydrodesulfurization Catalysts Particles Investigated by Scanning Tunneling Microscopy. *J. Catal.* 2019, *370*, 232–240. https://doi.org/10.1016/j.jcat.2018.12.014.

(41) Tuxen, A. K.; Füchtbauer, H. G.; Temel, B.; Hinnemann, B.; Topsoe, H.; Knudsen, K. G.; Besenbacher, F.; Lauritsen, J. V. Atomic-Scale Insight into Adsorption of Sterically Hindered Dibenzothiophenes on MoS_2 and Co-Mo-S Hydrotreating Catalysts. *J. Catal.* 2012, *295*, 146–154. https://doi.org/10.1016/j.jcat.2012.08.004.

(42) Lauritsen, J. V.; Nyberg, M.; Vang, R. T.; Bollinger, M. V.; Clausen, B. S.; Topsøe, H.; Jacobsen, K. W.; Lægsgaard, E.; Nørskov, J. K.; Besenbacher, F. Chemistry of One-Dimensional Metallic Edge States in MoS_2 Nanoclusters. *Nanotechnology* 2003, *14* (3), 385–389. https://doi.org/10.1088/0957-4484/14/3/306.

(43) Lauritsen, J. V.; Besenbacher, F. Atom-Resolved Scanning Tunneling Microscopy Investigations of Molecular Adsorption on MoS_2 and CoMoS Hydrodesulfurization Catalysts Dedicated to Haldor Topsøe. *J. Catal.* 2015, *328*, 49–58. https://doi.org/10.1016/j.jcat.2014.12.034.

(44) Walton, A. S.; Fester, J.; Bajdich, M.; Arman, M. A.; Osiecki, J.; Knudsen, J.; Vojvodic, A.; Lauritsen, J. V. Interface Controlled Oxidation States in Layered Cobalt Oxide Nanoislands on Gold. *ACS Nano* 2015, *9* (3), 2445–2453. https://doi.org/10.1021/acsnano.5b00158.

(45) Mom, R. V.; Melissen, S. T. A. G.; Sautet, P.; Frenken, J. W. M.; Steinmann, S. N.; Groot, I. M. N. The Pressure Gap for Thiols: Methanethiol Self-Assembly on Au(111) from Vacuum to 1 Bar. *J. Phys. Chem. C* 2019, *123* (19), 12382–12389. https://doi.org/10.1021/acs.jpcc.9b03045.

(46) Besenbacher, F.; Brorson, M.; Clausen, B. S.; Helveg, S.; Hinnemann, B.; Kibsgaard, J.; Lauritsen, J. V.; Moses, P. G.; Nørskov, J. K.; Topsøe, H. Recent STM, DFT and HAADF-STEM Studies of Sulfide-Based Hydrotreating Catalysts: Insight into Mechanistic, Structural and Particle Size Effects. *Catal. Today* 2008, *130* (1), 86–96. https://doi.org/10.1016/j.cattod.2007.08.009.

(47) Krebs, E.; Daudin, A.; Raybaud, P. A DFT Study of CoMoS and NiMoS Catalysts: From Nano-Crystallite Morphology to Selective Hydrodesulfurization. *Oil Gas Sci. Technol. - Rev. l'IFP* 2009. https://doi.org/10.2516/ogst/2009004.

(48) Kibsgaard, J.; Morgenstern, K.; Lægsgaard, E.; Lauritsen, J. V.; Besenbacher, F. Restructuring of Cobalt Nanoparticles Induced by Formation and Diffusion of Monodisperse Metal-Sulfur Complexes. *Phys. Rev. Lett.* 2008, *100* (11), 116104. https://doi.org/10.1103/PhysRevLett.100.116104.

(49) Kalff, M.; Comsa, G.; Michely, T. How Sensitive Is Epitaxial Growth to Adsorbates? *Phys. Rev. Lett.* 1998, *81* (6), 1255–1258. https://doi.org/10.1103/PhysRevLett.81.1255.

(50) Rupprechter, G.; Freund, H. J. Adsorbate-Induced Restructuring and Pressure-Dependent Adsorption on Metal Nanoparticles Studied by Electron Microscopy and Sum Frequency Generation Spectroscopy. *Top. Catal.* 2000, *14* (1–4), 3–14. https://doi.org/10.1023/A:1009094613850.

(51) Ciobîcă, I. M.; van Santen, R. A.; van Berge, P. J.; van de Loosdrecht, J. Adsorbate Induced Reconstruction of Cobalt Surfaces. *Surf. Sci.* 2008, *602* (1), 17–27. https://doi.org/10.1016/j.susc.2007.09.060.

(52) Pai, W. W.; Hsu, C. L.; Lin, M. C.; Lin, K. C.; Tang, T. B. Structural Relaxation of Adlayers in the Presence of Adsorbate-Induced Reconstruction: C60/Cu(111). *Phys. Rev. B - Condens. Matter Mater. Phys.* 2004, *69* (12). https://doi.org/10.1103/PhysRevB.69.125405.

(53) Wintterlin, J.; Trost, J.; Renisch, S.; Schuster, R.; Zambelli, T.; Ertl, G. Real-Time STM Observations of Atomic Equilibrium Fluctuations in an Adsorbate System: O/Ru(0001). *Surf. Sci.* 1997, *394* (1–3), 159–169. https://doi.org/10.1016/S0039-6028(97)00604-3.

(54) Gustafson, J.; Resta, A.; Mikkelsen, A.; Westerström, R.; Andersen, J. N.; Lundgren, E.; Weissenrieder, J.; Schmid, M.; Varga, P.; Kasper, N.; Torrelles, X.; Ferrer, S.; Mittendorfer, F.; Kresse, G. Oxygen-Induced Step Bunching and Faceting of Rh(553): Experiment and Ab Initio Calculations. *Phys. Rev. B - Condens. Matter Mater. Phys.* 2006, *74* (3). https://doi.org/10.1103/PhysRevB.74.035401.

(55) Ozcomert, J. S.; Pai, W. W.; Bartelt, N. C.; Reutt-Robey, J. E. Kinetics of Oxygen-Induced Faceting of Vicinal Ag(110). *Phys. Rev. Lett.* 1994, *72* (2), 258–261. https://doi.org/10.1103/PhysRevLett.72.258.

(56) Jiang, Y.; Li, H.; Wu, Z.; Ye, W.; Zhang, H.; Wang, Y.; Sun, C.; Zhang, Z. In Situ Observation of Hydrogen-Induced Surface Faceting for Palladium–Copper Nanocrystals at Atmospheric Pressure. *Angew. Chemie - Int. Ed.* 2016, *55* (40), 12427–12430. https://doi.org/10.1002/anie.201605956.

(57) Jakub, Z.; Hulva, J.; Ryan, P. T. P.; Duncan, D. A.; Payne, D. J.; Bliem, R.; Ulreich, M.; Hofegger, P.; Kraushofer, F.; Meier, M.; Schmid, M.; Diebold, U.; Parkinson, G. S. Adsorbate-Induced Structural Evolution Changes the Mechanism of CO Oxidation on a $Rh/Fe_3O_4(001)$ Model Catalyst. *Nanoscale* 2020, *12* (10), 5866–5875. https://doi.org/10.1039/c9nr10087c.

(58) Tenney, S. A.; Ratliff, J. S.; Roberts, C. C.; He, W.; Ammal, S. C.; Heyden, A.; Chen, D. A. Adsorbate-Induced Changes in the Surface Composition of Bimetallic Clusters: Pt-Au on $TiO_2(110)$. *J. Phys. Chem. C* 2010, *114* (49), 21652–21663. https://doi.org/10.1021/jp108939h.

(59) Tenney, S. A.; He, W.; Roberts, C. C.; Ratliff, J. S.; Shah, S. I.; Shafai, G. S.; Turkowski, V.; Rahman, T. S.; Chen, D. A. CO-Induced Diffusion of Ni Atoms to the Surface of Ni-Au Clusters on $TiO_2(110)$. *J. Phys. Chem. C* 2011, *115* (22), 11112–11123. https://doi.org/10.1021/jp2014258.

(60) Thiel, P. A.; Shen, M.; Liu, D.-J.; Evans, J. W. Adsorbate-Enhanced Transport of Metals on Metal Surfaces: Oxygen and Sulfur on Coinage Metals. *J. Vac. Sci. Technol. A Vacuum, Surfaces, Film.* 2010, *28* (6), 1285–1298. https://doi.org/10.1116/1.3490017.

(61) Hu, S.; Li, J.; Wang, S.; Liang, Y.; Kang, H.; Zhang, Y.; Chen, Z.; Sui, Y.; Yu, G.; Peng, S.; Jin, Z.; Liu, X. Detecting the Repair of Sulfur Vacancies in CVD-Grown MoS_2 Domains via Hydrogen Etching. *J. Electron. Mater.* 2020. https://doi.org/10.1007/s11664-020-07957-7.

(62) Delmon, B. Influence of Species Diffusing at Surfaces on Reactions of Solids and Catalytic Processes. *Solid State Ionics* 1997, *101–103* (PART 1), 655–660. https://doi.org/10.1016/s0167-2738(97)00288-9.

(63) Chu, X.; Schmidt, L. D. Processes in MoS2 Gasification. *J. Catal.* 1993, *144* (1), 77–92. https://doi.org/10.1006/jcat.1993.1315.

(64) Tuxen, A.; Kibsgaard, J.; Gøbel, H.; Lægsgaard, E.; Topsøe, H.; Lauritsen, J. V.; Besenbacher, F. Size Threshold in the Dibenzothiophene Adsorption on MoS_2 Nanoclusters. *ACS Nano* 2010, *4* (8), 4677–4682. https://doi.org/10.1021/nn1011013.

Chapter 6 - Supporting Information

1. Measured height of MoS_2 slabs

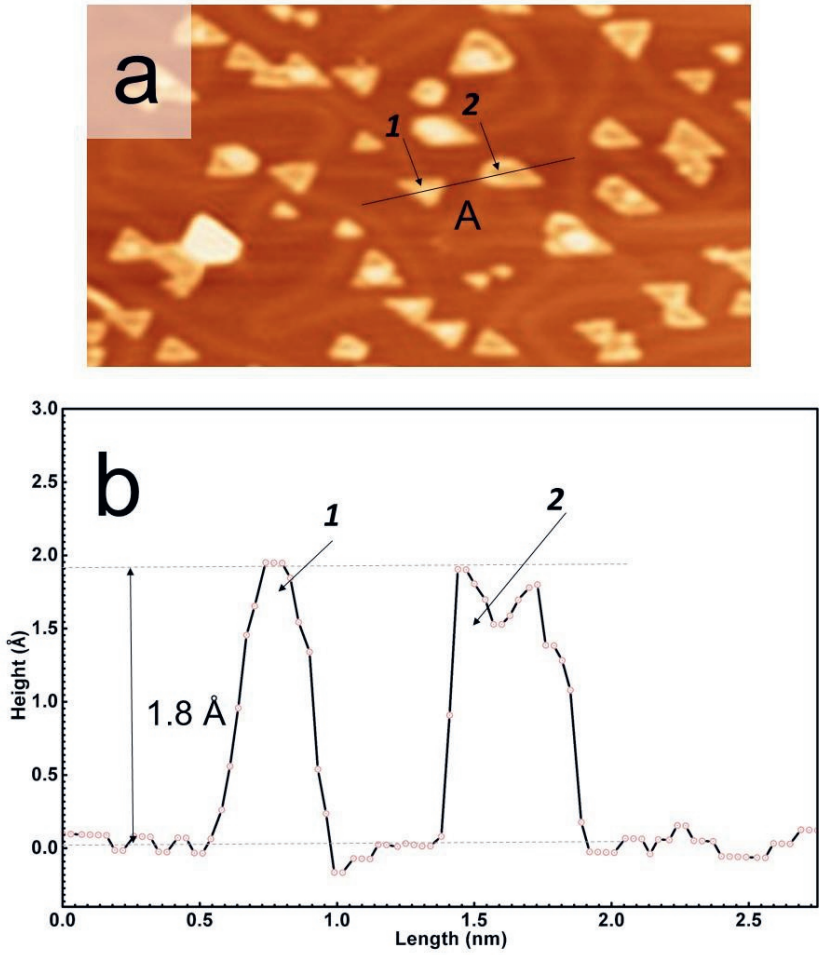

Figure S1: a) STM image of MoS_2 slabs supported on Au(111) measured in UHV with sample voltage = -1 V and tunneling current = 200 pA. b) Measured height along the line marked A in Figure S1a. The slabs marked 1 and 2 in Figure S1a are marked in the height profile as well. Most common normal filter is used to extract the height profile with correctly connected surfaces.

2. CH_3SH adsorption on Co edge

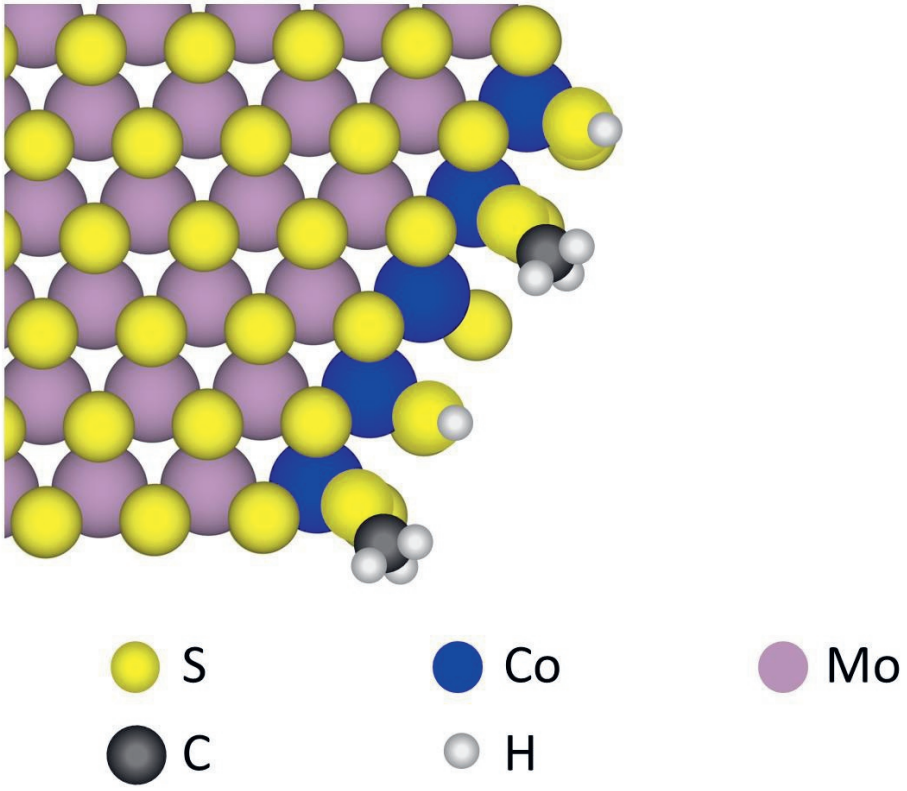

Figure S2: A possible candidate structure of a Co-substituted edge of a reduced CoMoS slab with adsorbed CH_3SH

3. Model for a CoMoS slab with high index terminated edges

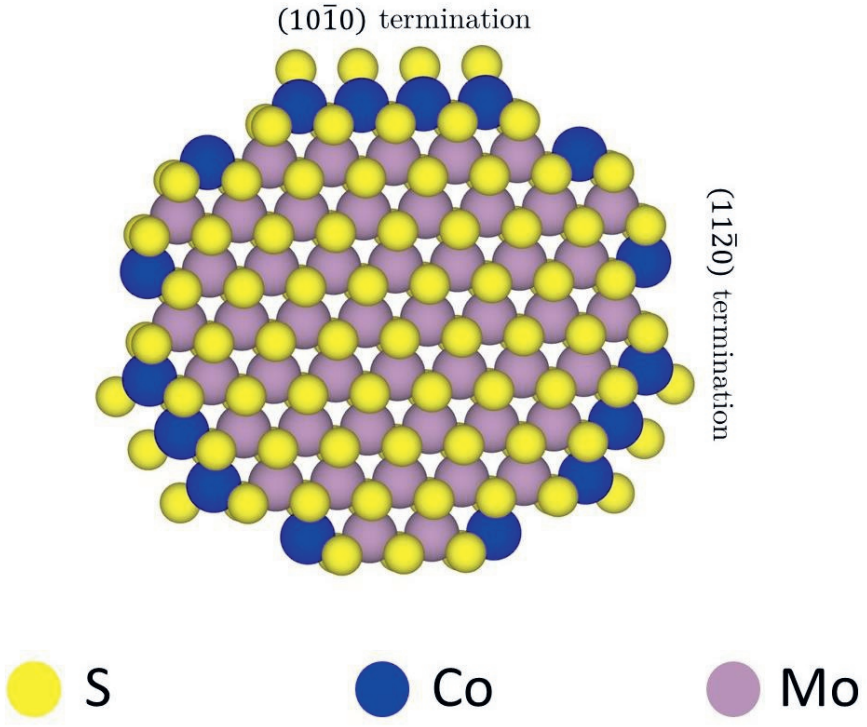

Figure S3: A possible candidate structure for a CoMoS slab with high index terminations

4. STM images of CoMoS slabs under HDS conditions

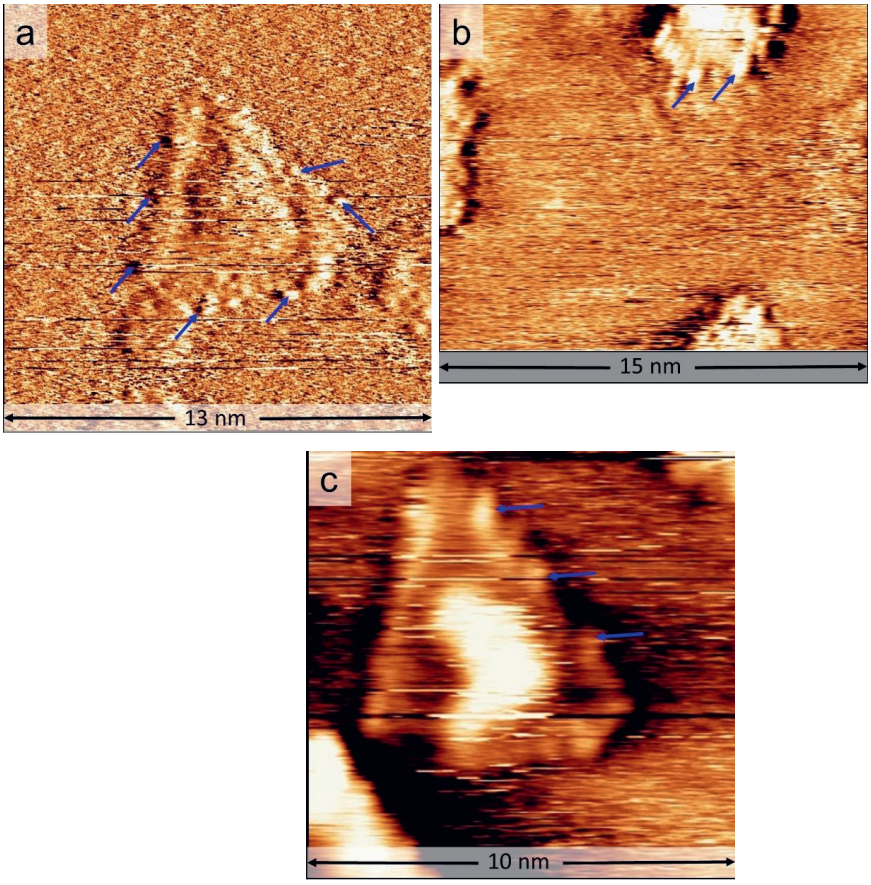

Figure S4: a-c) STM images of CoMoS slabs acquired in situ under HDS conditions. All the images are measured under the following conditions: total pressure = 1 bar (1:9 CH_3SH:H_2), T = 510 K, sample voltage = -0.2 V, tunneling current = 500 pA. The blue arrows indicate the bright and diffuse features on the edges,

5. Atom-resolved STM image of a CoMoS slab after HDS

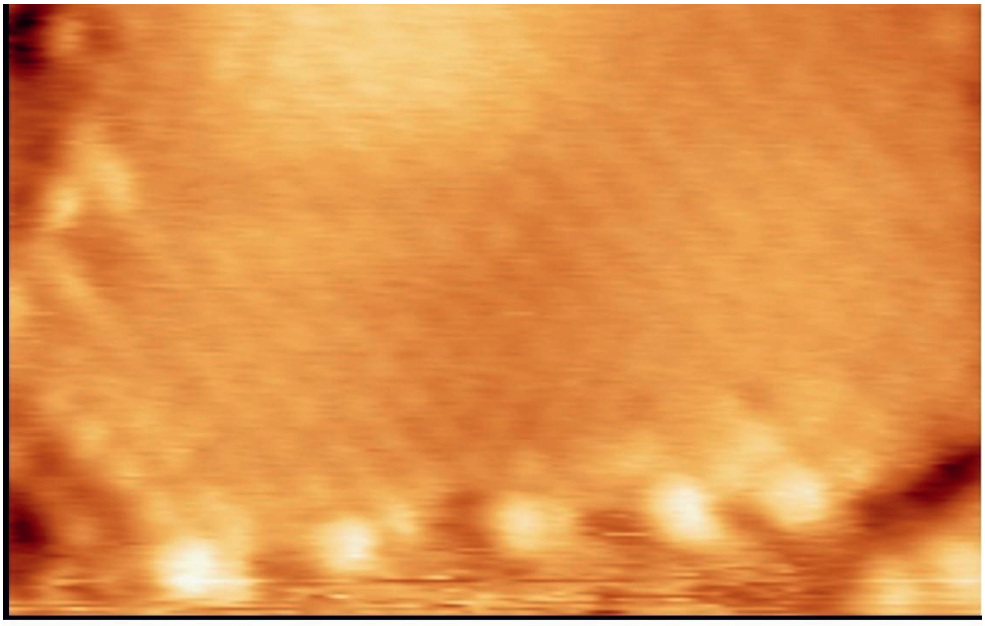

Figure S5: Atom-resolved STM image of a CoMoS slab supported on Au(111) acquired in UHV at room temperature after the HDS experiment; sample voltage = -0.3 V, tunneling current = 200 pA.

6. STM images of CoMoS slabs after HDS

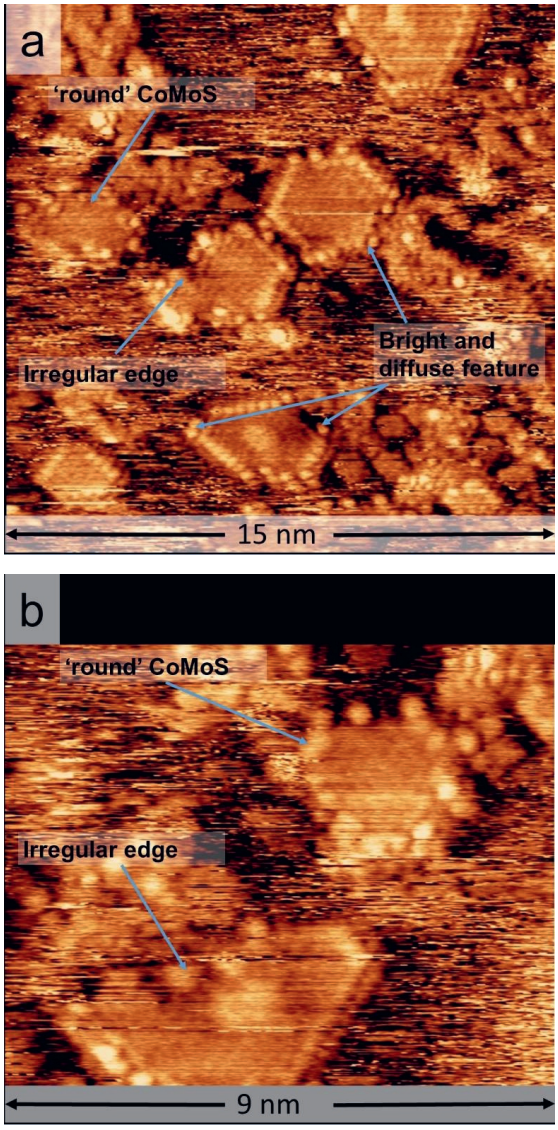

Figure S6: a,b) Large-scale STM images of CoMoS slabs supported on Au(111) acquired in UHV at room temperature after 16 hours of HDS; sample voltage = -0.3 V, tunneling current = 200 pA.

7. In situ STM movies of CoMoS slabs under HDS conditions

M1.mp4 : STM movie of a CoMoS slab measured during the desulfurization of methylthiol. The images have been acquired under the following conditions: total pressure = 0.3 bar (1:1 CH_3SH:H_2), T = 510 K, sample voltage = -0.2 V, tunneling current = 1.2 nA, acquisition time = 14 s/frame.

M2.mp4 : STM movie of a CoMoS slab measured during the desulfurization of methylthiol. The images have been acquired under the following conditions: total pressure = 0.6 bar (1:6 CH_3SH:H_2), T = 510 K, sample voltage = -0.2 V, tunneling current = 1.5 nA, acquisition time = 14 s/frame.

M3.mp4 : STM movie of a CoMoS slab measured during the desulfurization of methylthiol. The images have been acquired under the following conditions: total pressure = 0.6 bar (1:3 CH_3SH:H_2), T = 510 K, sample voltage = -0.2 V, tunneling current = 1.2 nA, acquisition time = 14 s/frame.

The movies can be found in the surfdrive link.

Chapter 7

Outlook

In this thesis, the ReactorSTM set up has been used to gain atomic-level insights into the formation and working of a Co-promoted MoS_2 HDS model catalyst. The work presented in this thesis raises many questions and opens up several avenues for future research. Herein, some of these questions and possible experiments to answer them are mentioned as a scope for future work.

Is it possible to grow multilayer 2D CoS_2 sheets? If yes, can we synthesize a new layered bulk Co sulfide purely by a bottom-up approach?
In the work presented in Chapter 3, the total coverage of CoS_2 has been <1 monolayer (ML). It is currently not known if 2D CoS_2 can also form multilayers supported upon itself. The results of the DFT calculations indicate that the stabilizing interactions with Au(111) are necessary for the formation of a single-layer S-Co-S sheet. Attempts to grow multilayers will test this result of our DFT model. Multilayer CoS_2 could be grown with a recipe that involves repeated deposition of Co followed by annealing in H_2S in a cyclic manner.

Do the other earth-abundant metal sulfides such as those of Cu, Ni and Fe which do not have a layered structure in the bulk also form TMDC structures on Au(111)?
The work done by Kibsgaard et al.[1] reports the formation of the sulfides of Cu, Ni and Fe as byproducts while attempting to grow Ni- Fe- and Cu- promoted MoS_2 respectively. All of these sulfides have an atomically-flat surface, grow strictly as a 2D layer and also have a moiré structure that appears similar to 2D CoS_2, as is evident from their STM images. However, in their work, the metal sulfides are merely identified as a separate phase and not investigated as a possible new TMDC. It is very likely that these metal sulfide sheets are also TMDCs similar to 2D CoS_2. A methodology similar to the one presented in Chapter 3 could be used to grow TMDCs of metals such Ni, Cu and Fe on Au(111) and perform their structural characterization in combination with DFT calculations, thus opening up new avenues for their potential applications. Furthermore, these experiments can also give us valuable insights into the trends for forming supported TMDCs in the periodic table.

Do the results presented in Chapter 4 correlate well with catalysts supported on oxide substrates such as titania or alumina?
To take another major step to bridge the materials gap with the real HDS catalysts, the simultaneous Co and Mo oxide sulfidation experiment could be repeated on a model oxide substrate such as TiO_2(110). The work presented in Chapter 5 takes a step in this direction by sulfiding partially oxidized Mo nanoparticles. Oxide substrates like titania are known to have strong interactions with oxides of Mo and Co. Given the stronger substrate interaction, we can expect a greater barrier to sulfidation and formation of the CoMoS phase.[2,3]

How does sulfidation with pure H_2S compare with using a mixture of H_2 and CH_3SH?

While controlled sulfidation in UHV can give us many structural insights, it is also necessary to perform the sulfidation under industrially-relevant conditions. Furthermore, organosulfur compounds like dimethyldisulfide are commonly used in the industry to sulfide the oxidic catalyst precursor, many a time, also in the presence of H_2. An experiment to gain insights into the relation between the sulfiding agent and the morphology of the CoMoS model catalyst could involve preparing identical mixed Mo- and Co- oxide precursors supported on Au(111) and TiO_2(110). The precursors could then be sulfided in the ReactorSTM using pure H_2S, CH_3SH, a mixture of H_2/H_2S and H_2/CH_3SH respectively. A similar experiment could also be performed with the help of synchrotron-based Near-Ambient Pressure XPS (NAP-XPS) to gain chemical insights into the sulfidation process in situ.

What is the atomic structure of the MoS_x stripes reported in Chapter 5?
To answer this question, diffraction techniques such as LEED, surface-XRD could be used to resolve the atomic structure and by combining these results with DFT calculations, a consistent atomic model can be constructed. A typical experiment could involve growing MoS_2 on the TiO_2(110) substrate using the recipe used in Chapter 5 with an Mo coverage of <0.2 ML. Analysis of the LEED pattern of the TiO_2(110) surface before and after the synthesis of MoS_2 can resolve the atomic structure of the MoS_x stripes. Additionally, the experiment could also be repeated with the addition of Co in the precursor prior to sulfidation. This could provide insights into the possibility of the incorporation of Co in the MoS_x phase. Furthermore, it is also possible that the formation of MoS_x striped phase is dependent on the sulfiding agent. The experiment to investigate this possibility has been discussed in the previous paragraph.

What are the key factors that contribute to the formation of curved CoMoS slabs with higher-index terminations?
In Chapter 6, we have observed the formation of CoMoS slabs with curved edges under HDS conditions. The effect of the partial pressure of methylthiol, the type of the organosulfur compound (aliphatic vs aromatic) and the reaction temperature could all play a key role in the formation of CoMoS slabs with high index edges. The CoMoS model catalyst used in Chapter 6 could be studied under higher partial pressure of CH_3SH, at higher HDS temperature and also with model aromatic thiols such as thiophene. The usage of aromatic thiol vapor will require minor modification of the gas dosing system of the ReactorSTM setup. These studies could be coupled with DFT calculations to investigate the stability of high index Co-substituted S edges such as the $(11\bar{2}0)$ termination.

What are the key factors that contribute to the mass transport along the Co-substituted edges of the CoMoS phase?
The 'chemically blind' nature of the STM makes it very difficult to identify the nature of the diffusing species. Some insights could be gained by studying the 2D-CoS_2 sheets separately under HDS conditions. Analysis of the step edges of these sheets as well as the XPS signatures of Co and S can give valuable insights into the mechanism of Co transport. Using synchrotron-based techniques such as the NAP-XPS, the transport of Co could potentially be tracked with some time resolution. The role of the support interactions could be investigated by using substrates such as TiO_2(110) and highly-oriented pyrolytic graphite (HOPG). These studies could be supported with DFT calculations to understand if the support interactions play a key role in stabilizing the promoter atoms on the edges.

How do the effects observed on CoMoS slabs compare with those of NiMoS slabs?
Ni-substituted MoS_2 slabs have also been synthesized by the Aarhus recipe on Au(111).[4] Such NiMoS model catalysts could be studied under the same HDS conditions as those of CoMoS slabs for a direct comparison of the behavior of Co-substituted and Ni-substituted edges. A follow-up experiment to compare NiMoS and CoMoS slabs could involve the usage of aromatic thiols such as thiophene and dihydrothiophene with isotopic markers, instead of CH_3SH. These experiments could give valuable insights into the relation between the atomic structure of the Co-substituted and Ni-substituted MoS_2 edges and the catalyst activity. Furthermore, theoretical modeling to calculate the barriers for organothiol sorption, C-S bond scission, H_2S desorption etc. can give more insights into the behavior and stability of the promoter-substituted edges.

References

(1) Kibsgaard, J. Atomic-Scale Investigation of MoS_2-Based Hydrotreating Model Catalysts, University of Aarhus, Denmark, 2008.

(2) Tougerti, A.; Simon, P.; Desjacques, C.; Girardon, J. S.; Mazzanti, F.; Pipolo, S.; Trentesaux, M.; Cristol, S. Rethinking Electronic and Geometric Structures of Real Hydrodesulfurization Catalysts by in Situ Photon-In/Photon-Out Spectroscopy. *J. Phys. Chem. C* **2020**, *124* (32), 17586–17598. https://doi.org/10.1021/acs.jpcc.0c03429.

(3) van Haandel, L.; Smolentsev, G.; van Bokhoven, J. A.; Hensen, E. J. M.; Weber, T. Evidence of Octahedral Co–Mo–S Sites in Hydrodesulfurization Catalysts as Determined by Resonant Inelastic X-Ray Scattering and X-Ray Absorption Spectroscopy. *ACS Catal.* **2020**, *10* (19), 10978–10988. https://doi.org/10.1021/acscatal.0c03062.

(4) Lauritsen, J. V.; Kibsgaard, J.; Olesen, G. H.; Moses, P. G.; Hinnemann, B.; Helveg, S.; Nørskov, J. K.; Clausen, B. S.; Topsøe, H.; Lægsgaard, E.; Besenbacher, F. Location and Coordination of Promoter Atoms in Co- and Ni-Promoted MoS_2-Based Hydrotreating Catalysts. *J. Catal.* **2007**, *249* (2), 220–233. https://doi.org/10.1016/j.jcat.2007.04.013.

Summary

The desire to understand the world for what it is, is the basis for fundamental experimental research. Typically, this understanding helps us in designing better technology to improve our life profoundly. Experimental research in the field of catalysis over the last hundred years has led to the advances in chemical technology that have drastically changed our lifestyle from one of survival to that of comfort. This, however, has damaged the environment so much that we are in need of better chemical technology that also preserves the planet for our future generations and the species after us. In order to develop such chemical processes, we first need to understand how the existing processes work using experiments at a very fundamental level, that being, at the atomic scale, so that we can use this information to design, for instance, better catalysts.

In this thesis, we address this challenge for a specific chemical process called Hydrodesulfurization (HDS) which is used for producing clean fuels and petroleum products that meet the stringent emission standards set by the local governments. Despite being a well-established process, we still do not completely understand how it works. In this work, we make an attempt to approach this problem systematically, first, by trying to understand the atomic structure of the hydrodesulfurization catalyst formed by various synthesis procedures and second, by observing the catalyst as the HDS reaction occurs. For this purpose, we make use of a state-of-the-art experimental setup called the ReactorSTM which is a self-contained machine specially designed to resolve the atomic structure of catalysts during the chemical reactions. In the following paragraphs, the findings of the four scientific chapters of this thesis are summarized.

Transition metal dichalcogenides (TMDCs) are a type of two-dimensional (2D) materials widely investigated by both experimentalists and theoreticians, because of their unique properties. In the case of cobalt sulfide, density functional theory (DFT) calculations on freestanding S-Co-S sheets suggest there are no stable 2D forms of cobalt sulfide, whereas experimental observations clearly show TMDC-like structures on Au(111). In chapter 3, we resolve this disagreement by using a combination of experimental techniques and DFT calculations, considering the gold surface explicitly. We find a 2D CoS(0001)-like sheet on Au(111) that delivers excellent agreement between theory and experiment. Uniquely this sheet exhibits a metallic character, contrary to most TMDCs, and exists due to the stabilizing interactions with the Au(111) substrate.

In chapter 4, we present the results of a study carried out to investigate the simultaneous sulfidation of Co and Mo oxide nanoparticles on Au(111) as a synthesis strategy to prepare a model catalyst for hydrodesulfurization (HDS). We make use of scanning tunneling microscope (STM) and X-ray photoelectron spectroscopy (XPS) to track the changes in chemistry and morphology through the synthesis of a mixed Mo and Co oxide precursor and the sulfidation to the respective sulfides. We investigate the effects of temperature and the duration of sulfidation on the completeness of the sulfidation process. Our study shows that the recipe can be used to make a CoMoS model catalyst. However, the yield of the Co-promoted MoS_2 slabs is low because of the kinetically hindered sulfidation of the Mo oxide phase.

MoS_2 supported on oxides like TiO_2 has a broad range of applications. The atomic structure of this system is therefore, very useful to study. Previous research work in this area has made use of high-temperature synthesis methods while the preparation of an MoS_2/TiO_2 in very important applications such as catalysis makes use of a low-temperature synthesis method. In chapter 5, we investigate a low-temperature synthesis strategy for MoS_2 slabs supported on rutile $TiO_2(110)$. Using STM and XPS, we demonstrate that not only flat MoS_2 slabs with irregular shapes but also MoS_x stripes with coordinatively unsaturated Mo atoms are formed. In particular, it becomes evident that for atomic structural characterization of MoS_2/TiO_2 and similar oxide-supported systems grown by low-temperature synthesis methods, the surface structure of the support becomes highly relevant.

In chapter 6, the first direct observations of a Co-promoted MoS_2 slab (CoMoS) under industrially-relevant HDS conditions using the ReactorSTM are presented. A model catalyst containing the Co-promoted MoS_2 slabs supported on an Au(111) substrate has been used. Initially, we image the CoMoS slabs under 100% H_2 and 100% CH_3SH atmospheres separately. We report a variety of new edge structures for the Co-substituted edges of the CoMoS slabs. Additionally, during the desulfurization of CH_3SH, we observe a dynamic edge structure on the Co-substituted edge. The HDS reaction gasses transform hexagonal CoMoS slabs into curved CoMoS slabs with high index edge terminations. Additionally, we also observe mass transport from the larger CoMoS slabs along the Co-substituted edges which causes the edges to appear highly irregular. XPS results show that this mass transport could likely be due to the loss of the Co promoter atoms. Our experimental observations emphasize the importance of studying a complex catalyst such as Co-promoted MoS_2 during the catalysis process. The results presented in this work open up avenues for more fundamental research on HDS and theoretical modeling with DFT calculations.

Samenvatting

De wens om de wereld te begrijpen is de basis voor fundamenteel experimenteel onderzoek. Doorgaans helpt dit begrip ons bij het ontwerpen van betere technologie om ons leven te verbeteren. In de afgelopen honderd jaar heeft experimenteel onderzoek op het gebied van katalyse geleid tot de vooruitgang in de chemische technologie die onze levensstijl drastisch heeft veranderd van overleven naar comfort. Dit heeft het milieu echter zo erg beschadigd dat we een betere chemische technologie nodig hebben die ook de planeet bewaart voor toekomstige generaties en de soorten na ons. Om dergelijke chemische processen te ontwikkelen, moeten we eerst begrijpen hoe de bestaande processen werken met behulp van experimenten op een zeer fundamenteel niveau, namelijk op atomaire schaal, zodat we deze informatie kunnen gebruiken om betere katalysatoren te ontwerpen.

In dit proefschrift gaan we in op deze uitdaging voor een specifiek chemisch proces genaamd hydro-ontzwaveling (HDS) dat wordt gebruikt voor het produceren van brandstoffen en aardolieproducten die voldoen aan de strenge emissienormen van de lokale overheden. Ondanks dat het een veel gebruikt proces is, begrijpen we nog steeds niet volledig hoe het werkt. In dit proefschrift doen we een poging om dit probleem systematisch te benaderen, ten eerste door te proberen de atomaire structuur te begrijpen van de hydro-ontzwavelingskatalysator gevormd door verschillende syntheseprocedures en ten tweede door de katalysator te observeren terwijl de HDS-reactie plaatsvindt. Voor dit doel maken we gebruik van een ultramoderne experimentele opstelling genaamd de ReactorSTM, een op zichzelf staande machine die speciaal is ontworpen om de atomaire structuur van katalysatoren tijdens de chemische reacties zichtbaar te maken. In de volgende paragrafen worden de bevindingen van de vier wetenschappelijke hoofdstukken van dit proefschrift samengevat.

Overgangsmetaaldichalcogeniden (TMDC's) zijn een soort twee-dimensionale (2D) materialen die op grote schaal worden onderzocht door zowel experimentatoren als theoretici, vanwege hun unieke eigenschappen. In het geval van kobaltsulfide suggereren berekeningen met behulp van dichtheidsfunctionaaltheorie (DFT) op vrijstaande S-Co-S-platen dat er geen stabiele vormen van 2D-kobaltsulfide zijn, terwijl experimentele waarnemingen duidelijk TMDC-achtige structuren op Au(111) laten zien. In hoofdstuk 3 lossen we dit meningsverschil op door een combinatie van experimentele technieken en DFT-berekeningen te gebruiken, waarbij we het goud oppervlak expliciet beschouwen. We vinden een laag van een 2D CoS(0001)-achtige structuur op Au(111) dat een uitstekende overeenkomst geeft tussen theorie en experiment. Uniek is dat deze structuur een metaalachtig karakter vertoont, in tegenstelling tot de meeste TMDC's, en bestaat vanwege de stabiliserende interacties met het Au(111)-substraat.

In hoofdstuk 4 presenteren we de resultaten van een studie die is uitgevoerd om de gelijktijdige sulfidering van Co- en Mo-oxide-nanodeeltjes op Au(111) te onderzoeken als een synthesestrategie om een modelkatalysator voor hydro-ontzwaveling (HDS) te maken. We maken gebruik van rastertunnel microscopie en röntgen fotoelektronenspectroscopie om de veranderingen in chemie en morfologie te volgen tijdens de synthese van een gemengde Mo en Co oxide precursor en de sulfidering naar de respectievelijke sulfiden. We onderzoeken de effecten van temperatuur en de duur van sulfidering op de volledigheid van het sulfideringsproces. Onze studie toont aan dat de vorming van MoS_2 met de

CoMoS-rand niet wordt beïnvloed door de tijd of de temperatuur van sulfidering. De opbrengst van de Co-gepromote MoS_2 katalysatoren wordt echter beperkt door de vorming van grote clusters als gevolg van de verspreiding van Mo- en Co-oxidefasen na sulfidering. Volledige sulfidering van de gemengde oxide precursor tot MoS_2 met Co promoter atomen kan worden versneld door de sulfideringstemperatuur te verhogen tot 730 K vanwege de thermisch geactiveerde aard van Mo oxide sulfidering. We tonen dus aan dat het gebruik van een gemengde Mo- en Co-oxide-precursor als uitgangspunt voor de MoS_2-fase met Co promoter atomen voor fundamentele katalytische studies een haalbare strategie is.

MoS_2 ondersteund op oxiden zoals TiO_2 heeft een breed scala aan toepassingen. Het is daarom erg nuttig om de atomaire structuur van dit systeem te bestuderen. Eerder onderzoek op dit gebied heeft gebruik gemaakt van synthesemethoden bij hoge temperatuur, terwijl het maken van een MoS_2/TiO_2 in zeer belangrijke toepassingen zoals katalyse gebruik maakt van een synthesemethode bij lage temperatuur. In hoofdstuk 5 onderzoeken we een lage-temperatuursynthesestrategie voor MoS_2 katalysatoren ondersteund op rutiel $TiO_2(110)$. Met behulp van rastertunnel microscopie en röntgen fotoelektronenspectroscopie laten we zien dat niet alleen vlakke MoS_2-lagen met onregelmatige vormen maar ook MoS_x-strepen met een groot aantal coördinatief onverzadigde Mo-atomen worden gevormd. In het bijzonder wordt het duidelijk dat voor structurele karakterisering op atomair niveau van MoS_2/TiO_2 en vergelijkbare oxide-ondersteunde systemen gegroeid met lage temperatuur synthesemethoden, de oppervlaktestructuur van de drager zeer relevant wordt.

In hoofdstuk 6 worden de eerste directe waarnemingen van een MoS_2 katalysator met Co promoter atomen (CoMoS) onder industrieel relevante HDS-omstandigheden met behulp van de ReactorSTM gepresenteerd. Er is een modelkatalysator gebruikt die de MoS_2-lagen met Co promoter atomen bevat die worden gedragen op een Au(111) substraat. Aanvankelijk beelden we de CoMoS katalysatoren afzonderlijk af onder 100% H_2- en 100% CH_3SH-atmosferen. We rapporteren een verscheidenheid aan nieuwe randstructuren voor de Co-gesubstitueerde randen van de CoMoS katalysatoren. Bovendien zien we tijdens de ontzwaveling van CH_3SH een dynamische randstructuur op de Co-gesubstitueerde rand. We nemen waar dat de ontzwaveling hexagonale CoMoS-lagen transformeert in afgeronde CoMoS-lagen met randen met een hogere index. Bovendien observeren we ook massatransport van de grotere CoMoS-lagen langs de Co-gesubstitueerde randen, waardoor ze een onregelmatige rand vertonen, waarschijnlijk met voorheen onbekende randafsluitingen. Onze experimentele waarnemingen benadrukken het belang van het bestuderen van een complexe katalysator zoals MoS_2 met Co promoter atomen tijdens het katalyseproces. De resultaten die in dit werk worden gepresenteerd, openen wegen voor meer fundamenteel onderzoek naar HDS en theoretische modellering met DFT-berekeningen.

Acknowledgements

I would like to thank my supervisor Dr. Irene Groot for giving me the freedom to select my own research projects while also providing sound scientific advice. Her supervision, generosity and support throughout this project have made this thesis a reality.

I am grateful to Dr. Marcel Rost and prof. Dr. Joost Frenken for the scientific discussions during the weekly group meetings that have helped me streamline my research work to answer key questions. Especially the technical discussions with Dr. Marcel Rost have helped me understand the hidden technical nuances of many of the surface characterization techniques used in this thesis. I thank prof. Dr. Eelco Vogt and Dr. Jaap Louwen for the discussion on hydrodesulfurization at Albemarle.

The work carried out in this thesis has also involved many collaborators without whose team work and effort, this thesis would not have been possible. I would like to thank Dajo Boden and Dr. Jörg Meyer for the DFT calculations and the scientific discussions. I would like to thank Angelique van Vark, Tori Andrewson, Maarten Stam, Cecelia Mweka and all the bachelor LO students for their contributions.

A good research environment is incomplete without friendly fellow students to share the time and space with. I thank Sabine Wenzel, Dajo Boden, Sabine Auras, Maud van Boven, Stefan Raaijman, Dr. Nakkiran Arulmozhi, Tjerk Benschop, and Richard van Lent for the making the environment fun to work in at all times. I thank Dr. Amir Mehdi Saedi for demonstrating the art of asking difficult scientific questions politely. I want to especially thank Gesa Welker for being there through the tough times and for regularly checking on my safety in the measurement hall.

Moving a dedicated STM and then making it work better than before would not have been possible without the indubitable and sound technical support from the Electronics and Fine mechanics departments. I would like to thank Mirthe Bergman, Fred Schenkel, Ko Koning, Bert Crama, and Peter van Veldhuizen for all their insights and support throughout this project.

Ultimately, I want to thank my parents and my sister for being infinitely patient with me and for all the silent encouragement and prayers. I am grateful to them for fully supporting my desire to pursue a scientific career throughout the last decade.

Curriculum Vitae

Mahesh Krishna Prabhu was born in Kochi, Kerala, India in March 1991. He completed his schooling from Kendriya Vidyalaya No. 1, Kalpakkam in the year 2008. Thereafter, he pursued a Bachelor degree in chemical engineering at the National Institute of technology, Trichy, India. He continued his studies further through a Master of Science degree in chemical engineering with a chemical product engineering specialization at the Technical University of Delft. During his master thesis project, he worked on developing atomic layer deposition processes for fabricating air-stable quantum dot films for optoelectronic applications in the groups of Dr. Arjan Houtepen and Prof. Dr. Ruud van Ommen. After his graduation, he continued his research in the group of Dr. Ranjani Vishwanatha at the Jawaharlal Nehru center for Advanced Scientific Research, India. Here, he developed an integrated liquid-phase atomic layer deposition process for synthesizing titanium dioxide-iron pyrite quantum dot films for heavy metal-free photovoltaic devices. Thereafter, he started his Ph.D. project in the Catalysis and Surface Chemistry group at Leiden University with Dr. Irene Groot as his co-promotor and prof. Dr. Marc Koper as the promotor. Most of the work carried out by him during this period is described in this thesis. After his Ph.D. defense, Mahesh Krishna Prabhu will pursue his academic research as a post doc in the group of Dr. Irene Groot at Leiden University.

List of publications

Peer-reviewed publications

1. David Valdesueiro*, Mahesh K. Prabhu*, Carlos Guerra-Nunez, C. S. Suchand Sandeep, Sachin Kinge, Laurens D. A. Siebbeles, Louis C. P. M. de Smet, Gabrie M. H. Meesters, Michiel T. Kreutzer, Arjan J. Houtepen, and J. Ruud van Ommen, Deposition Mechanism of Aluminum Oxide on Quantum Dot Films at Atmospheric Pressure and Room Temperature, *J. Phys. Chem. C* 2016, 120, 8, 4266–4275.

2. Mahesh K. Prabhu*, Dajo Boden*, Marcel J. Rost, Jörg Meyer and Irene M. N. Groot, Structural Characterization of a Novel Two-Dimensional Material: Cobalt Sulfide Sheets on Au(111), J. Phys. Chem. Lett. 2020, 11, 21, 9038–9044

3. Mahesh K. Prabhu and Irene M. N. Groot, Low-Temperature Synthesis Strategy for MoS_2 Slabs Supported on TiO_2(110), Surfaces 2020, 3(4), 605-621

4. Mahesh K. Prabhu and Irene M. N. Groot, Simultaneous sulfidation of Mo and Co oxides supported on Au(111), *Phys. Chem. Chem. Phys.*, 2021, 23, 8403-8412

5. Mahesh K. Prabhu and Irene M. N. Groot, Synthesis Strategy for Co-promoted MoS_2 Slabs Supported on TiO_2(110) *(manuscript under preparation)*

6. Mahesh K. Prabhu*, Dajo Boden*, Marcel J. Rost, Jörg Meyer and Irene M. N. Groot, Application of the DAS model for the structural characterization of TMDCs *(manuscript under preparation)*

7. Mahesh K. Prabhu, Jaap N. Louwen and Irene M. N. Groot, Structural characterization of the Co-substituted S edge of a CoMoS nanocluster:

Substrate effects on the 1D metallic edge states *(manuscript under preparation)*

8. Mahesh K. Prabhu, Jaap N. Louwen and Irene M. N. Groot, In situ observation of hydrodesulfurization on a Co-promoted MoS_2 model HDS catalyst at industrially relevant conditions *(manuscript under preparation)*

9. Mahesh K. Prabhu, Jaap N. Louwen and Irene M. N. Groot, Stability of the Co-substituted S edges of CoMoS nanoclusters under HDS conditions *(manuscript under preparation)*

10. Mahesh K. Prabhu and Irene M. N. Groot, Effect of hydrogen on the sulfidation of Co and Mo nanoparticles : A ReactorSTM study *(manuscript under preparation)*

* Authors have contributed equally to the work

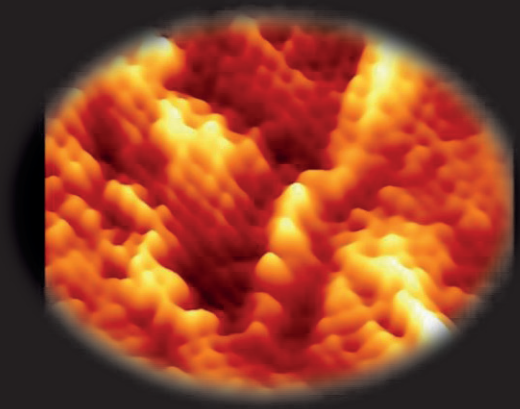

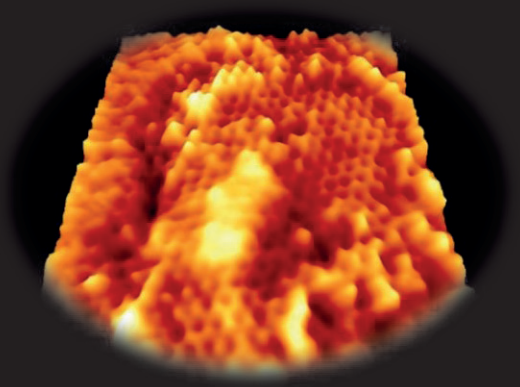

Universiteit Leiden